The production of ultrafine fibres using variations of the centrifugal spinning technique

Tom O'Haire

Submitted in accordance with the requirements for the degree of Doctor of Philosophy

The University of Leeds

School of Design

June 2015

The candidate confirms that the work submitted is his own except where work which has formed part of jointly-authored publications has been included. The contribution of the candidate and other authors to this work has been explicitly indicated below. The candidate confirms that appropriate credit has been given within the thesis where reference has been made to the work of others.

Some of the details of Chapter 6 are an extension of the following published paper:

O'HAIRE, T., RIGOUT, M., RUSSELL, S. & CARR, C. 2014. Influence of nanotube dispersion and spinning conditions on nanofibre nanocomposites of polypropylene and multi-walled carbon nanotubes produced through Forcespinning™. *Journal of Thermoplastic Composite Materials,* 27**,** 205-214.

The candidate (T O'Haire) performed the experiment and analytical works and prepared the initial draft along with graphical publication and presentation of the paper. The co-authors supervised the work and made suggestions to the initial draft.

Acknowledgements

Abstract

Centrifugal spinning uses high speed spinneret rotation to generate and elongate jets of polymeric material in to fine fibres. Variations of this basic technology has been used to form ultrafine fibres from: polypropylene (PP), ubiquitous in the nonwovens industry and a key material for nonwovens; polycaprolactone (PCL), a biocompatible polymer used previously as a biological scaffold; and polyvinylpyrrolidone with 1-triacontane (PVP/TA), a copolymer found in the cosmetics industry. This work demonstrated the melt centrifugal spinning of PP into sub-micron fibres ≤ 500 nm in diameter, and PCL fibres ≤ 900 nm in diameter. The influences of material properties and processing conditions on the fibre and webs properties were investigated and relationships established. For melt spinning, increasing the rotational speed will reduce the average fibre diameter and when solution spinning PCL a binary solvent produced finer fibres with increased surface textures. The spinning of PVP/TA into fibres demonstrated in this work has been previously unreported. PVP/TA fibres were created by centrifugal spinning at low temperatures were as fine as 1.5 µm on average. These fibres were used as an adsorbent and showed an affinity for the capture and retention of disperse dyes and hydrocarbons on the fibre surface. Carbon nanotube composite fibres were created by dispersing the nanotubes in both PP and PCL polymers using ultrasonic waves. The addition of carbon nanotubes significantly increased the level of beading during spinning in both PP and PCL as their presence causing an increase in Rayleigh instabilities. The addition of nanotubes did not improve web strength of the products compared to virgin polymer. Overall, centrifugal spinning has proven to be a highly versatile technique, capable of producing ultrafine fibres from a range of polymer feed materials which have potential to be utilised in a range of specialist applications.

Table of Contents

List of Tables

List of Figures

Chapter 1
Introduction

1.1 **Background**

This work considers the production and utilisation of materials known as nanofibres. The EU definition of a nanomaterial requires the article in question to be finer than 100 nm in at least one direction (European Commission, 2011). Thus, nanofibres are extremely thin materials that are substantially finer than conventional textile materials with unique properties as a result. Nanofibres are playing an increasingly significant role in high technology environments and are showing the potential to be utilised in an ever expanding range of applications. The stand-out applications thus far range from repairing human tissue and high tech chemical sensors to cheap, disposable and highly selective filter materials (Teo and Ramakrishna, 2006 and Ma et al., 2005). The production and utilisation of ultrafine fibres is difficult but there are significant advantageous properties of such materials. For example, nanofibre webs can be constructed in such a way that they have a distinctive pore size and a large surface area to weight ratio of the fibres which offers a high level of functionality (Li et al., 2005). Accordingly, researchers are increasingly exploring opportunities to exploit these advantageous properties.

Interest in nanofibres has "exploded" in recent years due to the ubiquity of simple electrospinning equipment, the principle means of producing such materials. (Teo and Ramakrishna, 2006). This low cost technology can convert a huge variety of materials into webs comprised of ultrafine fibres (Burger et al., 2006). However, electrospinning also has notable drawbacks which are well documented in the literature and include: a low throughput; poor uniformity; a limited material thickness and restrictive processing

tolerances (Greiner and Wendorff, 2007). For most materials and applications the low production rate of electrospinning is the primary barrier to widespread commercialisation and further adoption.

In contrast, centrifugal spinning, is proposed to be a simple and commercially viable method equally capable of producing nanofibres but with potentially higher throughputs (Sarkar et al., 2010). If this technique demonstrates that high throughput production of ultrafine fibres is achievable then it would broaden the horizon of commercial applications and nanofibres may soon be found in low cost and disposable product market sectors. In this study the structure and influence of polymers and the production techniques used to produce nanofibres are critically reviewed (Chapter 2), with specific emphasis on a version of centrifugal spinning as designed by Fiberio, which forms the main part of the experimental study presented in Chapters 3 - 6. The purpose of the research was to study the effects of process conditions on fibre properties using polymer systems that have not been extensively covered in the literature as well as to explore the structure and properties of the as-spun materials in relation to potential applications.

1.2 Fibres, microfibres and nanofibres

Fibres play a key role in life and human endeavour (Morton and Hearle, 1993). Naturally occurring fibres were adopted by early man for clothing, tools, weapons, shelter and decoration. Cotton, wool and silk have been valued commodities for thousands of years and 20th Century developments in polymer science introduced innovative new materials such as polyester and nylon filament. All textile products, regardless of construction method or desired application, are built using fibres as their primary base component. The

Textile Institute (Withers, 1952) defines fibres as: *"textile raw material characterised by flexibility, fineness and a high ratio of length to thickness."*

Fibres may be natural or synthetic, staple or filament and may be fully homogenous or composites of several materials (Morton and Hearle, 1993). Fibres vary significantly in terms of the physical and chemical properties which in term are determined by their molecular backbones but all require a minimum level of strength and elasticity if they are to be useful as a textile material. Most fibrous materials are made from long chain polymers which are large macromolecules made through repetitions of smaller chemical units: mers. The long chain lengths result in local interactions and entanglements between adjacent polymer structures; these interactions and knot points impart mechanical strength through arresting polymer chain movement (Young and Lovell, 1991).

Textile fibre lengths vary from short staple fibres a few mm in length to continuous filaments many kilometres long (Morton and Hearle, 1993). Along with length, the fibre diameter will also act to determine the potential use of a fibre and for most commodity products such as wool and cotton it is diameter that determines the value of a product. Textile filaments can vary from millimetres in diameter for industrial uses to as fine as 50 nm and smaller for some electrospun materials and fibres produced through highly specialised techniques (Zhou and Gong, 2008; Burger et al., 2006). For any given material the fineness of a fibre will determine its absolute strength, flexibility and handling properties along with many other parameters that will be discussed later in Section 1.3. Fineness is a key indicator determine the potential market for a fibre material. For example: crossbred wool is over 30 μm whereas merino wool is much finer, between 15 and 20 μm in diameter (Rae, 1973). This difference is significant enough that a merino

jumper is a luxury item whereas crossbred wool would form a garment that would potentially be uncomfortable and is more suited for the production of carpets. Typically, the traditional textile fibres found in apparel and domestic and light industrial applications have diameters in the range of tens of microns.

Separate to the conventional textiles market is the demand for speciality and high performance fibres with desirable properties that are not typical of commodity textile materials. With the surge in research and business in technical textiles there have been developments in making fibres much more functional in order to meet the demands of the application. For this research one significant area is the development and implementation of ultrafine fibres. The creation, characterisation and processing of these specific fibres has necessitated the development of a set of technologies not seen in the conventional textile industry.

As fibres became finer a new set of terms came into use to describe these new materials. Microfibres are commonly found in filters and in domestic cleaning cloths and typically possess a linear density less than one denier (Ramakrishnan et al., 2009). Finer fibres with diameters smaller than 1 μm fall into a new classification known as sub-micron. The term nanofibre is introduced to describe the ultrafine fibres produced by techniques such as electrospinning. The strict EU definition of a nanomaterial requires a material to be typically below 100 nm in at least one direction (European Commission, 2011). As a result fibres thinner than 100 nm are said to be *true nanofibres*. However, there are many articles which refer to any sub-micron fibre (<1000 nm) as a nanofibre and it is deemed acceptable to use the term nanofibre to report fibres with diameters under 1000 nm (Nguyen et al., 2012). Fibres reported in the literature are often highly varied in diameter

so where there may be mixture of true nanofibres and sub-micron fibres within a sample it is common to refer to all as nanofibres. As only a limited range of materials can be fashioned into fibres that are consistently under 100 nm in diameter this means that the broader definition is preferred by many academics and many commercial bodies (Ramakrishna et al., 2005). For clarification, from herein a fibre ≤1000 nm in diameter will be covered by the term *nanofibre* along with the term *ultrafine fibre*. Larger fibres that are still finer than 1 denier will be termed *microfibres*. The term *fibre* will be used interchangeably to describe fibres of any diameter.

Figure 1.1 is included to demonstrate the scale of a nanofibre and shows a nanofibrous membrane supported by a conventional spunbonded substrate with an average fibre diameter of 20 µm. The extreme fineness is well demonstrated in an example given by Burger et al. (2006), who pointed out that only 3 g of polymer would be needed to span the 380,000 km between the Earth and the Moon using a circular filament 100 nm in diameter.
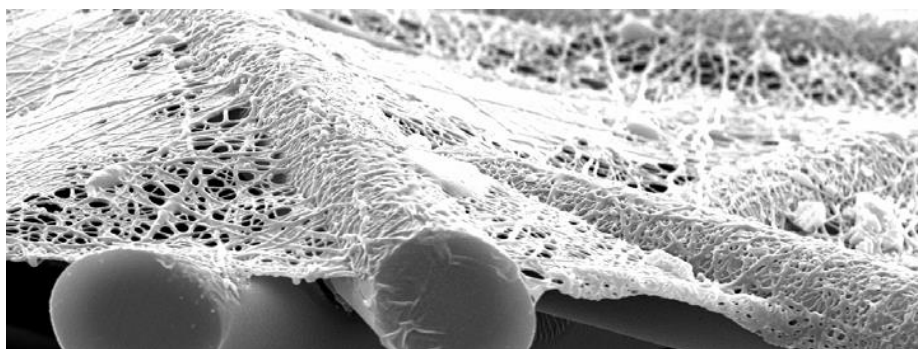
Figure 1.1: SEM micrograph of nanofibrous web mounted on a ~20 µm polyester spunbond substrate (Grafe and Graham, 2003).

Despite the readily quotable facts and figures the reality of producing and working with nanofibres is often done with difficulty, limitations and compromise (Li and Xia, 2004).

The form of material given Figure 1.1 is typical of nanofibre production and application where the fine nonwoven is mounted on a supporting substrate. The possibility of producing nanofibres as conventional filaments for yarn production is yet to be fully developed but is being pursued. Combining this difficulty in producing ultrafine fibres using conventional spinning lines with the low breaking load of any given fibre makes it difficult to process any filaments made into a yarn. As a result it is difficult to form sub-micron and nanofibres into a textile fabric using conventional weaving for example due to the high tension applied to the yarns during processing. As it stands, any report detailing the production of fibres of sub-micron diameter and smaller will likely involve the production of a thin nonwoven web.

1.3 Nanofibre properties

Conventional fibres were often graded based on fineness. Egyptian cotton, merino wool and silks were highly valued as the finer fibres were more flexible, form the highest quality yarns and have the best lustre. This desire for fineness continued in the 20th Century when low denier nylon stockings were seen as must have items in the post war period. Taking this to the extreme and creating fibres which are sub-micron in diameter has a significant impact on many material properties.

A key characteristic of nanofibres that is touted in the literature is the high surface area to volume ratio (Teo and Ramakrishna, 2006). This means that for a given weight of material there is more surface available for reactions, bonding and interaction with the environment. In addition to this, nanofibres have unique mechanical and constructive behaviour which can make them suitable for a wide variety of new applications. The

fineness of nanofibres imparts a low flexural rigidity which allows for close conformation with complex geometries such as a human tissue environment in the case of medical textiles.

Typically, in textiles, elongating a fibre of fixed volume will increase the length and decrease the diameter which will also have the effect of increasing the surface area of the fibre. Similarly, creating fibres through melt or solution spinning will increase the surface area compared to the polymer pellet. Creating nanofibres from said polymer will increase the surface area further still as per the relationship plotted in Figure 1.2.
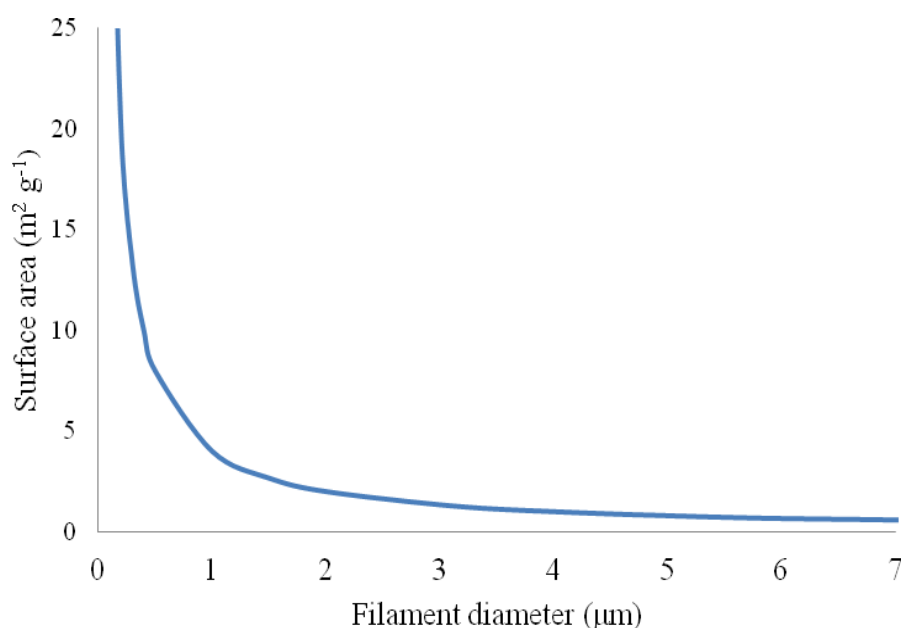
Figure 1.2: The relationship between the diameter of a circular filament and the available surface area. Valid for a total volume of 1 cm^3 of a 1 g cm^{-3} density polymer.

For example a spherical bead made of 1 g of a polymer of density 1 g cm^{-3} would have a surface area of 5.55 cm^2. If this bead was extruded into a circular filament 20 μm in diameter the surface area of 1 g of material would increase to 0.2 m^2. If the filament was made finer to 200 nm in diameter then the surface area would increase further to 20 m^2.

This large surface area means that ultrafine materials potentially offer a high level of surface functionality (Teo and Ramakrishna, 2006). The area available for adsorption, particle capture or product leeching is much greater than for the bulk materials or conventional filaments. High surface areas also increase the environmental response of a material. Molecules will diffuse into the centre of the fibre faster and fibres impregnated with chemical sensing elements will respond quicker (Li et al., 2008).

The flexibility of a fibre is also controlled by the fibre diameter; as fibres become finer they become far less rigid. Morton and Hearle (1993) modelled a fibre as a simple elastic beam and stated that stiffness was dependent on shape, density and most significantly, thickness. For a circular fibre it was determined that flexural rigidity is given by the equation:

$$flexural\ rigidity = \frac{1}{4\pi}\eta\frac{ET^2}{\rho} \qquad\qquad \text{Equation 1.1}$$

As:

$$T = linear\ density = \frac{\pi D^2}{4}\rho \qquad\qquad \text{Equation 1.2}$$

Then:

$$flexural\ rigidity = \frac{\pi}{64}\eta ED^4\rho \qquad\qquad \text{Equation 1.3}$$

Where D is the diameter of the fibre; η is the shape factor, which for a circle is 1; E is the Young's modulus; ρ is the bulk density and T is the linear density.

Equation 1.3 shows that fibre stiffness is proportional to the fourth power of the diameter. In the model presented, reducing the diameter of a filament by a factor of 10 would result in a fibre 10,000 times more flexible. This gives nanofibres improved flexibility over conventional fibres which results in a significantly reduced bending radii affording them

superior conformity over conventional fibres. However, the reduction in stiffness also means that nanofibre and sub-micron fibre webs are very unlikely to be self-supporting and will crumple and collapse easily under any load. The latter point is an example of the fineness of a fibre creating a potentially undesirable behaviour.

The small cross sectional area also means the force required to break a fibre is many magnitudes smaller than conventional filaments. A single electrospun nylon 6 sub-micron fibre with a diameter 800 nm can withstand a breaking load of only 152 μN (Bazbouz and Stylios, 2010) compared to 170 mN for a 15 denier filament (20 μm in diameter) of nylon 6 with a typical tenacity of 0.5 N tex^{-1} (Richards, 2005; Hearle and Cross, 1970). The handling of nanofibres is therefore problematic as even minute forces can deform or break the fibres. As a result processing ultrafine filaments through conventional textile processes is difficult. This fragility will also affect nonwoven web properties and nanofibres will exhibit reduced abrasion resistance and bursting strength. One possible solution to circumvent the lack of strength is to mount the fine webs on a supporting substrate designed to bear the majority of any external load and to help maintain shape and improve the product durability.

Nanofibre products are typically formed into nonwoven webs which are held together by entanglements and interactions between the filaments. The fineness and high level of conformity gives nanofibres the ability to overlap very closely to create webs which are very thin but have very small pore sizes. The fibres will have a random orientation but may have a bias introduced during production. As the fibres are laid down on top of each other there is usually very little Z direction strength unless this is introduced through

subsequent processing. Nonwoven webs produced using nanofibres can be produced to be extremely thin and highly porous.

A key feature of ultrafine fibrous webs is that very small pore sizes can be created using a minimal amount of material. This means that conventional nonwovens webs need to be much thicker to achieve low permittivity to fine molecules. Nanofibre and sub-micron fibre webs can be extremely thin for the same filter efficiency and a 'single' nanofibre layer web can be used to filter out very fine particles (Ziabari et al., 2008). This property is critical when nanofibres are applied in filtration applications,

1.4 **Nanofibre applications**

With the recent proliferation of the electrospinning technique there has been a significant push to find useful applications that can utilise the unique properties inherent to nanofibres whilst minimising or neutralising the disadvantages (Burger et al., 2006). The high cost of nanofibres compared to conventional filaments means there is a drive to find high value added applications which can capitalise on the use of novel nanofibres over conventional filaments. As it stands, until the cost of producing and applying nanofibres is reduced the bulk of research is focused on technically advanced applications that either require only a small volume of nanofibres or can justify the relatively lengthy and expensive production process. Up until 2006, two thirds of all patents using nanofibres related to medical applications and this heavy bias continues in published academic research (Burger et al., 2006). Within the medical field there are two primary focus areas: three-dimensional scaffolds for tissue engineering and the delivery of drugs using

nanofibres (Andrady 2008). Entering the medical market is seen as an immature research area with the potential for huge growth if nanofibre products gain approval for use in medical applications (Sridhar et al., 2011). The next major application for the use of nanofibres is to apply them as a means of separating and filtering various media (Hutten, 2007). This is a commercially mature area where fine melt blown fibres have been utilised for some time (Hassan et al., 2013). The filtration market is one of mass production and is cost driven. If there is to be significant deployment of nanofibrous filters then the production costs must be significantly reduced and the quality and consistency of nanofibres production must be higher.

In terms of the nanofibre formation, the majority of research articles use nanofibres produced through the electrospinning process, the nanofibres are therefore likely to be applied as a flat nonwoven. This typically involves the fibres overlaying each other as a thin two-dimensional web with fibres linked through fusion or entanglements. At present there is very little literature reporting the use of woven and knitted structures made from nanofibres due to the difficulty in producing and handling nanofibre yarns (Zhou and Gong 2008).

1.4.1 Medical applications

Textiles have been used in a broad range of medical applications and environments such as bandages and dressings, surgical gowns, bedding and hygienic items (Bartels, 2011). There has also been a significant increase in the use of specialised textile devices that help directly with patient care. Examples of this are highly technical medical products such as knitted stents for arteries and airways and braided materials for replacing tendons and ligaments. Nanofibres are seen to have great potential as a biomaterial which can

interact with living biological systems, such as human tissue. Tissue regeneration and engineering has become a complementary method to tissue or organ repair or replacement.

Various authors have postulated on using nanofibres as scaffolds to repair skin burns, muscle tissue and organ repair (Laine, 2013; Ma et al., 2005). One of the key factors in using fibrous tissue scaffolds is the degree of inflammatory response (Nguyen et al., 2012). Increasing the rate of cell growth can speed recovery and reduce scarring in burn injuries. This is done by providing an artificial framework along which cells can propagate. Natural connective tissues produced by the body have diameters from tens to hundreds of nanometres (Ma et al., 2005). Nanofibres are suited for mimicking this extra cellular matrix as the dimensions are similar. This similarity between electrospun fibres and the extracellular matrix allows rapid cell growth along the fibres which increases the rate of healing. When employing nanofibres the cells have directional support and can grow along the fibre length as shown in Figure 1.3. Nanofibrous webs have a high porosity and a very high surface area, this enables a high degree of surface functionality to be imparted if desired. The flexibility in processing means that different fibre morphologies and membrane densities can be produced, tailor made to the specific tissue environment (Burger et al., 2006). Using nanofibres as a scaffold in tissue engineering constructs will reduce this inflammatory response and also increase cellular attachment and proliferation compared to more traditional scaffolds (Smith et al., 2008).
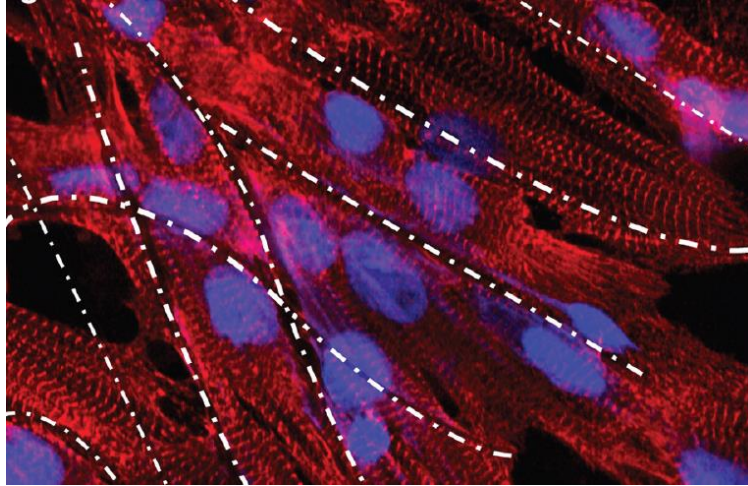
Figure 1.3: Confocal microscope image of cardiac muscles extending along poly(lactic acid) (PLA) fibres produced by centrifugal spinning (Badrossamay et al., 2010).

Nanofibres are also applied in the area of drug and chemical delivery (Prausnitz and Langer, 2008). Drugs are typically administered intravenously, topically or through the gastrointestinal system. These techniques have disadvantages in that the drug may need to be delivered in a high dose at intervals throughout the day. This high dose of certain drugs can be toxic and it is known that with oral delivery there is an initial rapid release of drugs in to the bloodstream (Zeng et al., 2003b). For some drugs it is more suitable to have a lower but more consistent dosing profile than observed with oral delivery. The concept behind nanofibres drug delivery is to provide a high level of control over the release rate of a drug over a prolonged period of time. The high surface area and biodegradability of certain nanofibres has opened up avenues of research in this area. Two distinct approaches have been reported in the literature, for example, Chew et al. (2005) encapsulated a protein within the amorphous regions of a fibre and were able to control the release of a β-nerve growth factor by electrospinning in a biodegradable polycaprolactone scaffold. Alternatively membrane release method has been reported where the fibres act as a barrier between the skin and a concentrated gel (Bartels, 2011).

In this method the rate of drug delivery is controlled by the pore size and diffusion characteristics of a nanofibrous membrane.

In the drug encapsulation system Zong and co-workers (2002) found that the drug Mefoxin was completely released from sub-micron PLA fibres after 48 hours which led them to conclude that the drug was agglomerating at the fibre surface, increasing the rate of release. Katti et al. (2004) also found that Cefazolin, an antibiotic, could be loaded into poly (lactide-co-glycolide) fibres at a 30 % concentration without significantly changing the fibre diameter. Drugs incorporated into fibres can desorb from the fibre at a controlled rate allowing for the creation of drug delivery membranes. Figure 1.4 shows how the release profile differs between oral deliver and transdermal membranes. The combination of high doping capability and controllable release rates means that drug doped nanofibres are potentially useful for transdermal drug delivery.
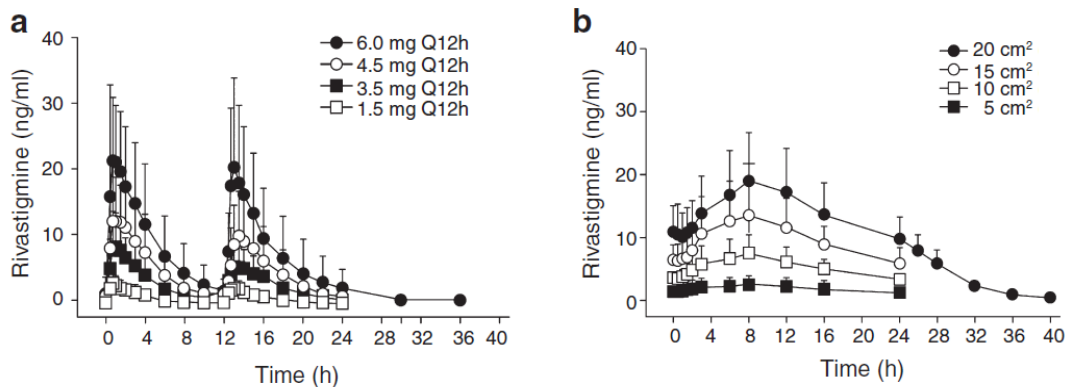
Figure 1.4: Release rates of the drug, Rivastigmine, over time when taken a) orally every 12 hours and b) as a transdermal membrane (Smith and Uhl, 2009).

There is also the potential for applying nanofibres directly to a conventional medical textile materials in order to impart additional functional capability. This is typified

through a recent patent filed by Daniels et al. (2012) where conventional filaments are covered with a nanofibre sheath, Figure 1.5. The purpose of this enhancement is to induce coagulation, reduce blood loss and increasing the effectiveness of the wound dressing.
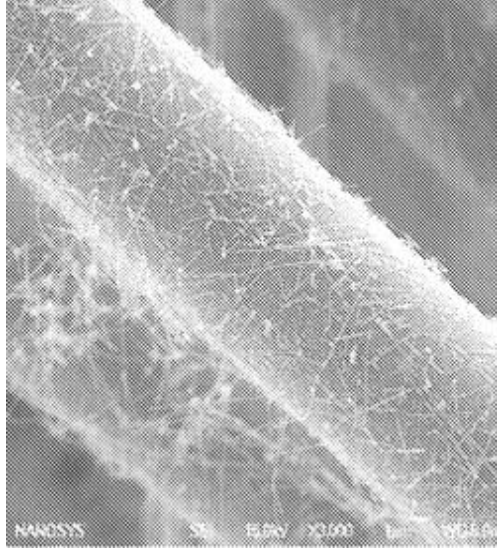
Figure 1.5: Nanostructure enhancement of conventional materials to aid haemostatic wound dressing (Daniels et al., 2012).

The research into using nanofibres in medical applications is intensive but is primarily focused on electrospun filaments. In comparison there is a paucity of research using centrifugal spun fibres in medical applications and it is proposed that centrifugal spinning could broaden the range of polymer feedstock that could be converted into ultrafine fibres for use in healthcare and therapeutics (Badrossamay et al., 2014).

1.4.2 **Filtration and separation**

Whilst a great deal of focus has recently been towards using nanofibres in biomedical applications the most significant commercial application for fine fibres remains in

filtration (Persano et al., 2013). Filtration is currently the largest market for melt blown fibres, the most obvious example being the use in the surgical facemask.

Section 1.4.1 touched upon using fibres as a separation medium was when describing drug delivery through a separation membrane. In simple terms, filtration efficiency increases linearly with decreasing filter thickness, and so having extremely thin, selective membranes can create high efficiency filters with low pressure drop. As mentioned previously, nanofibrous membranes have small pore sizes and can be used to create extremely efficient filters for gas and liquids. Andrady (2008) states that on a per weight basis all evidence points to nanofibre mats outperforming conventional filter media.

A fibrous filter consists of fibres, which may be entangled or bonded and which lie perpendicular or tangential to the fluid flow direction, depending on method of operation. As the stream passes through the filter there are numerous ways in which a particle can deposit on a fibre which rely on mechanical or electrostatic interactions. As the fibre diameter decreases towards the nanoscale the influence of the various methods of interactions changes. Wang and Otani (2012) and Yun et al. (2007) independently show that nanofibre mats can achieve the same level of collection efficiency as current commercial microfibre filters at a much lower material mass and with a lower pressure drop. A lower pressure drop across a filter is a consequence of a lower fluid resistance and allows for faster flow rates for the same applied pressure.

One area of filtration where nanofibre mats will be of great use is the filtration of extremely fine particles. Micron sized and sub-micron particles are easily collected by conventional filter media but to capture nanoparticles efficiently the fibrous filter must

be made from finer fibres. In addition, the interfibre spaces are much smaller for finer fibres resulting in finer fibres. By controlling the pore size nanofibrous webs can be produced to create a highly selective membrane. There has been a high level of research effort focussed on accurately controlling the size, shape and uniformity of nanofibrous webs for precise separation and drug delivery applications (Ziabari et al., 2008). The small pore size and fibre profile means they can more effectively hold a nanoporous coating capable of accurate molecular separation.

Nanofibres have the potential to be utilised in all the primary particle capture and separation mechanisms including: surface straining, depth straining, depth filtration and cake filtration (Sutherland and Purchas, 2002). In surface straining the particle is larger than the pores and simply cannot pass through. This separation method is most commonly found in membrane materials with uniform pore sizes. Using nanofibres would allow for extremely fine pore sizes which could potentially surface strain particles at a very high efficiency.

Depth straining is performed by thicker nonwovens with variable pore sizes. The particles travel through the pores until they reach one that is too small to pass through, trapping the particle at this point. Depth filtration does not rely on pore size separation but captures particles using various molecule to fibre interactions where the particle is actively drawn to the fibre surface as shown in Figure 1.6. This enables the filtration of particles that may be much smaller than the pore sizes.

Cake filtration uses a build-up of particulate on the substrate surface to perform the majority of the filtration. This is often used where the cake has potential value. Nanofibres

would act as a pre-filter, ensuring that smaller particles from an external cake do not foul the main filter media (Homaeigohar and Elbahri, 2014).

An alternative approach focuses on the possibility of direct collection of nanoparticles onto the fibres using functionalised surface treatments on the polymer. For example, the smaller fibre diameters allow for salt crystals to form, with the nanofibres acting as a nucleating agent. The crystals are bound by ionic forces to the surface of the fibres removing them from the solution as shown in Figure 1.6. This method of attracting particles to the fibre for retention is known as an affinity membrane and nanofibres have been used as a binding site for ligands for solid phase extraction (Yoshimatsu et al., 2008).
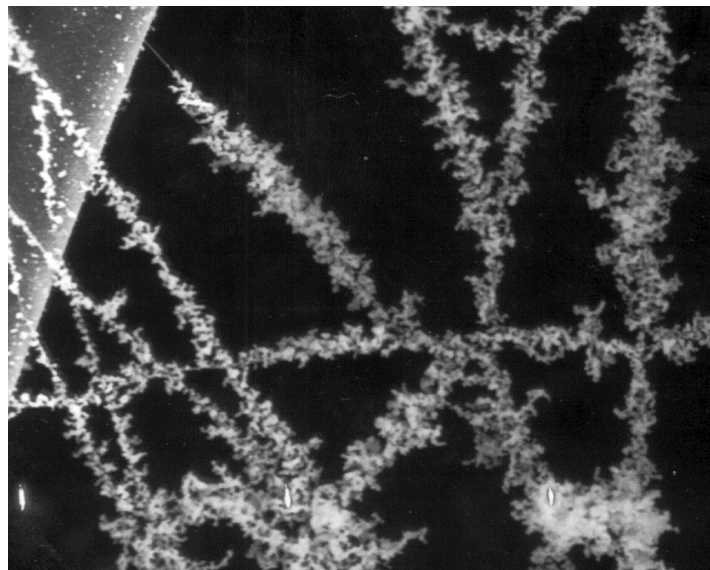
Figure 1.6: SEM micrograph of sodium chloride crystals captured on sub 500 nm fibres mounted on a poly(ethylene terephthalate) substrate (Grafe and Graham, 2003).

1.4.3 Other application areas

There are numerous other potential applications for nanofibres. In addition to the previous applications outlined above there are more niche examples that have received attention.

For example, speciality polymers such as perfluorosulfonic acid are being electrospun into nanofibrous mats which act as proton exchange membranes in hydrogen fuel cells (Choi et al., 2010). In this form the membrane separates the anode and cathode and prevents the exchange of fluids while the perfluorosulfonic acid allows transport of protons but not electrons. In another example, electrospun polyacrylonitrile (PAN) fibres were carbonised and used in a microbial fuel cell and were found to significantly enhance the current density across an anode (Chen et al., 2011).

There is also the potential for use of nanofibres in other high end applications such as electrostatic dissipation, photovoltaic devices and electronic and biological sensors (Bhardwaj and Kundu, 2010). The area of nanofibre sensor application and development has been recently reviewed by Nguyen et al. (2012) who identified this area as one of significant growth.

Nanofibre applications are currently limited by high costs due to low throughput compared to conventional nonwovens. It is clear from this literature review that current research is heavily biased towards finding high value applications for nanofibres. If the apparent cost of nanofibres was to be reduced and availability increased then a wider range of uses could be explored beyond high technology medical applications and could potentially move into domestic and disposable markets where the conformity and high surface area could prove useful for next-to-skin and liquid retention applications.

1.4.4 Nanofibre nanocomposites

Another distinct area in the use of nanofibres is as a medium for carrying an active medicinal ingredient. In this format the polymeric nanofibres act as a composite matrix

for nanoscale additive fillers. For example, by incorporating circular silver nanoparticles in an electrospinning solution a nanofibrous polymer matrix encapsulating the silver particles within the fibres will be created. Alongside active agents for drug delivery there is also a desire to add other components to sub-micron and nanofibres to improve their functionality and change the subsequent properties. These fillers may be simple particles or they may have a significantly large aspect ratio. Long and thin additives are of particular interest as they can significantly change the tensile behaviour of a fibre. An example of this is given by Rojas et al. (2009) who added cellulose nanowhiskers to polystyrene, these 10 - 20 nm thick artefacts significantly increased the elastic modulus and modified the thermal behaviour. The possibility of using nanofibres in fast response sensors is significantly more achievable and commercial the addition of electrically conductive filler. Carbon nanofibres are one such filler material that allows for electrically insulating polymers to conduct electricity via an internal conducting network material (Bouvree et al., 2009). When carbon nanotubes are applied correctly they will enhance the strength of the fibre, or film they are encased within (Qian, 2002). The reported dramatic increase in tensile strength has earned carbon nanotubes (CNTs) near mythical status as a wonder material (Thostenson et al., 2001). Naturally, significant research has already been conducted using fibres containing CNTs but the translation of "wonder material" properties to useful composite is fraught with difficulties that will be discussed later in this work.

1.5 **Polymers**

All fibrous materials are constructed from polymers. Polymeric materials are one of the key ingredients of life, for example deoxyribonucleic acid (DNA); keratinous material

(hair); proteins and enzymes are all long chain molecules that are essential for biological functions. Polymers are also prevalent in the natural world around us, cellulose, lignin and natural rubbers being the obvious examples. More recently, synthetic polymers were developed as substitutes for natural materials due to the demands of industry, war and natural shortages. Key synthetic polymers include the polyamides, polyesters, polyethylene and polypropylene. Various synthetic polymers are of interest in this study and it is these fabricated polymers, rather than the natural materials, that will guide the discussion below.

Synthetic polymers, such as polypropylene and polyester are produced through a process known as polymerisation which involves initiating and propagating the growth of the monomeric units into the formation of a polymer (Hirte, 1984). Polymerisation usually does not produce polymers that are of constant size but rather the process will yield a distribution of molecular weights. The average molecular length of a sample of polymer will often determine the properties of the material as the chain length will influence solubility, flow behaviour and elasticity of the chains (Ferguson, 1995).

As a rule, fibre forming synthetic polymers can be separated into two classes: thermoplastic and thermosetting (Hamley, 2004; Lyons, 2004). Thermoplastic polymers have linear chains that can become increasingly mobile as the temperature is increased. Thermoplastic "freezing/crystallisation" and melting is an entirely physical, and thus, reversible interaction. Thermoset polymers in contrast, cure upon heating and chemically change, thus making this transition irreversible.

Polymers that are thermoplastic can be easily melt processed and there is a wealth of information available on the melt processing of such materials. For non-thermoplastics it may be necessary to dissolve the polymers in solvent to induce fluid behaviour and allow for the formation of new shapes and conformations.

1.6 **Centrifugal spinning**

The earliest patent found pertaining to centrifugal spinning was published by Manning (1943) which concerned the production of nonwoven materials. Further patents were granted in the 1980's detailing the use of a spinning apparatus using centrifugal spinning, Figure 1.7 (Snowden, 1982, Keuchel, 1988). Developments and variants of this technology have been reported only sporadically since: more often being used to produce filaments from metallic elements (Sedaghat et al., 2006). Therefore, the widespread adoption of this form centrifugal spinning by the fibre processing industry did not occur and academic and commercial interest in the processing technique dissipated.
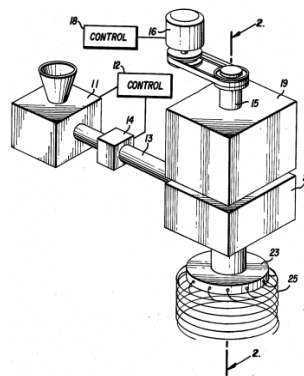
Figure 1.7: A schematic from early patent detailing the principle components of centrifugal spinning (Keuchel, 1988).

This lack of widespread adoption was likely due to conventional spinning allowing for easier control of the drawing process for filament production and rival technologies such

as melt blowing and spunbonding dominating the nonwoven production side. However, interest was reignited when the potential for producing ultrafine fibres became apparent. Electrospinning had demonstrated that webs produced from nanofibres had interesting properties and efforts were directed into finding alternative means of producing such fibres. In 2009 a paper was published by a group at the Pan-American University, Texas, that detailed the production of nanofibres through a process commercialised under the name Forcespinning^{TM} (Lozano and Sarkar, 2009). Simultaneously a Harvard research group published an article where filaments were created using a technique called rotary jet spinning (Badrossamay et al., 2010). In reality both these techniques are versions of the principles laid out in the early patents and the term *centrifugal spinning* has been reapplied to these new research techniques. These recent publications and rapid commercialisation acted as a trigger for renewed academic and commercial interest in this technique and it is now thought that this process could bridge the gap between academic research into nanofibres and large scale production (Raghavan et al., 2011).

Producing nanofibres using this technology has advantages over the more established electrospinning (Lozano and Sarkar, 2009). There is no need for a high voltage supply and as such there no conductivity constraints on the polymer choice. Centrifugal spinning increases the production rate dramatically compared to single jet electrospinning. Currently electrospinning using the polymer melt is far less attractive than solution electrospinning.

This chapter will introduce the principles underpinning centrifugal spinning and will discuss literature findings for how production parameters and relevant material characteristics relate to fibre formation. This section will also detail the current selection

of polymers processed using centrifugal spinning. The advantages of centrifugal spinning will be presented and brief comparisons to other nanofibre production techniques will be drawn.

1.6.1 Principle of centrifugal spinning

Centrifugal spinning is a method of producing nanofibres using high speed rotation of a radial spinneret (Lozano and Sarkar, 2009). In essence, centrifugal spinning requires only high speed rotation of a porous spinneret containing fluid polymer and the fundamental elements are drawn in Figure 1.8.
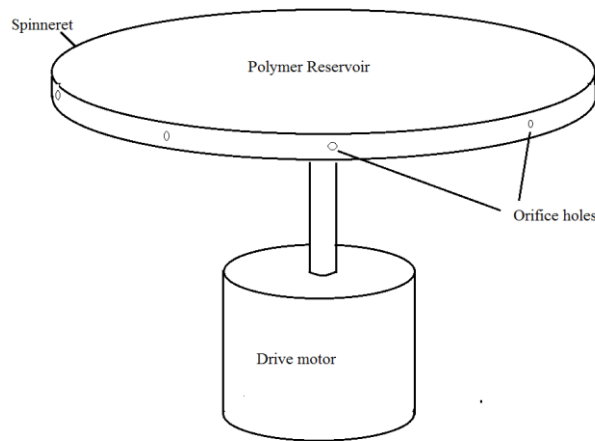
Figure 1.8: Simplistic view of the key components of centrifugal spinning (Lozano and Sarkar, 2009).

The simplicity of the system shown above allows for processing of polymers in either solution or melt. Polymer in fluid form escapes the spinneret through fine orifice holes under the influence of high speed rotational forces. The polymer stream encounters aerodynamic resistance due to the high jet velocity on exit, along with a drawing tension due to the centrifugal force on the steam which both act to reduce the jet diameter. The polymer then solidifies in the ambient air before coming to rest on the collector. The spinning of molten sugar into candy floss is an example of centrifugal spinning and

Huttamen and Kellomaki (2011) used a shop bought candy floss machine with an operating speed of 2800 rpm to spin fibres from polylactide.

1.6.2 Fundamental concepts

Within the rotating spinneret there are competing interactions that will determine the flow of a fluid through a spinneret orifice: the outward inertia of the fluid; the viscous resistance within the orifice and the "hydrostatic pressure". These three parameters will be considered individually with respect to the possible processing parameters.

1.6.2.1 Centrifugal force

Centrifugal force is the apparent "centre fleeing" force associated with circular motion. It is commonly explained as the force which acts in opposition to the centripetal (centre seeking) force acting on an object rotating about an axis. However, in classical mechanics centrifugal force does not exist, the centre fleeing behaviour is in fact the inertia of moving objects. Newton's first law of motion states that all moving objects continue in the same direction of current travel unless they are acted on by an unbalanced force. The case of a ball affixed to a central point by a piece of string provides a useful example. This is a case of uniform circular motion and provides a useful example for the forces experienced in the spinneret. The ball has rotational motion due to the tension in the string applying an unbalanced force, causing the path of the ball to divert through an arc.

A bobsled sliding down a course, a rollercoaster performing a loop and the ball on a string all exhibit the concepts of inertia and a reactive centripetal force. In the examples given centripetal force is the unbalanced action which causes the sled, rollercoaster car or ball to deviate from straight line motion.

In uniform circular motion the centripetal acceleration component is always directed toward the centre and is calculated through.

$$centripetal\ acceleration, a_c = \frac{4\pi R^2}{t}$$
<div align="right">Equation 1.4</div>

Where t is the time period of one revolution and R is the radius of the circle. The centrifugal force, F_c, can be calculated using $F_c = m\ a_c$ where m is the mass of the object in question.

In centrifugal spinning the inertia of the fluid is therefore dependent on the rotational speed and the radius about which it is rotating. Increasing the speed or the radius of the spinneret will result in a higher level of inertia in the fluid. By making the radius of a spinneret larger a higher fluid will have a higher inertia at a same rate of rotation.

There is a temptation, given the name of the present topic of discussion, to state that there is an outwards acting centrifugal force that "holds the fluid against the sides" or "balances" the centripetal force. To reiterate the use of this descriptor is incorrect as the fluid is constantly in motion and this outward 'force' is actually straight line inertia of the mass.

1.6.2.2 Fluid pressure

A fluid rotating at sufficient speed within a spinneret will be held against the sides of the container by inertia. Depending on the volume of liquid there will also be a variable pressure throughout the depth due to hydrostatic pressure.

The hydrostatic pressure, P_h is determined by the pressure exerted by the influence of gravity and is given by the equation: $P_h = \rho gh$, where ρ is the fluid density, g is the force due to gravity and h is the height of the fluid column. However, in a batch, spinning system where there is no direct injection of fluid the hydrostatic pressure is many magnitudes smaller than the inertial force and so is often omitted from calculations. However, the principle of hydrostatic pressure can yield a relationship between centripetal acceleration and pressure generation.

Consider Figure 1.9, where there is an enclosed tube of length R rotating at speed ω about one end with internal fluid of such a volume that the tube has height h:
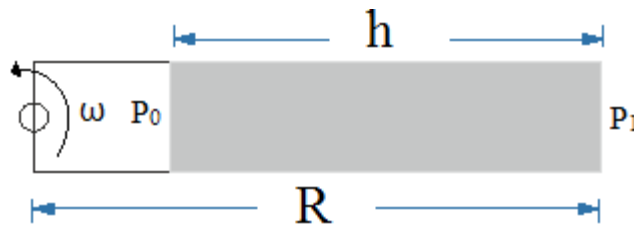
Figure 1.9: Rotating cylinder containing a fluid.

If this tube was stood vertically the pressure at the outer wall, P_1, is found using the equation $P_1 = P_0 + \rho gh$. In the rotating situation presented above, where ω is sufficiently high that the centripetal acceleration $a_c \gg g$ the relationship becomes $P_1 = P_0 + pga_c$ with a_c replacing g. However, whereas in the vertical setup the acceleration due to gravity, g, remains constant the centripetal acceleration felt at any point now varies along the length of the fluid tower. If x is a given position along the length of the spinneret then the pressure difference due to hydrostatic effects in a rotating medium ΔP_c is found using Equation 1.5.

$$\Delta P_c = \rho\, \omega^2 \int_{R-h}^{R} x\, dx \qquad \text{Equation 1.5}$$

In the real spinneret the system becomes more complex as there are now two tube diameters to consider because there is an orifice component as well as a reservoir. A simplistic diagram depicting a needle tipped spinneret is shown in Figure 1.10.
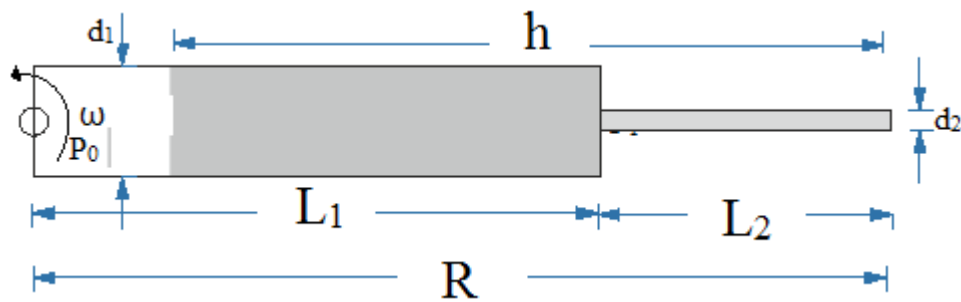
Figure 1.10: Rotating spinneret with orifice aspect.

However, Pascal's Law dictates that in any irregular shaped system the hydrostatic pressure is independent of the shape. Applying this law to the new system means that the inertial pressure felt at the needle tip is merely the sum of the forces felt in an imaginary column of fluid that has an equal surface area to the needle. This new term is defined as ΔP_c. As atmospheric pressure applies at both ends of the fluid it cancels so that: $P_1 = \Delta P_c$. Thus, for any spinneret shape Equation 1.5 holds under static fluid conditions to produce Equation 1.6:

$$\Delta P_c = \omega^2 \rho \left(Rh - \frac{h^2}{2} \right) \qquad \text{Equation 1.6}$$

The implications of Equation 1.6 are that if fluid density, angular velocity or spinneret circular diameter increase then ΔP_c increases. In the initial condition when the spinneret is full, $R = h,$ the overlying pressure is at a maximum value. As the fluid is depleted, h decreases until such a time that that $h = 0$ rendering $\Delta P_c = 0$.

If continuous systems are realised the polymer may be actively pumped into the spinneret at a real pressure. In this case value the initial value for P_0 could be significantly higher than ΔP_c. However, in the batch system explored here this value remains significant.

1.6.2.3 **Viscous forces**

In centrifugal spinning the centripetal force is present as frictional resistance within the spinneret. The contained fluid in the spinning reservoir will experience a combination of pushing and frictional centripetal forces. As the spinneret accelerates to operating speed the fluid polymer is forced to the walls of the spinneret by the circular velocity forces. At orifice points the fluid may escape but must overcome the high resistive forces as it passes through the channel. This resistive force is a combination of frictional resistance between the polymer and orifice surface and the rheological capillary resistance. This internal frictional resistance is more often described using the property of viscosity. Viscosity describes the physical behaviour of a liquid that is in motion where the flowing of a product is generated by the application of a shear stress. Most plastics are non-Newtonian and don't begin to flow until a yield point is exceeded by the shear rate. Below this yield point the shear energy is simply absorbed by the fluid.

Capillary resistance is the force that acts to resist the flow of a fluid down a narrow channel and will depend on the capillary profile and the viscoelastic behaviour of the

fluid. This resistive capillary force, F_{S1} is given by Mellado et al. (2011) to be a function or surface tension and capillary diameter ac given by Equation 1.7

$$F_{S1} = \sigma d_2 \qquad \text{Equation 1.7}$$

Where σ is the surface tension and d_2 is the capillary radius. This function does not consider viscosity despite a thin liquid such as alcohol having obviously less resistance to capillary flow than a viscous liquid such honey. The function σd_2 is further limited as it only considers the orifice interface whereas the true viscous resistance to capillary flow a function of the length and is found using extrapolation of the Hagen-Poiseulle laminar flow equation. This new equation is given in Equation 1.8 below (Gooch, 2011):

$$\Delta P_\eta = Q \frac{8\eta L}{\pi d_2{}^4} \qquad \text{Equation 1.8}$$

Where ΔP_η is the pressure drop through a capillary in Pascals; L is the capillary length in metres and d_2 is the capillary radius in metres. The pressure drop is therefore dependent on the volumetric flow rate Q in m^3 s^{-1}. Equation 1.8 makes a variety of assumptions in that the pipe is sufficiently long and narrow such that the fluid displays laminar flow

From this it can be seen that increased fluid viscosity or a reduction in capillary diameter will increase the resistance to flow within the capillary. Shortening the length of the capillary reduces the capillary resistance. In a static situation the flow rate is zero and so the viscous force falls to 0. However, the viscous resistance is large at any given flow rate.

1.6.2.4 **Surface tension**

A fluid will have a tendency to occupy the least surface area possible. This phenomenon is known as surface tension and comes from the intermolecular cohesive forces that act within a fluid. At a boundary the net force is directed away from the edge and acts to pull the boundary molecules inwards in order to assume a shape of minimal surface area. It was proposed by Padron et al. (2013) that as the solution or melt reaches the orifice exit it remains bound to the walls of the spinneret and assumes a form of a pendant drop. They propose that the fluid tip is held in place doe to the interfacial surface tension. At the orifice edge this surface tension acts as to resist the flow of fluid outwards. The magnitude of this force is derived from orifice diameter, surface tension and bead angle via the relationship shown in Equation 1.9 (Padron et al., 2013):

$$F_{s2} = \pi d_2 \sigma sin\alpha \qquad \text{Equation 1.9}$$

Where α is the angle between the fluid bead and the orifice plane at the point of contact.

1.6.2.5 **Critical spinning condition**

There have been attempts to define the above interactions in a unifying equation which would link the required spinning speed to the parameters. In a simple centrifugal spinner, the flow of the polymer through a spinneret orifice will depend primarily on the rotational speed and viscous resistance to flow. At a rotational speed of zero the polymer is entirely under the influence of gravity and surface tension. As the spinneret accelerates in rotation the fluid polymer is forced, by inertia, to the outer walls of the mandrel. At the orifice capillary the fluid must have sufficient inertia to overcome the viscous resistance and enter the capillary. Once in the capillary, inertia will drive the polymer towards the end

of the needle/channel and under steady state conditions it is proposed that a pendant drop will form which is held in place by polymer surface tension.

At a moderate rotational speed, where the polymer inertia exceeds the capillary resistance the polymer will travel through the capillary and reach the exit point. This condition was termed by Mellado et al. (2011) as the critical rotational speed, ω_c; a term also adopted by Padron and co-workers (2013). They hypothesise that at the critical rotational speed a pendant drop forms, the various forces are balanced and a new surface tension derived component must be overcome before the jet can escape. These models have tried to balance the forces to create a situation where the internal resistive forces are equal to the inertia of the polymer. Mellado et al. (2011) modelled this balancing situation as a balancing of centrifugal force to the capillary force, Equation 1.10:

$$F_C = F_{S1}$$

$$\rho \omega_c{}^2 R d_2{}^3 = \sigma d_2$$

Solving for ω_C
$$\omega_c \sim \sqrt{\sigma/\rho d_2{}^2 R}$$
Equation 1.10

Where F_C and F_{S1} are the outward 'centrifugal force' and resistive capillary force as determined by Mellado et al. (2011). This differs from the equation found by researchers working out of the Pan-American Texas University. Padron et al. (2013) also modified the equation with respect to surface tension and critical rotation speed, Equation 1.11:

$$\omega_c = \sqrt{\frac{2\pi r \sigma sin\alpha}{\rho V_{pd} R}}$$
Equation 1.11

Both these models consider a steady state critical jet exit condition, ω_c, as being completely independent to the fluid viscosity and length of the needle. This oversight implies that a material with a high surface tension, such as water, would require a higher rotational speed than a viscous melt. It is also incorrectly implied that a fluid travelling through a long needle where $L_2 \gg d_2$ would require the same rotational speed to create a jet as a fluid travelling through a hole where $L_2 > d_2$. However, Xu et al. (2014), working from Equation 1.11 added in a viscous component to create the equilibrium condition, Equation 1.12:

$$\pi r \sigma sin\alpha + \frac{\pi \Delta P d^3}{12 L_2} = \rho V_{pd} r \omega_c^2$$

Which yields:

$$\omega_c = \sqrt{\frac{12 L_2 \pi r \sigma sin\alpha + \pi \Delta P d_2^{\,3}}{12 \pi \rho V_{pd} R}} \qquad \text{Equation 1.12}$$

Where ΔP is the pressure drop across a capillary orifice of length, L_2 and diameter d_2 and V_{pd} is the volume of the pendant drop.

A search of the literature indicates that there is no conclusive mathematical model published that accurately details the jet formation procedure in centrifugal spinning. The equations above do not account for the variable pressure experienced by a fluid as it is subject to acceleration as detailed in Equation 1.5. Modifying Equation 1.12 to include the cumulative pressure component a more accurate relationship equation can be derived, Equation 1.13:

$$\pi d_2 \sigma sin\alpha = \rho V_{pd} R \omega^2 + 4 \frac{\Delta P_C - \Delta P_\eta}{\pi d_2^{\,2}} \qquad \text{Equation 1.13}$$

The theoretical implications of Equation 1.13 are:

- Increasing the viscosity, η, will increase ΔP_η and therefore requires an increase in ω;

- Decreasing the orifice diameter will also increase ΔP_η as it is inversely proportional to the fourth power, as per Equation 1.8. Increasing the length of the orifice will also increase ΔP_η as the pressure drop is directly related to L_2;

- Increasing the density of the fluid will reduce the required angular velocity to meet the critical condition;

- Increasing the spinneret size, R, will also reduce the required angular velocity.

However, it is the opinion of this author that the critical condition is only satisfied for an instant and that the relationship proposed above is only realised in situations of negligible aerodynamic and extensional forces. In real centrifugal spinning, any polymer on the outer edge of the spinneret will be subjected to large shear forces due to air resistance (a solution spinneret ($R = 80$ mm) spinning at 10,000 rpm has a surface velocity in excess of 80 m s^{-1}) and tension from. This high drag force will disrupt the formation of the pendent drop and will initiate jet or droplet formation through shearing.

1.6.2.6 **Jet formation**

Once the critical condition is met the polymer is able to escape from the spinneret. Once this occurs the balancing condition, Equation 1.13, no longer applies as there is a new drag component, a tensor component, and the surface tension function $\pi d_2 \sigma \sin\alpha$ is no longer acting against the direction of flow. Padron et al. (2013) propose that during jet production there are several forces acting on the jet: the force due to inertia, F_{cf}, and a component generated by the Coriolis force, F_R, both these forces act roughly along the jet

axis and are seen as extensional forces; acting perpendicular to the jet is the force due to aerodynamic drag and the Coriolis, F_d; acting to resist the outwards is the viscous force, which they denote with F_η. On the jet that is in a mature stage of flight there is a tensor component, σ_ε, that acts to elongate the jet further. These forces and directions according Padron et al. (2013) are illustrated in Figure 1.11.
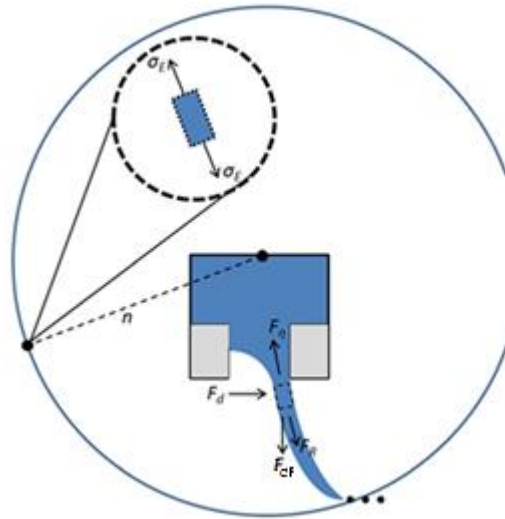
Figure 1.11: The various forces acting upon a fibre immediately after leaving the orifice (Padron et al., 2013)

Once the jet escapes the spinneret the continuous stream of the jet means that there is now a tension acting on the fluid at the tip; this tension will act to pull polymer away from the orifice and will also disrupt the expected shape of the polymer jet as it leaves the orifice.

This tension acts to elongate the jet, creating finer fibres. The amount of tension applied depends on the rotational speed and the mass of the fluid currently in flight that provides the pulling force. Reaching the critical rotational speed and jet initiation does not guarantee fibre formation: the polymer jet could indeed form a jet but could break up into droplets depending on the fluid properties. The process of jet elongation and fibre formation is indeed complex and the previous studies detailed in this section have

attempted to establish the controlling factors and relationships but with only limited success.

How the polymer jet behaves after escape from the spinneret is dependent on the fluid and the processing conditions. As mentioned before there are extensional forces, generated by rotational inertia of the fibrous mass, that place the jet under stress This stress then causes jet elongation. However there is also a significant drag component that works to elongate the fibres. If the balance between extensional and viscoelastic forces is favourable then the jet will extend evenly and solidify into a fibre. In an unbalanced situation the jet will become disturbed and will break up. When a jet disintegrates the polymer stream is no longer subject to an external extensional force and surface tension acts to condense the fragment into a spherical droplet. Bead formation during fibre production is a common occurrence in melt blowing, electrospinning and centrifugal spinning and is largely regarded as undesirable (Fong et al., 1999). The formation of droplets in fluid streams is understood to be controlled by Plateau-Rayleigh instabilities (Badrossamay et al., 2010).

A classical understanding of synthetic fibre spinning suggests that increasing the throughput for the same level of draw will create a thicker fibre (Zieminski and Spruiell, 1988). The principle similarly holds true in centrifugal spinning. Polymer throughput rate is linked to the balance of forces introduced in Equation 1.8 and in Equation 1.13. A decrease in viscous resistance or an increase in inertial forces will increase the throughput rate under identical conditions. Inertia is the most significant force driving the polymer through the capillary so the rotational speed will also contribute to the polymer throughput rate. In centrifugal spinning, lowering the angular velocity will reduce throughput rate

but will inevitably reduce the drawing force applied so a finer diameter may not be achieved.

With centrifugal spinning Badrossamay et al. (2010) suggested that the fibres assume a roughly tangential path to the collector and that total flight path was slightly larger than the collector distance. In work performed by Mellado et al. (2011) it was proposed that the final jet diameter could be linked by the relationship, Equation 1.14:

$$d_f \approx \frac{d_2\sqrt{U}\sqrt{\nu}}{\sqrt{R_c{}^3\,\omega}} \qquad \text{Equation 1.14}$$

Where d_f is the final jet diameter; U is the jet exit velocity; and ν is the kinematic viscosity.

Equation 1.14 suggests that the final jet diameter is influenced significantly by the collector distance. Research conducted since then has identified that the viscoelasticity of the fluid anchors the jet to the circular rotation of the spinneret (Padron et al., 2013). The aerodynamic drag will act on the polymer jet to bend the jet stream away from the collector. The path of the fluid jet will assume a flight path that depends upon the fluid properties and rotational speed. Padron et al. (2013) using high speed cameras, observed that the initial flight path is significantly different based on spinneret speed, Figure 1.12. They concluded that the jet actually completes several orbits of the spinneret before it reaches the collector; thus, allowing additional time for elongation.
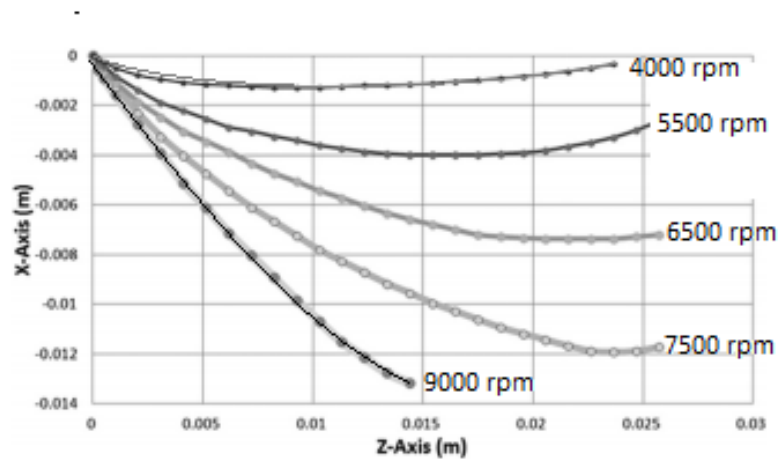
Figure 1.12: Model of fibre jet flight path based on rotational speed (Padron et al., 2013).

As the fibres are attenuated by passing a high speed fibre through air there is a significant amount of turbulent interaction. Padron et al. (2013) has tried to explain the influences on a jet at various points based around the universal continuity equation but ultimately, the motion of the jet is chaotic and mathematically explaining the jet interactions from abstract coordinates is of limited academic interest given the field in which this technology is relevant. In the same work, the empirical observations made by Padron et al. are of far more use.

The fibre is not immediately forced to the collection system upon leaving the spinneret, rather the polymer stream is pushed outwards but then settles at a radial distance for a few spinneret rotations, mimicking the action of a spinning lasso. This is shown in Figure 1.13. The fibre continues to stretch for 2 - 5 spinneret rotations and this action means that the distance and time available for elongation is much greater than that afforded by the spinneret to collector distance. Once the fibre has solidified it is forced radially outwards by the aerodynamic forces generated by the rotating spinneret (Padron et al., 2013).
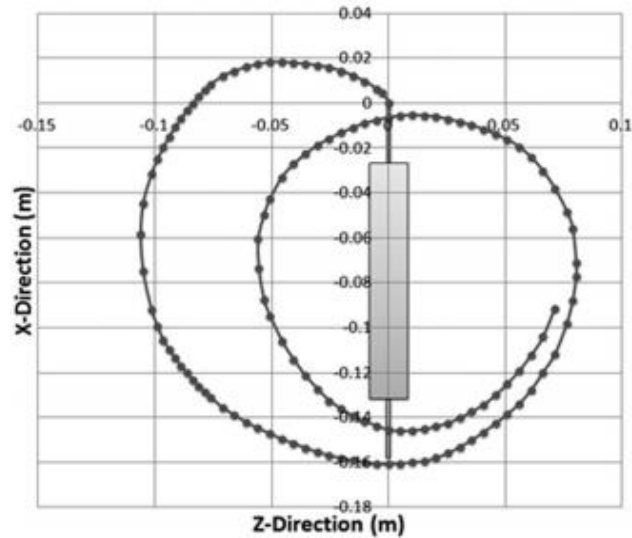
Figure 1.13: Fibre trajectory of the centrifugal spinning of PEO at 4,000 rpm.
(Padron et al., 2013).

1.6.2.7 **Jet breakup**

Of particular concern in ultrafine fibre production is the final fibre diameter distribution
and the level of defects such as polymer beads. The formation of beaded nanofibres in
electrospinning is caused by the capillary break up of jets due primarily to surface tension
(Fong et al., 1999). Balancing the surface tension and viscoelastic properties of the
material with external processing forces is necessary in order to eliminate jet breakup and
control the resulting fibre diameter. An imbalance in surface tension and viscosity is what
causes a slow leak to drip from a tap rather than form a fine constant stream. The same
principles apply to a jet produced through centrifugal spinning where for any unanchored
fluid in flight the surface tension will cause the liquid to contract into a sphere. This
breakup of a stream was described in a seminal paper by Rayleigh (1890) which has
resulted in this phenomena being known as Rayleigh instabilities. Rayleigh instability
occurs when the surface tension forces cause the development of necking of the fibre at
intervals along the fluid stream. The necked regions, if allowed to grow unchecked will
eventually pinch off the fibre which results in a fluid droplet or droplet escaping. These
droplets will contract into a sphere due to surface tension.

There are forces which act to resist surface tension changes. The first of these are the internal friction where the viscosity of a fluid can restrict the movement of chains and prevent instabilities forming. The second force is an extensional stress where the jet stream is held under tension by the outward movement of polymer further along the filament. This extensional force acts on the polymer chains to restrict surface tension contractions.

If the viscosity is too low the fluid jets will form beads in a very short distance as they leave the spinneret. At slightly higher viscosities the jet may breakup further along the length of the jet. At appropriately high viscosities there is enough internal friction to resist the formation of perturbations. If fibre production is achieved fluid viscosity will determine how much elongation of the jet occurs and therefore the final jet diameter and level of beading. Extensional forces also have a smoothing effect, which iron out any perturbations that form. It is known that the build-up of extensional stress on a filament will retard surface tension driven fibre breakup (Chang et al., 1999).

1.6.3 **Processing thermoplastics**

Thermoplastic materials have a melting point beyond which the crystal structure becomes disordered and the polymers display flow behaviour. The viscosity of a melt will primarily depend on the polymer chain mobility and chain length and temperature (Bower, 2002; Brandrup et al. 1999) Additional elements may also be added to increase or reduce the polymer flow rate at a certain temperature.

A fluid leaves the spinneret at a temperature, T_p, with an initial intrinsic viscosity, η and the melt viscosity of the material increases rapidly as the temperature decreases. This viscosity increase becomes clearly obvious as the thermoplastic crystallises at temperature, T_c and solidifies. This increase in viscosity changes the behaviour of a material in response to applied tension and aerodynamic shear.

For many thermoplastics the point of crystallisation is much higher than room temperature so active cooling or jet quenching is not required. Jet attenuation only occurs between the range $T_c < T < T_p$. The high shear rates experienced by the molten jets mean that it is highly likely that the polymer solidifies very soon after leaving the spinneret. It is thought that attenuation time, and the fineness of fibres could be increased by increasing this processing "window". One option is to increase the processing temperature, T_p by using a fluid that is at a higher initial temperature. The second option is to extend the window by reducing the rate of heat loss; this is done by elevating the ambient temperature. The latter option is much more expensive on an energy cost basis.

When melt spinning the fibre diameter will be depending on the viscoelastic properties of the jet and the cooling rate of the polymer. The ambient air is at room temperature in this technique. A molten polymer introduced to strong aerodynamic forces will undergo cooling and solidify rapidly.

The grade of polypropylene chip for melt blowing has a relatively high melt flow index of 1800 g 10 min^{-1}, whereas typical fibre grade polypropylene has a melt flow index of 35-100 g 10 min^{-1}. This MFI characteristic is controlled though using metal catalysts to increase the flow rate by inducing chain scission at spinning temperatures. For most

polymers, increasing the temperature will reduce the viscosity as more energy is available for generating bond mobility. However, at elevated temperatures the polymers may begin to degrade or cross-link which can significantly affect the viscoelasticity as polymer cross links hinder mobility.

1.6.4 **Processing polymer solutions**

When spinning from solution there are three governing properties that will significantly affect the spinning properties of a fluid (Golecki et al., 2014):

1. Polymer chain length;

2. Polymer concentration;

3. Solvent choice.

The polymer concentration is a significant factor in determining the solution viscosity and surface tension of a fluid; the greater the concentration of polymer the more entanglements and resistance to flow (Ueberreiter and Yamaura, 1997). The factors determining the melt viscosity of thermoplastics will also impact on the viscosity of polymers in solution as the level of chain entanglement and resistance within a solution will depend on the polymer used; chain length; branching and temperature and level of excitation. Relatively short chains are less likely to entangle and non-polar chains tend to interact to lesser extent than polar chains, whilst these considerations dominate; solvent choice will also impact the overall solution properties.

Solvents differ in volatility; intrinsic viscosity and miscibility with the polymer. For solution spinning the propensity for fibre formation is often governed by the solvent removal rate (Golecki et al., 2014). Whilst the polymer is in solution it is able to flow and

elongate, once the solvent is removed the polymer is largely fixed and the diameter will remain constant. A polymer jet must transition from solution to fibre and where solidification will depend on the solvent evaporation rate. In centrifugal spinning the solvent evaporation rate will largely depend on the solvent used. The rate of evaporation is linked to the temperature and the volatility of a solvent. It has been stated by Golecki et al. (2014) that fibre diameter increases with increasing volatility. Solvents that evaporate too rapidly will create a polymer jet that solidifies before elongation is complete. Conversely, if the solvent evaporates too slowly the fibre may still be fluid when it hits the collector and may disintegrate or spread out into other fibres, losing shape. The evaporation rate can be accelerated or retarded by adding a non-solvent. The use of a non-solvent/solvent mixture such as by adding methanol to a chloroform/polycaprolactone solution can significantly influence the spinning behaviour as the evaporation rate and viscosity are affected (Jeun et al., 2005).

Golecki et al. (2014) published research trying to create a model that links the conditions for steady state continuous production of fibres as opposed to beads. They proposed Equation 1.15 which establishes the condition for continuous jet production over bead formation:

$$\omega \mu P^2 > C_{fit} \sigma \left(\frac{R_g T}{M} \right)^2 \frac{D(\rho_O - \bar{\rho})^2}{D_{air} R} \qquad \text{Equation 1.15}$$

Where P is the solvent vapour pressure; C_{fit} is a constant; R_g is the gas constant, T is the temperature; M is the molar mass of the solvent; D is the solvent diffusion constant in solution; D_{air} is the solvent diffusion constant for air and $\rho_O - \bar{\rho}$ is the change in solvent mass concentration.

However, many of the factors listed in Equation 1.15 are immeasurable at any given moment rendering the equation difficult to use to model fibre production. To date, the equations published by researchers do not accurately model the process such that the fibre diameters of a new fluid could be predicted without empirical measurements. This reinforces the author's opinion that jet behaviour and fibre formation in centrifugal spinning is highly complex and chaotic and that accurately modelling the various interactions is difficult and as yet some aspects still uncertain.

1.6.5 **Nonwoven formation**

The fibres produced by centrifugal spinning are laid in the form of a nonwoven web. The nonwoven web can be free standing or spun directly onto a substrate. Collection systems may either be active or static. The static collection system is a support arranged around the spinneret to collect and support the fibres as they form a web. In centrifugal spinning, the static system may be a series of radial bars or a variation on this such as a cylindrical collector (Badrossamay et al., 2010). Active collection systems use secondary forces to attract the fibres onto a supporting mesh or fabric. Vacuum collection uses air flow to draw the fibres down onto a conveyor for collecting. Fiberio Corporation, United States, has developed an electrostatic collection system that uses weak electrostatic forces in the range of 45 volts to attract the fibres to a collection plate (Peno et al., 2014). Unlike electrospinning there is no need for a grounded collection plate, consequently, fibres can be spun into a free standing web or directly onto a supporting textile substrate.

Hutmacher and Dalton (2011) conducted a review on melt electrospinning and concluded that for most polymers there has been very little success in producing nanofibres or even

sub-micron fibres. In comparison, polypropylene has been melt centrifugally spun and produced fibres finer than 200 nm (Raghavan, 2011).

The polymers must be carefully selected to ensure that they can be processed into fibres. The challenge in centrifugal spinning is optimising the polymer fluid behaviour and processing parameters, as highlighted in Section 1.6.2, to ensure not only ultrafine fibres are produced but also prevent jet breakup and shot formation. The rheological parameters that are dominant in fibre formation are viscosity and surface tension (Badrossamay et al., 2010). Understanding of these fluid properties and appropriate spinning condition selection is necessary to ensure successful fibre formation. Incorrect solution concentration, polymer temperature or spinneret settings may not result in the formation of fibres.

1.6.6 **State of the art**

At the time of writing centrifugal spinning has been used to make nanofibres from poly(ethylene oxide) (PEO), poly(lactic acid) (PLA), bismuth, polypropylene (PP) and polystyrene (PS) along with those already mentioned (Sarkar et al., 2010). However, as spinning is primarily dependent on fluid properties and surface tension there is theoretically no reason why a wider range of polymers cannot be spun into fibres.

Work has already been conducted on making centrifugal spinning more applicable to commercial application. A significant part of this is converting the loose fibres into a flat nonwoven that can then be used in a commercial application. Raghavan et al. (2013) has demonstrated that the centrifugal spun fibres can be drawn on to a substrate using a vacuum conveyor to produce a two layer product much like SMS melt blown products,

Figure 1.14. Here the substrate provides the strength and integrity and the nanofibres provide the active surface area.

Figure 1.14: Composite structure composed of PP fibres spun directly onto a substrate (Raghavan et al., 2013)

The production of a flat nonwoven in roll-to-roll continuous production is seen as essential if centrifugal spun fibres are to be used in high volume applications such as filtration. The ultrafine fibres can be used to coat a sufficiently strong substrate to give the functionality or performance required. The speed of production will depend on the level of coating required and the throughput of the polymer. A basic outline of a continuous roll-to-roll centrifugal spinner is shown in Figure 1.15. This would allow for long runs of substrate to be coated in a continuous process.
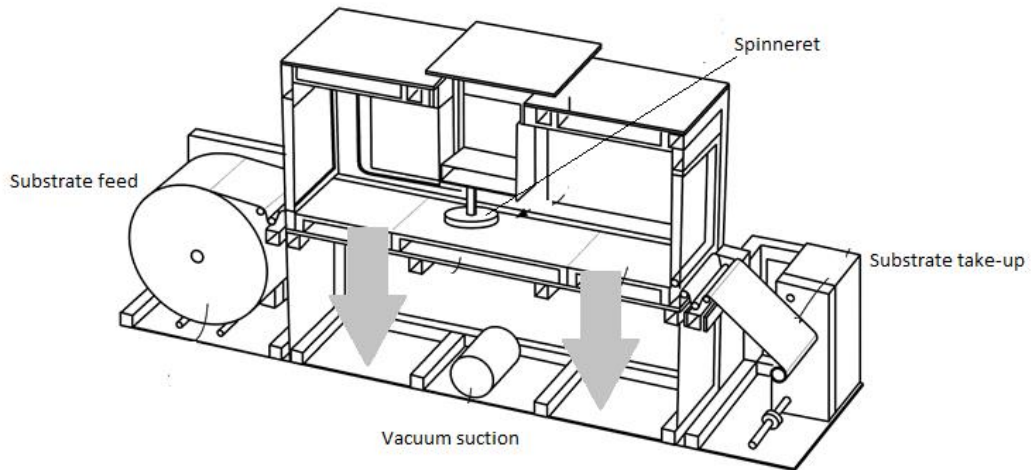
Figure 1.15: Diagram illustrating the schematic structure of a continuous centrifugal spinning line. Patent granted to Kay et al. (2014) on behalf of Fiberio Technology Corporation.

In the work by Raghavan et al. (2013), they calculated that melt PP production operates at 0.04 to 0.08 g min^{-1} per orifice which can be scaled up using multiple spinnerets and orifices. This ease of scaling means that process can be expanded to cover any width of material with a high density of coating. There is also the possibility of coating a substrate with multiple polymers to create a complex sandwich structure in the same process; this can be achieved by feeding different polymers to separate banks of spinneret.

Due to the inherent simplicity of centrifugal spinning there is also the potential to create bicomponent fibres. This process would behave very much like bicomponent melt blowing but could also work with polymer solutions in addition to thermoplastic materials. This would require a modified spinneret design and potentially a direct polymer feed system to ensure that both polymers were delivered at a consistent and controllable rate.

When compared to electrospinning centrifugal spinning can allow for thicker coatings due to no restriction on the density of polymer deposition. In addition, there is also easier scale-up as there is no electrostatic interference and with centrifugal spinning there is no restriction on the electrostatic or conductive properties of the material.

Centrifugal spinning avoids the high energy costs of melt blowing as there is no demand for high volumes of hot air. The energy consumption of a commercial system is estimated by the Raghavan et al. (2013) to be 13 kWh kg^{-1} of fibre. In a multiple orifice system centrifugal spinning is reported to have a higher throughput than needleless electrospinning (Nurwhara et al., 2013).

The processing conditions and mean fibre diameters of polymers that have been processed into fibres to date are collated in Table 1.1. This list is by no means comprehensive but shows the broad range of materials that can be processed into fibres using centrifugal spinning.

Table 1.1: Polymer processing reported in the literature using centrifugal spinning

Polymer	Parameters	Mean Diameter	References
Polycaprolactone	Solution spun in dichloromethane at a concentration of 16 %, 3,000rpm 9,000 rpm	264 nm 220 nm	(McEachin and Lozano, 2012)
Polyethylene oxide (PEO) conjugated with BEH-PPV	Solution spun in chloroform at a concentration of 1.5 %, 5,000 rpm	580 nm	Pardon et al. (2012)
Nylon 6	Solution spun in formic acid at a concentration of: 20 % 7,000 rpm 15-25 %, 4,000-9,000 rpm	165 ± 55 nm 188-825 nm	(Raghavan, 2011) (Hammami et al., 2014)
PVDF	Solution spun in 1:1 dimethylacetamide/acetone, 7,000rpm	201 ± 86 nm	(Raghavan, 2011)
Poly(vinyl butryl) with carbon nanotubes	Solution spun in 7:3 ethanol/methanol, 3,000-9,000 rpm	400 nm	(Weng et al., 2014a)
Tin Fluorophosphate	Melt spun, 10,000 rpm and 270 °C	2.43 ± 1.16 μm	(Fang et al., 2014)
Poly(methyl methacrylate)	Solution spun in chloroform at a concentration of 9-11 % 3,000 – 9,000 rpm	370 to 800 nm	(Weng et al., 2014b)
Polystyrene	Melt spun, 3,000 rpm	unreported	(Sarkar et al., 2010)
Polypropylene	Melt spun, 12,000rpm and 225 °C	372 ± 238 nm	(Raghavan, 2011)

1.7 **Other nanofibre production techniques**

In addition to centrifugal spinning there are alternative methods to producing nanofibres such as melt blowing, electrospinning, flash spinning, template synthesis, phase separation, self-assembly and shear precipitation. The nature of these techniques will be discussed in this section.

Melt blowing is a major manufacturing technique in the nonwovens sector. It is currently the largest commercial method of creating sub-micron fibres by volume and so is also a very important method for producing in fine fibres (Zhou and Gong, 2008). Where conventional systems use drawing rollers to elongate polymer stream, melt blowing uses the drag of pressurised air. Using thermodynamic analysis Shambaugh (1988) estimates that ~ 1 % of the energy in the hot air is applied to elongating the fibre and the remaining energy dissipates into the ambient air. There are reports of average fibre diameters of under 400 nm for polystyrene and polypropylene (Ellison et al.,2007) and polypropylene blown with averages of 250 nm claimed by Hills Incorporated, USA (Zhou and Gong, 2008).

The majority of journal articles that are involved in discussing nanofibres are utilising nanofibres produced through electrospinning. If a specified electrostatic force is applied to a fluid, it will form a Taylor cone (Burger et al., 2006). If the electrostatic force is increased, the shape of the cone will deform and if the force exceeds the surface tension within the droplet then a liquid jet is emitted. Electrostatic repulsion between like charged polymer chains results in an increase in surface area, reducing the diameter of the expelled jet and increasing the length. Electrospinning is able to produce ultrafine fibres as fine as

50 nm in diameter but is limited in terms of overall production rate; the ability to process thermoplastics and a limitation on the electrical properties of filaments. A diagram, illustrating the key components of simple electrospinning equipment is shown in Figure 1.16.
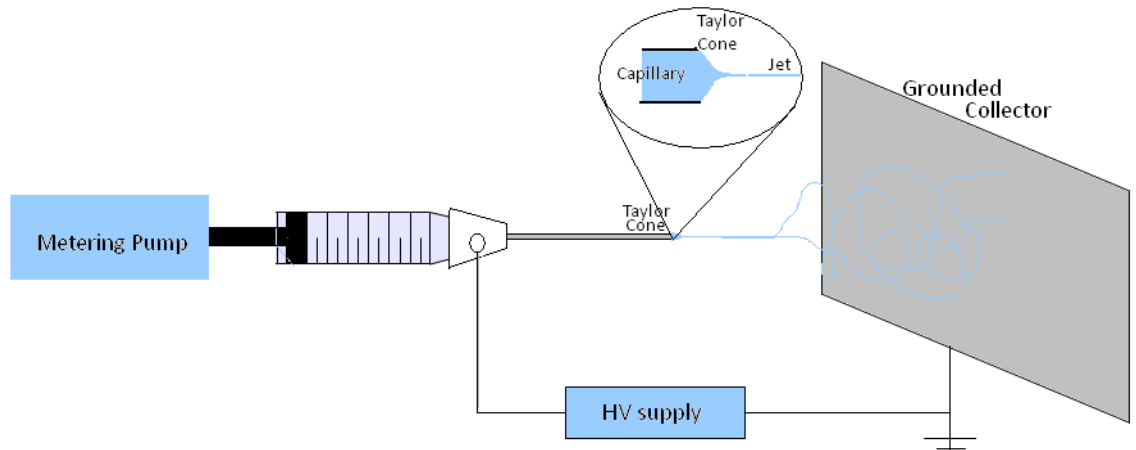
Figure 1.16: Conventional electrospinning configuration with high voltage supply providing an electrostatic charge between the tip and the grounded collector. This creates a Taylor cone and a jet in the solution being forced through the needle (Burger et al., 2006)

Flash spinning is described by Zhou and Gong (2008) as a modified version of spunbonded technology. In flash spinning a polymer solution is created using a solvent which evaporates at the spinneret. This rapid evaporation causes the filaments to fibrillate which are then collected onto a moving screen forming a web. This system was first recognised in a patent in 1963 and since then over 90 patents have been filed improving the process. Template synthesis involves forcing polymer fluids through fine pores in a membrane (Martin, 1996). A variation of this is template melt extrusion which involves forcing a molten polymer through a membrane which is subsequently cooled under pressure and processed to produce nanofibres (Nayak et al., 2011). In both cases, the use of fibres is limited to highly specialised applications.

Fibres with diameters as low as 100 nm were wet spun in a design patented by Velev et al. (2010) who dispersed droplets of polymer solution into a coagulating bath under high shear forces. As the polymer precipitated out the droplets were elongated into very fine fibres, Figure 1.17. It was proposed by Sutti et al. (20011) that this technique could be scaled up to provide a high volume of nanofibres but much more research would need to be conducted prior to deliver this objective (Sutti et al., 2011).
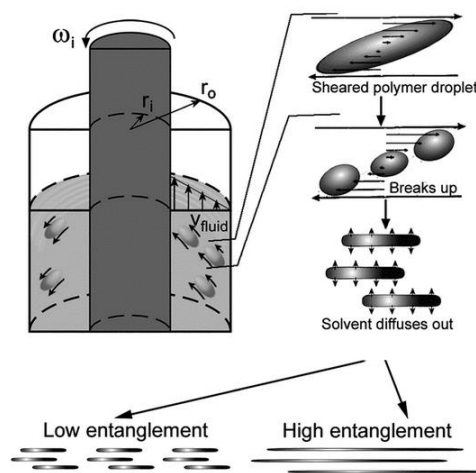
Figure 1.17: Shear spinning of polymer nanofibres (Velev et al., 2010).

A well cited article by Ma and Zhang (1999) described using phase separation to create a three-dimensional fibrous network of poly(lactic acid). The interconnectivity and three-dimensional structure means these materials are best described as highly porous foams as opposed to traditional nanofibres. However, phase separation was described by Laine (2013) as a laboratory scale procedure at best.

This is by no means an exhaustive list but covers but covers some of the latest ideas in alternative nanomaterial production. These techniques are highly specialised and many of them are used to produce loose or anchored fibres which are difficult to process or

incorporate into products. At present they are not considered as significant from an industrial perspective and represent a small fraction of academic research.

1.8 **Summary and objectives of work**

Nanofibres are materials which could find their way into a large number of high value applications. The prospect of spinning varied and unconventional materials into fine fibres is of great interest both academically and commercially. Yet research has shown that the most popular technique, electrospinning, has processing challenges which have limited the ability to scale up some of the research conducted in recent years. These include a low production rate, limited choice of material and in particular little progress in melt electrospinning. There is also concern over the potential instability of material in the electrostatic field. This latter point is significant when spinning conductive materials such as carbon nanotubes or sensitive materials such as proteins.

Potentially straddling the capabilities of melt blowing and electrospinning lays centrifugal spinning. This is a technology capable of spinning from both solution and melt, producing fibres at a moderate production rate with diameters acceptable for use in biomedical and filtration applications. Centrifugal spinning as a nanofibre production technique still in its infancy and there is still a great deal to be understood. Previous work on centrifugal spinning has been focused simply on the production and characterisation of a new material with some depth into optimising the conditions. Controlling and understanding the production of fibres will allow for more diverse materials to be processed into fibres through centrifugal spinning. The overall aim of this work was to establish the effect of processing conditions on fibre properties using common thermoplastic and solution spun

polymers and to use this information to produce fibres from novel and modified materials that may have potential applications. By doing this the prospect of using centrifugal spinning as a means of delivering speciality ultrafine fibres was demonstrated.

The polymers used for establishing the effect of various processing parameters on fibre properties from both melt and solution were:

1. Polypropylene;

2. Polycaprolactone.

Polypropylene is a thermoplastic that is used often in spun bonding and melt blowing. Here it will be processed into fibres using centrifugal spinning. The temperature and speed of rotation will be varied and linked to the end fibre diameter and fine structure assessed.

Polycaprolactone (PCL) is also a thermoplastic polymer but was solution spun in this study. This material will be used for a direct comparison between centrifugal spinning and needleless electrospinning. Polymer concentration and solvent were varied along with spinning conditions and the processing versatility was investigated in addition to the end fibre morphology, material fine structure and possible applications.

The second part of the research was to spin fibres from polymeric material that was atypical. Fibres were formed using centrifugal from three additional materials:

3. Polyvinylpyrrolidone with 1-triacontane;

4. Polycaprolactone doped with carbon nanotubes;

5. Polypropylene doped with carbon nanotubes

Polyvinylpyrrolidone with 1-triacontane is a polymer found in the cosmetics industry and is known to be hydrophobic. The processing conditions for fibre formation were investigated along with fibre properties. The potential use of these fibres as a dye or oil adsorbent was also considered.

Carbon nanotubes are a conducting additive with high tensile strength. These were added to polycaprolactone to create a compound material with unique viscosity and flow behaviour. The impact of carbon nanotube addition on the spinning and end fibre properties was also investigated.

1.9 **References**

ANDRADY, A., 2008. *Science and Technology of Polymer Nanofibers.* Wiley Publishing, United States.

BADROSSAMAY, M. R., BALACHANDRAN, K., CAPULLI, A. K., GOLECKI, H. M., AGARWAL, A., GOSS, J. A., KIM, H., SHIN, K. & PARKER, K. K., 2014. Engineering hybrid polymer-protein super-aligned nanofibers via rotary jet spinning. *Biomaterials,* 35**,** 3188-3197.

BADROSSAMAY, M. R., MCILWEE, H. A., GOSS, J. A. & PARKER, K. K., 2010. Nanofiber assembly by rotary jet-spinning. *Nano Letters,* 10**,** 2257-2261.

BARTELS, V. T., 2011. *Handbook of Medical Textiles.* Woodhead Publishing, United Kingdom

BHARDWAJ, N. & KUNDU, S. C., 2010. Electrospinning: a fascinating fiber fabrication technique. *Biotechnology Advances,* 28**,** 325-347.

BOWER, D. I., 2002. *An Introduction to Polymer Physics.* Cambridge University Press, United Kingdom.

BRANDRUP, J., IMMERGUT, E. H. & GRULKE, E. A,M 1999. *Polymer Handbook*, Fourth Edition. John Wiley and Sons, United States.

BURGER, C., HSIAO, B. S. & CHU, B., 2006. Nanofibrous materials and their applications. *Annual Review of Materials Research,* 36**,** 333-368.

CHEN, S., HE, G., CARMONA-MARTINEZ, A. A., AGARWAL, S., GREINER, A., HOU, H. & SCHRODER, U., 2011. Electrospun carbon fiber mat with layered architecture for anode in microbial fuel cells. *Electrochemistry Communications,* 13, 1026-1029.

BOUVREE, A., FELLER, J.-F., CASTRO, M., GROHENS, Y. & RINAUDO, M., 2009. Conductive polymer nano-biocomposites (CPC): chitosan-carbon nanoparticle a good candidate to design polar vapour sensors. *Sensors and Actuators B: Chemical,* 138**,** 138-147.

CHANG, H. C., DEMEKHIN, E. A. & KALAIDIN, E., 1999. Iterated stretching of viscoelastic jets. *Physics of Fluids,* 11**,** 1717-1737.

CHEW, S. Y., WEN, J., YIM, E. K. F. & LEONG, K. W., 2005. Sustained release of proteins from electrospun biodegradable fibers. *Biomacromolecules,* 6**,** 2017-2024.

CHOI, J., LEE, K. M., WYCISK, R., PINTAURO, P. N. & MATHER, P. T., 2010. Nanofiber composite membranes with low equivalent weight perfluorosulfonic acid polymers. *Journal of Materials Chemistry,* 20**,** 6282-6290.

DANIELS, R. H., LI, E. & ROGERS, E. J., 2012. *Nanostructure-enhanced platelet binding and hemostatic structures.* United States Patent: 8,319,002 B2, Application: 12/720,297, 27th Novemeber 2012.

ELLISON, C. J., PHATAK, A., GILES, D. W., MACOSKO, C. W. & BATES, F. S., 2007. Melt blown nanofibers: fiber diameter distributions and onset of fiber breakup. *Polymer,* 48**,** 3306-3316.

EUROPEAN COMMISSION, 2011. Definitions of 'nanomaterial', Commission recommendation 2011/696/EU. Available online at: https://ihcp.jrc.ec.europa.eu/our_databases/web-platform-on-nanomaterials/general-information/definitions-of-nanomaterial. [Accessed: 6th February 2014]

FANG, Y., HERBERT, M., SCHIRALDI, D. & ELLISON, C., 2014. Tin fluorophosphate nonwovens by melt state centrifugal Forcespinning. *Journal of Materials Science,* 49**,** 8252-8260.

FERGUSON, J., 1995. Application of rheology to polymer processing. *In:* COVAS, J. A., AGASSANT, J. F., DIOGO, A. C., VLACHOPOULOS, J. & WALTERS, K. (eds.) *Rheological Fundamentals of Polymer Processing.* Kluwer Academic Publishers, Netherlands.

FONG, H., CHUN, I. & RENEKER, D. H., 1999. Beaded nanofibers formed during electrospinning. *Polymer,* 40**,** 4585-4592.

GOLECKI, H. M., YUAN, H., GLAVIN, C., POTTER, B., BADROSSAMAY, M. R., GOSS, J. A., PHILLIPS, M. D. & PARKER, K. K., 2014. Effect of solvent evaporation on fiber morphology in rotary jet spinning. *Langmuir,* 30**,** 13369-74.

GREINER, A. & WENDORFF, J. H., 2007. Electrospinning: a fascinating method for the preparation of ultrathin fibers. *Angewandte Chemie International Edition,* 46**,** 5670-5703.

GRAFE, T. & GRAHAM, K., 2003. Polymeric nanofibers and nanofiber webs: a new class of nonwovens. *Proceedings of the Porceedings of the International Nonwovens Technical Conference* (INDA-TAPPI), 22nd-24th September, Georgia, United States.

HAMLEY, I. W., 2004. *Developments in block copolymer science and technology,* Wiley Online Library, United Kingdom.

HAMMAMI, M. A., KRIFA, M. & HARZALLAH, O., 2014. Centrifugal force spinning of PA6 nanofibers – processability and morphology of solution-spun fibers. *The Journal of The Textile Institute***,** 1-11.

HARDY, V.-G., 2008. *Design and construction of smart structures for technical textiles.* Doctor of Philosophy Thesis, University of Leeds.

HASSAN, M. A., YEOM, B. Y., WILKIE, A., POURDEYHIMI, B. & KHAN, S. A., 2013. Fabrication of nanofiber meltblown membranes and their filtration properties. *Journal of Membrane Science,* 427**,** 336-344.

HEARLE, J. W. S. & CROSS, P. M., 1970. The fractography of thermoplastic textile fibres. *Journal of Materials Science*, 5, 507-516.

HIRTE, R., 1984. *Textile science and technology: Production and applications of polypropylene textiles*. Elsevier Scientific Publishing Company, Akademie Verlag GmbH, Germany.

HOMAEIGOHAR, S. & ELBAHRI, M., 2014. Nanocomposite electrospun nanofiber membranes for environmental remediation. *Materials,* 7**,** 1017-1045.

HUTMACHER, D. W. & DALTON, P. D., 2011. Melt electrospinning. *Chemistry – An Asian Journal,* 6**,** 44-56.

HUTTEN, I. M., 2007. *Handbook of Nonwoven Filter Media*, Elsevier, United States.

HUTTUNEN, M. & KELLOMAKI, M., 2011. A simple and high production rate manufacturing method for submicron polymer fibers. *Journal of Tissue Engineering and Regenerative Medicine*, 5, 239-243.

JEUN, J. P., LIM, Y. M., CHOI, J. H., LA, H. S., KANG, P. H., & NHO Y. C., 2007. Preparation of ethyl-cellulose nanofibres via electrospinning. *Solid State Phenomena*, 119, 255-258.

KAY, S., NER, Y. & CASTELLANO, L., 2014. *Devices and methods for the production of microfibers and nanofibers in a controlled environment*. United states Patent Application: 2013/053808, 3rd February 2014.

KATTI, D. S., ROBINSON, K. W., KO, F. F. & LAURENCIN, C. T., 2004. Bioresorbable nanofiber-based systems for would healing and drug delivery: optimisation of fabrication parameters. *Journal of Biomedical Materials Research*, 70B, 286-296.

KEUCHEL, H. W., 1988. *Apparatus for centrifugal fiber spinning with pressure extrusion*. European Patent: Application: 85108904.5, 13th December 1988.

LAINE, K., 2013. *Rotational melt spinning as a manufacturing method for tissue engineering scaffolds.* Masters of Science Thesis, Tampere University of Technology, Finland.

LI, D., HUANG, J. & KANER, R. B., 2008. Polyaniline nanofibers: A unique polymer nanostructure for versatile applications. *Accounts of Chemical Research,* 42, 135-145.

Li, D., McCann, J. And Xia, Y., 2005. Use of electrospinning to directly fabricate hollow nanofibres with functionalised inner and outer surfaces. *Small*, 1, 83-86.

LI, D. & XIA, Y., 2004. Electrospinning of nanofibers: reinventing the wheel? *Advanced Materials,* 16, 1151-1170.

LI, X., ZHANG, Y., LI, H., CHEN, H., DING, Y. & YANG, W., 2014. Effect of oriented fiber membrane fabricated via needleless melt electrospinning on water filtration efficiency. *Desalination,* 344**,** 266-273.

LOZANO, K. & SARKAR, K., 2009. *Methods and apparatus for making superfine fibres*. United States Patent Application: 12/404,907, 14th March 2009.

LU, Y., LI, Y., ZHANG, S., XU, G., FU, K., LEE, H. & ZHANG, X., 2013. Parameter study and characterization for polyacrylonitrile nanofibers fabricated via centrifugal spinning process. *European Polymer Journal,* 49**,** 3834-3845.

LYONS, J., LI, C. & KO, F., 2004. Melt-electrospinning part I: processing parameters and geometric properties. *Polymer,* 45**,** 7597-7603.

MA, P. X. & ZHANG, R., 1999. Synthetic nano-scale fibrous extracellular matrix. *Journal of Biomedical Materials Research Part A*, 46, 60-72.

MA, Z., KOTAKI, M., INAI, R. & RAMAKRISHNA, S., 2005. Potential of nanofiber matrix as tissue-engineering scaffolds. *Tissue Engineering,* 11**,** 101-9.

MANNING, F. W., 1943. *Method and apparatus for spinning unwoven fabrics.* United States Patent 2,336,743, 14th December 2014.

MARTIN, C. R., 1996. Membrane-based synthesis of nanomaterials. *Chemistry of Materials,* 8**,** 1739-1746.

MCEACHIN, Z. & LOZANO, K., 2012. Production and characterization of polycaprolactone nanofibers via forcespinning™ technology. *Journal of Applied Polymer Science,* 126**,** 473-479.

MELLADO, P., MCILWEE, H. A., BADROSSAMAY, M. R., GOSS, J. A., MAHADEVAN, L. & KIT PARKER, K., 2011. A simple model for nanofiber formation by rotary jet-spinning. *Applied Physics Letters,* 99**,** 203107.

MORTON, W. & HEARLE, J., 1993. *Physical Properties of Textile Fibres*. The Textile Institute, Manchester, United Kingdom.

NATTA, G. & CORRADINI, P., 1960. Structure and properties of isotactic polypropylene. *Il Nuovo Cimento Series 10,* 15**,** 40-51.

NAYAK, R., KYRATZIS, I., TRUONG, Y., PADHYE, R., ARNOLD, L., PEETERS, G., O'SHEA, M. & NICHOLS, L., 2013. Fabrication and characterisation of polypropylene nanofibres by meltblowing process using different fluids. *Journal of Materials Science,* 48**,** 273-281.

NAYAK, R., PADHYE, R., KYRATZIS, I., TRUONG, Y., ARNOLD, L., 2011. Recent advances in nanofibre fabrication techniques. *Textile Research Journal*, 82, 129-147.

NGUYEN, L. T. H., CHEN, S., ELUMALAI, N. K., PRABHAKARAN, M. P., ZONG, Y., VIJILA, C., ALLAKHVERDIEV, S. I. & RAMAKRISHNA, S., 2012. Biological, chemical, and electronic applications of nanofibers. *Macromolecular Materials and Engineering***,** 822-867

PADRON, S., FUENTES, A., CARUNTU, D. & LOZANO, K., 2013. Experimental study of nanofiber production through forcespinning. *Journal of Applied Physics,* 113**,** 024318.

PADRON, S., PATLAN, R., GUTIERREZ, J., SANTOS, N., EUBANKS, T. & LOZANO, K., 2012. Production and characterization of hybrid BEH-PPV/PEO conjugated polymer nanofibers by forcespinning™. *Journal of Applied Polymer Science***,** 3610-3616.

PALL, D. B. & CONNORS, J. T., 1996. *Bag filter*. United States Patent: 5,586,997, Application: 08/389,264, 24th Decemeber 1996.

PENO, E., LIPTON, R. & KAY, S., 2014. *Apparatuses and methods for the deposition of microfibers and nanofibers on a substrate*. United States Patent Application: 13/368,074, 22nd November 2012.

PERSANO, L., CAMPOSEO, A., TEKMEN, C. & PISIGNANO, D., 2013. Industrial upscaling of electrospinning and application of polymer nanofibres: a review. *Macromolecular Materials and Engineering*, 298, 504-520.

PRAUSNITZ, M. R. & LANGER, R., 2008. Transdermal drug delivery. *Nature Biotechnology*, 26, 1261-1268.

QIAN, D., WAGNER, G. J., LIU, W. K., YU, M.-F. & RUOFF, R. S., 2002. Mechanics of carbon nanotubes. *Applied mechanics reviews*, 55, 495-533.

RAE, A., 1973. *The WIRA textile data book.* Wool Industries Research Association, Leeds, United Kingdom.

RAGHAVAN, B., SOTO, H. & LOZANO, K., 2013. Fabrication of melt spun polypropylene nanofibers by forcespinning. *Journal of Engineered Fabrics & Fibers (JEFF)*, 8, 52-58.

RAGHAVAN, B., STINSON, G., PENO, E. GOMEZ, C. & LOZANO, K., 2011. Forcespinning: an advancement in nanofibers production. *Proceedings of the Nonwovens Innovation Conference,* 13th-15thSeptember, 2011.

RAMAKRISHNA, S., FUJIHARA, K., TEO, W.-E., LIM, T.-C. & MA, Z., 2005. *An introduction to electrospinning and nanofibers.* World Scientific, Singapore.

RAMAKRISHNAN, G., DHURAI, B. & MUKOPADHYAY, S., 2009. An investigation into the properties of knitted fabrics made from viscose microfibres. *Journal of Textile and Apparel Technology and Management,* 6, 1-9.

RAYLEIGH, L., 1890. XXXIV, On the theory of surface forces. *The London, Edinburgh, and Dublin Philosophical Magazine and Journal of Science*, 30**,** 285-298.

ROJAS, O. J., MONTERO, G. A., & HABINI, Y.*,* 2009. Electrospun nanocomposites from polystyrene loaded with cellulose nanowhiskers. *Journal of Applied Polymer Science,* 113, 927-935

SANDLER, J. K. W., PEGEL, S., CADEK, M., GOJNY, F., VAN ES, M., LOHMAR, J., BLAU, W. J., SCHULTE, K., WINDLE, A. H. & SHAFFER, M. S. P., 2004. A comparative study of melt spun polyamide-12 fibres reinforced with carbon nanotubes and nanofibres. *Polymer,* 45**,** 2001-2015.

SARKAR, K., GOMEZ, C., ZAMBRANO, S., RAMIREZ, M., DE HOYOS, E., VASQUEZ, H. & LOZANO, K., 2010. Electrospinning to Forcespinning™. *Materials Today,* 13**,** 12-14.

SEDAGHAT, A., TAHERI-NASSAJ, E. & NAGHIZADEH, R., 2006. An alumina mat with a nano microstructure prepared by centrifugal spinning method. *Journal of Non-Crystalline Solids,* 352**,** 2818-2828.

SHAMBAUGH, R. L., 1988. A macroscopic view of the melt-blowing process for producing microfibers. *Industrial & Engineering Chemistry Research,* 27**,** 2363-2372.

SMITH, L. A., LIU, X. & MA, P. X., 2008. Tissue engineering with nano-fibrous scaffolds. *Soft Matter,* 4**,** 2144-2149.

SMITH, B. & UHL, K., 2009. Drug delivery in the twenty-first century: a new paradigm. *Clinical Pharmacological Therapy,* 85**,** 451-455.

SNOWDEN, P., 1982. *Production of fibres.* United States Patent: 4,323,524. 6th April 1982.

SRIDHAR, R., VENUGOPAL, J. R., SUNDARRAJAN, S., RAVICHANDRAN, R., RAMALINGAM, B. & RAMAKRISHNA, S., 2011. Electrospun nanofibers for pharmaceutical and medical applications. *Journal of Drug Delivery Science and Technology*, 21, 451-468.

SUTHERLAND, K. & PURCHAS, D. B., 2002. *Handbook of Filter Media*, Elsevier, United Kingdom.

SUTTI, A., LIN, T. & WANG, X., 2011. Shear-enhanced solution precipitation: a simple process to produce short polymeric nanofibers. *Journal of Nanoscience and Nanotechnology*, 11, 8947-8952.

TEO, W. E. & RAMAKRISHNA, S., 2006. A review on electrospinning design and nanofibre assemblies. *Nanotechnology,* 17, R89-R106.

THOSTENSON, E. T., REN, Z. & CHOU, T.-W., 2001. Advances in the science and technology of carbon nanotubes and their composites: a review. *Composites Science and Technology*, 61, 1899-1912.

UEBERREITER, K. & YAMAURA, K., 1977. Dependence of surface tension and polymer concentration in surface on solvent interaction of polystyrene solutions. *Colloid and Polymer Science*, 255, 1178-1180.

VELEV, O., SMOUKOV, S. & MARQUEZ, M., 2010. *Nanospinning of polymer fibres from sheared solutions*. United States Patent Application: 12/730,644, 8th October, 2010.

WANG, C. & OTANI, Y., 2012. Removal of nanoparticles from gas streams by fibrous filters: a review. *Industrial and Chemical research*, 52, 5-17.

WENG, B., XU, F., SALINAS, A. & LOZANO, K., 2014b. Mass production of carbon nanotube reinforced poly(methyl methacrylate) nonwoven nanofiber mats. *Carbon,* 75**,** 217-226.

WIERTZ, P., 2014. Challanges and opportunities facing the global nonwovens industry. *Man-made Fibres Congress*.10th-12th September 2014, Dornbrin, Austria.

WITHERS, J. C., 1952. *Textile Terms and Definitions, Issue 2*. The Textile Insitute, Manchester, United Kingdom.

XU, H., CHEN, H., LI, X., LIU, C. & YANG, B., 2014. A comparative study of jet formation in nozzle- and nozzle-less centrifugal spinning systems. *Journal of Polymer Science Part B: Polymer Physics,* 52**,** 1547-1559.

YOSHIMATSU, K., YE, L., LINDBERG, J. & CHRONAKIS, I. S., 2008. Selective molecular adsorption using electrospun nanofiber affinity membranes. *Biosensors and Bioelectronics,* 23**,** 1208-1215.

YOUNG, R. J. & LOVELL, P. A., 1991. *Introduction to Polymers (Second Edition).* London, Chapman and Hall.

YUN, K. M., HOGAN, C. J., MATSUBAYASHI, Y., KAWABE, M., ISKANDAR, F. & OKUYAMA, K., 2007. Nanoparticle filtration by electrospun polymer fibers. *Chemical Engineering Science*, 62, 4751-4759.

ZENG, J., XU, X., CHEN, X., LIANG, Q., BIAN, X., YANG, L. & JING, X., 2003b. Biodegradable electrospun fibers for drug delivery. *Journal of Controlled Release,* 92**,** 227-231.

ZHOU, F.-L. & GONG, R.-H., 2008. Manufacturing technologies of polymeric nanofibres and nanofibre yarns. *Polymer International,* 57**,** 837-845.

ZIABARI, M., MOTTAGHITALAB, V. & HAGHI, A., 2008. Evaluation of electrospun nanofiber pore structure parameters. *Korean Journal of Chemical Engineering,* 25**,** 923-932.

ZIEMINSKI, K. F. & SPRUIELL, J. E., 1988. On-line studies and computer simulation of the melt spinning of nylon-66 filaments. *Journal of Applied Polymer Science*, 35, 2223-2245.

ZONG, X., LI, S., CHEN, E., GARLICK, B., KIM, K-W., FANG, D., CHIU, J., ZIMMERMAN, T., BRATHWAITE, M. D., HSIAO, B. J. & CHU, B., 2004. Prevention of postsurgery induced abdominal adhesions by electrospun bioabsorbable nanofibrous poly(lactide-co-glycolide) based membranes. *Annals of Surgery*, 240, 910-915.

Chapter 2
Methods and technology

2.1 **Fiberio L-1000M Forcespinner**

The centrifugal spinner used in this study was a Forcespinning™ Cyclone L-1000M supplied by Fiberio Corporation, USA. This is a laboratory scale spinning system capable of producing nanofibres from both solution and melt. The bench top equipment is designed to replicate the fibres produced using the commercial variant of this technology detailed earlier in Section 1.6.6.

The system consists of a central shaft on to which differing spinneret systems can be attached. For melt spinning the system was comprised of a tri-orifice disc spinneret created from two parallel plates, Figure 2.1 and Figure 2.2.

Figure 2.1: Tri-orifice melt spinning plates for high MFI polymers

The spinneret also acts as the polymer reservoir; the lower plate has a concave profile to accommodate a fixed volume of dry polymer. The radius of the spinning reservoir used was 45 mm. There were two orifice diameters available for melt spinning: a high MFI

spinneret with orifice diameter 159 μm and a coarser low MFI design with inner orifice diameter of 602 μm. Both spinnerets have an orifice length of 6 mm.
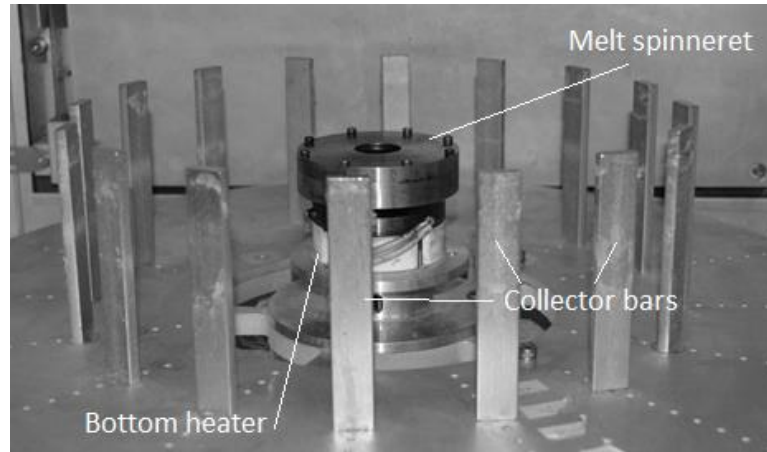
Figure 2.2: Centrifugal spinner fitted with melt spinneret surrounded by static collector bars.

For polymer heating, the spinneret was sandwiched between two disc heaters which bring the spinneret and the polymer to a desired temperature. The heater and polymer temperatures are monitored through independent thermocouples. Once the desired material temperature is reached the heaters are retracted and the spinneret is rotated via a high speed stepper motor. For melt spinning the L-1000M can accelerate the spinneret to a maximum speed of 20,000 rpm which can be adjusted in 100 rpm increments.

The solution spinneret is a double headed reservoir onto which two needles are fitted as orifices, Figure 2.3.

Figure 2.3: Top-down view of solution spinneret fitted with 27 gauge needles.

The radius of this spinneret was 80 mm when fitted with 0.5 inch needle tips. The diameter of the orifices depended on the gauge of the needle fitted and in this body of work ranged from 159 to 260 μm. The spinneret reservoir could accommodate up to 2 cm^3 when full. Once the reservoir is loaded and fitted the spinneret was rotated at high speed until a predetermined stop point or allowed to continue until solution exhaustions. When solution spinning there was a rotational speed limit of 12,000 rpm applied.
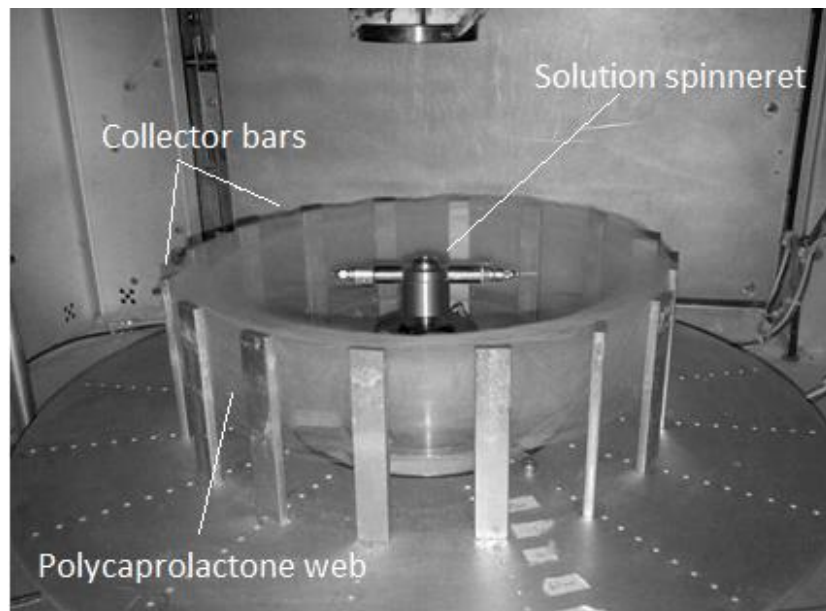
Figure 2.4: Solution spinneret configuration with a web produced from PCL in chloroform. The double ended syringe spinneret is shown in the centre.

Fibre collection was carried out using a passive system as seen in Figure 2.2 and Figure 2.4. Posts are arranged in a disc around the spinneret at a distance designed to capture a

fibre in flight and provide a support for the web. For some preliminary runs a woven filament fabric was inserted on to the inside of the posts to aid in determining if fibre formation occurred.

2.2 Scanning electron microscopy

The fineness of the fibres produced in this work require a means of imaging that provides sufficient detail to make measurements and investigate the morphology. Conventional optical microscopy is limited by the wavelengths of visible light so as objects become smaller optical microscopes are unable to differentiate between separate points. This is known as the diffraction limit. Ultrafine fibres are so fine that they difficult to resolve using a conventional microscope. Scanning electron microscopy (SEM) is a widely used technique used to produce high quality images of fine structures beyond the capability of conventional optical microscopes. The images are used to establish material dimensions, investigate surface topography and to determine elemental make-up using complementary energy dispersive X-ray spectroscopy.

By reducing the wavelength of the incident beam the diffraction limit is reduced to allow smaller points to be resolved. This stems from the equation: $R_{min} = \frac{\lambda}{2nsin\theta}$ which indicates that an electromagnetic wave of wavelength, λ, travelling in a medium with a refractive index, n and converging at a spot with angle θ will form a spot size, R_{min} (Vernon-Parry, 2000). The fixed wavelength of visible light limits the fineness of the focusing spot and the microscopes ability to resolve objects. In comparison, an electron has a variable wavelength, λ_e, but this value is many magnitudes smaller than the

wavelength of visible light, this smaller wavelength allows for a wider range of possible magnifications with an improved depth of field which allows analysis for relatively large area analysis of non-flat surfaces such as fibrous webs can be conducted within a single focal plane (Vernon-Parry, 2000).

The focussed electron beam penetrates the sample surface and generates a series of secondary emissions. These include back scattered electrons, secondary electrons, X-rays and cathode luminesce. Back scattering occurs where electrons from the incident beam are reflected elastically by atoms in the sample. Secondary electron emission is caused by interactions between incident electrons and the valence electrons of atoms in the specimen. Secondary electrons strike the detector and are collated into an image.

The narrow electron beam is focused on a spot using a series of lenses. This spot will yield only limited information about a small area. To create an SEM micrograph the beam scans across the sample collecting information from precise areas which is then collated into a typical image.

This study imaged non-conductive materials in an electron beam which required that a conductive coating be applied to prevent excessive charging within the image. The samples were coated in gold using a sputtering machine prior to imaging. The samples were then placed into the SEM analysis chamber and observed under high vacuum. The samples were then exposed to an electron beam and an image built up from secondary electron emission. A working acceleration voltage of 5 - 15 kV and a typical working distance of 100 mm was used for most fibrous samples that were observed in this body of work.

2.2.1 **Procedure**

It was important to have a consistent procedure when conducting fibre diameter measurements to ensure a fair and unbiased set of results that are representative of the whole sample (Lyons, 2004). An ideal fibre distribution measurement would record a huge number of fibres from multiple repeats. However, in practice limited resources prevent excessive sampling so a more effective technique must be utilised. There is no definitive consensus on how many fibres should be measured and there are varying techniques in the literature on how fibres are sampled and analysed. The method chosen was one modified from Lyons (2004). They reported a technique that uses a consistent method of SEM image acquisition where five specific areas of the SEM stub were magnified for diameter measurements but neglects to state how many fibres are collected. This general procedure was replicated in this work but with a specification to record a minimum of 150 fibre diameter measurements for each sample and a minimum of 5 micrographs taken from each sample unless otherwise stated.

2.3 **Rheology measurements**

Viscosity measurements allow for a direct comparison between the fluid properties of two materials. This study used rotational viscometry and capillary rheometry to measure the dynamic viscosity of solutions and thermoplastics respectively. Dynamic viscosity measurements are dependent on the configuration and shear stress applied to the polymers and therefore the results defined as *apparent viscosity,* useful for comparison within systems but not between systems.

2.3.1 **Rotational dynamic viscometry**

Rotary viscometry is an established technique with its use having been reported in the recent literature by Krishnappa and co-workers (2003) and Geng et al. (2005). Rotary viscometers work by measuring the torque required to rotate a spindle at a fixed revolution rate against a liquid medium. Shear and viscoelastic forces will act on the spindle to resist rotation so a more viscous solution will impart more shear resistance. The torque required to maintain this rotation is measured through the viscometer and the viscosity is calculated using Equation 2.1:

$$viscosity, \eta = \ \sigma_s/\gamma \qquad\qquad \text{Equation 2.1}$$

Where σ_s and γ are the shear stress and shear strain, respectively, and are calculated using Equation 2.2 and Equation 2.3 (Mitschka, 1982; Geng et al., 2005):

$$shear\ rate, \gamma = \frac{2\omega Rc^2 Rb^2}{(Rc^2 - Rb^2)} \qquad \text{Equation 2.2}$$

$$shear\ stress, \sigma_s = \frac{M}{2\pi Rb^2 L} \qquad \text{Equation 2.3}$$

Where ω is the angular velocity of the spindle, Rc, Rb and L are all dimensional constants, as shown in Figure 2.5, M is the torque acting the spindle shaft in dyne cm^{-1}.
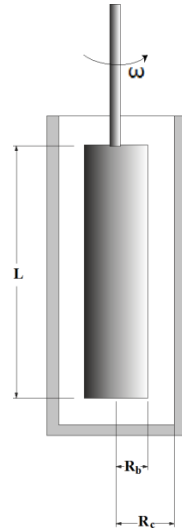
Figure 2.5: Generic dimensional parameters of a rotational viscometer.

Rotational viscosity measurements are often quoted using the centigram system based unit of centipoise which is a measure of shear viscosity and is equivalent to 10^{-3} Pa s^{-1}.

The equipment used in this experiment was a Brookfield D-VE viscometer. The spindle factors used to convert torque measurements to viscosity readings were determined by the manufacturer. The required volume of polymer was injected using a 10 ml syringe. The solution was allowed to settle for a short period and a measurement was taken at an appropriate testing speed. The measurement was allowed to stabilise before a reading was taken. Unless otherwise stated measurements at each condition were taken from 3 discrete solutions. To limit the effect of temperature measurements were only taken when the ambient temperature was recorded to be 22 ± 2 °C.

2.3.2 Melt rheology measurement

The molten flow behaviour of polypropylene and polyvinylpyrrolidone/triacontane was investigated using capillary rheometry. This is a technique in melt processing which is often used to characterise thermoplastics as it enables material flow and deformation

properties to be characterised. The polymer is loaded into a barrel and then heated until thermal equilibrium is reached. The polymer is then extruded through a die using a piston. Figure 2.6 shows the general arrangement for a common capillary rheometer.
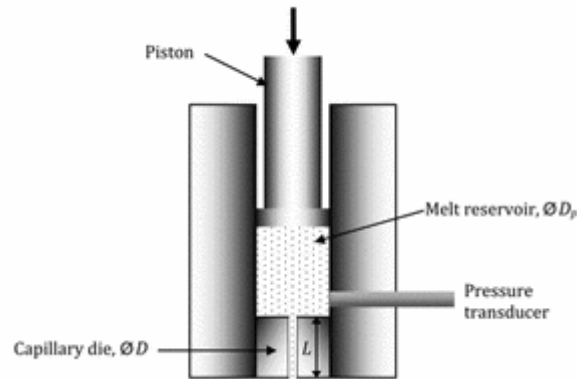
Figure 2.6: Schematic of operating principles of a capillary rheometer.

Due to the viscoelastic nature of polymers significant pressure is generated at the die entrance as an external force is applied. The shear viscosity is then calculated using Equation 2.1, page 68, inserting values for shear stress and shear rates which are calculated using Equation 2.4 and Equation 2.5 (Larsson, 2014):

$$Wall\ shear\ stress, \sigma_s = \frac{Pr}{2\,l} \qquad \text{Equation 2.4}$$

$$Wall\ shear\ rate, \gamma = \frac{4\,Q}{\pi r^3} \qquad \text{Equation 2.5}$$

Where: P is the pressure drop at the die (N m^{-2}); Q is the volume flow rate m^3 s^{-1}; r is the capillary radius (m) and l is the capillary length (m).

Capillary rheometry is often used for measuring and comparing the melt rheology of thermoplastic materials. It can be used to observe how the rheology changes with temperature and can help to understand and refine the operating conditions when centrifugal spinning.

The specific equipment used in this experiment was a RH2000 capillary rheometer produced by Bohlin Instruments, UK, with a 16 mm barrel and a 1 mm die. Polymer was packed into the chamber, heated to a desired temperature and extruded at a specific flow rate by altering the piston speed. A pressure sensor at the die records the pressure once an equilibrium condition is reached and the flow has stabilised. Equilibrium was determined by recording 16 measurements that are within a specific tolerance, normally 0.5 % of the pressure reading. The measurement taken value was an average of the next 8 values recorded and is accepted if there is no out-of-tolerance deviation. The specific conditions used to measure each polymer is listed in the appropriate chapter.

2.4 Differential scanning calorimetry

Differential scanning calorimetry (DSC) is a well-established method used in a range of research and quality control applications. DSC allows thermal transitions within a sample to be readily identified and the energetic requirements of said transitions to be calculated.

2.4.1 Theoretical basis

The thermal changes and transitions of materials can be studied through the technique of differential scanning calorimetry (DSC). In DSC the sample sits on a platform adjacent

to an empty reference pan. The identical platforms are connected to a common heating source. The empty reference pan creates an energy imbalance compared to the sample pan. The difference in energy required to heat/cool the sample pan is recorded by a computer. This differential energy measurement across a range of temperatures is the essence of DSC analysis.

By scanning through a range of temperatures a change in heat flow can be observed as a sample undergoes a state change. Thermoplastic behaviour of a sample such as glass transitions, melting and crystallisation require or release different amounts of energy compared to non-transitional temperature changes and will be visible in a typical DSC scan. Melting of crystalline regions in a non-amorphous material requires additional energy so there will be an endothermic slope in a DSC scan around the T_{melt} of a material. Melting is a first order transition and the temperature within a region will not rise until the crystals have melted so more energy will be required to keep the pans heating at the same rate. This will begin when the smallest crystals begin to melt, at T_{onset} and the energy required will increase and peak where the majority of crystals are melting, creating the largest energy difference between the sample and reference pans. When the material is fully molten the energy difference will stabilise.
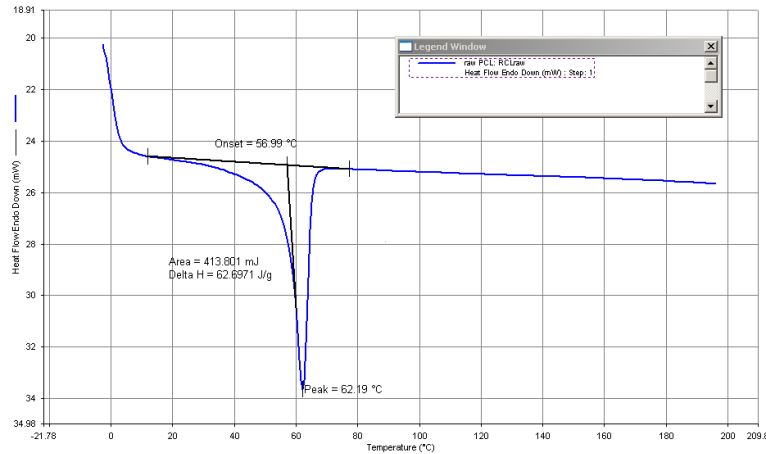
Figure 2.7: Typical DSC graph of a copolymer poly (vinyl pyrrolidone) with 1-triacontene.

In a typical DSC analysis a material scanned at an appropriate temperature will consist of a baseline and observable peaks, Figure 2.7. The peak may point up or down depending on whether the change is exothermic or endothermic. Comparison of the peak gradient compared to the baseline allows plotting of the extrapolated T_{onset}, which is considered to be the minimum point of a major thermal transition. The apex of the peak is when the maximum energy difference occurs and so is used to determine the melt point or the crystallisation temperature. In a melting transition the area of the endotherm allows for the enthalpy of melting and is calculated using the area under the melting curve on the DSC graph. If the enthalpy information is available for a single, perfect crystal of the same material then a degree of crystallinity can be estimated.

Thermal transitions in a sample are often determined by its thermal history. Rapid quenching will generate a differing material crystallinity to natural cooling. This difference would be detecting through a change in T_{melt}, T_{onset} and enthalpy.

2.4.2 **Procedure**

The samples were sealed in aluminium pans and then accurately weighed. It is important that pan weights are not excessively high or low: Menczel and co-workers (2008) recommend using a sample weight of between 3 and 10 mg for most calorimeters in operation presently, a recommendation which was observed in this work. Careful pan preparation was also important as any impurities on the inside or outside of the pan affects the results.

The sample was then heated from a set temperature at a pre-determined rate. A dry purge gas, in this case nitrogen, was used to prevent condensation within the cell and to ensure a constant atmosphere.

2.5 **X-ray diffraction**

X-ray diffraction (XRD) has enabled huge advances in the field of crystallography. It is discussed extensively in the literature as a means to investigate polymer fine structure and crystal orientation. When past researchers have investigated fibre fine structure X-ray diffraction is often used as a complementary technique to DSC.

2.5.1 **Theoretical basis**

Polymer crystals have a regular structure that is capable of scattering incident radiation (Pope, 1997). X-rays have a wavelength such that the gaps between crystal planes act like

a diffraction grating when struck by incident X-rays at a correct angle. An incident X-ray, of wavelength, λ, is scattered by the amorphous regions and diffracted by crystalline regions when it strikes the material (Murthy and Barton, 1999). In a wholly amorphous material there is no long range order so the X-rays are diffusely scattered and create no significant sharp peaks. A significant amorphous region will result in a broad area known as the amorphous halo. In a crystalline sample the lattice planes will diffract the beam at an angle that depends on the size of the unit cell. If the X-rays are diffracted at such an angle that the overall path difference in neighbouring beams was a multiple of the wavelength, then constructive superposition occurs and the reflected beam is very intense. Any deviation from the critical angle, θ, will lead to destructive interference and the intensity will decrease abruptly.

The spacing between two diffracting planes will determine when superposition of an incident beam occurs. Working on this principle, the plane spacing of a diffracting crystal is then calculated using Bragg's law, as given by Pope (1997):

$$2d\sin\theta = n\lambda \qquad \text{Equation 2.6}$$

where d is the spacing causing the diffraction, θ is the angle of incidence, λ is the wavelength of the incident beam and n is the order of diffraction. A semi-crystalline polymeric material will most likely return a range of d spacing from which the dimensions of the unit cell can be calculated by using Equation 2.7 as given by de Villiers et al. (1998):

$$\frac{1}{d^2} = \frac{h^2}{a^2} + \frac{k^2}{b^2} + \frac{l^2}{c^2} \qquad \text{Equation 2.7}$$

Where h, k and l are Miller indices of the crystallographic plane selected and a, b and c are the dimensions of the resulting unit cell. A unit cell can be considered to have lengths a, b and c in the x, y and z directions from an arbitrary reference point. A unit cell is capable of defining the point of all other atoms within that crystal from a discrete starting position.

2.5.2 **Procedure**

To assess the fine structure of the fibres and raw materials powder XRD was conducted using a P'AN analytical X'Pert MPD X-ray diffractometer operating at room temperature. The X-ray tube target was CuKα radiation (λ = 1.540 Å). Scans were taken in the theta:theta orientation scanning in the Bragg angle, 2θ, through 4° to 60° with a step size of 0.066°.

2.6 **References**

DE VILLIERS, M. M., WURSTER, D. E., VAN DER WATT, J. G. & KETKAR, A., 1998. X-Ray powder diffraction determination of the relative amount of crystalline acetaminophen in solid dispersions with polyvinylpyrrolidone. *International Journal of Pharmaceutics,* 163, 219-224.

GENG, X., KWON, O.-H. & JANG, J., 2005. Electrospinning of chitosan dissolved in concentrated acetic acid solution. *Biomaterials,* 26**,** 5427-5432.

KRISHNAPPA, R. V. N., DESAI, K. & SUNG, C., 2003. Morphological study of electrospun polycarbonates as a function of the solvent and processing voltage. *Journal of Materials Science,* 38**,** 2357-2365.

LYONS, J., LI, C. & KO, F., 2004. Melt-electrospinning part I: processing parameters and geometric properties. *Polymer,* 45**,** 7597-7603.

LARSSON, M., 2014. An introduction to capillary rheometry: a method for evaluation material properties under process relevant conditions. *Malvern Instruments webcast*, 28th August 2014.

MENCZEL, J. D., JUDOVITS, L., PRIME, R. B., BAIR, H. E., READING, M. & SWIER, S., 2008. Differential scanning calorimetry (DSC). *In:* MENCZEL, J. G.

& PRIME, R. B. (eds.) *Thermal Analysis of Polymers.* John Wiley & Sons, United States.

MITSCHKA, P., 1982. Simple conversion of Brookfield R.V.T readings into viscosity functions. *Rheologica Acta*, 21, 207-209.

MURTHY, N. S. & BARTON, R., 1999. Polymer industry. *In:* SMITH, F., (ed.) *Industrial Applications of X-ray Diffraction.* CRC Press, United States.

POPE, C. G., 1997. X-Ray diffraction and the Bragg equation. *Journal of Chemical Education,* 74**,** 129.

VERNON-PARRY, K. D., 2000. Scanning electron microscopy: an introduction. *III-Vs Review*, 13, 40-44.

Chapter 3
Centrifugal spinning of polypropylene fibres

One of the capabilities of centrifugal spinning is the ability to process thermoplastic polymers into sub-micron diameter fibres. This chapter discusses the centrifugal spinning of polypropylene (PP); a major thermoplastic polymer for the production of nonwovens. Despite the prevalence of PP in the nonwovens industry there are only a limited number of papers detailing the centrifugal spinning of PP and available research has been largely limited to reports published by Raghavan et al. (2013) and Sweester and Zander (2014). This chapter investigated the production of polypropylene fibres by means of melt centrifugal spinning and discusses the impact of processing conditions on fibre and web characteristics and documents findings when the fibre's fine structure was scrutinised.

3.1 Introduction

Polypropylene (PP) nonwoven materials account for over half of all nonwoven products produced and PP nonwovens generated $16.4 billion in revenue in 2012 which is expected to surpass $25 billion by 2019 (Houte, 2014). If centrifugal spinning is to become an adopted technology it is important that it is seen to be capable of using polymers familiar to the industry. Using centrifugal spinning to produce polypropylene nonwovens would be a logical bridge for high volume manufacturers to cross as the resources for processing PP exist and the broad scope of applications is established. Using polypropylene also affords a direct comparison to the current progress in melt blowing and the electrospinning molten polymers. This chapter will demonstrate the spinning of

polypropylene using melt centrifugal spinning and will explore the impact of processing conditions on fibre characteristics and any observable change in the fibre fine structure. In particular it will use a broad range of processing temperatures, an area where there is a paucity of research thus far with regards to centrifugal spinning.

Polypropylene is a synthetic polymer ubiquitous as a plastic and industrial filament material. PP is a polyolefin and its monomer constituent, propylene, is refined from crude oil, and thus the long term prosperity of this filament is intrinsically linked to the harvesting and use of oil as a resource (Hirte, 1984). Polypropylene, along with polyethylene (PE), is widely used in the packaging, insulation and filtration industries along with some uptake in clothing and medical applications. Despite the emergence of biosynthetics such as poly(lactic acid), polypropylene products occupied 63 % of the overall nonwovens market in 2007 and comprised 83 % of the direct polymer-to-web nonwovens market in 2014 (Wiertz, 2014). The extensive demand for polypropylene products shows no signs of abating with Exxon Mobil recently investing in a new multi-billion dollar polypropylene and polyethylene chemical plant in Singapore (Exxon Mobil Online, 2013). This continued and widespread use is due to the ease of polymer processing coupled with chemical inertness, lightweight and good mechanical properties. This was not always the case as early PP and PE grades were susceptible to UV, chemical and heat degradation. To overcome this technical deficiency stabilising elements were added during polymerisation to increase the stability of the polymers (Carlsson and Wiles, 1976).

Polypropylene is produced through the addition reaction of propylene to create a polymer with an ethylene backbone with pendant methyl group as shown in Figure 3.1. The chemical mer unit of polypropylene is –CH_2-CH(CH_3)-.
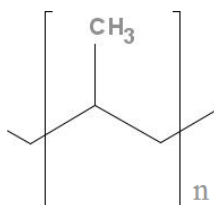
Figure 3.1: Chemical structure of polypropylene CH_2-CH(CH_3) mer.

Polypropylene can be produced in atactic, syndiotactic or isotactic confirmations which determines the chemical and rheological characteristics of the polymer. The isotactic form, Figure 3.2, contains all the methyl branches on the same stereo centre. At present, the isotactic form is the form more commonly used in the textile and plastics industry.
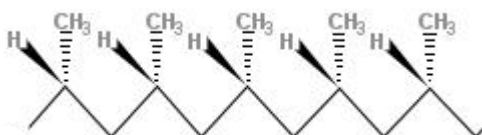
Figure 3.2: Chemical structure of the isotactic form of polypropylene.

Varying grades of polypropylene are used in industry which can vary significantly in terms of average chain length and in polydispersity, which is the distribution of chain lengths within a sample. The trade of polypropylene is graded using the melt flow index (MFI) measure which states the rate of polymer flow through a die for a given pressure and temperature. The units for MFI are grams of polymer per 10 minutes (g 10 min^{-1}) and is usually quoted alongside the testing conditions. However, the use of MFI is criticised by Bremner (1990) as the value is test specific and may not replicate polymer behaviour

in processing conditions. Despite this criticism melt flow index continues to persist as a recognised index for both polyethylene and polypropylene. The melt flow index of a material will primarily be determined by the average molecular weight and from this Besco et al. (2014) proposed the relationship given in Equation 3.1:

$$\frac{k}{MFI} = M_w^x$$
Equation 3.1

Where k is a constant, determined by the polymer and processing parameters, M_w is the weight average molecular weight and x is a value related to polydispersity and is usually between 3.4 and 3.7. Equation 3.1 can then be used to estimate the average molecular weight as shown in Table 3.1.

Table 3.1: Calculated molecular weight from melt flow index (Besco et al., 2014).

Grade of Polypropylene	Melt flow index (230 °C / 2.16 kg) (g 10 min^{-1})	Calculated M_w (kDa)	Application
Lyondell Basel MF650Y	1800	72.5	Melt blowing
Borflow HL504FB	35	210.2	Filament spinning

Conventional fibre grade polypropylene used in fibre production has a typical MFI of 30 - 40 g 10 min^{-1} which correlates to a molecular weight of around 200 kDa whereas commercial melt blown polypropylene will have a typical MFI ranging from 1200 - 1800 g 10 min^{-1} which translates into 70 - 100 kDa molecular weight. The long chains in conventional polypropylene afford the material superior mechanical properties such as higher tensile strength but also significantly increase the viscosity of the molten fluid. This higher viscosity makes this grade of polymer unsuitable for melt blowing as the level of airflow needed to induce polymer stream elongation is limited. For melt blowing, high

MFI polypropylenes are significantly less viscous at a similar processing temperature; the shorter chains allow for a much higher rates of flow that are required in order for attenuation by aerodynamic forces to occur. Short chain polypropylene is produced by introducing chain scission catalysts to crack the long polypropylene macromolecules into shorter chains under the influence of elevated temperature.

Polypropylene forms a semi-crystalline structure that can change significantly depending on the processing route. Most grades of PP can typically reach a crystallinity of 50-60 %. This value is lower than the 75-85 % observed in linear polyethylene due to the pendant methyl groups on PP restricting chain registration. The $-CH_3$ side group also causes polypropylene molecules to take up a helical form in the crystal lattice, with three repeats in one turn of the helix. A three-dimensional representation of this structure is shown below in Figure 3.3.
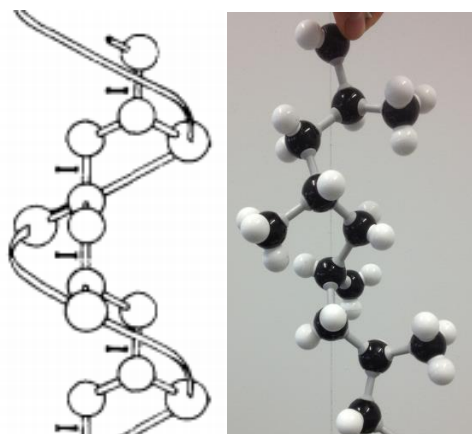
Figure 3.3: The helical carbon chain at drawn by Natta and Corradini (1960) and represented using a ball and stick molecular model

3.2 **Spinning polypropylene in to fine fibres**

Polypropylene is a thermoplastic and is almost exclusively melt processed to create usable products. PP melts are highly stable with rheological properties favourable to the production of fibre and films. Solution processing of PP is limited by the difficulty in dissolving PP as it requires the use of less benign solvents such as decalin and cyclohexane (Blackadder and Le Poidevin, 1976). Further problems with solution spinning PP were encountered by Zhou (2007) who was unable to dissolve PP at a sufficiently high concentration in a room temperature solvent to enable fibre formation. The lack of solution processability has resulted in polypropylene being largely ignored as a medium for electrospinning by the research community. So far, production of ultrafine PP fibres has been limited to refined melt blowing. Thus, there exists a gap in capability that a new technology such as centrifugal spinning could occupy.

Polypropylene has been melt blown into sub-micron fibres of ≤ 500 nm using finely optimised commercial equipment. This work is best exemplified by Ellison et al. (2007) who created PP fibres with mean diameters of 300 nm and more recently by Uppal et al. (2013) who produced fibres 260 nm in diameter. Both authors used a melt blown grade of polypropylene with a relatively short chain length. Using a higher molecular weight PP, Nayak et al. (2013) produced fibres 438 nm in average diameter by introducing air and water into the fluid stream.

The high melt fluidity of melt blowing grade PP has been used as the base material for fibres electrospun by Lyons (2004) creating webs as fine as 1.8 μm. Melt electrospinning is not capable of producing fibres as fine as solution electrospinning and the 1 μm

diameter barrier is identified as a significant hurdle by Lyons et al. (2004). More recently, Li et al. (2014) melt electrospun low M_w polypropylene and created webs with diameters above 2 μm and Fang et al. (2012) used needleless electrospinning to produce fibres less than 2 μm when adding a plasticiser to the polypropylene melt. Currently, the outstanding work in the literature was performed by Dalton (2007) who added a plasticiser to a 15 MFI polypropylene and achieved fibres as fine as 800 nm mean diameter.

Along with the above techniques, centrifugal spinning has been proven capable of producing ultrafine fibres from polypropylene. The study by Sarkar et al. (2010) was the first published account demonstrating centrifugal spinning of molten polypropylene into ultrafine fibres. However, the publication lacked depth and a more comprehensive study was reported by Raghavan et al. (2013) who created fibres using various grades of polypropylene using the Forcespinning™ variant of centrifugal spinning. They looked at four grades of polypropylene and measured the fibre distributions at a fixed temperature of 225 °C and found that sub-500 nm average fibres could achieved with a melt blowing grade of polypropylene. The full results for this study are detailed in Table 3.2. This result agrees with the inverse relationship between molecular weight and fineness of diameter as found by Lyons et al. (2004).

Table 3.2: Various polypropylene grades spun through centrifugal spinning by Raghavan et al. (2013) and measured fibre diameters.

Polypropylene grade	Melt flow index (g 10 min^{-1})	Average fibre diameter (nm)
Exxon Mobil homopolymer 3155	36	1230 ± 630
Lyondell Basell Metocene MF 650 W	500	898 ± 470
Lyondell Badel Metocene MF650 F	1200	863 ± 451
Exxon Mobil Achieve 69361G	1550	441 ± 243

This was then followed by work by O'Haire et al. (2014) who used centrifugal spinning to produce 510 nm mean diameter fibres using homogenous Lyondell Basel MF650Y polypropylene (MFI 1800 g 10 min^{-1}). Sweester and Zander (2014) produced polypropylene fibres using centrifugal spinning at temperature conditions 200, 230 and 250 °C. They found that the finest fibres with the least beading were produced at 200 °C but conducted no further research in to the effect of temperature. They found that fibre diameter decreased as the spinning speed was increased from 6,000 rpm to 10,000 rpm cannot say if further increases in speed produce finer fibres. Finally, they were unable to produce fibres finer than 1.5 μm average, reporting a mean diameter of 1.91 ± 0.86 μm as the finest web observed. This report failed to report the grade of PP used so it is difficult to compare it to the results found elsewhere.

3.3 **Summary**

Melt electrospinning and melt centrifugal spinning are discussed in less detail in the literature compared to solution spinning (Lozano and Sarkar, 2009; Sarkar et al., 2010; Sweester and Zander, 2014). One consequence of this is that there has been limited success in producing nanofibres from polypropylene using both melt blowing and melt electrospinning. This is despite polypropylene being a widely used material in the nonwovens industry. There has been work performed previously looking at the melt centrifugal spinning of polypropylene with some success reported in achieving sub-micron fibres. However, there is a paucity of publications detailing the effect of polymer temperature and spinning speed on end fibre diameter, fibre morphology and internal fine structure. Thus far, the work by Sweester and Zander (2014) is the most complete as

multiple temperatures are studied, however, they only considered a limited range of spinning conditions and were not producing submicron fibres.

3.4 **Experimental**

Given the limited published data with the effect of polymer temperature on the resultant end fibre diameter and fibre morphology, diameter and internal fine structure an experimental work was conducted with the following objectives:

1. To characterise the flow behaviour an appropriate grades of polypropylene across a range of temperatures;

2. To successfully melt spin polypropylene using centrifugal spinning and optimise the spinning conditions in regards to temperature and rotational speed;

3. To characterise the fibres produced using microscopy to determine morphology and typical fibre diameters and investigate how internal fine structure of material changes with spinning conditions.

Given the limited published data in this area, the experimental work was intended to identify trends between processing conditions and final mean fibre diameter, enabling optimum conditions for consistent ultrafine fibre production to be established. The experimental part of this research was designed to identify trends between processing conditions and end fibre diameter and to establish the range of conditions that allow for consistent ultrafine fibre production.

3.4.1 **Materials**

Different grades of polypropylene are available with varying chain lengths and melt viscosity behaviour. For non-direct attenuation techniques, such as melt blowing and centrifugal spinning, high MFI grades of polypropylene are required. This chapter used a low viscosity polymer suitable for melt blowing and processed into a fibre using melt centrifugal spinning. Lyondell MF650Y melt blowing grade polypropylene was used for this investigation and has a melting point of 154 °C and a melt flow index of 1800 g 10 min^{-1}.

3.4.2 **Capillary rheometry**

The Malvern RH2000 capillary rheometer was used to assess the shear viscosity of molten polypropylene at a range of temperatures. The testing regime performed used constant rate of shear tests using a 1 mm wide and 16 mm long capillary die with an entry angle of 180°. A preliminary study of the melting behaviour of MF650Y PP indicated that consistent flow was difficult to maintain at temperatures below 180 °C, at a test extrusion conduction at 160 °C the polymer was observed to be highly viscous and difficult to extrude in to fibres. Therefore, the melt viscosity of MF650Y was tested at varying barrel and melt temperatures, the range 180 °C to 230 °C was studied working in increments of 10 °C. The sample was tampered down during pellet loading to remove air, this is necessary as the presence of gas reduces the viscous resistance of a melt. A pre-test heating and compression cycle was performed where the piston compressed the sample to a pressure of 0.06 MPa which was then held for 4 minutes to allow heat to permeate through the sample. The test was then performed using piston speeds on 14, 25, 50, 70, 120 and 200 mm min^{-1}.

3.4.3 **Centrifugal spinning of fibres**

In order to establish the effect of processing conditions on the properties of the fibre and web produced the selected polymer grade was spun under a range of conditions. The polymer was added to a preheated High MFI tri-orifice spinneret, Figure 3.4.
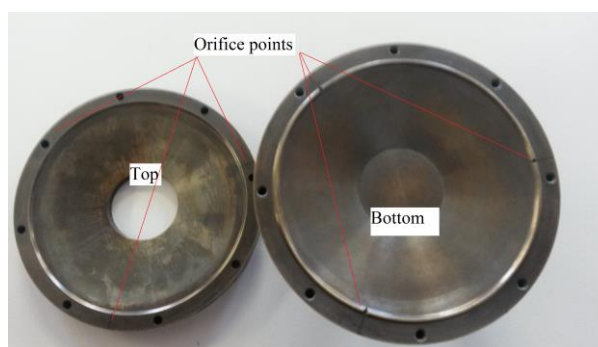
Figure 3.4: Opened tri-orifice melt spinneret for high MFI materials.

The polypropylene was centrifugally spun into fibres over a temperature range of 170 to 230 °C using rotational speeds ranging from 11,000 to 16,000 rpm. The polymer temperature was measured using a platinum resistance thermometer inserted directly into the polymer reservoir. The testing intervals were 10 °C and 1,000 rpm, respectively, for the two parameters. The spinnerets were preheated to the desired temperature and then 100 mg of dry PP was added. The polymer temperature was measured using a thermocouple interested directly in to the molten fluid. When the polymer temperature reached the required value the spinneret was accelerated to the processing speed. The spinneret was rotated at the desired speed for 40 seconds before decelerating and coming to rest. Successful fibre production and web quality was noted at each spinning condition.

3.4.4 **Fibre analysis**

3.4.4.1 **Scanning electron microscopy analysis**

SEM was used to assess fibre morphology and to facilitate measurement of average diameter and fibre diameter distributions. The SEM equipment and sampling procedure and the subsequent fibre measurement technique is detailed in Chapter 2. Each successful spinning condition used was imaged using SEM.

3.4.4.2 **Differential Scanning Calorimetry**

The DSC measurements were obtained using a Perkin Elmer Jade DSC through a heat-cool-heat cycle operating from 0 °C to 240 °C at a rate of 20 °C per minute under a nitrogen atmosphere delivered at 30.0 cm^3 min^{-1}. DSC measurements were recorder for fibres produced at 180, 200 and 220 °C for each rotational speed condition.

3.4.4.3 **X-ray diffraction**

The X-ray diffraction was performed on both the bulk material and on the fibres in order to determine structural differences. The bulk material was extruded into a 2 mm thick film at 200 °C and allowed to cool in ambient conditions. This process is designed to mimic a slower cooling process to replicate polymer crystallisation behaviour in film and fibre extrusion. Extrusion in to a film also created a flat surface which is better suited to X-ray analysis compared to the granule form. The fibres were pressed into a relatively flat surface by overnight compression. Scans were taken in the theta: theta orientation scanning in the Bragg angle, 2θ, through 4° to 60° with a step size of 0.066°.

3.5 **Results and discussion**

3.5.1 **Capillary rheometry**

The results of the capillary rheometry measurements for MF560Y, Figure 3.5, shows the relationship between polymer shear stress and the shear viscosity at a range of temperatures. It was difficult to attain a measurement for the fluid at 230 °C for shear rates above 50 mm min^{-1} as the polymer supply would exhaust before an acceptable equilibrium was reached. Examination of Figure 3.5 indicates that for a given shear stress, the viscosity is lower at higher temperatures as the temperature is increased from 180 to 230 °C. In addition, at a given temperature the viscosity of polypropylene also reduced with increasing shear rate. This behaviour is known as shear thinning and is due to the elastic nature of polymeric materials.

It should be noted that the measurements provided here correlate to apparent, not true, shear stress and shear viscosity. This is due to die entrance and exit effects that influence the final measurement and the magnitudes of these effects are dependent on the geometric specification of the die. Thus, the measurements are only valid when quoted in conjunction with the measurement conditions. However, when making comparisons using the same material, apparent viscosity is sufficient to establish changes in viscosity with temperature or shear rate.
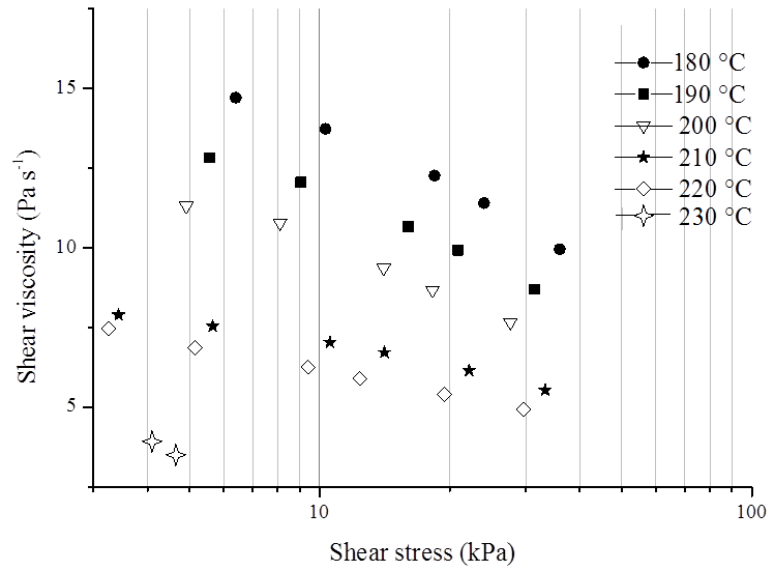
Figure 3.5: Logarithmic plot of apparent shear viscosity against shear stress for MF650Y polypropylene across a range of temperatures

From Figure 3.5 it can be seen that an increase in temperature leads to a marked decrease in shear viscosity. The capillary rheometer results in Figure 3.5 agree with the empirical results found by Ellison et al. (2007) and also agree with the theoretical relationship for intrinsic viscosity η_o, is given by the Arrhenius equation (Bower, 2002):

$$\eta_o = A \, exp \left(\frac{Evis}{R_g T} \right)$$

Equation 3.2

Where A is a pre-exponential constant, R_g is the gas constant and T is the temperature in Kelvin. $Evis$ is an activation energy term which is related to molecular weight, chain mobility, branching and intermolecular forces.

The Arrhenius equation predicts that as polymer temperature increases the viscosity will fall providing there is sufficient energy in the system. This temperature dependence of shear viscosity was relevant as it influenced the fibre formation process.

This information regarding viscosity change can be linked to equations presented in Chapter 3 to determine the effect of temperature on orifice throughput rate: in batch centrifugal spinning it is known that for a given volume, the hydrostatic and inertial forces are constant at a given speed, Equation 1.6, page 29; assuming the orifice diameter remains constant then it can be said that at a fixed condition the shear stress is also constant. As the viscosity is reduced by temperature than applying the same shear stress will result in a different shear rate at each temperature condition; thus, the throughput of a polymer increases with temperature.

3.5.2 Fibre production

Polypropylene was successfully centrifugally spun into fibrous webs using a range of processing conditions. The fibres were produced as a web that was freestanding when supported by the collector bars. The polypropylene webs had a high level of loft and were not produced as a flat sheet. In fact the webs produced a cone-like shape; the inner edge of the ring migrated closer to the spinneret as the spinning progresses. This shape is shown in Figure 3.6. The webs also contained discrete areas of non-uniformity which contained a more densely packed assembly of fibres compared to the surrounding nonwoven. The webs were self-supporting with enough strength to be handled but without a fabric support they condensed to form a circular rope upon removal from the spinneret.
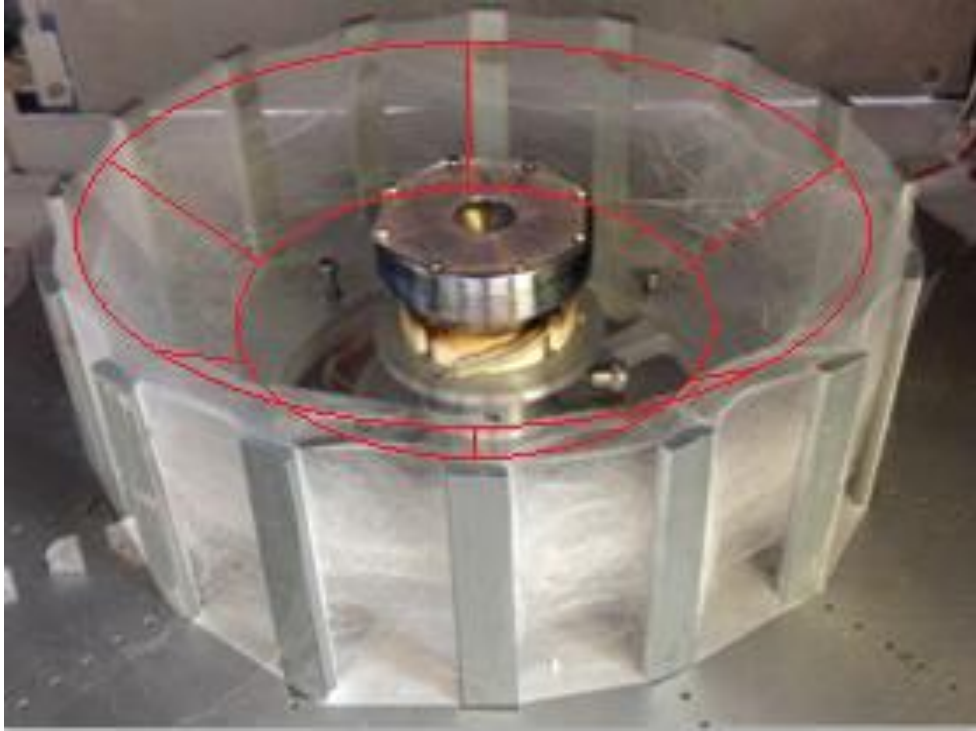
Figure 3.6: Fibrous web produced from polypropylene using centrifugal spinning. The red lines are drawn to show the approximate shape of an inverted frustum.

A summary of the conditions necessary production of centrifugally spun PP webs is shown in Table 3.3. The mass of the webs collected was found to be consistently lower than the initial in-feed polymer mass which was fixed at 100 mg. This can be partly explained by a small residual amount of polymer left in the spinneret which was observed upon opening. This links into the relationship given previously in Equation 1.13, page 34: as the polymer is exhausted the centrifugal pressure reduces to an extent that production ceases due to a drop in cumulative pressure. Deposition of additional fibres exhausted after 40 seconds even though residual polymer was still present in the reservoir. Extending the spinning time beyond this period made no difference and the residual polymer remained. The difference between the in-feed and deposited fibre mass can also be explained by the fact that not all the fibres were collected by the main deposition zone. It was also observed that some fibres are lost to the outer wall of the equipment during

the start of the spinning phase. Without a substrate or established webs, broken fibres are not captured by the collector posts.

Table 3.3: Results of fibre production using MF650Y PP at a range of matrix and rotational speeds using the high MFI spinneret.

Temp (°C)	Rotational speed (rpm)							
	10,000	11,000	12,000	13,000	14,000	15,000	16,000	17,000
170	x	x	-	o	-	o	-	-
180	x	✓	✓	✓	✓	✓	✓	b
190	x	✓	✓	✓	✓	✓	✓	-
200	x	✓	✓	✓	✓	✓	✓	✓/b
210	x	✓	✓	✓	✓	✓	✓	-
220	o	✓	✓	✓	✓	✓	✓	o/b
230	o	o	o	o	o/b	o/b	o/b	-

x- fibres were not produced
o- fibres were produced but a cohesive web was not produced
✓- fibrous webs were successfully produced
b- excessive beading observed

Fibres were difficult to form at a processing temperature of 170 °C. A large volume of polymer was observed to be retained within the spinneret after a spinning cycle. It is proposed that at this low temperature, the viscosity is sufficiently high that the flow through the capillary is restricted, limiting fibre formation. At 230 °C the 'quality' of the web deteriorates at all spinning conditions observed. The suggested reason for this is an increased level jet breakup, creating shorter continuous lengths preventing web establishment. There was a significant decrease in the weight and quality of the webs collected as the processing temperature was increased to 230 °C. This change in web structure is linked to increasing levels of filament breakup during the spinning. The higher temperatures reduce the polymer viscosity sufficiently that the jet is more inclined to break into beads and shorter fibres. This prevents a cohesive web from building up as there are fewer longer filaments to overlap and form an entangled nonwoven.

Increasing the spinning speed to 17,000 rpm also had a negative impact on the volume and quality of web produced. At all temperature conditions observed (180, 200 and 220 °C) it was difficult to build a cohesive web. It is proposed that at this rotational speed the drawing due to tension and aerodynamic resistance are sufficiently high that jet formation is disrupted and droplets are formed. In addition, it was noted by the author that at 17,000 rpm and beyond the vibration and noise produced by the centrifugal spinner is excessive compared to slightly lower spinning speeds.

The web form shown in Figure 3.6 and the SEM images shown in Figure 3.7 are typical images of the webs produced between 180 °C and 220 °C. The observed fibre morphology was of smooth fibres with very little surface texture. This type of fibre was found across the range of processing conditions. The high magnification SEM images show that the polypropylene fibres produced were smooth, approximately cylindrical in shape with very few fibre ends observed. This leads to the estimation that the filaments are generally continuous in length. In melt processing there was no evaporating component to generate any surface deformation; the surface tension of the fluid acts to maintain the cylindrical shape and prevents texture formation resulting in smooth and roughly cylindrical fibres (Lee and Wadsworth, 1992). However, this surface tension can also create instabilities which can lead to periodic wave like filament profiles observed in polypropylene melt blown products (Ellison et al., 2007).
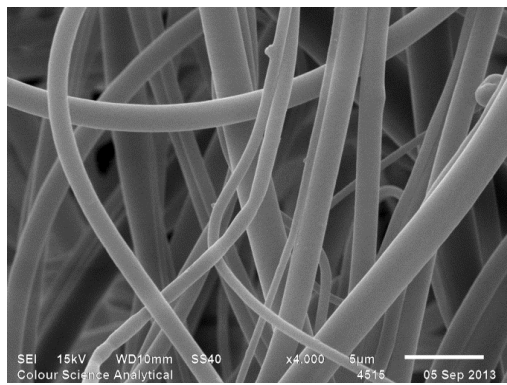
180 °C and 11,000 rpm
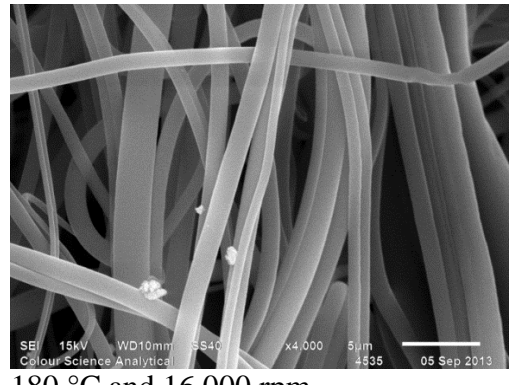
180 °C and 16,000 rpm
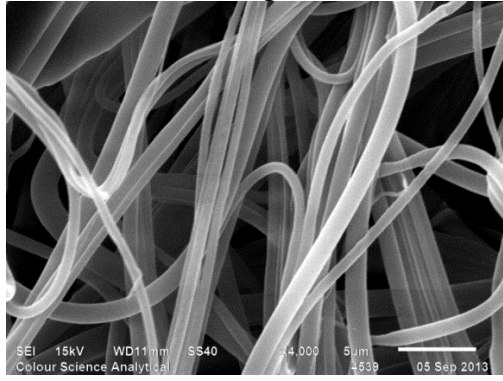
190 °C and 11,000 rpm
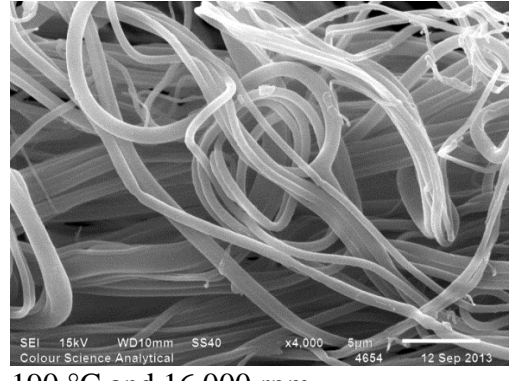
190 °C and 16,000 rpm

200 °C and 11,000 rpm
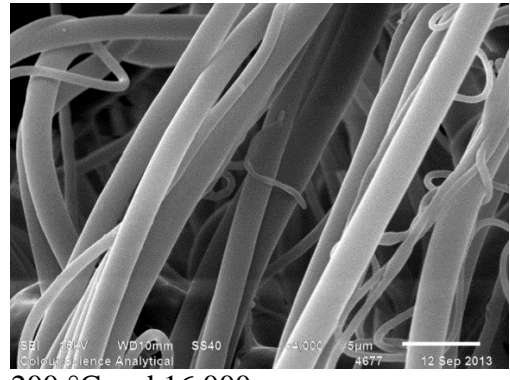
200 °C and 16,000 rpm

Figure 3.7a: SEM image of polypropylene fibres centrifugal spun across the temperature spectrum at the two spinning speeds.

210 °C and 11,000 rpm

210 °C and 16,000 rpm

220 °C and 11,000 rpm

220 °C and 16,000 rpm
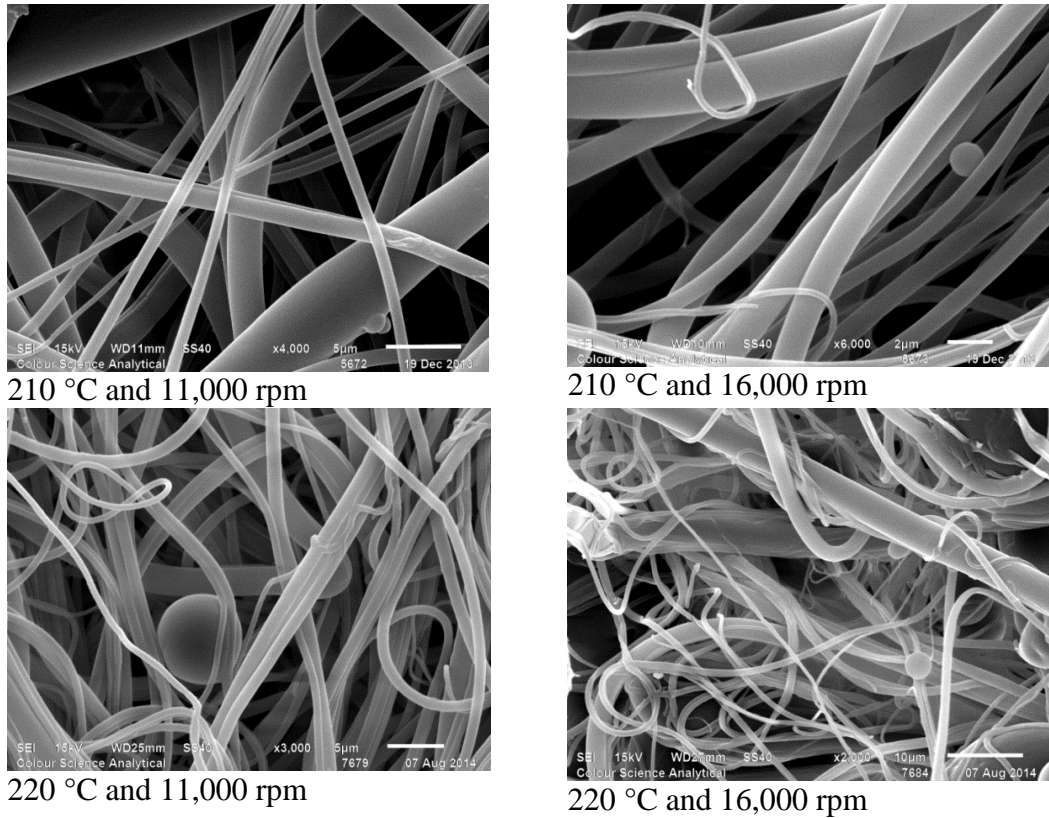
Figure 3.7b: SEM image of polypropylene fibres centrifugal spun across the temperature spectrum at two spinning speeds.

There are additional features that are seen in Figure 3.7 that merit discussion. The first is that the finer fibres have a visibly smaller bending radius compared to the larger elements. To illustrate this, the bending radius of curved fibres was measured and compared against filament diameter. The bending radius was found by fitting a circle that best represented the point of highest curvature. Only fibres bending beyond 90 degrees were measured. The results are shown in Figure 3.8.
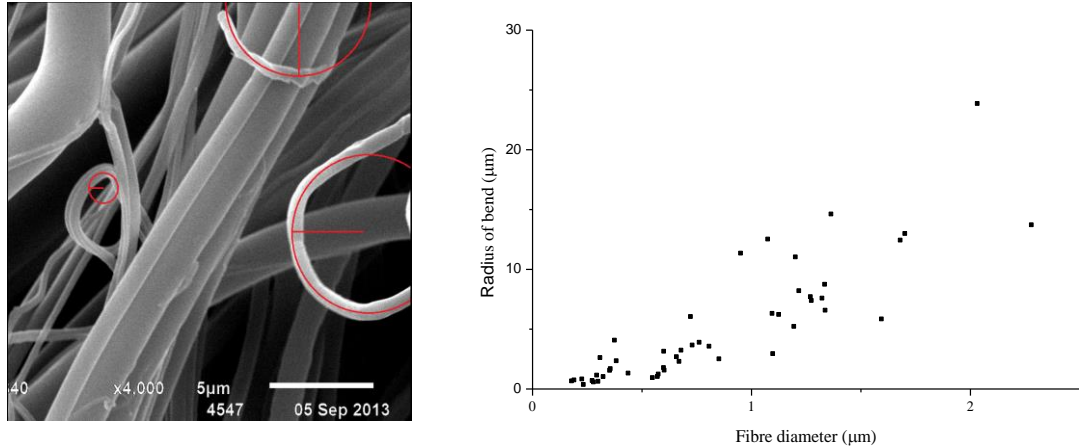
Figure 3.8: Measurement of bending radius with a graph showing relationship between fibre diameter and radius of bend.

It should be noted that the fibres in the SEM micrographs are not subjected to any external forces so are unlikely to be at the maximum level of bend possible and that in reality the fibres are bending in three dimensions. However, the results do show that the finest fibres are more likely to bend in a much smaller curve profile. This links to Equation 1.3, page 9, which describes flexural rigidity as a function of filament diameter. As the filaments become finer they become more flexible as per the rigid rod model presented in Section 1.3. The more flexible fibres are more easily deformed external forces and collisions resulting in tighter coils within the fibre.

Another feature of the polypropylene webs, seen across the spectrum of processing conditions is the twinning of fibres. Fibre twinning is the apparent agglomeration of two or more fibres into a larger element giving the impression of highly orientated fibre structure. A typical image of this phenomenon is shown in Figure 3.9:
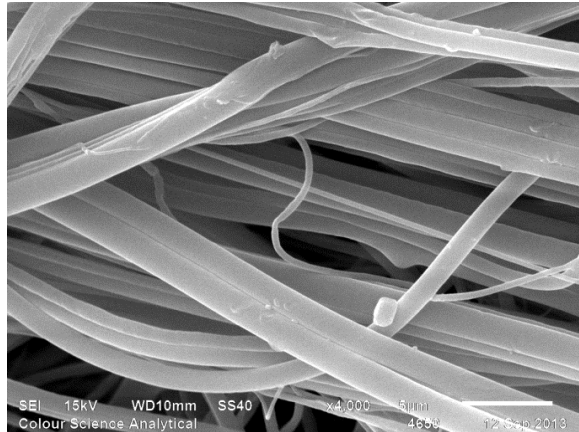
Figure 3.9: High density of fibre twinning in a PP web formed at 190 °C and 15,000 rpm

Twinning is the phenomenon of fibres appearing to be aligned and parallel with a bonding interaction between them. Twinning can actually occur between more than two fibres as observed in Figure 3.9. Twinning has been observed previously in SEM images of melt blown PP webs however this is the first report of this phenomenon in centrifugal spun fibres (Hassan et al., 2013; Pall and Connors, 1996). These twinned fibres may be physically merged or may be brought together by other attractive forces. It is proposed here that it is more likely the former and that still molten fibres come into contact with other fibres during spinning, resulting in a slight fusing of the fibres. When centrifugal spinning several polymer jets will exist in the spinning gap at any given time, all taking a roughly similar path to the collector, it is possible that the fibre jets overlap and touch following the elongation phase.

Occasional flaws were observed in the web with fibre necking seen in several SEM images, Figure 3.10. Necking is a phenomenon observed in the processing of many thermoplastics into fibres. It is associated with the cold drawing of plastics where the fibre is disrupted by a narrow neck. The length of these necks may be relatively short or may be sufficiently long that they are seemingly endless when observed in the SEM. The

presence of necking indicates that the attenuation process in centrifugal spinning is not applied evenly to all regions of the filament in flight. It is thought the necking occurs as a partially solidified jet continues to elongate in a localised region, creating the neck. No relationship could be found between the frequency of necking and processing conditions.
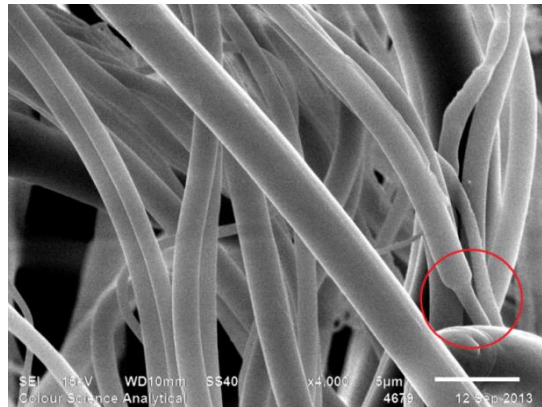
Figure 3.10: MF650Y PP produced using centrifugal spinning at 200 C at a rotational speed of 16,000 rpm. Circled is an example of fibre necking.

Shot or beading was observed in the images of the fibres spun at the higher temperatures. There was a marked increase in beading as the temperature was increased from 210 °C to 220 °C. The beading within a web at this temperature is shown in Figure 3.11.
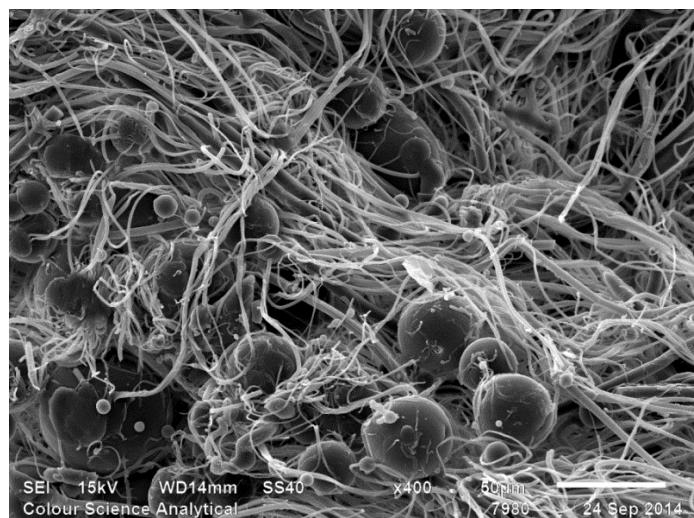
Figure 3.11: Bead formation in PP fibres spun at 220 °C at a speed of 12,000 rpm.

It is thought that a polymer temperature of 220 °C marks the approximate upper limit between stable filament production and excessive bead formation due to instability driven jet breakup. If the temperature is increased further to 230 °C, a cohesive web cannot be produced indicating that the jet is forming a greater number of beads. Numerous researchers have postulated the cause of bead formation in melt blown and electrospun processes where the cause of breakup is due to surface tension induced jet contraction which is unchecked by internal frictions (viscosity). Surface tension acts to minimise the surface area and will pull any fluid into a bead (the minimum surface area condition). The viscosity of a fluid resists any movement and the various chain entanglements and interactions will act to maintain the current state and shape. As per the capillary rheometry results the fluid has the lowest viscosity at the highest temperature setting. The result is that spinning PP at 220 °C and 230 °C will create fine fibres, but the jets are more inclined to collapse into a bead during processing.
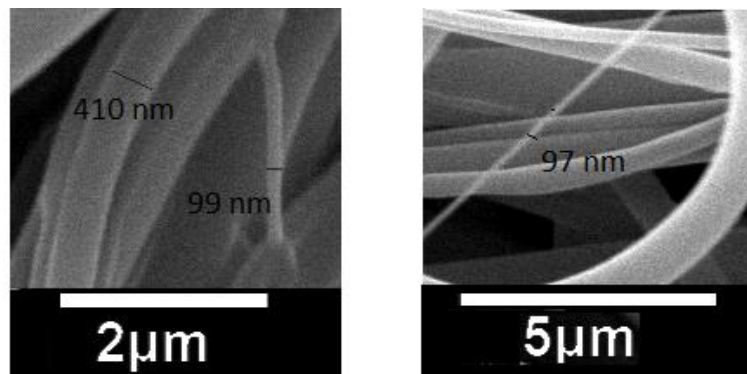
Figure 3.12: Examples of sub 100 nm fibres observed when centrifugal spinning PP at 190 °C and 16,000 rpm (left) and 210 °C and 14,000 rpm (right)

The fibre diameters were measured in the SEM micrographs at each production condition. Whilst some true nanofibres were observed (Figure 3.12), the majority of fibres were larger and the mean diameters were in the sub-micron range for the most part. The mean diameter and standard deviation are shown in Table 3.4.

Table 3.4: Mean diameter and standard deviation of centrifugal spun polypropylene.

Rotational speed (rpm)	180 °C		190 °C		200 °C		210 °C		220 °C	
	Mean	SD	Mean	SD	Mean	SD	Mean	SD	Mean	SD
11,000	1.36	0.82	0.78	0.79	0.97	0.57	0.83	0.47	0.83	0.47
12,000	0.83	0.43	0.82	0.50	0.63	0.40	0.64	0.39	0.75	0.51
13,000	0.79	0.39	0.62	0.35	0.65	0.40	0.77	0.38	0.77	0.47
14,000	0.68	0.29	0.56	0.38	0.65	0.40	0.74	0.36	0.77	0.41
15,000	0.63	0.39	0.58	0.39	0.67	0.34	0.53	0.30	0.50	0.31
16,000	0.75	0.37	0.47	0.29	0.71	0.44	0.54	0.29	0.69	0.47

All measurements in μm

Table 3.4 confirms that the average fibre diameter within the webs was typically in the sub-micron range. Previous researchers also found a similar range of data when spinning polypropylene; Raghavan et al. (2013) melt spun 225 °C polypropylene at 12,000 rpm recorded diameters of 863 ± 451 nm. Table 3.4 also shows that the webs contain a broad range of fibre diameters which leads to a significantly large standard deviation and the coefficient of variation observed was typically over 50 %.

The fibre diameter measurements also show a statistically significant reduction in mean diameter as the rotational speed is increased from 11,000 to 15,000 rpm. This was true at 180 °C (($p > 0.05$, F (54.3) > Fcrit (3.88)); 190 °C ($p > 0.05$, F (78.1) > Fcrit (3.87)); 200 °C ($p > 0.05$, F (16.7) > Fcrit (3.88); 210 °C ($p > 0.05$, F (57.7) > Fcrit (3.86)) and 220 °C ($p > 0.05$), F (4.09) > Fcrit (3.86) when the data was analysed using the single variable Analysis of Variance (ANOVA). The data in Table 3.4 is also represented graphically in Figure 3.13 and the trend for increasing fineness with increasing speed is illustrated. This

relationship is expected as the higher angular velocity leads to a higher centrifugal force which increases the level of attenuation on the jet. There is a limit to this relationship: higher angular velocities will also increase the throughput rate at the orifice which acts to increase the volume of the jet and thus the end fibre diameter.

Analysis of the data summarised in Table 3.4 indicated that as the temperature was increased from 180 °C to 190 °C the fibre diameter decreased significantly for all but the 12,000 rpm condition, which was a decrease in the mean but was not found to be significant. Beyond 190 °C further differences between the operating temperatures were not seen to result in statistically finer fibres. It is proposed that increasing jet temperature also increases the fibre attenuation time as previously discussed, page 41, as the higher T_p of the hotter polymer jet takes longer to cool to T_c and solidify. However, this was not borne out in the results and there was no decrease in diameter observed by Sweester and Zander (2014) in the only other pertinent work on this topic. They found an increase in fibre diameter from 1.91 to 2.27 µm as the temperature was increased from 200 to 230 °C, however, the fibres were also found to be variable and no test for significance was conducted on the raw data.
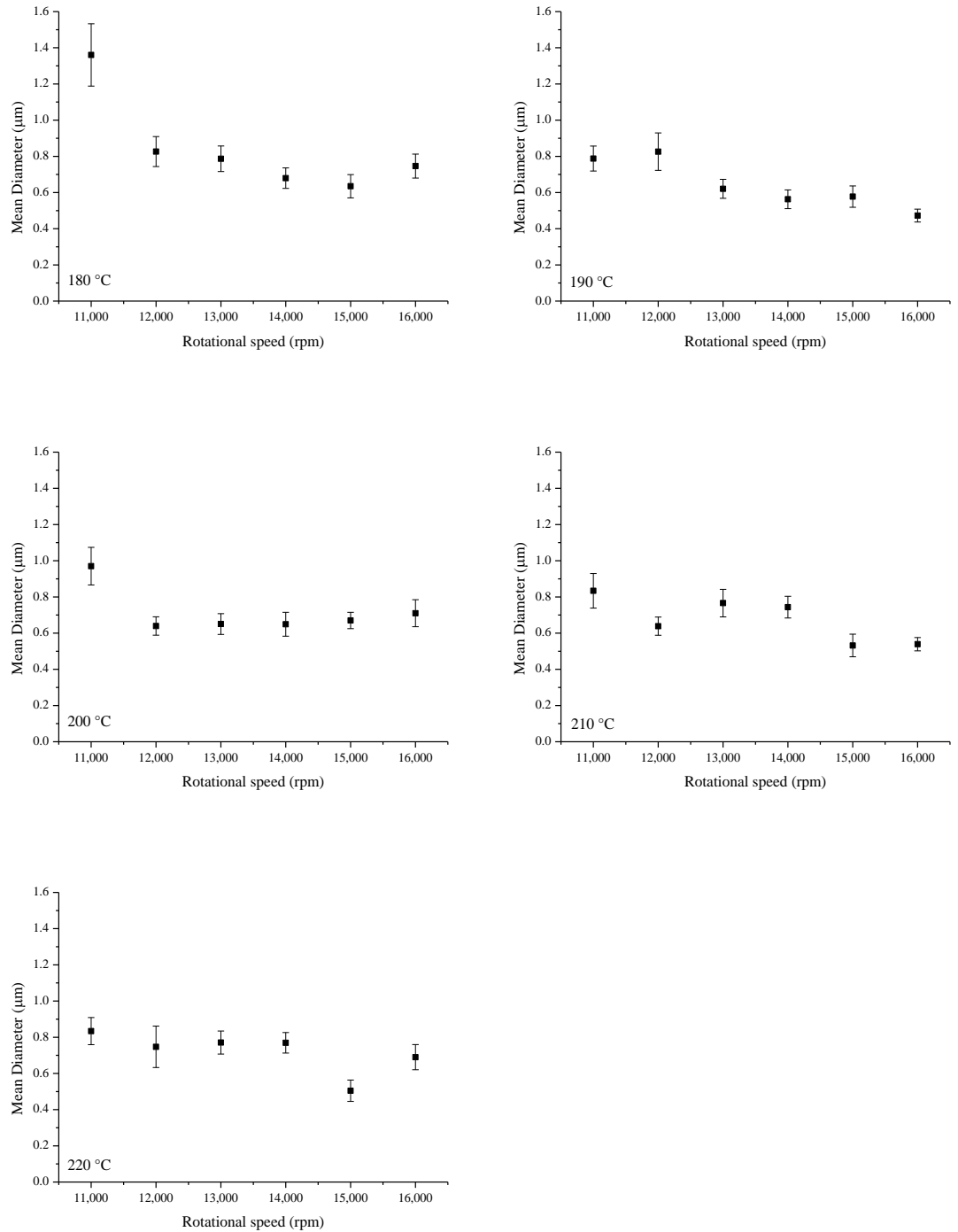
Figure 3.13: Graphs showing the mean and the 95 % confidence interval for the fibre diameter of PP webs based on rotational speed of centrifugal spinner. Each graph indicates an isothermal condition investigated.

This high variability in fibre diameter presented problems when trying to establish firm relationships between processing speed and fibre diameter. The broad distributions results in a relatively high standard deviation with respect to the mean. In order to establish reliable data a large number of fibres must be measured. Table 3.4 indicated that the diameter distributions of centrifugal spun polypropylene are inherently broad. This high In addition, any discussion using mean fibre diameter as the principle measure can become meaningless when there is the obvious presence of larger diameter fibres which may be orders of magnitude bigger than the smaller elements, Figure 3.7. Due to the limited sample size these larger diameter elements can have a significant impact on the overall mean diameter recorded. However, very large diameter fibres can represent a significant mass fraction of any web produced and so must be included in any characterisation methods. The larger fibres are potentially formed during acceleration and deceleration of the spinneret. During this period, acceleration forces are non-uniform which could lead to a reduction in polymer jet extension. It is thought that once the spinneret is spinning at a constant speed the resulting fibre diameter is generally finer and more uniform. This is supported by research conducted by McEachin and Lozano (2012) who measured fibre diameter and dispersity based on spinning time. They found that fibre diameter is typically larger and more varied during shorter run periods. To circumvent this effect a wholly continuous, commercial centrifugal spinning machine would have much longer spinneret running times which would potentially remove the impact of spinneret acceleration/deceleration on web quality. It is proposed that any full-scale spinning process would have this ability to consistently introduce polymer into the spinneret via a screw and metering pump system. This direct feed would allow the polymer flow rate and hydrostatic pressure within the spinneret to be controlled. As a

result processing conditions can be tailored and further optimised for maximum throughput or desired fibre properties.

3.5.3 **Differential scanning calorimetry**

The DSC traces for the virgin PP flake and a selection of PP fibres are shown in Figure 3.14. The trace for the polymer pellet shows an endothermic peak that has a maximum at 168.8 °C. This peak is the melting transition of the initial polymer granules; the transition has a T_{onset} of 148.8 °C and an enthalpy of 97.7 J g^{-1}.
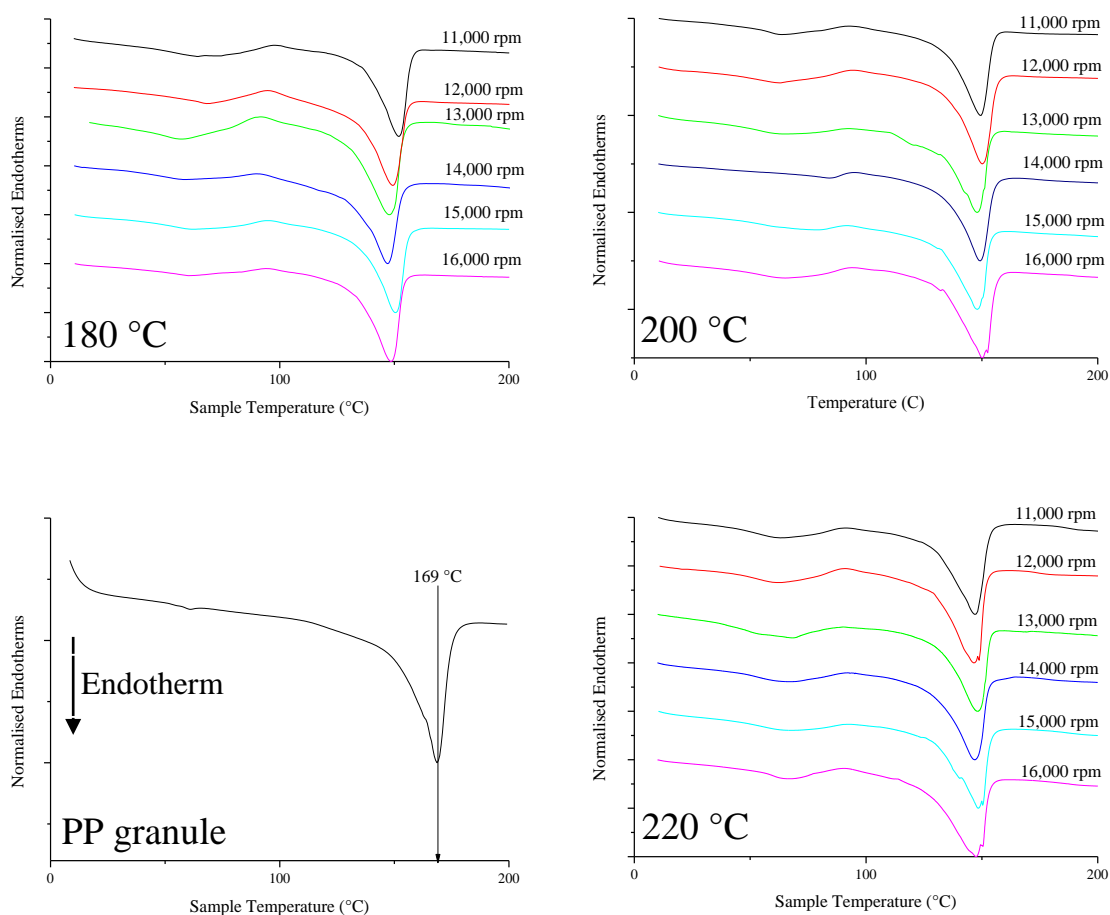
Figure 3.14: DSC heat flow traces from PP flake and fibres produced at selected processing temperatures.

In comparison to the unprocessed polymer the MF650Y fibres produced through centrifugal spinning recorded a melting T_{onset} ranging from 135 to 139 °C and a peak T_{melt}

typically less than 150 °C. This downward shift in melt temperature is due to changes in the PP crystal configuration during spinning. Smaller crystals are formed in the fibre which will melt at a lower temperature than the crystals formed during polymerisation. The rapid quenching of the fibres restricts the propagation of crystal sizes which will also limit the final crystalline fraction.

Pure crystalline PP has an enthalpy of fusion of 207 J g^{-1} and so the apparent crystallinity of the granules and fibres can be estimated using Equation 3.3 (Longo et al., 2011).

$$Crystallinity\ (\%) = \frac{\Delta H_m}{\Delta H_o} \times 100 \qquad \text{Equation 3.3}$$

Where: ΔH_m is the enthalpy of fusion for the polymer as measured through DSC and ΔH_o is the enthalpy of fusion of 100 % crystalline PP, measured at 207 J g^{-1}.

The enthalpy values recorded for the fibres range from 54.5 to 94.8 J g^{-1} which corresponds to an apparent crystallinity of 26 to 48 %. In comparison the crystallinity of the unprocessed granules was estimated as 47 %. Further inspection of the fibre endotherm traces yields the presence of a small and broad exothermic peak preceded by an endothermic peak. These features, highlighted in Figure 3.15 are only observed in the fibres and are erased by the first heating scan.
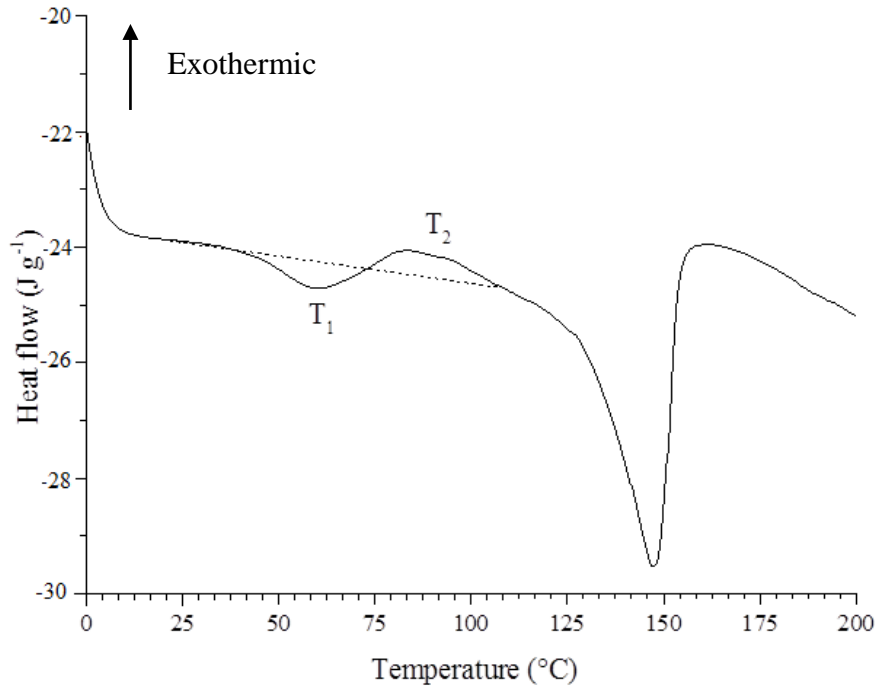
Figure 3.15: DSC trace of PP fibres spun at 210 °C with a 15,000 rpm spinning speed. T_1 and T_2 are endothermic and exothermic peaks prior to the primary melt transition.

Peak T_1 is endothermic and has a peak maxima at around 63 - 66 °C, this then moves to an exothermic transition, T_2, with a peak at 90 - 100 °C. It is proposed that T_1 is caused by the melting of imperfect crystals and T_2 is a crystallisation process Alberola et al. (1995). The XRD data presented later in this chapter indicate that the polypropylene fibres are comprised of a disordered structure known as a smectic phase. As the fibres are heated, partially ordered regions gain enough thermal energy to transition to α-crystals generating heat. The presence of a smectic phase means that the enthalpy calculations recorded deviate from the true value as the preceding crystallisation transition will increase the melting endotherm which is account for in the use of the term *apparent crystallinity*.

Whilst there is a significant difference in the DSC trace shape and peak locations between virgin PP and the fibres there was no observable relationship between the spinning conditions and the melting behaviour of the fibres as changes to T_{onset}, T_{peak} and enthalpy

remained inconsistent. The current thinking on the mechanism of smectic phase formation will be discussed around the XRD results in Section 3.5.4.
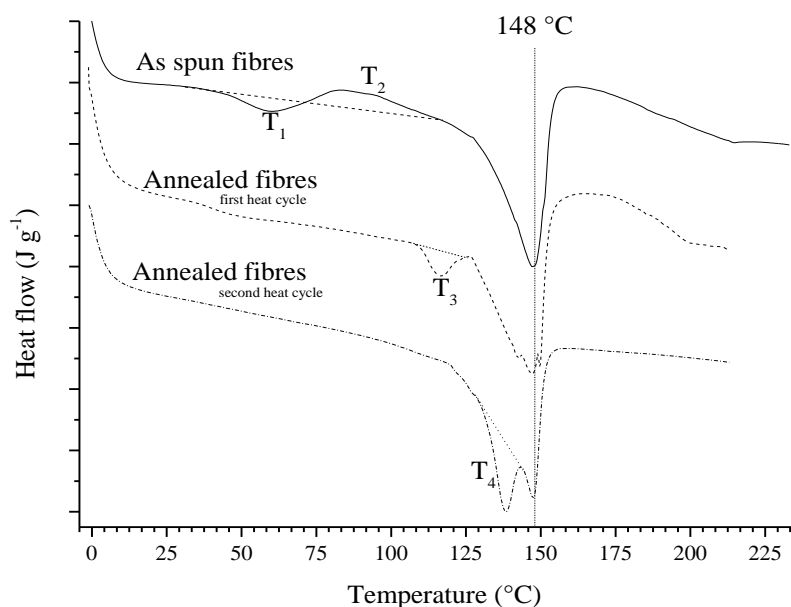
Figure 3.16: Normalised DSC endotherms showing the effect of annealing on melting behaviour.

The polypropylene fibres were annealed through a secondary process: selected fibres were annealed for 1 hour at 120 °C in a laboratory oven and then allowed to cool in ambient conditions. No tension was applied to the fibres. The DSC scans of untreated and annealed polypropylene fibres are shown in Figure 3.16 along with a second heating scan of the annealed fibres. By annealing the fibres the low temperature endothermic and exothermic transitions (T_1 and T_2) observed in the as-spun material are erased, replaced by an endothermic transition, T_3 that peaks at ~116 °C and then returns to the baseline before transitioning to the primary melting peak. Allowing the melted sample to cool and reheating in the DSC also yields further change: the T_3 peak is now erased, and a new secondary peak shoulder, T_4, has formed with endothermic maxima at ~138 °C. Throughout these phase changes the primary melting endotherm has a T_{melt} of 148 °C

which indicates that the primary melt transition point is unaffected by the annealing process. This follows as the annealing occurs below the temperature required to break down the order in the polypropylene. However it is sufficiently high such that the phase changes observed in T_1 and T_2 can occur. Annealing thus provides the energy to allow the polypropylene chains to transition from smectic to semi-crystalline. It is also thought that the smaller crystals with low melting points ~120 °C also melt. Upon cooling these mobile units form into crystals of a discrete size, which results in the new peak T_3. The influence of annealing on fibre fine structure will be revisited as part of the discussion around the XRD results.

3.5.4 **X-ray diffraction**

The XRD patterns of polypropylene fibres produced in this work show regions of high count volumes at positions across the spectrum.
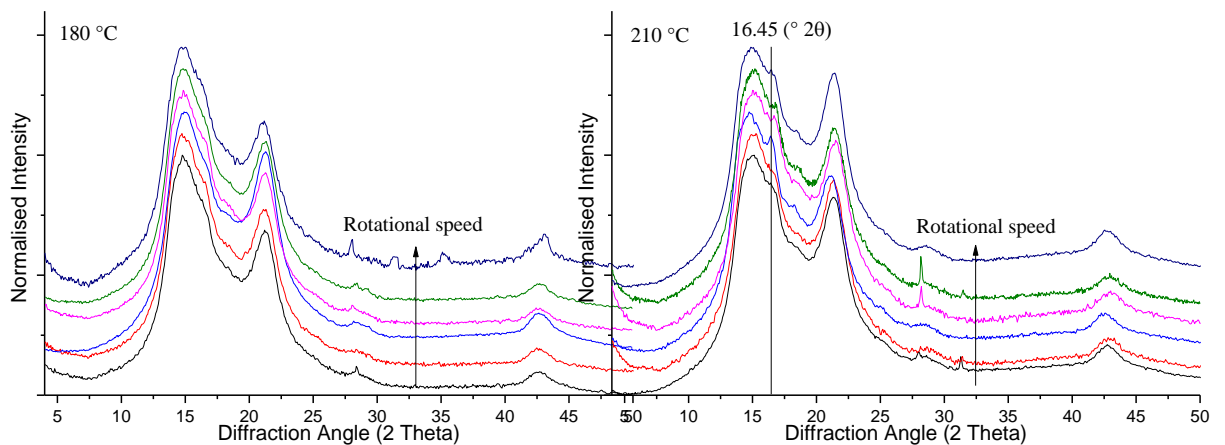
Figure 3.17: XRD spectra of PP centrifugal spun at 180 °C and at 210 °C with spinning speeds ranging from 11,000 rpm (black) to 16,000 (navy). Graphs are normalised with respect to temperature. The shoulder that occurs ~ 16.45° 2θ at higher temperatures is labelled for clarity.

This indicates that X-ray superposition occurs at specific angles of beam incidence and from that it can be argued that the polypropylene fibres contains long range order in some aspects. The patterns produced from typical centrifugal spun MF650Y polypropylene fibres, Figure 3.17, have been normalised as the raw data demonstrated differences in absolute intensity measured as a result of the sample preparation rather than molecular structure. The XRD patterns are normalised to make the height of the highest peak the same for all samples. The normalised curves presented show that the peak locations and shape were largely consistent for all the fibres regardless of processing temperature. The only difference observed in the traces was a slight increase in a shoulder height at 16.45° 2θ as the processing temperature is increased, this has been labelled for clarity in Figure 3.17. In terms of processing speed no significant changes in the XRD pattern was observed as the spinning speed was increased from 11,000 to 16,000 rpm. The peak heights observed in these diffraction patterns have a similar shape and the relative peak height remained consistent. Despite the slight shoulder observed at higher temperatures it can be surmised that the diffraction patterns produced by the polypropylene fibres were largely similar regardless of the processing conditions.

The inspection of the pattern shape and location of the features yields information regarding the order of the system. The XRD traces collected from fibres contain a broad hump which occurs between 10 and 30° 2θ. This feature is highlighted in Figure 3.18 and occurs where an increase in intensity above the background baseline can be observed. This broad increase in diffraction intensity is caused by the scattering of the X-rays by the amorphous parts of the PP. Discretely separate from the amorphous halo is the presence of more defined peaks that have intensity maxima at 14, 21.5 and 42° 2θ. These peaks are created by regions of order within the PP fibres.
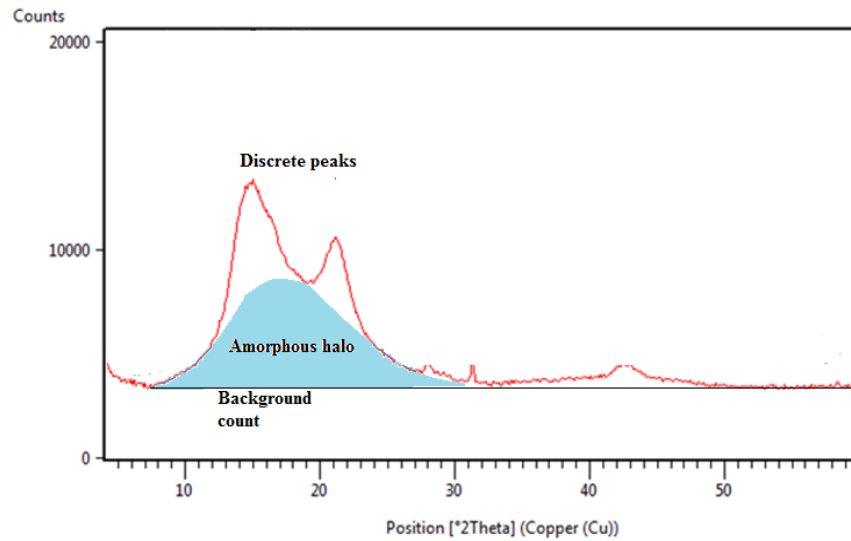
Figure 3.18: XRD trace of polypropylene fibres produced by melt centrifugal spinning at 180 °C and 13,000 rpm. The background count baseline and amorphous halo region are explicitly shown.

This two phase structure is expected as most high polymers are actually semi-crystalline: comprising long range molecular order amongst areas of disorder. In long chain polymers the two phases are considered to be intrinsically linked and through defects in the crystal and disordered chain alignment, lack definite boundaries. There are several ways of describing and modelling the phase separation of semi-crystalline materials

The XRD peaks of the PP fibres shown above in Figure 3.17 are not sharp enough to be linked to the classic crystal structure of PP. By comparing the XRD trace of as-spun PP fibres to the diffraction pattern of MF650Y PP that had been pressed into a film and cooled slowly there is a clear difference in the shape and form of the trace from the two forms of the same material. The XRD traces of pressed film and fibres is shown in Figure 3.19.
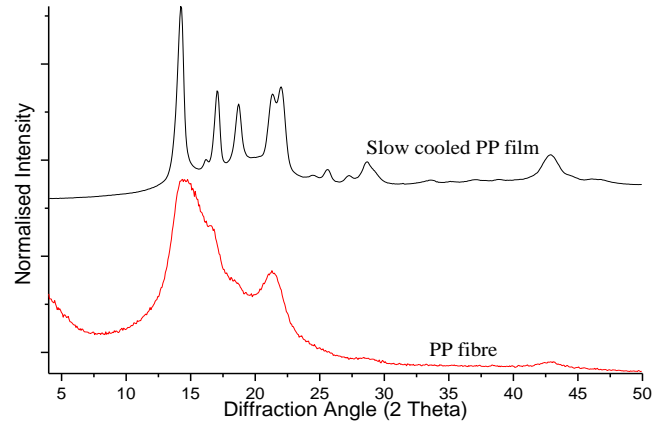
Figure 3.19: Normalised XRD traces showing MF650Y slow cooled PP film compared to the traces of the centrifugal spun fibres.

The location and shape of the peaks is the major difference between them: film PP has primary peaks at 12, 17, 18.5° 2θ with a doublet at 21.5 and 22° 2θ that are not seen in the fibre traces. The peaks are also much sharper than those observed for the fibres. These peaks are consistent with those observed elsewhere for conventional semi-crystalline polypropylene. However, the crystal structure of polymers can vary depending on how the chains conform. Crystallisation of PP is known to be complex with the possibility of forming three crystalline forms: α-monoclinic, β-pseudo-hexagonal and γ-orthorhombic. Van der Meer (2003) models each isotactic PP helix as a triangle and draws the three crystal forms with their respective unit cells, Figure 3.21. As-received and slow cooled polypropylene is usually found in the α-monoclinic, the structure and dimensions of which are shown in Figure 3.22 (Cho et al., 2010). This means that the X-ray diffraction patterns observed in the fibrous polypropylene produced in this study are a result of a different fine structure being present and this means that the fibrous polypropylene produced through melt centrifugal spinning is not crystallising in the same manner as conventional polypropylene. This is not the first time such XRD patterns have been observed: Raghavan et al. (2013) also observed a similar XRD trace in melt blown polypropylene and concluded that this was due to crystal deformation and faults.

However, it is known in the art that polypropylene, under the right conditions can form a paracrystalline structure known as a smectic phase (Natta and Corradini, 1960). The reasons for this and the exact structure of this phenomenon varies throughout the literature but a comprehensive hypothesis was supplied by Corradini et al. (1986). They concluded that the smectic phase observed was not due to microcrystals or crystal defects but caused by amorphic chain alignment in an arrangement more akin to the α-monoclinic unit cell than the β or γ-crystal forms. The cause of this structure is rapid quenching and elongation of the polymer chains during processing. This rapid quenching is observed in melt blowing but would also apply to centrifugal spinning. In the latter technique polymer exiting the spinneret is exposed to ambient air which leads to rapid cooling and solidification of the jet. The polymer solidifies so rapidly that the chain mobility is limited before crystallisation can occur.

The close approximation of the smectic phase to the α-monoclinic unit cell means that the fibre can be induced to crystallise through the application of heat. This additional thermal energy provides the mobility for the smectic phase to flip to the crystal form. This transition is observed via DSC through the low temperature exothermic peak. To evaluate this theory that temperature can induce a crystallisation below the melting point an annealing process was performed. Selected fibres were annealed for 1 hour at 120 °C and then cooled in a laboratory oven prior to XRD analysis. The different trace generated is shown in Figure 3.20.
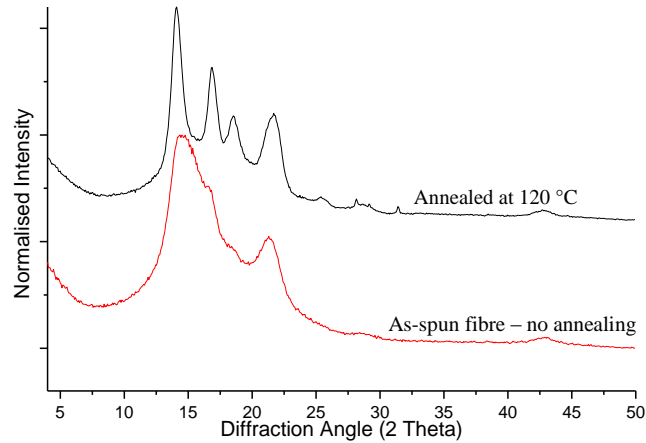
Figure 3.20: Annealed polypropylene fibres compared to untreated source fibre.

The annealed fibres exhibit primary peaks at 14.1, 16.8 and 18.6° 2θ which correlate to the peaks observed for slow cooled polypropylene film, Figure 3.17. In the position of the doublet observed in the film there is now single peak at 21.66° 2θ, proving that annealing of the fibres induces crystallisation. The process of annealing raises the fibres above the glass transition which increases chain mobility and allows the partially orientated fibres to form α-crystals.

The structure formed are known to be α-crystals as the crystal form and size can be calculated using Equation 2.6 and Equation 2.7 along with known information regarding polypropylene (de Villiers et al., 1998). The structure formed in the PP fibres is likely the monoclinic α-crystal but there are also alternative forms of polypropylene, Figure 3.21 (Van der Meer, 2003).
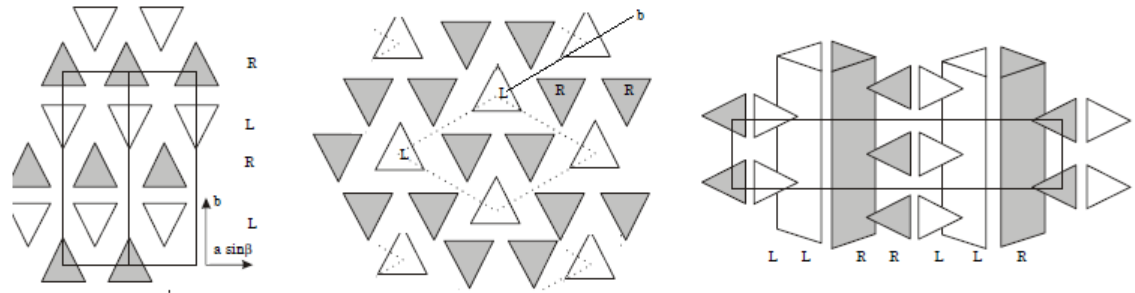
Figure 3.21 : Unit cell models of left: α-monoclinic, centre: β-pseudo-hexagonal and right: γ-orthorhombic. The grey triangles represent a right handed helix and the blank triangles a left handed helix (Van der Meer, 2003).

The polypropylene β-crystal has a triangular unit cell of dimensions a = b = 11.0 Å, c = 6.5 Å angle γ= 120° (Hirte, 1984). The β-crystals has been previously observed in fibres through the presence of peaks in DSC and XRD scans and are known to form in polypropylene melts experiencing high elongation and deformation of PP in conjunction with rapid solidification (Zhou, 2007). The conditions required for β-crystal formation are similar to those applied to the centrifugal spun fibres. The γ-crystal form is considered to be rare and usually requires a nucleating agent to be present in the melt (Van der Meer, 2003). However, the diffraction peaks typical of these structures are not observed in the XRD trace of either untreated or annealed fibres.
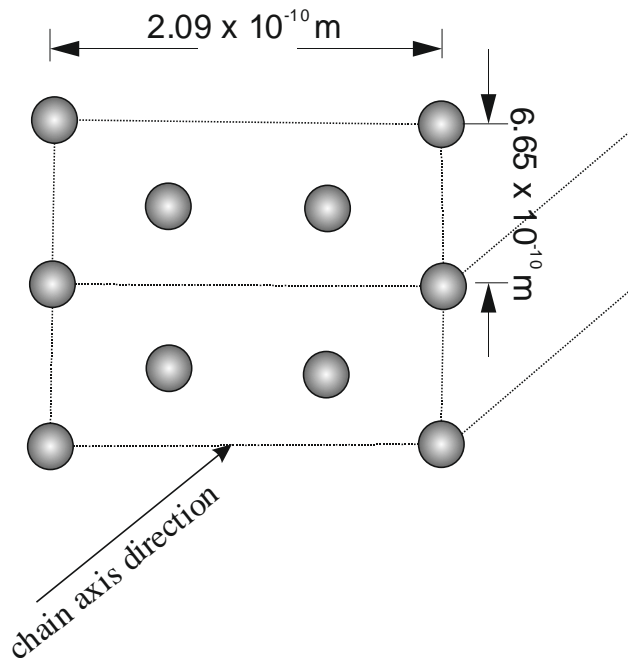
Figure 3.22: α-crystal form of PP in the 001 plane. The view is along the chain axis. Sketched from (Hirte, 1984).

The implication for processing is that in order to obtain semi-crystalline polypropylene a secondary heating process must occur to allow the chains to move from smectic to crystalline phases. This heating could occur within the centrifugal spinner, relying on either residual heat or auxiliary heating. Alternatively this could be done in a subsequent annealing process as performed in this study.

In summary, the XRD data provided here, combined with the DSC results indicate that centrifugally spun PP has a different fine structure compared to generic PP products. This new form is caused by the rapid quenching that occurs during melt centrifugal spinning. It is thought that rotational speed of the process plays only a marginal role in the quenching rate as the minimum speed required for spinning (11,000 rpm) provides a very high quenching rate and no trend was found to link the level of smectic phase to operating speed.

3.6 **Conclusions**

Fibres were successfully produced from polypropylene using melt centrifugal spinning at a range of temperatures and speeds. Fibres as fine as 100 nm were observed but typically average diameters of around 500 nm could be achieved. A broad distribution of fibre diameters was observed under all processing conditions. This is potentially a symptom of the acceleration and deceleration periods typical of the short batch spinning times. It is thought that commercial centrifugal spinning equipment would circumvent this problem by having much longer periods spinning at optimal speed.

The fine fibre diameters observed means that melt centrifugal spinning can produce PP fibres fine enough to be used in highly selective filter membranes. Fibres as fine as 470 nm average with filaments observed with individual filaments finer than 100 nm being observed is comparable and demonstrably finer than the > 800 nm average fibres reported for the melt electrospinning of polypropylene. An additional advantage to centrifugal spinning PP in the arrangement used here is that there is the option of using the fibres as a freestanding web, without a supporting substrate.

The influence of processing conditions was also investigated and the melt viscosity of polypropylene was shown to fall as the temperature increases. However, this did not translate into a reduction in fibre diameters but the degree of beading did increase at the higher processing temperature. This has implications for commercial production as much lower energy costs, and a higher quality web could be achieved by reducing the processing temperature.

X-ray diffraction and thermal analysis indicate that the as-spun polypropylene fibres contained a disordered smectic phase as opposed to a partially ordered semi-crystalline material typical of melt spun polypropylene filament. This was due to the rapid quenching of the polymer jet that occurs during centrifugal spinning. A secondary annealing process was applied to convert the fibres from an amorphous-paracrystalline material to a conventional semi-crystalline one.

3.7 **References**

BESCO, S., LORENZETTI, A., HRELJA, D., BOARETTI, C., ROSO, M., FERRI, D. & MODESTI, M., 2014. Influence of melt viscosity on the structure and properties of electrically conductive nanocomposites produced by masterbatch process. *Macromolecular Materials and Engineering,* 299**,** 814-824.

BLACKADDER, D. A. & LE POIDEVIN, G. J., 1976. Dissolution of polypropylene in organic solvents: 1. Partial dissolution. *Polymer,* 17**,** 387-394.

BOWER, D. I., 2002. *An Introduction to Polymer Physics.* Cambridge University Press, United Kingdom.

BREMNER, T., RUDIN, A. & COOK, D. G., 1990. Melt flow index values and molecular weight distributions of commercial thermoplastics. *Journal of Applied Polymer Science,* 41**,** 1617-1627.

CARLSSON, D. J. & WILES, D. M., 1976. The photooxidative degradation of polypropylene, part I: photooxidation and photoinitiation processes. *Journal of Macromolecular Science, Part C,* 14**,** 65-106.

CORRADINI, P., PETRACCONE, V., DE ROSA, C. & GUERRA, G., 1986. On the structure of the quenched mesomorphic phase of isotactic polypropylene. *Macromolecules*, 19, 2699-2703.

DALTON, P. D., GRAFAHREND, D., KLINKHAMMER, K., KLEE, D. & MÖLLER, M., 2007. Electrospinning of polymer melts: phenomenological observations. *Polymer,* 48, 6823-6833.

DE VILLIERS, M. M., WURSTER, D. E., VAN DER WATT, J. G. & KETKAR, A., 1998. X-Ray powder diffraction determination of the relative amount of crystalline acetaminophen in solid dispersions with polyvinylpyrrolidone. *International Journal of Pharmaceutics*, 163, 219-224.

EXXONMOBIL ONLINE., 2013. Singapore chemical plant expansion in operation. [Online] Available: http://exxonmobilchemical.newshq.businesswire.com/press-release/english/exxonmobil-singapore-chemical-plant-expansion-operation. [Accessed: 14th January 2015].

ELLISON, C. J., PHATAK, A., GILES, D. W., MACOSKO, C. W. & BATES, F. S., 2007. Melt blown nanofibers: Fiber diameter distributions and onset of fiber breakup. *Polymer,* 48**,** 3306-3316.

FANG, Y., HERBERT, M., SCHIRALDI, D. & ELLISON, C., 2014. Tin fluorophosphate nonwovens by melt state centrifugal Forcespinning. *Journal of Materials Science,* 49**,** 8252-8260.

HASSAN, M. A., YEOM, B. Y., WILKIE, A., POURDEYHIMI, B. & KHAN, S. A., 2013. Fabrication of nanofiber meltblown membranes and their filtration properties. *Journal of Membrane Science,* 427**,** 336-344.

HIRTE, R., 1984. *Textile science and technology: Production and applications of polypropylene textiles*. Elsevier Scientific Publishing Company, Akademie Verlag GmbH, Germany.

HOUTE, F., 2014. The European man-made fibres industry: global challenges and political changes in the EU. *Man-made Fibers conference*, 10th-12th September 2014, Dornbirn, Austria.

LEE, Y. & WADSWORTH, L. C., 1992. Effects of melt-blowing process conditions on morphological and mechanical properties of polypropylene webs. *Polymer,* 33**,** 1200-1209.

LI, X., ZHANG, Y., LI, H., CHEN, H., DING, Y. & YANG, W., 2014. Effect of oriented fiber membrane fabricated via needleless melt electrospinning on water filtration efficiency. *Desalination,* 344**,** 266-273.

LOZANO, K. & SARKAR, K., 2009. *Methods and apparatus for making superfine fibres*. United States Patent Application: 12/404,907, 14th March 2009.

LYONS, J., 2004. *Melt-electrospinning of thermoplastic polymers: an experimental and theoretical analysis*. Doctor of Philosophy Thesis, Drexel University, United States

LYONS, J., LI, C. & KO, F., 2004. Melt-electrospinning part I: processing parameters and geometric properties. *Polymer,* 45**,** 7597-7603.

MCEACHIN, Z. & LOZANO, K., 2012. Production and characterization of polycaprolactone nanofibers via forcespinning™ technology. *Journal of Applied Polymer Science,* 126**,** 473-479.

NATTA, G. & CORRADINI, P., 1960. Structure and properties of isotactic polypropylene. *Il Nuovo Cimento Series 10,* 15**,** 40-51.

NAYAK, R., KYRATZIS, I., TRUONG, Y., PADHYE, R., ARNOLD, L., PEETERS, G., O'SHEA, M. & NICHOLS, L., 2013. Fabrication and characterisation of polypropylene nanofibres by meltblowing process using different fluids. *Journal of Materials Science,* 48**,** 273-281.

O'HAIRE, T., RIGOUT, M., RUSSELL, S. & CARR, C., 2014. Influence of nanotube dispersion and spinning conditions on nanofibre nanocomposites of polypropylene and multi-walled carbon nanotubes produced through Forcespinning™. *Journal of Thermoplastic Composite Materials,* 27**,** 205-214.

PALL, D. B. & CONNORS, J. T., 1996. *Bag filter*. United States Patent: 5,586,997, Application: 08/389,264, 24th Decemeber 1996.

RAGHAVAN, B., SOTO, H. & LOZANO, K., 2013. Fabrication of melt spun polypropylene nanofibers by forcespinning. *Journal of Engineered Fabrics & Fibers (JEFF)*, 8, 52-58.

SARKAR, K., GOMEZ, C., ZAMBRANO, S., RAMIREZ, M., DE HOYOS, E., VASQUEZ, H. & LOZANO, K., 2010. Electrospinning to Forcespinning™. *Materials Today,* 13**,** 12-14.

SWEESTER, D. M., and ZANDER, N. E., 2014. Parameter study of melt spun polypropylene fibers by centrifugal spinning. *Article ARL-TN-0619*, Army Research Lab, Maryland, United States.

UPPAL, R., BHAT, G., EASH, C. & AKATO, K., 2013. Meltblown nanofiber media for enhanced quality factor. *Fibers and Polymers,* 14**,** 660-668.

VAN DER MEER, D. W., 2003. *Structure-property relationships in isotactic polypropylene.* Doctor of Philosophy Thesis, University of Twente, Netherlands.

WIERTZ, P., 2014. Challanges and opportunities facing the global nonwovens industry. *Man-made Fibres Congress,* 10th-12th September 2014, Dornbrin, Austria.

ZHOU, H., 2007. *Electrospun fibres from both solution and melt: processing, structure and property.* Doctor of Philosophy Thesis, Cornell University, United States.

Chapter 4
Centrifugal spun polycaprolactone nanofibers and comparisons to the electrospinning technique

As described in Section 1.6.4, centrifugal spinning is capable of producing fibres from polymer solutions. Solution processing allows for the use of non-thermoplastic polymers which broadens the range of polymers that can be formed into fibres. A review of the literature indicated that research is heavily biased towards producing fibres from dissolved solutions typically using electrospinning (Persano et al., 2013). This wealth of knowledge in regards to producing fibres from polymer solutions allows for a direct comparison to be made between fibres produced through centrifugal spinning and electrospinning techniques.

This chapter details the centrifugal spinning of polycaprolactone (PCL), a polymer well covered in the electrospinning literature and that has also been identified as a potential biomaterial or carrier agent in a drug delivery membrane (Zeng et al., 2003a; Ma et al., 2005). PCL was chosen as the material for this chapter as it features in a growing number of publications identifying the potential applications in bioengineering but also that establish the relationships governing electrospinning. Whilst there is a large number of papers covering the electrospinning of PCL, at present there are only a limited number of publications concerning centrifugal spinning this potentially life-saving material with little exploration in alternative solvents beyond dichloromethane (McEachin and Lozano, 2012). Nor has there been direct comparisons by one group to PCL fibres produced using needleless electrospinning.

Chapter 3 described the spinning of polypropylene using melt centrifugal technology. This chapter will cover the solution spinning of polycaprolactone fibres using two techniques: centrifugal spinning and needleless electrospinning. The effect of concentration and solvent on processing using both techniques was investigated and the fibre morphology and fine structure was analysed along with cytotoxicity.

4.1 **Introduction**

PCL belongs to the group of aliphatic polyester materials where the mer is composed of an ester element and an aliphatic ($-C_2H_4-$) element, Figure 4.1. PCL is thermoplastic with a low melting point due to enhanced chain segment mobility resulting a melting temperature of around 59 - 64 °C depending on molecular weight and thermal history. This low melting point means that PCL is currently only applied in niche applications outside of the apparel and industrial textile chain. Whilst PCL has reasonable mechanical performance; with a tensile strength ~38 MPa; it is not favoured for apparel or industrial products as commodity materials such as poly(ethylene terephthalate) possesses superior mechanical properties along with a much higher melting temperature and lower material cost (Wong et al., 2008).
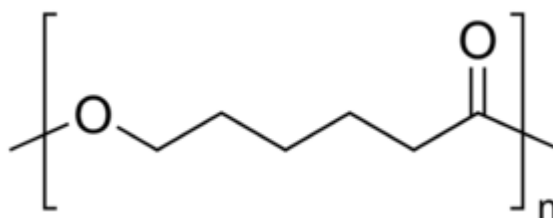
Figure 4.1: Chemical structure of the polycaprolactone mer.

The property of PCL that is of particular interest to academia and medicine is its inherent biocompatibility with human tissue and the ability to biodegradable in vivo. Biocompatibility means the fibres be used in a wound or tissue growth setting and not trigger inflammation or biological rejection (Badrossamay et al., 2014). The polymer biodegrades in vivo as natural enzymes produced by biological tissue are capable of breaking the polymer chain through hydrolysis so after a specified period the polymer chains are broken down into smaller components and then simply absorbed into the tissue. A key advantage of using PCL in vivo is that the biological breakdown does not result in an acidic environment unlike alternative materials such as poly(lactic-co-glycolic acid (Amalorpava Mary et al., 2013). It has been demonstrated that PCL spun from dichloromethane and N,N-dimethylformamide induces no cytotoxic response in human or mouse cells (Wutticharoenmongkol et al., 2006). Crucially, recent research in this area has concluded that PCL fibres supported cell growth (Zander, 2014). Due to a combination of the ease of processing and the useful biological properties, polycaprolactone has been proposed as a material for use in external wound dressings or implantable cell scaffolds (Choi et al., 2008; Zander, 2014).

For the use as a medical implant it is essential that the fibres are ultrafine in order to function as cell scaffolds and that the production steps avoid the use of potentially hazardous solvents in fibre spinning where residues may affect successful bioimplantation (Woodruff and Hutmacher, 2010). However, for PCL it is still acceptable to process the fibres using solution processing, despite the use of organic solvents such as chlorinated hydrocarbons as there is typically an insignificant amount of solvent retained within the PCL fibres (Nam et al., 2007).

Whilst most grades of polycaprolactone are known to be thermoplastic a review of the literature indicated that solution processing is the most likely way to achieve sub-micron fibres using either electrospinning or centrifugal spinning. This is due to PCL having poor melt strength during processing making it unsuitable for high levels of drawing and demanding blow and injection moulding procedures (Darwis et al., 1999). Previous work conducted on processing PCL into fibres through melt processing was unable to create ultrafine fibres: Li et al. (2012) used a CO_2 laser to heat the needle tip and melt the polymer, producing fibres between 3 and 12 µm; rotational melt spinning of PCL was performed by Laine (2013) who achieved fibres with diameters in the range 15 - 70 µm and Zander (2014) further confirmed these observation where PCL was melt centrifugally spun into fibres 7.05 µm in diameter and then alternatively solution spun PCL polymer into 0.81 ± 0.5 µm fibres.

When solution spinning the choice of solvent is of key importance; PCL readily dissolves in chlorinated solvents and by changing the polymer concentration a range of fluid viscosities can be created from a single PCL grade. This ease of processing via dissolution has been critical in allowing the high volume of academic papers detailing the electrospinning of polycaprolactone. However, the inclusion of natural additives and polymers into electrospun biocompatible fibres has proven difficult due to the potential for biological denaturing during processing due to the solvents used (Zeugolis et al., 2008). Expanding the range of compatible solvents for a given polymer will aid the solvent selection process for future research. This is especially pertinent where the fibres are intended to include an additive that may be adversely affected by the presence of particular solvents and alternatives are needed.

Work on the solution centrifugal spinning of PCL was performed by workers during the development and reporting of the Forcespinning^{TM} iteration of this technology (Lozano and Sarkar, 2009; Sarkar et al., 2010). Polycaprolactone was one of the first polymers used in the early Forcespinning^{TM} publications by McEachin and Lozano (2012) where PCL of $70,000 - 90,000$ M_n was spun into using dichloromethane as a solvent. They found that spinning at 9,000 rpm produced an average fibre diameter 220 ± 98 nm and used DSC and XRD to compare it to the results of the electrospun PCL reported separately by Wong et al. (2008). Working from the diameters quoted above it is apparent that a refined iteration of centrifugal spinning technology is able to match the fineness of electrospun PCL fibres.

The structural advantages that can be achieved using centrifugal spinning were appreciated by Badrossamay et al. (2014); who created highly aligned fibres of PCL with varying fractions of collagen and gelatin. These "super" aligned fibres, shown in Figure 4.2, create the possibility of using directional cell growth scaffolds for load bearing areas of the body such as knee and shoulder ligaments (Agarwal et al., 2008).
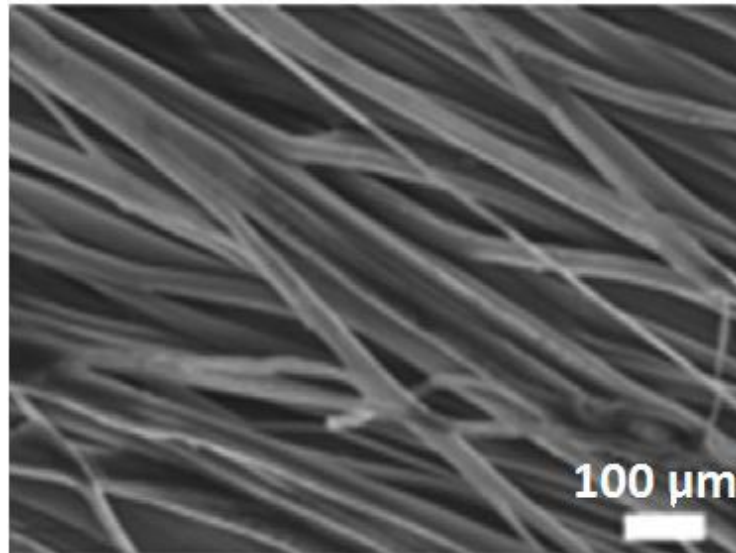
Figure 4.2: Aligned fibres of PCL produced from HFIP solvent using centrifugal spinning (Badrossamay et al., 2014).

The work by Badrossamay et al. (2014) demonstrated that PCL has the ability to be used as a carrier polymer for difficult to spin materials such as collagen to be formed into fibres. Further exemplification of this versatility is demonstrated by the centrifugal spinning of polycaprolactone with polyvinylpyrrolidone (PVP) by Amalorpava Mary et al. (2013). In this work the hydrophilic PVP element was used to increase the rate of biodegradation to engineer the persistence of any biological scaffold or drug release membrane. As a consequence, understanding how the spinning of PCL can be adapted to potentially accommodate other materials would aid future work in this area.

4.1.1 Choice of solvent

Working with polymer solutions means that the choice of solvent will often play a significant role in the spinnability of a fibre in solution (Yang et al., 2004). Key solvent parameters for fibre formation are: evaporation rate (volatility); inherent viscosity; polarity and compatibility with the polymer (Dhanalakshimi et al., 2015).

Chlorinated solvents are commonly used in the electrospinning of PCL Cipitria et al. (2011). However, research has indicated that using chloroform may not be the most appropriate solvent for achieving fine fibres and that the high volatility may reduce the total attenuation time available during jet flight (Van der Schueren et al., 2011). Despite this, chlorinated solvents such as chloroform continue to be used to spin PCL fibres using electrospinning and centrifugal spinning as the solutions are easy to produce and create uniform, bead free webs (McEachin and Lozano, 2012, Zander, 2014). A review by Cipitria et al. (2011) has indicated that many researchers are using a mixture of chloroform and methanol to produce nanofibres from PCL. The methanol functions as a non-solvent for PCL and is done to retard the evaporation of chloroform but can also facilitate the spinning of additives that are not miscible in pure chloroform or dichloromethane (Venugopal et al., 2005). This inclusion of a solvent into which the polymer is not dissolvable creates a binary solvent system. Research has shown that the use of chloroform/methanol as a solvent can result in finer PCL fibres when electrospinning (Gluck, 2007). PCL fibres produced from chloroform/methanol have been observed by some to have surface pores or pock marking on the fibres (Lubasova et al., 2010). This surface morphology could have impact on the cell growth properties of a material. There is also scant information available on the cytotoxic response of PCL fibres spun from chloroform and chloroform/methanol (Pant et al., 2011).

The use of multiple and binary solvents appears often in the literature on electrospinning but there is only limited information on the use of these solvent systems in centrifugal spinning or on the morphology of solution processed centrifugal spun fibres (Luo et al., 2010).

4.2 **Summary**

Centrifugal spinning from a polymer solution allowed for an investigation into the various effects of polymer concentration and solvent on the formation of fibres. Polycaprolactone was chosen as the focus of this chapter as there has been limited research in producing PCL fibres using centrifugal spinning and there is only limited information on the use of binary solvents on PCL fibre formation with a particular gap in knowledge concerning biocompatibility of spinning fibres from chloroform and chloroform solvents. In addition, the electrospinning of PCL nanofibres has been well documented allowing for comparisons to be made between centrifugal spun and electrospun PCL fibres (McEachin and Lozano, 2012).

With solutions there are multiple factors that will influence the viscosity and spinning behaviour of a solvent-polymer system and it has been demonstrated by Geng et al. (2005) that the addition of a small amount co-solvent or non-solvent into the solution can significantly reduce the surface tension with little effect on viscosity. This change in the viscosity-surface tension relationship can alter the jet elongation process, resulting in finer fibres but with increased potential for jet collapse. The presence of a co-solvent or non-solvent can also affect the morphology of electrospun fibres and could possibly change the morphology of PCL fibres produced using centrifugal spinning. A review of the literature reveals that there is a gap in knowledge with regards to understanding the cytotoxic response of cells to PCL fibres formed from chloroform and chloroform based binary solvent systems. By further understanding the range of solvents that are appropriate for the manufacture of fibres designed to be used *in vivo* processes can be designed and readily adapted to use alternative solvents. This is particularly appropriate

when one solvent or solvent system is known to damage or interfere with an additive necessary for the application.

4.3 **Experimental**

The purpose of this chapter was to determine the relationships that govern the centrifugal spinning of polycaprolactone fibres with respect to polymer solution concentration and solvent composition and to establish how this differs to needleless electrospinning. Changes in fibre morphology was also studied along with internal fine structure. The suitability of these fibres for biological applications was also assessed. The work was conducted with the following objectives:

1. To create solutions of PCL in two solvent systems and measure solution viscosity and surface tension changes;

2. To spin PCL into fibres using centrifugal spinning and needless electrospinning and observe the effect of solution concentration on production;

3. To characterise the fibres produced using microscopy to determine the morphology and typical fibre diameters. Changes to the internal fine structure will be observed using thermal analysis and X-ray crystallography;

4. To perform a cell growth study on the centrifugal spun fibres to determine cytotoxic response of fibres formed from chloroform and chloroform/methanol solvents.

4.3.1 **Materials**

Sigma Aldrich supplied polycaprolactone, M_w 80,000, with a melt flow index 1.9 g 10 min^{-1} (80 °C and 0.3 MPa) and was used throughout the study. Laboratory grade chloroform >99.9 % and methanol solvents > 98 %, both from Sigma Aldrich, were used for the preparation of spinning solutions.

For the cytotoxicity study, 3-(4,5-dimethylthiazol-2-yl)-5-(3-carboxymethoxyphenyl)-2-(4-sulfophenyl)-2H-tetrazolium, also known as MTS assay, was supplied by Sigma Aldrich was used in conjunction with L929 mouse fibroblast cells supplied by the University of Leeds School of Dentistry but are also available via Sigma Aldrich. Formazan dye, also known as MTT formazan powder was supplied by Fischer Scientific along with Dulbecco's modified Eagle's medium (DMEM) and dimethyl sulphoxide (DMSO) > 98 %.

4.3.2 **Preparation of solutions**

The solvent systems used were chloroform and a binary solvent of 4:1 chloroform and methanol (v/v) which was premixed prior to solution preparation. A ratio of 3:1 has been used previously by Tam and Lim (2004) and by Wang et al. (2009). However it was observed that at a ratio of 3:1 it was increasingly difficult to maintain the high concentration of solutions in solution and the polymer would precipitate out quickly. Thus a chloroform to methanol ratio of 4:1 (4:1 CM) was chosen, as used by Suganya et al. (2010). Solutions of PCL in the two solvent systems were prepared with polymer concentrations ranging from 6 - 19 % w/v. The PCL was dissolved in a sealed glass jar with the aid of a magnetic follower. Moderate heat was applied for less than hour in order

to raise the solution temperature to 40 °C in order to fully dissolve the polymer at concentrations of 18 and 19 %. The dissolved solutions were left to stir for over 12 hours at room temperature before use in subsequent measurements or processing.

4.3.3 Rheology and surface tension

Solution viscosity measurements were made using rotational viscometry, previously discussed on page 68, using a Brookfield LV viscometer. Prepared solutions were added to the small sample adapter supplied by the manufacturer which had a nominal internal volume of ~10 mL. This adapter uses a common sample holder and holds the measuring spindle at a fixed depth allowing for accurate reproduction of experiments. A syringe was used to dispense 9.4 mL of polymer solution into the container and required spindle (34) was then placed into the solution. The spindle was rotated at 30 rpm unless otherwise quoted. The solutions containing PCL concentrations of 7 and 8 % required that a spindle speed of 100 rpm was used to satisfy the lower torque limit suggested by the manufacturer. This is a higher rate of shear and will result in a slightly lower viscosity reading due to the non-Newtonian behaviour of polymer solutions. The results from these atypical have been marked with a * to indicate that testing conditions have changed.

In addition to solution viscosity the surface tension was also quantified to determine if there is a tangible difference when using the two solvent systems. The surface tension of a 12 % PCL solution in both the chloroform and the 4:1 CM binary solvent was measured using a K100 tensiometer produced by Kruss, Germany. Around 50 ml of solution was decanted into a 67 mm diameter Pyrex dish and then raised to a 10 mm wide platinum plate. Slight adjustments of probe vertical height, at a rate of 6 mm of travel per minute brought the probe into definite contact with the surface. The force on the probe due to

surface tension was then measured over a period of 20 seconds. An absolute value for surface tension in mN m^{-1} was then generated by averaging the results taken over this time period.

4.3.4 **Centrifugal spinning of PCL fibres**

Fibres were produced using the Fiberio Forcespinning^{TM} L1000M system described in Section 2.1. The effect of polymer concentration was assessed on centrifugal spinning using a spinning speed of 9,000 rpm. PCL solutions using chloroform and 4:1 chloroform/methanol were prepared at concentrations of 10-19 % (w/v). Multiple solutions were prepared at each condition and numerous spinning trials were conducted at each condition. This was to allow direct comparisons with previous work which found a speed of 9,000 rpm to be optimum spinning speed for producing fine fibres from 16 % in dichloromethane (McEachin and Lozano, 2011) and from methylene chloride at 10 and 15 % (Zander, 2014).

When spinning, 1 mL of the required solution was added to each end of the dual 30 gauge needle spinnerets. This was then accelerated to a rotational speed of 9,000 rpm and remained at this condition for a period of 1 minute before decelerating and coming to rest. The collection system used was a static arrangement of posts positioned 115 mm from the spinneret orifice tips. The free standing web was collected in bulk for subsequent analysis.

The 'quality' of the web as observed immediately after production was noted. This refers to the state and cohesiveness of the web. A web that is substantial and well formed, being uniform in height and density throughout the circumference of the collector is deemed

'satisfactory; a web that is poorly formed, asymmetrical and contains fibrous elements that are not formed in to a nonwoven is deemed to be poor quality and 'unsatisfactory'.

4.3.5 **Electrospinning of PCL fibres**

For electrospinning the Nanospider NS LAB 200, manufactured by Elmarco, Czech Republic, was used. This is a needleless, free surface spinning system fitted with a wire electrode as shown in Figure 4.3.
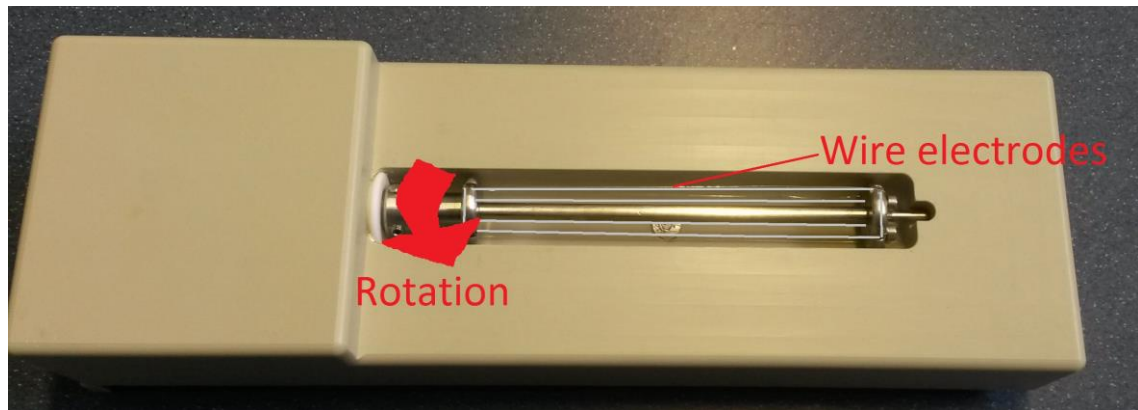
Figure 4.3: Interior of Elmarco Nanospider fitted with wire electrode.

The Elmarco Nanospider operates in a vertical arrangement where the polymer solution and electrode sits at the bottom, a voltage is applied and the polymer jets travel upwards towards a grounded collection plate. The current collection system in the Elmarco is a conveying polyester spunbond fabric belt which sits beneath a grounded collection plate. The speed of the substrate can be controlled to vary the level of nanofibre deposition. For small samples a square of aluminium foil is pinned to the static spunbond substrate.

The Nanospider is compatible with various electrode fittings, including vertical prongs; rotating rollers and rotating wires. For this study, rotating wire roller electrodes were

used. In this setup, polymer solution is poured into a reservoir into which a partly submerged electrode rotates slowly. Multiple Taylor cones form on the surface of the rotating electrode, Figure 4.4, which form into jets and fibres.
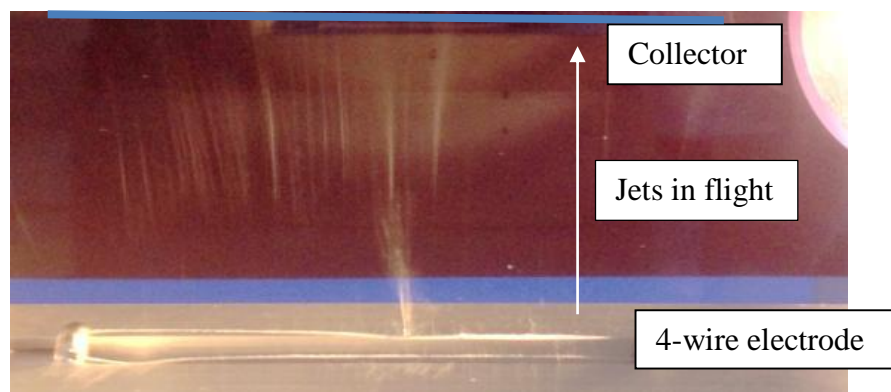
Figure 4.4: Photograph showing 7 % PCL in 4:1 CM solvent being spun from a wire electrode using a 60 kV charge at a distance of 172 mm.

The Elmarco Nanospider spinning chamber has no control over ambient conditions. This means that the air temperature and humidity inside the spinning chamber may vary significantly. There is also a significant extraction flow within the chamber which will increase the solvent evaporation rate.

The conditions for the needleless electrospinning of PCL solutions in the concentration range 6 - 12 % (w/v), using both chloroform and chloroform/methanol solvents, was investigated. Multiple solutions were prepared at each condition and numerous attempts were made to produce fibres from each solution. The wire electrode used in this study was a 160 mm long electrode that consists of steel wire wrapped around a frame to create 4 spinning surfaces. This sits within a reservoir to which 25 ml of polymer solution was added and a voltage of 60 kV applied to induce jet formation. A preliminary study indicated that voltages less than 55 kV would not induce Taylor cone and jet formation for the solutions and set-up described. The rotational speed of the electrode was 2.0 rpm

and spinning occurred for 4 minutes or until polymer deposition on the electrode became visible. The spinning distance used for all electrospinning samples was 154 mm. The electrospun fibres were deposited on to a foil sheet, 150 mm x 200 mm, that was affixed to the static collector substrate using pins.

The webs are also assessed for apparent 'quality'. When electrospinning a 'satisfactory' web is determined by uniform and consistent web coverage on the foil substrate with fibrous matter. An 'unsatisfactory' web is defined as one with evidence of significant spraying, uneven web coverage or a relatively short jet production window.

4.3.6 Fibre analysis

4.3.6.1 SEM analysis

As in previous chapters SEM will be the primary tool in analysing the fibre diameter and morphology. The fibre sampling and measurement procedure will follow the method listed in Section 2.2.1 with a minimum of 150 fibres taken from multiple points on an SEM stub.

4.3.6.2 Differential scanning calorimetry

DSC was used to assess any changes to the thermal properties as a consequence of spinning polymer into fibres. The DSC measurements were obtained using a Perkin Elmer Jade DSC and scanned on a heat-cool-heat cycle from 0 °C to 240 °C at a rate of 20 °C per minute under a nitrogen atmosphere delivered at 30.0 cm^3 min^{-1}. DSC measurements were taken at fibres made from 12, 14 and 16 % using both solvents via centrifugal spinning. In addition, electrospun webs produced from 7, 8 and 9 % PCL in 4:1 Chloroform/Methanol solvent were also measured using DSC.

4.3.6.3 **X-ray diffraction**

The X-ray diffraction was performed on both the bulk material and on the fibres to determine any structural differences. Pelletised virgin PCL is not an ideal form for diffraction analysis as flat materials are preferred. This allows for comparisons between rapidly quenched fibres and slow cooled PCL film. Bulk PCL was prepared for XRD measurement by film casting a 16 % PCL solution in both solvent systems. This ensured a flat surface which is better suited to X-ray analysis compared to the pellet form. PCL fibres from centrifugal spinning were pressed into a flat shape for fitting to the sample mount. Scans were taken in the theta: theta orientation scanning in the Bragg angle, 2θ, through 4° to 60° with a step size of 0.066°. XRD measurements were taken at fibres made from 12, 14 and 16 % using both solvents via centrifugal spinning. In addition, electrospun webs of 7, 8 and 9 % PCL in 4:1 Chloroform/Methanol solvent were analysed with XRD without prior preparation due to the two-dimensional nature of the web.

4.3.7 **Cytotoxicity**

The cytotoxicity of centrifugal PCL fibres was investigated using fibre samples based on 12 % PCL in chloroform and 12 % PCL in chloroform/methanol solvent. In addition, a PCL fibre web containing carbon nanotubes produced using centrifugal spinning was also evaluated as part of a wider study into PCL-CNT fibres, Section 6.3. The solvent was removed from the fibres through vacuum drying for 72 hours at 25 °C under 1020 mbar of pressure. The samples were sterilised using gamma radiation exposure.

An extract cytotoxicity study was then performed using L929 mouse fibroblast cells according to BS EN ISO 10993-5:2009. Extracts of the samples were brought into contact with cells on Agar plates and incubated for 48 hours. Phase contrast microscopy images

were then taken of the cells in a supernatant to assess cell morphology. A 3-(4,5-dimethylthiazol-2-yl)-5-(3-carboxymethoxyphenyl)-2-(4-sulfophenyl)-2H-tetrazolium (MTS) assay solution was then added and incubated for 4 hours. This was done to provide a quantitative measure of cell viability and was determined by measuring the presence of a formazan dye using spectrophotometry (Vistica et al., 1991). This dye was created from the MTS solution in the presence of cell metabolic activity. In conjunction to the fibre cytotoxicity measurements cells were also exposed to a cell culture medium in the form of Dulbecco's modified Eagle's medium (DMEM) and dimethyl sulphoxide (DMSO) as positive and negative controls respectively.

4.4 Results and discussion

4.4.1 Rheology measurements

The dynamic rotational viscosity measurements for a range of PCL concentrations in chloroform and chloroform/methanol solvents are plotted as a scatter diagram in Figure 4.5.
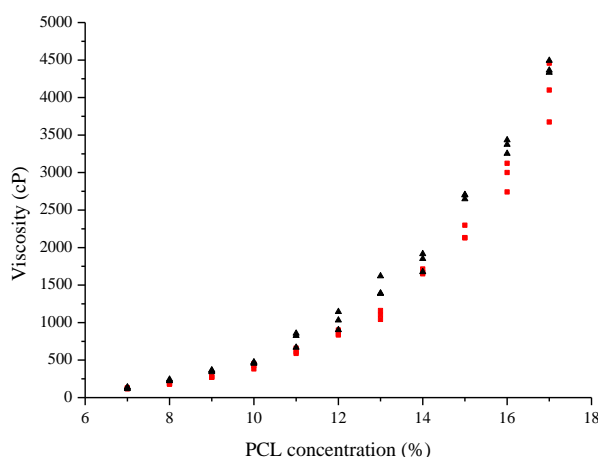
Figure 4.5: Viscosity measurements of PCL dissolved in chloroform (▲) and 4:1 chloroform/methanol (■) solvents.

Figure 4.5 confirms that the viscosity of the solution increased as the PCL concentration increased for both solvents. A viscosity increase resulting from higher polymer concentration was expected and the shapes of curve recorded can also yield important information about levels of polymer entanglement. A long chain polymer in solution can be said to be in three regimes, dilute, concentrated and concentrated entangled (Zhang and Hsieh, 2008; Gupta et al., 2005).

In a dilute condition the chains are unlikely to interact and entangle so the viscosity of the solvent dominates. There is little evidence of researchers producing fibres from dilute solutions (Gupta et al., 2005). When the number of polymer chains increases to a level where there mobility is restricted by the addition of further polymer then it is in the concentrated regime. As more polymer is added the solution shifts to the concentrated entangled regime, in this regime the addition of polymer has a greater relative effect on viscosity as the chains are already highly entangled and free space to accommodate further chains is limited compared to more dilute solutions. The viscosity of concentrated solutions often follow an exponential curve as seen in Figure 4.5. The concentrated regimes play a key role in determining spinnability in centrifugal and electrospinning systems. For example, it was found by Shenoy et al. (2005) that PLLA only produces continuous filaments from entangled, high concentration solutions.

A comparison of the two solvent systems leads to the conclusion that PCL dissolved in the 4:1 chloroform: methanol solvent results in a marginally lower viscosity compared to 100 % chloroform. This marginal decrease in viscosity was also found in research conducted by Gluck (2007) who observed that the viscosity of a chloroform/methanol based PCL solution decreased as the fractional content of methanol increased. It is

proposed that the non-solvating methanol acts as a fluid barrier between PCL chains and reduces the level of entanglements.

4.4.2 **Surface tension**

Table 4.1 shows the surface tension at two PCL concentrations when using both solvent systems. The surface tension decreased marginally at both PCL concentrations when 4:1 chloroform/methanol was used as a solvent in comparison to solutions in homogenous chloroform. The results found here compare closely to those recorded by Gluck (2007) who measured a surface tension of 30.75 mN m^{-1} in 10 % PCL in 4:1 CM using different equipment. Methanol has a surface tension of 22.1 mN m^{-1} compared to 26.7 mN m^{-1} for chloroform; thus, the addition of methanol may reduce the surface tension of the solution through a simple reduction in inherent solvent properties (Yaws and Richmond, 2009).

Table 4.1: Mean and 95 % confidence intervals for the surface tension of PCL solutions.

PCL concentration (w/v)	Solvent	Mean surface tension (mN m^{-1})
10 %	Chloroform	30.65 ± 0.21
10 %	4:1 CM	29.23 ± 0.13
12 %	Chloroform	28.19 ± 0.09
12 %	4:1 CM	27.55 ± 0.10

There is also a decrease in surface tension as the concentration of PCL is increased. This relationship has been observed in other PCL solutions using alternative solvent systems (Deitzel et al., 2001, Zhang et al., 2005). This relationship also holds true for other polymer solutions as Fong et al. (1999) also reported a decrease in surface tension with increased concentration of PEO. The explanation for this is that with increasing concentration the number of polymeric molecules also increases; the presence of these

polymeric chains typically reduces the surface tensions of a fluid (Ueberreiter and Yamaura, 1977).

4.4.3 **Centrifugal spinning of PCL**

Fibres were produced from both solvent types at a range of solution concentrations. If the polymer solution was too dilute the fibres would not spin and the material would spray. The fibres were formed into a free standing, voluminous web which was strong enough to be handled without breaking. A typical web produced through centrifugal spinning is shown below in Figure 4.6. The frustum shape that was observed when spinning PP was no longer observed and the fibres were formed in to a much flatter shape.

Figure 4.6: Appearance of typical 14 % PCL web after centrifugal spinning at 9,000 rpm.

The conditions that allowed for successful web production are shown in Table 4.2 which indicates that the workable concentration range for centrifugal spinning was 12 % and above for the given experimental conditions. Fibres could be potentially spun at concentrations beyond 17 % in both solvent systems but there is difficulty in producing a solution that remains stable and does not precipitate in this range. Below 12 %

concentration the spinning process resulting in significant spraying of the polymer film due to jet breakup with poor levels of fibre formation.

Table 4.2: Fibre production using centrifugal spinning of PCL in either chloroform of 4:1 CM solvent system.

Concentration \\ Solvent	10 %	11 %	12 %	13 %	14 %	15 %	16 %	17 %	18 %	19 %
Chloroform	x	x	✓	✓	✓	✓	✓	✓	o	o
4:1 CM	x	x	✓	✓	✓	✓	✓	o	o	o

x-indicates that mostly beads were produced.
o-indicates that a cohesive web could not be produced.
✓-indicates that a satisfactory and cohesive web was produced

A polymer concentration of 12 % marks the critical entanglement value at which the polymer is said to be sufficiently concentrated to permit centrifugal spinning. At this concentration and upwards there is sufficient overlap of the PCL chains to allow a cohesive jet to form.

The low magnification SEM micrographs presented in Figure 4.7 show dense webs containing little beading but also indicate that centrifugal PCL fibres are highly variable in diameter.
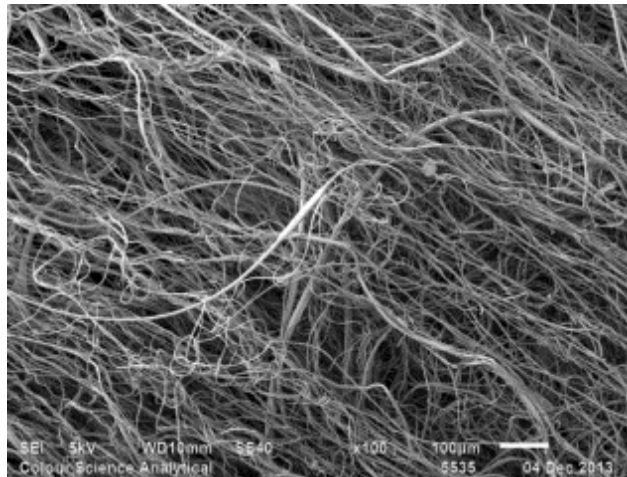
12 % w/v PCL
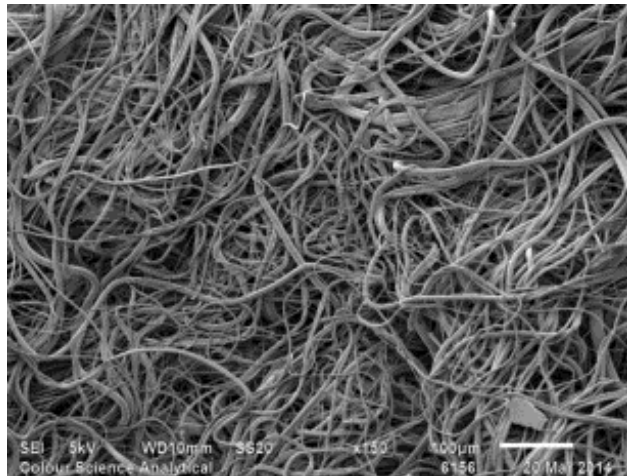
15 % w/v PCL

Figure 4.7: SEM micrograph of 12 % PCL (top) and 15 % PCL (bottom) spun from chloroform at 9,000 rpm. Magnification 150X.

It is evident that the webs contained a mixture of fine fibres combined with much larger filaments. This variability was observed in fibres produced from both solvent systems. This fibre variability is thought to manifest itself due to the short spinning times in the lab scale equipment; the acceleration and deceleration of the spinneret will introduce variable spinning conditions which will lead to a broad range of fibre sizes. In a commercial system is it expected that the system would spin for extended periods on continuous operation so the impact of acceleration and deceleration is minimised. It is

also evident, particularly in Figure 4.7 that the diameter of any one filament is not consistent across a meaningful length; a filament can measure < 1 μm at one point and can increase to over 5 μm within a few mm of length, however this is relatively rare and the majority of filaments are uniform along the length within an SEM image scan. It is thought that this variation is due to uneven elongational loading leading to localised areas of deformation. It should be noted that the presence of larger fibres will significantly affect the average fibre diameter which could limit the effectiveness of this kind of product where high surface area per weight is critical.

Figure 4.8 to Figure 4.10 show high magnification SEM images of fibres produced from chloroform allowing for close observation of fibre morphology and the measuring of fibre diameter. In terms of morphology the fibres produced are generally round with some visible surface morphology.
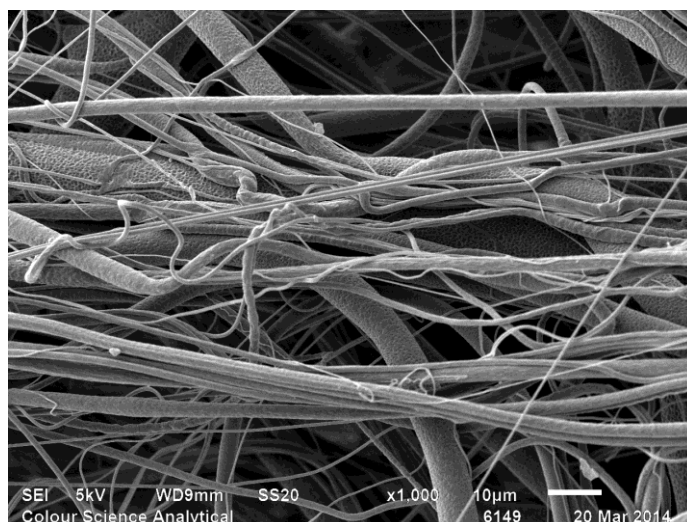
Figure 4.8: Micrograph of 12 % PCL spun from chloroform at 9,000 rpm. Unique texture can be observed on the larger fibres in the background. Magnification 1000X.
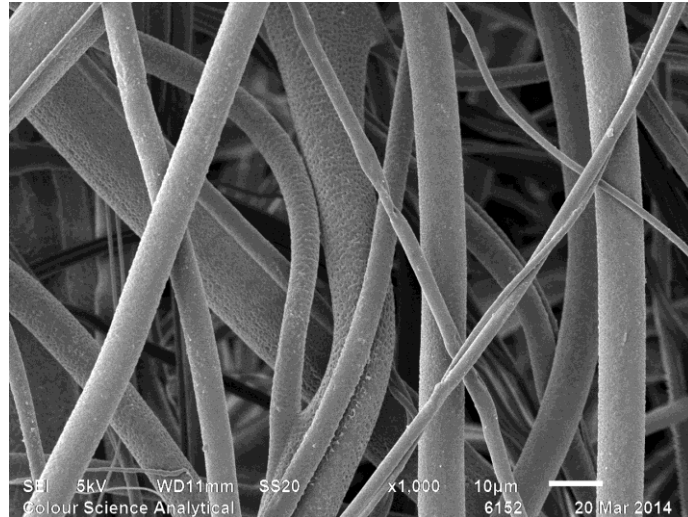
Figure 4.9: Surface texture of PCL fibres spun from chloroform. Fibres are formed from 13 % PCL solution spun at 9,000 rpm. Magnification 1000X.
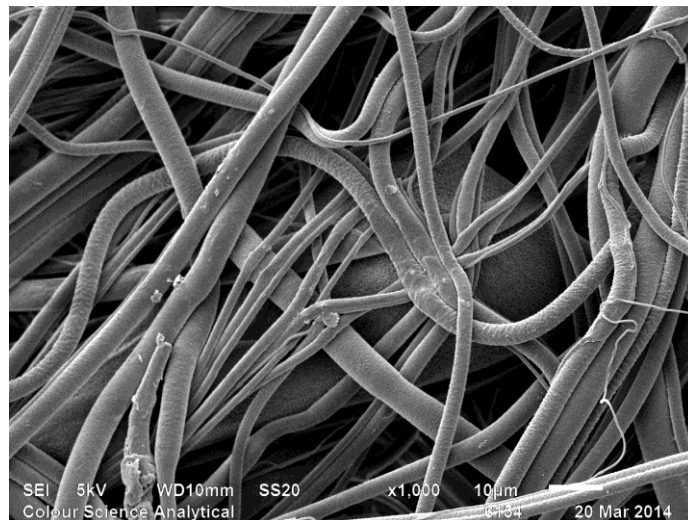
Figure 4.10: SEM micrograph of 15 % PCL spun from chloroform at 9,000 rpm. Magnification 1000X.

Close examination of the fibre surface reveals a texture more evident on the coarser fibres which are best described as shallow pores or pits, Figure 4.11. This texture is less pronounced or entirely absent on the smaller (>300 nm diameter) fibres as it thought the high surface area ratio allows solvent to flash off more uniformly which limits the level of surface texture created. The proposed action that creates these features is the dry skin

model that is discussed in conjunction with the SEM the results for the fibres spun from

the 4:1 CM solvent.
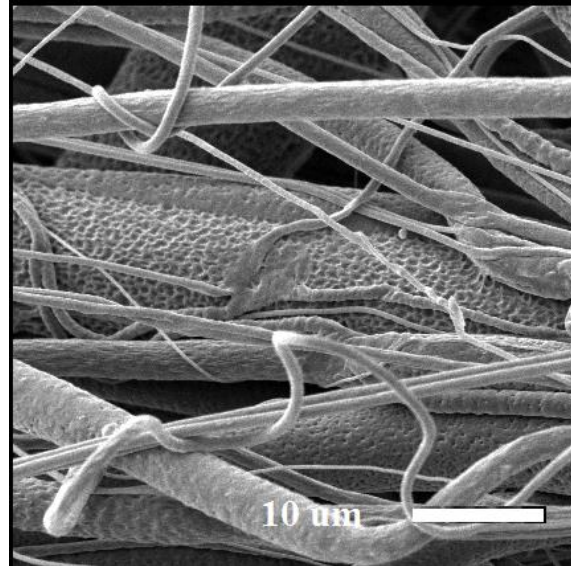
Figure 4.11: Expanded SEM micrograph of 12 % PCL spun from chloroform showing pores on surface. Digitally enlarged from an original magnification of 1000X.

For a meaningful comparison to be made between the two productions systems the

resulting fibre diameters must be discussed. Table 4.3 presents the mean diameters for

the polycaprolactone fibres spun using centrifugal spinning.

Table 4.3: Mean fibre diameters of centrifugally spun PCL for the two solvent systems.

Solvent		PCL concentration (%)				
		12 %	13 %	14 %	15 %	16 %
Chloroform	Mean (µm)	1.60	1.73	2.30	2.91	2.96
	SD (µm)	1.24	1.69	1.47	1.73	1.83
4:1 CM	Mean (µm)	1.04	1.36	2.16	2.19	2.55
	SD (µm)	0.85	1.47	1.83	2.14	2.58

Table 4.3 shows that for both solvent systems, the finest were produced from the lowest

concentration solutions (12 %) and the coarser fibres were produced by the highest

polymer concentration. This indicates that a reduction in polymer concentration produced finer fibres; however, this relationship is limited by fibre breakup at below critical entanglement concentrations ($>11 - 12$ %). Whilst the mean diameter for the fibres produced from chloroform/methanol were lower at each condition, statistical analysis using ANOVA revealed that significant differences were only observed at the PCL concentration of 12 % ($p > 0.05$, F (13.5) > Fcrit (3.9)) and 15 % ($p > 0.05$, F (25.9) > Fcrit (3.9)) and that the data was not statistically significant at the other concentrations. This mix of significant and insignificant data means that it cannot be firmly argued that adding methanol to the solvent produced significantly finer fibres. However, it can be argued that the additional of methanol does not adversely affect the fineness of a PCL web.

Plotting the relationship between PCL concentration and fibre diameter confirmed the trend that the fibre diameters increased as the polymer concentration increased. This relationship is shown in the graph in Figure 4.12.
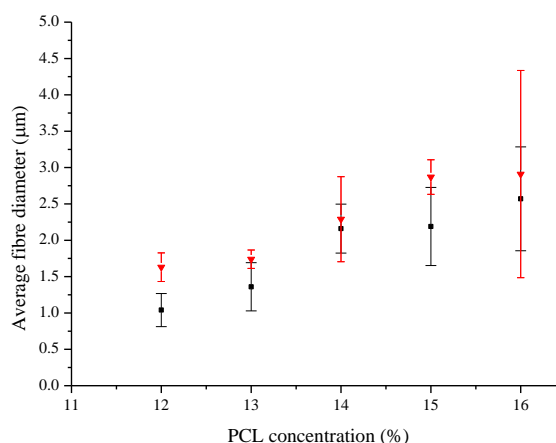
Figure 4.12: Relationship between initial PCL concentration and resulting fibre diameter. Fibres were spun from 27G needle tips at a speed of 9,000 rpm. The graph shows the two solvent systems: chloroform (▲) and 4:1 chloroform/methanol (■) with the bars showing the upper and lower 95 % confidence interval.

The relationship between here is an agreement with results observed in the electrospinning literature and also the recent research on centrifugal spinning; Zander (2015) found that the diameter of fibres increased when the PCL in methylene chloride concentration was increased from 10 % to 20 % when processing at 6,000 rpm.

It is known from the viscosity measurements on PCL solutions, page 138, that increasing the polymer concentration in a solution will act to increase the solution viscosity. The viscosity increase renders the solutions more resistant to flow and thus more resistant to elongation for a given applied force. The reduced solvent-to-polymer ratio in the higher concentration fluids also results in a more rapid solidification process. Additionally there is more PCL present in the fluid so the solidifying jet has more solid mass within it, increasing the size of the final yet.

4.4.4 Comparison of centrifugal spun fibres and electrospun fibres

Fibre production was only possible within a limited range of polymer concentrations. A list of all the successful operating conditions observed to form fibres is found in Table 4.4. For both solvent systems steady state fibre production occurred when using PCL concentrations of 7 - 11 % when using the processing parameters listed on page 134.

At low concentrations the solution viscosity was too low which does not promote steady state fibre production. When working in the operating concentration range and the rotating wire electrode, the Elamrco Nanospider was able to spin for prolonged periods (> 10 minutes) until such a time that the polymer solution began to agglomerate on the

wires, destabilising the system. The web produced was a flat, thin membrane supported by a substrate and typical of electrospun products.

Table 4.4: Fibre production conditions of electrospinning.

Solvent	PCL concentration (w/v)						
	6 %	7 %	8 %	9 %	10 %	11 %	12 %
Chloroform	x	✓	✓	✓	o	o	x
4:1 CM	x	✓	✓	✓	o	o	x

o- high quality webs were not produced.
x- no fibres were produced.
✓- satisfactory webs were produced.

Electrospinning occurred below the critical entanglement concentration (~11 %) and instead occurred in a viscosity phase known as semi-dilute entangled (Lu et al., 2013). The rheological range that allows electrospinning is relatively narrow and Taylor cone formation and jet elongation does not occur if the entanglement is insufficient or the solution is considered to be too concentrated. This failure to spin would manifest itself through jet breakup (low concentrations) or rapid solidification resulting in large artefacts or *blobs* (high concentrations).

By comparing Table 4.4 with Table 4.2, page 142, the argument can be made, in conjunction with the results found in the literature (McEachin and Lozano, 2012; Deitzel et al. 2001), that centrifugal spinning requires a significantly higher concentration solution than the needleless electrospinning technique when using a comparable solvent-polymer system. In the literature, typical PCL electrospinning in chlorinated solvents works at a concentration range between 7 and 10 % (Deitzel et al., 2012; Zeng et al., 2003) whereas in centrifugal spinning this concentration figure is typically higher, ranging from 12 %, as found by Amalorpava Mary et al. (2013), to as high as 18 %

(McEachin and Lozano, 2012). Based on these previous studies and the data collected here it can be argued that centrifugal spinning and electrospinning require the polymer viscosity to be in different regimes. Centrifugal spinning only occurred when the solution concentration was greater than the c^e identified in the viscosity results (~11 %). In comparison electrospinning requires a lower viscosity to produce fibres in steady state conditions. In practical terms, the closed spinneret used in centrifugal spinning means there is no premature polymer solidification which has been identified as a potential problem in free-surface electrospinning. Aside from the practical aspects of polymer build up on the free surface there is also the postulated reason that the lower concentration range is necessary for Taylor cone formation.

4.4.4.1 Morphology of electrospun webs

When spinning from homogenous chloroform the electrospun webs were fused together in a non-uniform way to form the film like structures, Figure 4.13 to Figure 4.15. These webs were deemed satisfactory as they are predominantly fibrous and appeared uniform to the human eye.
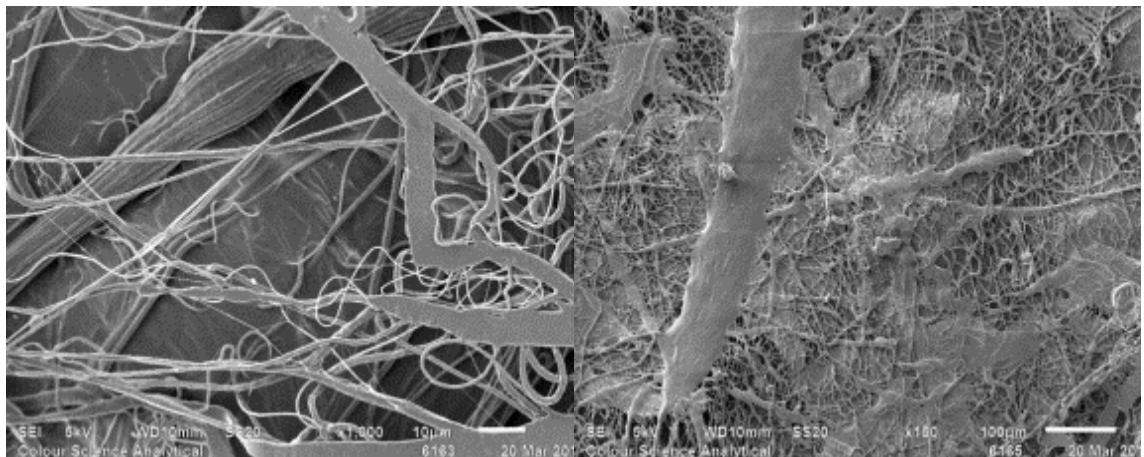
Figure 4.13: 1000X (left) and 150X (right) SEM micrographs of 9 % PCL spun from chloroform using needleless electrospinning.
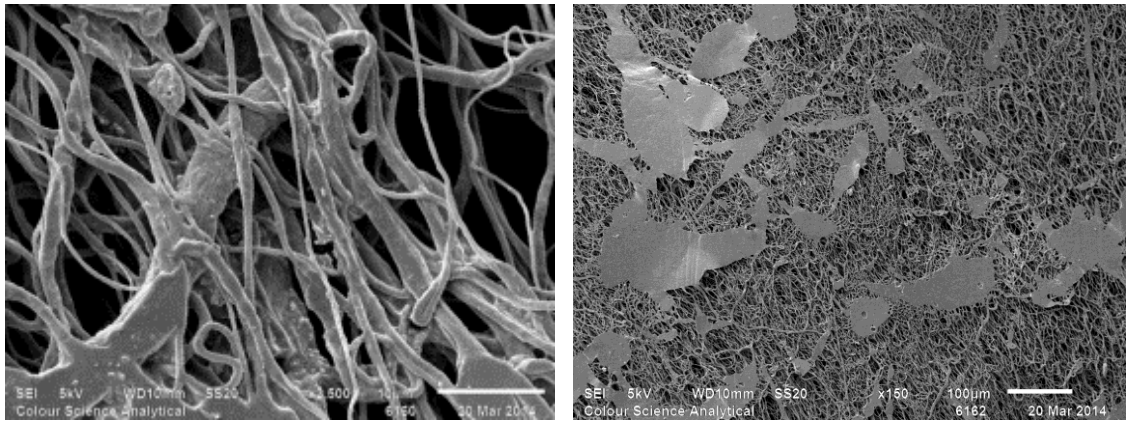
Figure 4.14: 1000X (left) and 150X (right) SEM micrographs of 8 % PCL spun from chloroform using needleless electrospinning.
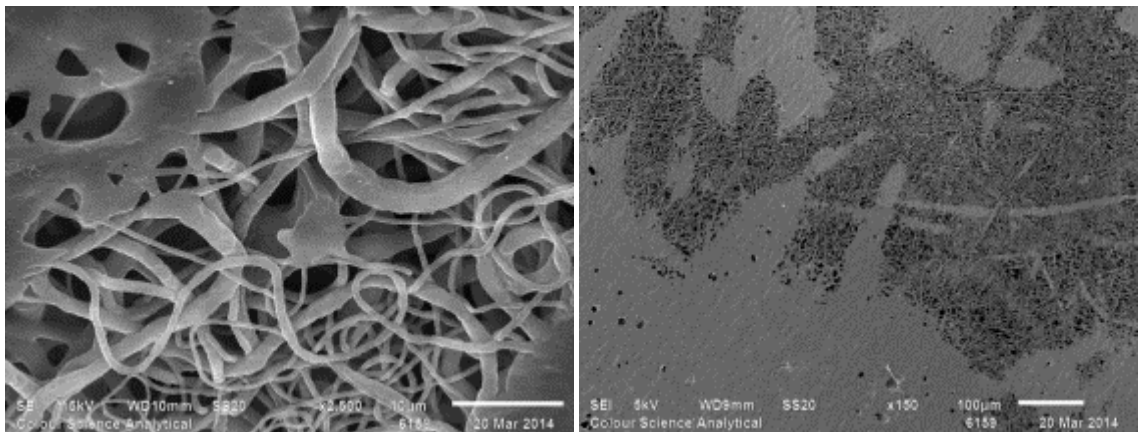
Figure 4.15: 1000X (left) and 150X (right) SEM micrographs of 7 % PCL spun from chloroform using needleless electrospinning.

However, this merging of fibres to form areas of film detracts from some of the desired 'advantageous' properties and is undesirable for most likely applications. It is proposed that this phenomena was due to the jet only partially solidifying before it reaches the collector. The solvent remaining in the web spreads and causes neighbouring fibres to fuse together. The level of web fusion was observed to reduce as the PCL concentration increased, being lowest in the 9 % solution. This fusion was not seen in centrifugal spinning. It is proposed the higher initial polymer to solvent ratio combined with a longer jet drying step results in fibres that reach the collector fully solidified.

Incomplete solvent evaporation also created different fibre morphology when compared to the centrifugal spun fibres. The fibres are less spherical, adopting a flatter, almost cottonesque appearance. There was also localised bonding between neighbouring fibres observed in all the concentration ranges. This fibre fusion occurred over entire areas of the web at the 7 % concentration, Figure 4.15, where patches of the web became film like.

4.4.4.2 **Analysis of Fibre diameters of electrospun webs**

The mean fibre diameters of the PCL fibres produced using needleless electrospinning are shown in Figure 4.16.
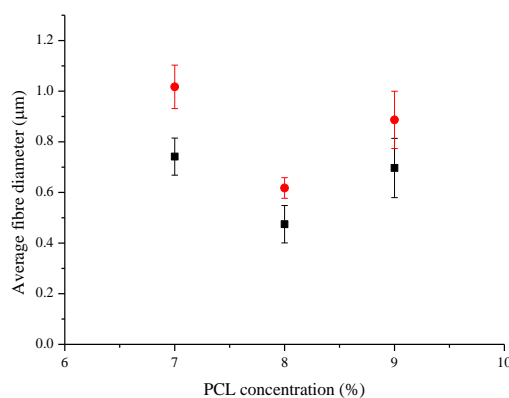
Figure 4.16: Mean diameters and 95 % confidence interval of fibres produced using electrospinning. The solvents used were chloroform (●) and 4:1 chloroform/methanol (■).

The observed range of fibre diameters, Figure 4.16, suggested the fibre diameter reached a minimum as the concentration passed from 7 % to 8 %. This indicates that as with centrifugal spinning, the initial PCL concentration also influenced the mean fibre diameters in electrospun webs. The average diameters varied from ~500 nm average to ~1 μm depending on concentration and conditions. This is only marginally finer than what was achieved using centrifugal spinning; however electrospinning produced much more

uniform fibre distributions within the webs evident through the narrower coefficient of variations as shown in Table 4.5 and Table 4.6.

Table 4.5: Descriptive statistics of fibres produced from chloroform using electrospinning and centrifugal spinning.

		PCL Concentration (%)									
		7	8	9	10	11	12	13	14	15	16
Electrospun	Mean	1.02	0.62	0.89	-	-					
	SD	0.36	0.34	0.59	-	-					
	CV	0.35	0.56	0.67	-	-					
Centrifugal spun	Mean				-	-	1.60	1.73	2.30	2.91	2.96
	SD				-	-	1.24	1.69	1.51	1.73	1.83
	CV				-	-	0.78	0.97	0.66	0.59	0.62

Table 4.6: Descriptive statistics of fibres produced from 4:1 CM solvent using electrospinning and centrifugal spinning.

		PCL Concentration (%)									
		7	8	9	10	11	12	13	14	15	16
Electrospun	Mean	0.74	0.47	0.70	-	-					
	SD	0.42	0.22	0.48	-	-					
	CV	0.57	0.46	0.70	-	-					
Centrifugal spun	Mean				-	-	1.04	1.36	2.16	2.19	2.57
	SD				-	-	0.86	1.47	1.83	2.14	2.58
	CV				-	-	0.83	1.08	0.85	0.98	1.00

Electrospinning of PCL could be further optimised to produce finer fibres using needless electrospinning. However, there is the potential for films to form when electrospinning PCL as seen in Figure 4.23 and Figure 4.24. This film formation has to be considered in any optimisation process as it could have potentially negative consequences on certain web properties making it unsuitable for certain applications.

4.4.5 The use of binary solvent

The data presented previously Figure 4.12, page 147, and Figure 4.16, page 152, shows that whilst the use chloroform/methanol solvent produced finer mean diameters compared to fibres spun from chloroform, these were not always significant, particularly in the

centrifugal spun products. However, reduction in fibre diameter through the addition of methanol has previously reported by Gluck (2007) when electrospinning PCL. This reduction in diameter was linked to retardation in the rate of evaporation with increasing methanol content; the jets remain fluid for longer allowing for more elongation.

Thus far only the morphology of PCL centrifugal spun from chloroform has been presented and discussed. Sections 4.4.5.1 and 4.4.5.2 presents the morphological features of PCL fibres produced from 4:1 chloroform/methanol using centrifugal spinning and electrospinning respectively. Section 4.4.5.3 explores the mechanism of mechanism of pore formation.

4.4.5.1   **Chloroform/methanol in centrifugal spun webs**

In section 4.4.3 it was shown that fibres centrifugal spun from chloroform displayed some pore formation on the fibres, Figure 4.8 to Figure 4.11. SEM analysis of the fibres produced from 4:1 chloroform/methanol, Figure 4.17 to Figure 4.20, revealed that spinning PCL from this solvent system significantly increased the number of magnitude of these surface pores and it appears the level of texture is increased through the use of methanol as a co-solvent. This agrees with the conclusion drawn elsewhere that surface deformation is more severe when using binary solvent systems (Luo et al., 2010).
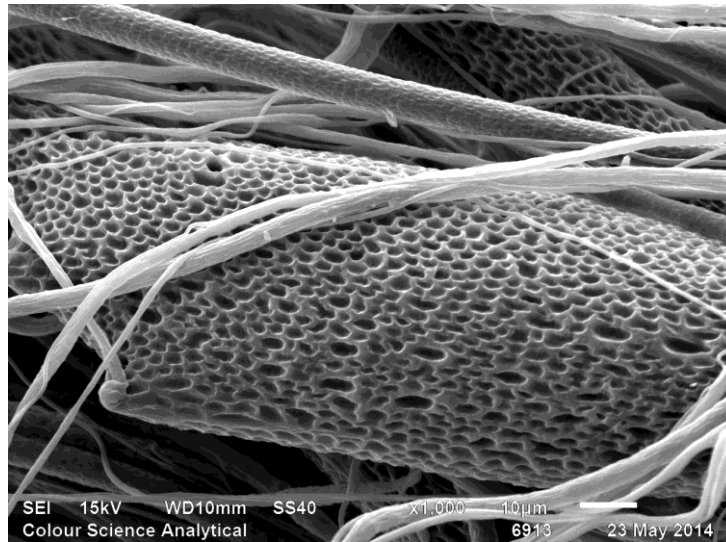
Figure 4.17: SEM micrograph of 12 % PCL spun from 4:1 CM at 9,000 rpm. Deep surface features are observed on the larger diameter fibres. Magnification 2000X.
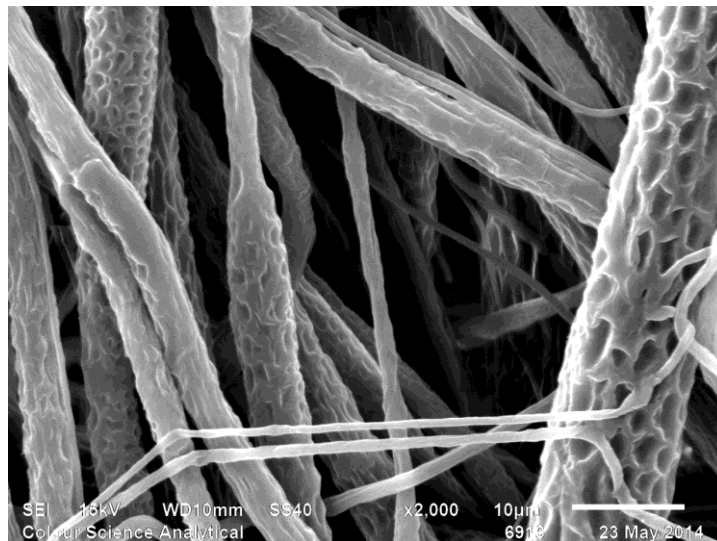
Figure 4.18: SEM micrograph of 13 % PCL spun from 4:1 CM at 9,000 rpm. Magnification 2000X.
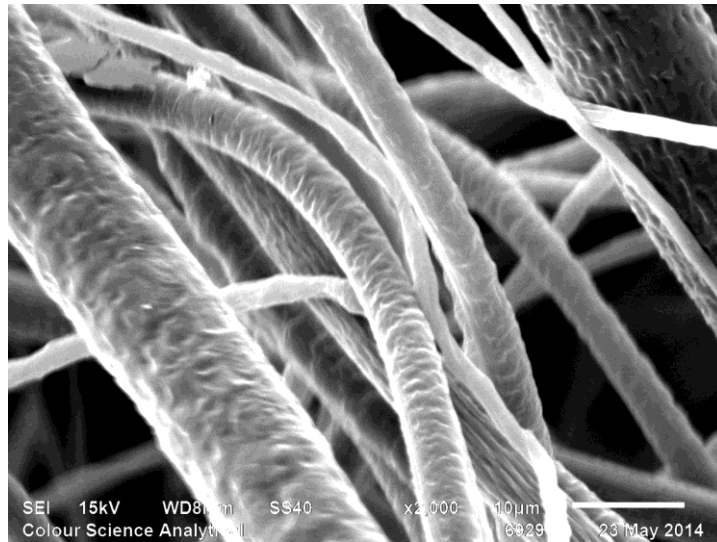
Figure 4.19: SEM micrograph of 15 % PCL centrifugal spun from 4:1 CM 9,000 rpm. Magnification 2000X.
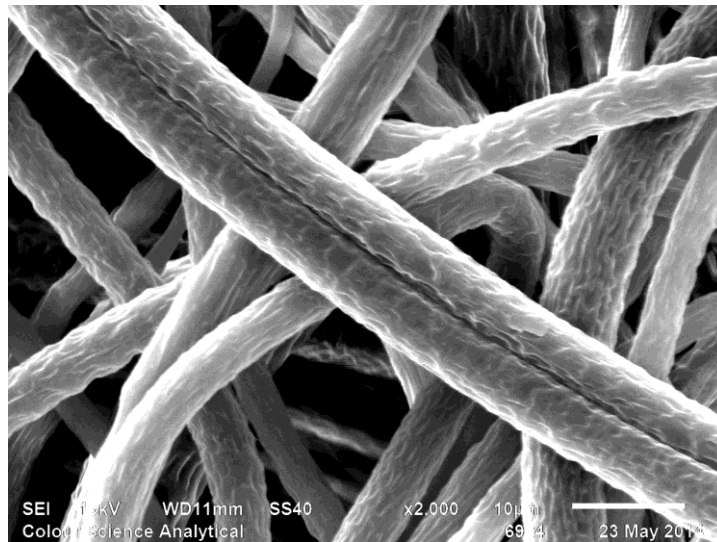
Figure 4.20: SEM micrograph of 16 % PCL centrifugal spun from 4:1 CM at 9,000 rpm. Magnification 2000X.

Figure 4.17 to Figure 4.20 shows that as the polymer concentration is increased the surface texture shifts from one of deep pores to one of shallow surface crinkling. Solutions of 15 % and 16 % w/v showed a significant reduction in surface texture. The polymer jet is much more viscous and solidifies quicker, resisting deformation. This reduction in pore formation with increasing polymer concentration was also observed by Zeng et al., (2003a).
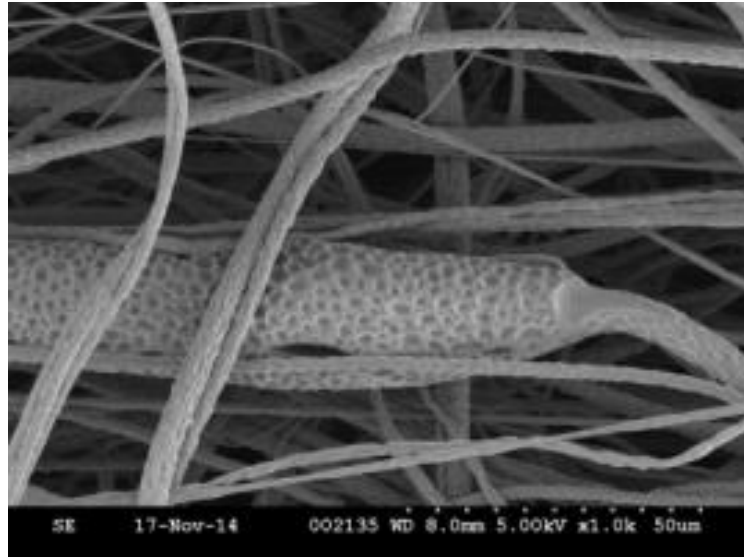
Figure 4.21: SEM micrograph of pore formation on a 12 % PCL fibre centrifugally spun from 4:1 CM at 9,000 rpm. Magnification 1000X.
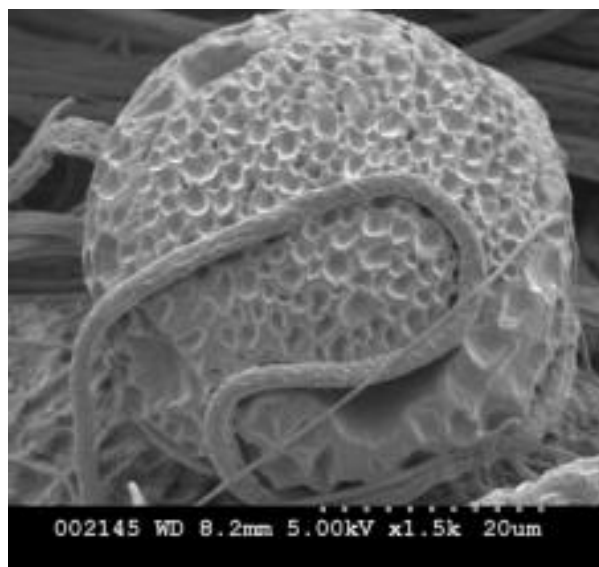
Figure 4.22: SEM micrographs of pore formation on a bead of 12 % PCL. Magnification 1500X.

So far, PCL has been successfully centrifugal spun from a single solvent system but there have been no reportable publication, to date, that has established the effect of a secondary non-solvent on the fibre formation process when using this polymer. In addition, there is only limited information on the effect of binary solvent systems on the surface tension. To the authors knowledge this is the first time textures such as those observed here have been reported in centrifugally spun fibres from this polymer.

4.4.5.2 **Electrospinning from chloroform/methanol**

Low magnification SEM micrographs of the webs formed from 4:1 CM solvent are shown in Figure 4.23 where it was observed that the webs electrospun from a 4:1 CM solvent showed comparatively little film formation compared to the homogenous chloroform system as shown previously in Figure 4.13 to Figure 4.15, page 150.

8 %   9 %
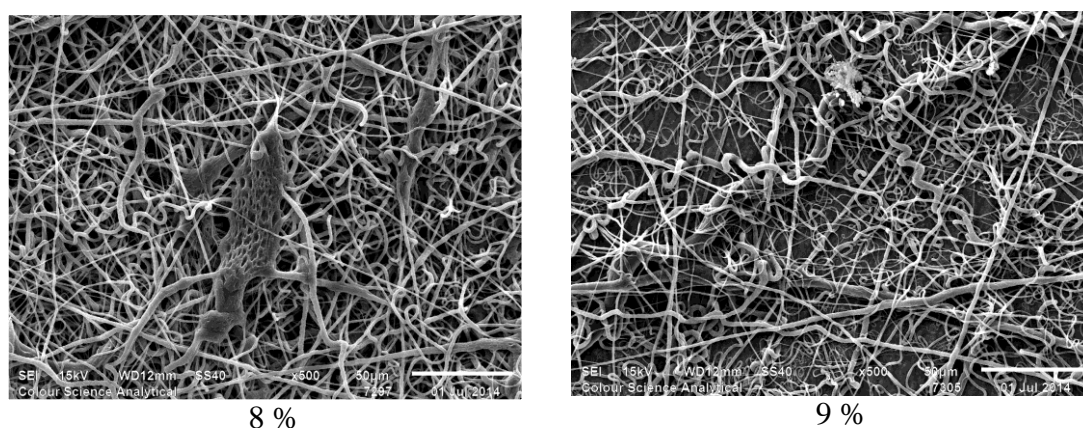
Figure 4.23: SEM micrographs of the webs produced by electrospinning on the Nanospider of 8 % (left) and 9 % (right) PCL in 4:1 chloroform/methanol solvent. Magnification 500X.

This reduction in observed film formation suggests that the fibres are reaching the collector with increased solidification. It is suggested that a co-solvent can change the evaporation behaviour of the solution (Luo et al., 2010). The consequence of this is that the webs can be produced that retain the desirable properties of nanofibres but by varying solvent levels the process could be tailored to create a range of mechanical and filtration behaviours depending on the required application. The fibres also appeared more regular but did demonstrate pore formation on the larger elements and have a surface texture as observed in the high magnification images presented in Figure 4.24.

7 % w/v   8 % w/v
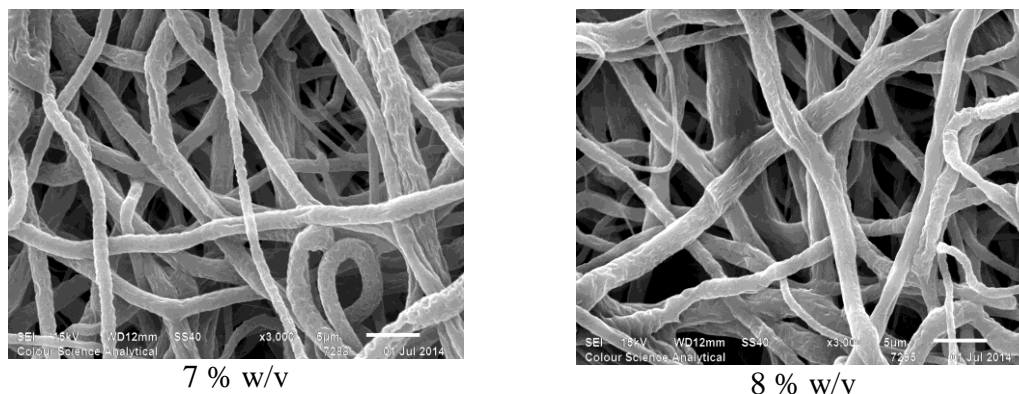
Figure 4.24: SEM image of 7 % and 8 % PCL in 4:1 CM spun using the wire roller electrode. Magnification 3000X.

The electrospun webs were different in form and appearance compared to the centrifugal spun webs. Here the webs were mounted flat onto a spunbond substrate. The morphology of the fibres showed shared some similar surface features but overall had a different fine scale appearance.

4.4.5.3   Pore formation mechanism

It is known from the literature that the addition of a second solvent can change the surface morphology of the fibres (Bognitzki et al., 2001). This can lead to the formation of pores within the surface of the fibre as observed in this section of work. Pore formation has been previously observed in electrospun PLLA by Zeng et al. (2003a) and by Badrossamay et al. (2010) who also identified the porous structure in PLA fibres web using a form of centrifugal spinning. Attempts have been made to explain the formation of unique texture in fine fibres: Krishnappa et al. (2003) noted that electrospun polycarbonate fibres spun from a binary solvent exhibited puckering to form a surface structure they likened to a raisin. They attributed this to a hypothetical dry skin model where the outer solvent evaporates off, creating a skin that must collapse inwards as the interior solvent evaporates, leaving a void, Figure 4.25. They argued that the use of binary

solvents increases the level of phase separation which results in a high solvent vapour pressure which deforms the surface.
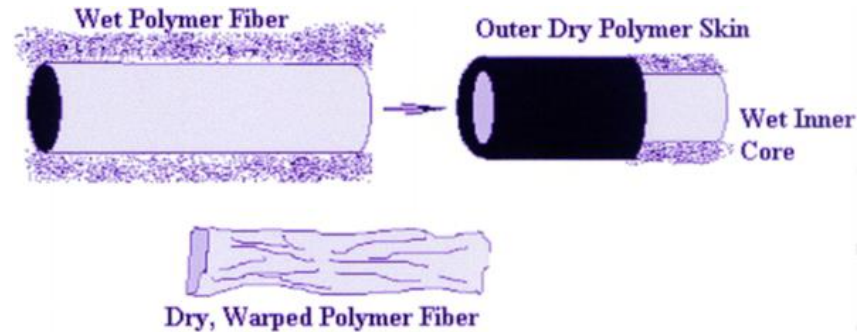
Figure 4.25: The dry skin model of binary solvent spinning of polycarbonate resulting in textured fibres (Krishnappa et al., 2003).

However, the dry skin model does not explain the creation of structures seen in Figure 4.21and Figure 4.22 where the pores are shallow and create a dimpling effect similar to that of a golf ball. The pores here are typically circular in shape with a depth that appears to be less than the pore radius. These shallow pores appear to have been formed on the fibre surface rather than the escape of a solvent interior. The circular pore shape is typically seen on the larger fibres and is also seen on a number of beads, typified in Figure 4.17, Figure 4.22 and Figure 4.26. Circular pores were also reported in the work by Badrossamay et al., (2010).
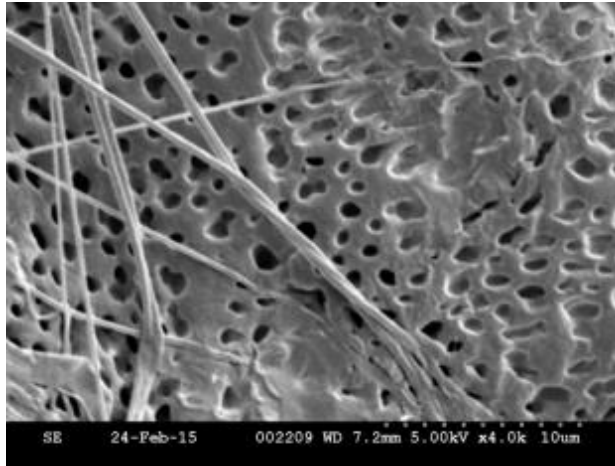
Figure 4.26: SEM micrograph of pores on an artefact in 12 % PCL in chloroform/methanol. Magnification 4000X.

The finer fibres formed through centrifugal spinning PCL in chloroform/methanol have an elongated pore shape with a pore depth that decreases in conjunction with the fibre diameter, Figure 4.20. This can be explained by the phase separation of the two solvents during spinning. The methanol agglomerates into regions on the fibre surface, as it evaporates it leaves behind an imprint that remains in the rapidly solidifying polymer. In regions of high deformation (finer fibres) these imprints become elongated in the direction of fibre extension and reduce in absolute size as the jet shrinks during stretching. The very large fibre elements and beads will have undergone less extensional deformation and as a result the imprints are not deformed and remain circular.

4.4.6 **Differential scanning calorimetry**

DSC was used to measure the thermal properties of the fibres produced using the techniques listed above and the initial pellet. Selected DSC traces are drawn in and the T_{onset}, T_{melt} measured are reported, where relevant as part of the discussion.
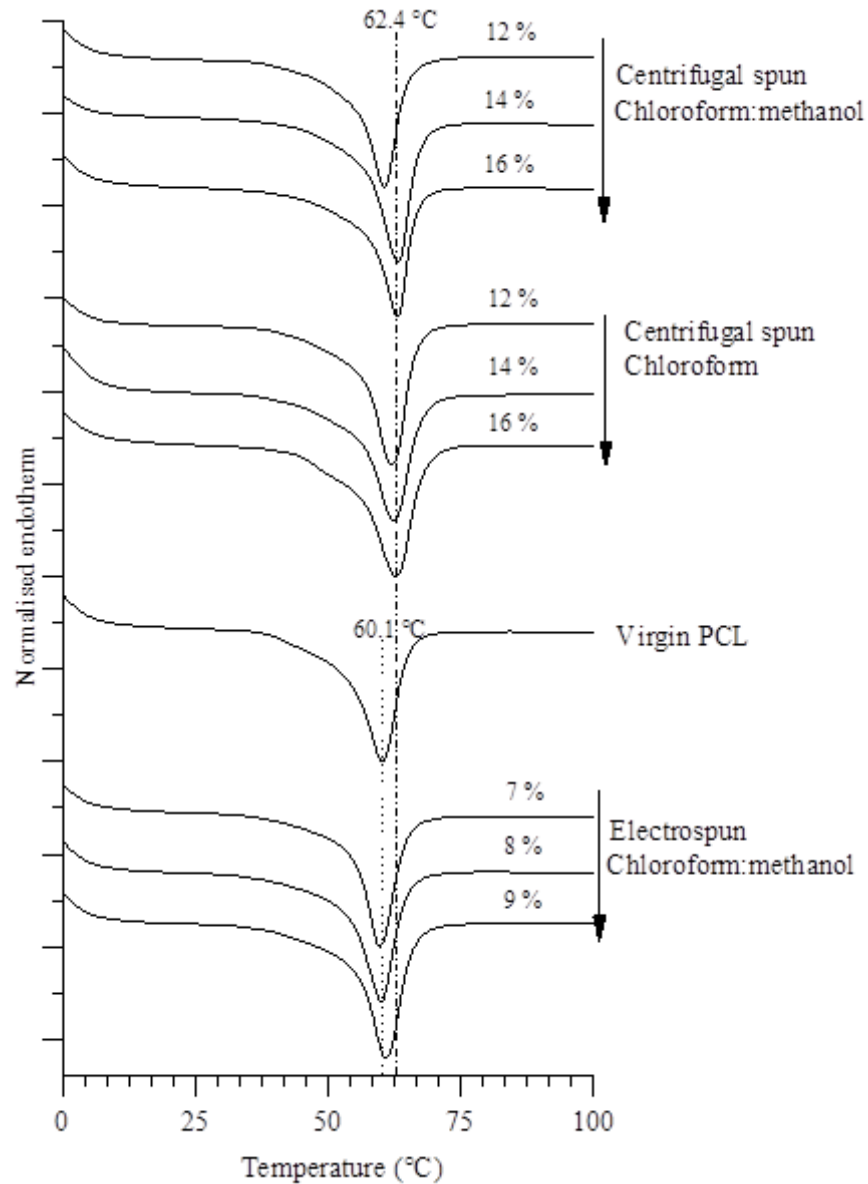
Figure 4.27: DSC thermograms for centrifugal spun PCL fibres (top) alongside virgin PCL pellet and electrospun PCL fibres (bottom).

The PCL fibres produced through centrifugal spinning had a single melting endotherm with a T_{onset} at around 52 °C to 55 °C with a T_{melt} occurring at ~62.4 °C. The DSC traces of the centrifugal spun showed little deviation between processing conditions and were largely similar regardless of starting concentration. No significant differences were observed between solvent systems. The unprocessed pellet and electrospun fibre endotherms are apparently similar but had a slightly lower T_{onset} and a T_{melt} that reached a maxima at around 60.1 °C. This suggests that the centrifugal spun fibres had a slightly larger average crystallite size which would result in a higher T_{melt}. However, this higher T_{melt} was not observed for all centrifugal spun fibres.

Apart from this shift in T_{melt} it can be argued from that the fine structure of centrifugal spun PCL is largely similar to both virgin PCL and electrospun PCL fibres. As the fibres are not melt processed they had a very similar thermal history so had melting peaks with a similar onset, similar shape and marginally different T_{melt} points. Whereas melt centrifugal spun polypropylene (Chapter 3) quenched quickly in cool air and generated a radically different DSC trace; solution processed material takes longer to solidify fully which results in a similar fibre fine structure compared with the virgin material.

In comparison to other work, McEachin and Lozano (2012) found that centrifugal spun PCL created an endothermic shoulder at around 40 °C. They attribute this to a disordered mesophase much like the one observed in polypropylene previously in this work. This peak was not found in this work and it is thought that the choice of solvent may have influenced this difference. They used dichloromethane (DCM) as a solvent which has a vapour pressure of 350 Torr whereas chloroform has a vapour pressure of 150 Torr. The rapid evaporation of DCM could result in equally rapid solidification, resulting in a

mesophase structure. This discrepancy in findings indicates that the fine structure of the PCL fibre is determined by the solvent system it was produced from and could be potentially tailored to produce fibres with variable crystal forms.

4.4.7 **X-ray diffraction of PCL samples**

The diffraction patterns of film cast PCL and selected PCL fibre samples are shown in Figure 4.28.
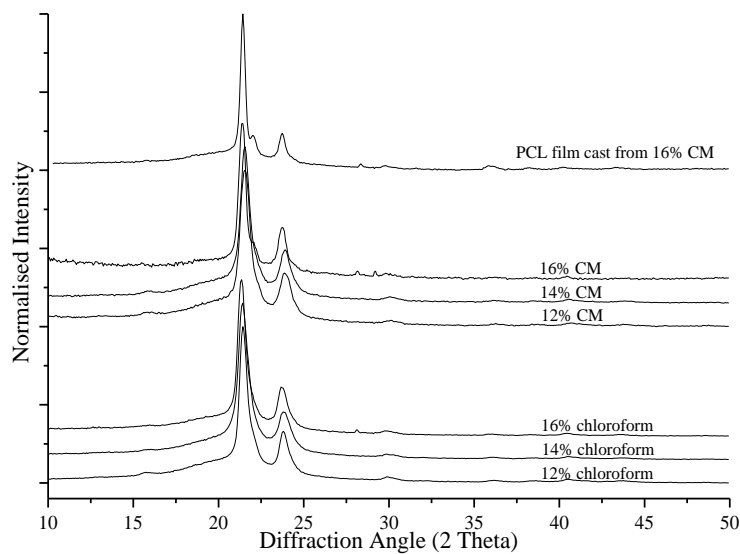
Figure 4.28: Wide angle X-ray diffraction traces of PCL film and centrifugal spun fibres using 12, 14 and 16 % polymer concentrations in both solvent options.

The XRD patterns of the PCL fibres produced through centrifugal spinning, Figure 4.28, show consistently sharp peaks in definite regions across the spectrum. This indicates that unlike melt spun polypropylene; PCL fibres contain definite crystal regions without a subsequent annealing step. The normalised curves presented show that the peak locations and shape was largely consistent for all the PCL flake and fibres regardless of starting concentration or solvent. The XRD traces of PCL spun using needleless electrospinning display a similar pattern with peaks in near identical positions, Figure 4.29.
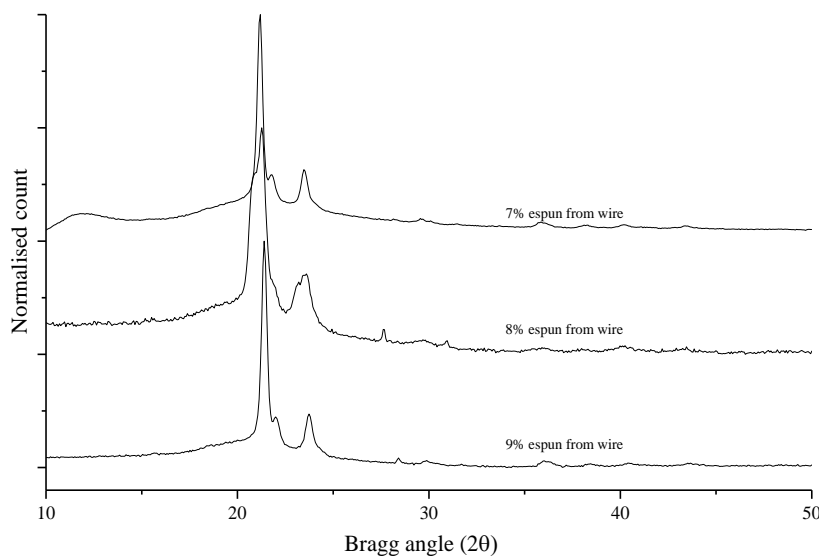
Figure 4.29: Wide angle X-ray diffraction traces of PCL electrospun from the wire roller using 7, 8 and 9 % polymer concentrations in chloroform solvent.

The peaks lie on top of an amorphous hump that occurs between 15° and 25° 2θ. The crystalline regions are identified by the sharp peaks at 21.4° 2θ and 23.8° 2θ along with a minor peak at 30° 2θ. This combination of order and disorder suggests that PCL is a semi-crystalline material with crystalline regions interspersed with amorphous regions. By using Equation 2.6 and Equation 2.7 with the peak positions 21.4°, 23.8° and 30° 2θ the unit cell dimensions of the PCL fibres can be calculated (Hartman et al., 2010). The precise peak positions confirm that the PCL fibres produced through both techniques forms an orthorhombic crystal with dimensions: a = 7.47 Å, b= 4.97 Å and c =17.30 Å.

The XRD traces of PCL fibres allowed for an estimation of crystallinity for the as-spun materials using the method described by Young and Lovell (1991). The XRD curve is separated into two distinct regions representing the amorphous and crystalline components (Statton, 1963).
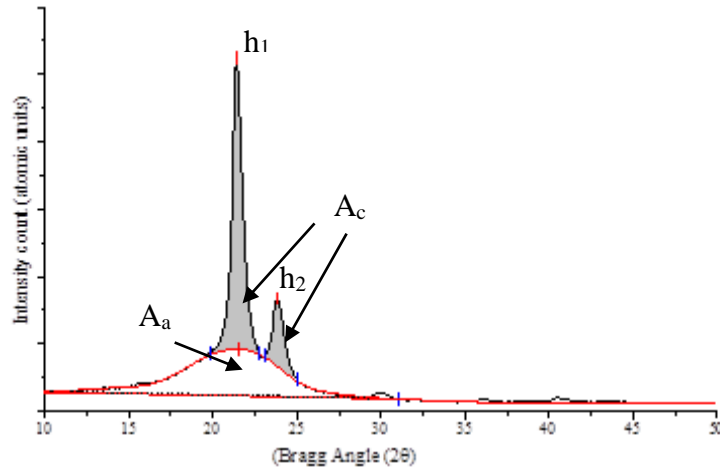
Figure 4.30: XRD trace of PCL fibres with notation marking crystalline peak are and height and amorphous halo area.

Once the peak areas are separated, as shown in Figure 4.30, the total areas can be compared and the crystallinity estimated using Equation 4.1.

$$X_c = \frac{A_c}{A_a + A_c} \times 100 \qquad \text{Equation 4.1}$$

Where X_c is the estimated crystallinity, A_c is the area of the crystalline peaks and A_a is the area of the amorphous halo. The peak areas were calculated using curve fitting and integration software provided in the software package OriginPro 8.1.

In addition the relative peak heights of the crystalline regions, h_1 and h_2 in Figure 4.30, and can be taken as a ratio to determine if there is a change in crystal formation. The full width at half maximum for the crystalline regions was also measured which yields information regarding crystallite size. The relative peak heights, full widths at half maximum and estimated crystallinity are listed for the centrifugal spun webs in Table 4.7.

Table 4.7: Peak positions and estimates of crystallinity from XRD results on centrifugal spun PCL fibres.

Concentration	Solvent	Peak relative height	FWHM of h_1 (° 2θ)	Estimated Crystallinity
12 %	Chloroform	3.62	0.59	51 %
14 %	Chloroform	4.33	0.66	41 %
16 %	Chloroform	3.51	0.54	49 %
12 %	CM	3.67	0.67	48 %
14 %	CM	3.61	0.61	51 %
16 %	CM	3.49	0.48	59 %

No patterns or marked changes were observed between processing conditions and the parameters calculated in Table 4.7. There is only slight variation in the location of the peaks and the relative heights of the primary peak for the centrifugal spun fibres. This agrees with the DSC data which suggested that the fine structure of the material was largely independent of spinning speed or processing conditions regardless of processing. The estimated crystallinity was found to vary but the calculation technique is known to be only a rough guide. The crystallinity estimates for centrifugal spun PCL webs are similar to the 42 - 60 % X_c values found by Hartman et al. (2010) for film cast and electrospun PCL webs suggesting there is little variation between centrifugal spinning and electrospinning on the fine structure formation in PCL fibres.

4.4.8 **Cytotoxicity**

The phase contrast microscope images for the five samples are shown in Figure 4.31. These images show the shape of cells in a supernatant containing elements of the fibres or chemical reference.
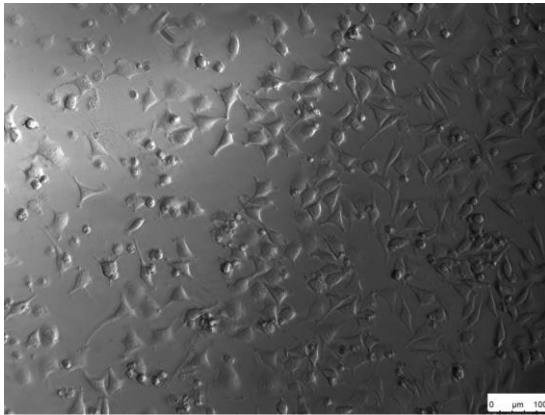
A- 12 % PCL in chloroform
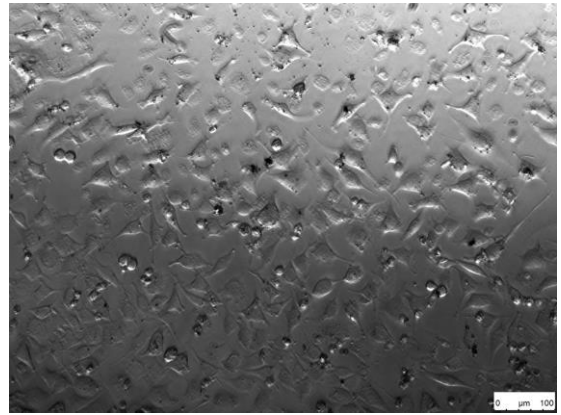
B- 12 % PCL in chloroform/methanol
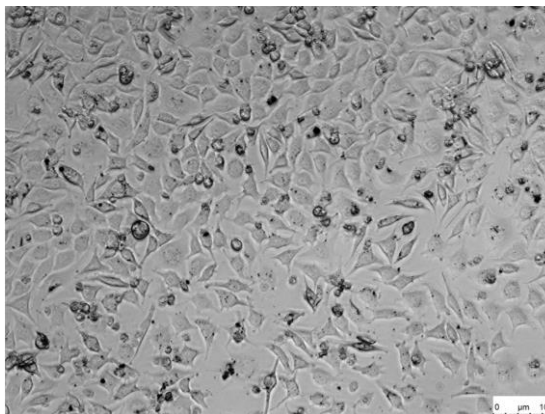
C- 12 % PCL + 0.25 % CNTs in chloroform
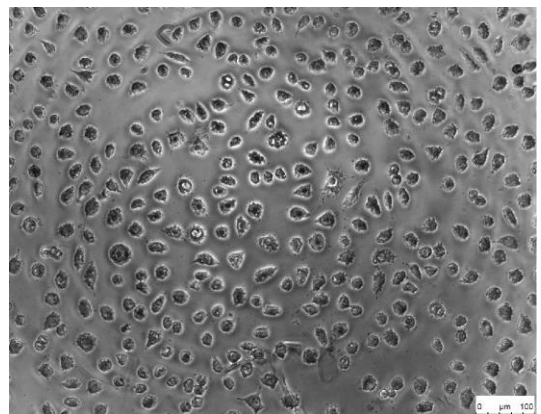
D- DMEM culture medium
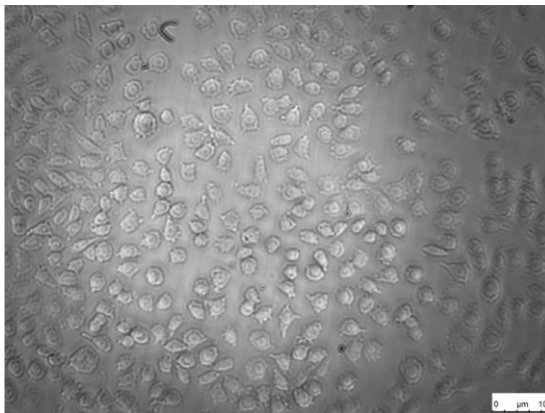
E- DMSO

Figure 4.31: Phase contrast microscopy images showing cell morphology after cytotoxicity study.

With these images it is not the number of cells that is critical but the shape. Elongated, elliptical cells are typical of cells that are attempting to spread and divide into their surroundings. This only occurs when cells are tolerant to the environment in which they are located. In comparison, round and more clearly defined cells are more likely observed in cytotoxic environments (Theriault et al., 2012). The images generated from cytotoxicity wells using the centrifugal spun fibres demonstrated cell spreading, a sign of an acceptable environment for cell growth. In contrast, the cells shown in samples D and E, Figure 4.32, show less spreading, with a more rounded cell perimeter indicating that the cells are less tolerant of the environment. On this occasion, the positive control, DMEM did not permit cell proliferation and spreading as observed in phase contrast microscopy. However, in the subsequent assay the cells were found to be viable.

A semi-quantitative means of assessing cell growth can be done using a colourimetry assay. An increasing number of viable cells convert MTS to the dye formazan through metabolic activity. This increase in colour can be detected using spectrophotometry. The quantitative formazan absorbance measurements for the three fibres studied are shown in Figure 4.32 alongside the results from cells exposed to references DMEM and DMSO.
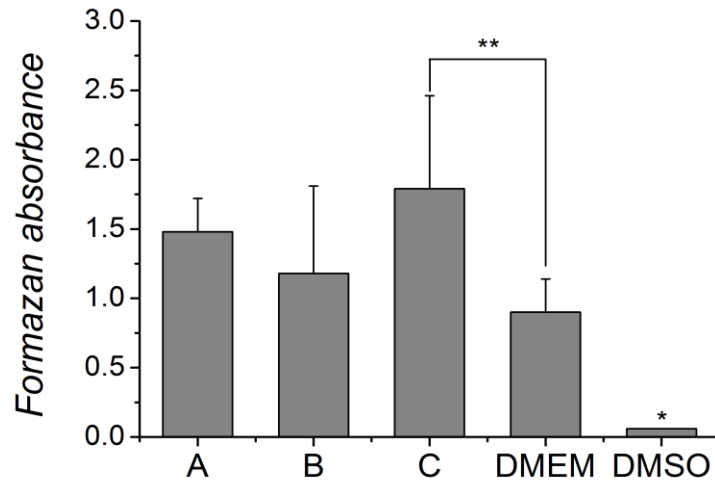
Figure 4.32: MTS cytotoxicity assessment of PCL fibres compared to DMEM and DMSO. A, B are the PCL fibres produced from 12 % chloroform/methanol and 12 % chloroform using centrifugal spinning respectively, and C are the 12 % PCL+ 0.5 % CNT fibres produced from chloroform.

Figure 4.32 indicates that the PCL fibres induced a less toxic cellular response in the mouse fibroblast cells. There was no significant change in toxicity when using either chloroform or chloroform/methanol as a solvent. Sample C in Figure 4.32 is the PCL-CNT composite fibre (discussed further in Chapter 6) and there was no significant change in toxicity with the addition of carbon nanotubes. The fibres and the DMEM were all significantly more tolerant compared to DMSO. DMSO is a cytotoxic compound and is seen as a negative control whereas DMEM is a cell culture medium and is seen as a positive control (Da Violante et al., 2002). There were no significant differences between the fibres and only the PCL-CNT fibres showed a significant improvement in cell viability over the reference culture medium, DMEM. The demonstrated tolerance in vitro means that PCL fibres spun from both chloroform and chloroform/methanol could be applied as an external cellular scaffold for wounds or for in vivo applications.

4.5 **Conclusions**

The experimental section of this chapter demonstrated that solutions of PCL can be spun into fibres using needleless electrospinning and solution centrifugal spinning. PCL fibres were spun from both chloroform and 4:1 chloroform/methanol solvents at varying concentrations depending on the processing technique used. Electrospinning was possible at a significantly lower concentration range compared to centrifugal spinning. Combining in the viscosity results and it was observed that the electrospinning of PCL only occurred when the solution was in the entangled regime up until the 11 % w/v mark; whereas, centrifugal spun fibres are ideally produced at higher concentrations (c > ~11 %), most likely the concentrated entangled regime. In both production systems the fibre diameters observed was linked to the initial solution concentration and for centrifugal spinning an increase in PCL concentration increased the fibre diameter. However, the overarching principles are the same for both techniques as incorrect solution rheology resulted in beading when the viscosity was too low or excessive large diameter fibres when the viscosity was too high. The finest fibres were produced using the electrospinning technique, with a mean fibre diameter of 470 nm recorded compared to a mean fibre diameter observed as fine as 1040 nm for centrifugal spinning.

By changing the solvent the spinning conditions and fibre morphology was significantly varied for both electrospun and centrifugal spun PCL fibres. Film formation was visibly reduced when electrospinning from chloroform/methanol. When spinning fibres from chloroform resulted in some pore formation being observed but this was limited to larger diameter fibres and shot. However, with the addition of a non-solvent such as methanol this pore formation can be exaggerated and a high level of surface pores can be introduced

due the fibres due to differences in solvent evaporation properties. This texture has not been previously reported in fibres produced using centrifugal spinning. Using methanol as a non-solvent also reduced the diameters of the fibres with both centrifugal spinning and electrospinning.

This chapter also noted differences in web construction which could impact on utilisation; centrifugal webs had much greater loft than the electrospun webs and the latter formed as densely packed webs laid on to a flat substrate whereas centrifugal spun webs are self-supporting cylinder with no substrate. There were also differences in the web morphology as revealed by SEM analysis; the electrospun webs also showed higher levels of film formation which was not seen in the centrifugal spun webs which was caused by residual solvent remaining in the jet.

This research has also shown that fibre production can be adapted from one system to another with some adjustments to solution properties. As a result it is possible that a broad selection of polymers currently being spun using electrospinning could be transferred to centrifugal spinning.

The fine structure was analysed using DSC and XRD and the results indicated that the crystal structure was entirely typical of solution processed PCL. There were no notable differences in the fibre fine structure between the fibrous PCL produced using either technique. The results correlate with reports elsewhere detailing the fine structure of electrospun and film cast PCL.

The extract cytotoxicity study of the PCL fibres showed that the fibres produced by centrifugal spinning from chloroform and chloroform/methanol solvents. The results of this experiment indicates that centrifugal spun fibres formed using these solvents could be applied to cell growth scaffolds and other medical devices where cell compatibility is required. The versatility of centrifugal spinning allows for production of fibres from a range of solvents. Research presented here demonstrates that the solvent can be varied to what is found in found in the literature and non-solvent can be added to achieve novel textural effects on the fibre surface. The potential for using a biologically acceptable solvent in the future would allow the inclusion of potentially sensitive additive such as proteins and drug compounds.

4.6 **References**

AGARWAL, S., WENDORFF, J. H. & GREINER, A., 2008. Use of electrospinning technique for biomedical applications. *Polymer,* 49**,** 5603-5621.

AMALORPAVA MARY, L., SENTHILRAM, T., SUGANYA, S., NAGARAJAN, L., VENUGOPAL, J., RAMAKRISHNA, S. & DEV, V., 2013. Centrifugal spun ultrafine fibrous web as a potential drug delivery vehicle. *Express Polymer Letters,* 7**,** 238-248.

BADROSSAMAY, M. R., BALACHANDRAN, K., CAPULLI, A. K., GOLECKI, H. M., AGARWAL, A., GOSS, J. A., KIM, H., SHIN, K. & PARKER, K. K., 2014. Engineering hybrid polymer-protein super-aligned nanofibers via rotary jet spinning. *Biomaterials,* 35**,** 3188-3197.

BOGNITZKI, M., CZADO, W., FRESE, T., SCHAPER, A., HELLWIG, M., STEINHART, M., GREINER, A. & WENDORFF, J. H., 2001. Nanostructured fibers via electrospinning. *Advanced Materials,* 13**,** 70-72.

CIPITRIA, A., SKELTON, A., DARGAVILLE, T. R., DALTON, P. D. & HUTMACHER, D. W., 2011. Design, fabrication and characterization of PCL electrospun scaffolds-a review. *Journal of Materials Chemistry,* 21**,** 9419-9453.

CHOI, J. S., LEE, S. J., CHRIST, G. J., ATALA, A. & YOO, J. J., 2008. The influence of electrospun aligned poly(caprolactone)/collagen nanofibre meshes on the formation of self-aligned skeletal muscle myotubes. *Biomaterials*, 29, 2899-2906.

DARWIS, D., NISHIMURA, K., MITOMO, H. & YOSHII, F., 1999. Improvements to processability of poly(e-caprolactone) by radiation techniques. *Journal of Applied Polymer Science,* 74, 1815-1820.

DA VIOLANTE, G., ZERROUK, N., RICHARD, I., PROVOT, G., EACUTE, RARD, CHAUMEIL, J. C. & ARNAUD, P., 2002. Evaluation of the cytotoxicity effect of dimethyl sulfoxide (DMSO) on Caco2/TC7 colon tumor cell cultures. *Biological and Pharmaceutical Bulletin*, 25, 1600-1603.

DEITZEL, J. M., KLEINMEYER, J., HARRIS, D. & BECK TAN, N. C., 2001. The effect of processing variables on the morphology of electrospun nanofibers and textiles. *Polymer,* 42**,** 261-272.

DHANALAKSHMI, M., LELE, A. K. JOG, J. P., 2015. Electrospinning of nylon 11: effect of processing parameters on morphology and microstructure. *Materials Today Communications*, in press.

FONG, H., CHUN, I. & RENEKER, D. H., 1999. Beaded nanofibers formed during electrospinning. *Polymer,* 40**,** 4585-4592.

GENG, X., KWON, O.-H. & JANG, J., 2005. Electrospinning of chitosan dissolved in concentrated acetic acid solution. *Biomaterials,* 26**,** 5427-5432.

GLUCK, J. M., 2007. *Electrospung nanofibrous poly(e-caprolactone) (PCL) scaffolds for liver tissue engineering.* Master of Science Thesis, North Carolina State University, Rayleigh, United States.

GUPTA, P., ELKINS, C., LONG, T. E., WILKES, G. L., 2005. Electrospinning of linear homopolymers of poly(methyl methacrylate): exploring relationships between fiber formation, viscosity, molecular weight and concentration in a good solvent. *Polymer,* 46, 4799-4810.

HARTMAN, O., ZHANG, C., ADAMS, E., FARACH-CARSON, M. C., PETRELLI, N. J., CHASE, B. & RABOLT, J. F., 2010. Biofunctionalization of electrospun PCL-based scaffolds with perlecan domain IV peptide to create a 3-D pharmacokinetic cancel model. *Biomaterials,* 31, 5700-5718.

KRISHNAPPA, R. V. N., DESAI, K. & SUNG, C., 2003. Morphological study of electrospun polycarbonates as a function of the solvent and processing voltage. *Journal of Materials Science*, 38, 2357-2365.

LAINE, K., 2013. *Rotational melt spinning as a manufacturing method for tissue engineering scaffolds.* Master of Science Thesis, Tampere University of Technology, Finland.

LI, X., LIU, H., WANG, J. & LI, C., 2012. Preparation and characterization of poly(ε-caprolactone) nonwoven mats via melt electrospinning. *Polymer,* 53**,** 248-253.

LOZANO, K. & SARKAR, K., 2009. *Methods and apparatus for making superfine fibres*. United States Patent Application: 12/404,907, 14th March 2009.

LUBASOVA, D., MARTINOVA, L., MAREKOVA, D. & KOSTECKA, P., 2010. Cell growth on porous and non-porous polycaprolactone nanofibres. *Nanoco 2010,* 12th-14th October 2010, Oloumouc, CZE.

LU, Y., LI, Y., ZHANG, S., XU, G., FU, K., LEE, H. & ZHANG, X., 2013. Parameter study and characterization for polyacrylonitrile nanofibers fabricated via centrifugal spinning process. *European Polymer Journal,* 49**,** 3834-3845.

LUO, C. J., NANGREJO, M. & EDIRISINGHE, M., 2010. A novel method of selecting solvents for polymer electrospinning. *Polymer,* 51**,** 1654-1662.

MA, Z., KOTAKI, M., INAI, R. & RAMAKRISHNA, S., 2005. Potential of nanofiber matrix as tissue-engineering scaffolds. *Tissue Engineering,* 11**,** 101-9.

MCEACHIN, Z. & LOZANO, K., 2012. Production and characterization of polycaprolactone nanofibers via forcespinning™ technology. *Journal of Applied Polymer Science,* 126**,** 473-479.

PANT, H. R., NEUPANE, M. P., PANT, B., PANTHI, G., OH, H-J., LEE, M. H. & KIM, H. Y., 2011. Fabrication of highly porous poly(e-caprolactone) fibres for novel

tissue scaffold via water bath spinning. Colloids and Surfaces B: Biointerfaces, 88, 587-592.

NAM, J., HUANG, Y., AGARWAL, S. & LANNUTTI, J., 2007. Materials selection and residual solvent retention in biodegradable electrospun fibers. Journal of Applied Polymer Science, 107, 1547-1554.

PANT, H. R., NEUPANE, M. P., PANT, B., PANTHI, G., OH, H-J., LEE, M. H. & KIM, H. Y., 2011. Fabrication of highly porous poly(e-caprolactone) fibres for novel tissue scaffold via water bath spinning. Colloids and Surfaces B: Biointerfaces, 88, 587-592.

PERSANO, L., CAMPOSEO, A., TEKMEN, C. & PISIGNANO, D. 2013. Industrial upscaling of electrospinning and application of polymer nanofibres: a review. *Macromolecular Materials and Engineering*, 298, 504-520

SARKAR, K., GOMEZ, C., ZAMBRANO, S., RAMIREZ, M., DE HOYOS, E., VASQUEZ, H. & LOZANO, K., 2010. Electrospinning to Forcespinning™. *Materials Today,* 13, 12-14.

SHENOY, S. L., BATES, W. D., FRISCH, H. L. & Wnek, G. E., 2005. Role of chain entanglements on fiber formation during electrospinning of polymer solutions: good solvent, non-specific polymer–polymer interaction limit. *Polymer*, 46, 3372-3384.

STATTON, W. O., 1963. An X-Ray crystallinity index method with application to poly(ethylene terephthalate. *Journal of Applied Polymer Science,* 7, 803-815.

SUGANYA, S., SENTHIL RAM, T., LAKSHMI, B. S. & GIRIDEV, V. R., 2010. Herbal drug incorporated antibacterial nanofibrous mat fabricated by electrospinning: an excellent material for wound dressings. *Journal of Applied Polymer Science,* 121, 2893-2899.

TAN, E. P. S., Ng, S. Y. & LIM, C. T., 2004. Tensile testing of a single ultrafine polymeric fiber. *Biomaterials,* 26, 1453-1456.

UEBERREITER, K. & YAMAURA, K., 1977. Dependence of surface tension and polymer concentration in surface on solvent interaction of polystyrene solutions. *Colloid and Polymer Science*, 255, 1178-1180.

VAN DER SCHUEREN, L., DE SCHOENMAKER, B., KALAOGLU, Ö. I. & DE CLERCK, K., 2011. An alternative solvent system for the steady state electrospinning of polycaprolactone. *European Polymer Journal,* 47, 1256-1263.

VENUGOPAL, J., MA, L., YONG, T. & RAMAKRISHNA, S., 2005. In vitro study of smooth muscle cells on polycaprolactone and collagen nanofibrous matrices. *Cell Biology International,* 29, 861-867.

VISTICA, D. T., SKEHAN, P., SCUDIERO, D., MONKS, A., PITTMAN, A. & BOYD, M. R., 1991. Tetrazolium based assays for cellular viability: a critical examination of selected parameters affecting formazan production. *The Journal of Cancer Research*, 51, 2515. WANG, Y., WANG, B., WANG, G., YIN, T. & YU, Q., 2009. A novel method for preparing electrospun fibers with nano-/micro-scale porous structures. *Polymer Bulletin*, 63, 259-265.

WONG, S.-C., BAJI, A. & LENG, S., 2008. Effect of fiber diameter on tensile properties of electrospun poly(e-caprolactone). *Polymer,* 49, 4713-4722.

WOODRUFF, M. A. & HUTMACHER, D. W., 2010. The return of a forgotten polymer—Polycaprolactone in the 21st century. *Progress in Polymer Science,* 35, 1217-1256.

WUTTICHAROENMONGKOL, P., SANCHAVANAKIT, N., PAVASANT, P. & SUPAPHOL, P., 2006. Preparation and characterization of novel bone scaffolds

based on electrospun polycaprolactone fibers filled with nanoparticles. *Macromolecular Bioscience, 6,* 70-77.

YANG, Q., LI, Z., HONG, Y., ZHAO, Y., QIU, S., WANG, C. & WEI, Y., 2004. Influence of solvents on the formation of ultrathin uniform poly(vinyl pyrrolidone) nanofibers with electrospinning. *Journal of Polymer Science Part B: Polymer Physics,* 42, 3721-3726.

YAWS, C. L. & RICHMOND, P. C., 2009. Chapter 21 - Surface tension—Organic compounds. *In:* YAWS, C. L. (ed.) *Thermophysical Properties of Chemicals and Hydrocarbons.* William Andrew Publishing, United States.

YOUNG, R. J. & LOVELL, P. A., 1991. *Introduction to Polymers (Second Edition).* Chapman and Hall, London.

ZANDER, N. E., 2014. Formation of melt and solution spun polycaprolactone fibers by centrifugal spinning. *Journal of Applied Polymer Science,* 132, 41269.

ZHANG, L. & HSIEH, Y.-L., 2008. Ultra-fine cellulose acetate/poly(ethylene oxide) bicomponent fibers. *Carbohydrate Polymers,* 71, 196-207.

ZENG, J., CHEN, X., XU, X., LIANG, Q., BIAN, X., YANG, L. & JING, X., 2003a. Ultrafine fibers electrospun from biodegradable polymers. *Journal of Applied Polymer Science,* 89, 1085-1092.

ZHANG, C., YUAN, X., WU, L., HAN, Y. & SHENG, J., 2005. Study on morphology of electrospun poly(vinyl alcohol) mats. *European Polymer Journal,* 41, 423-432.

ZHANG, L. & HSIEH, Y.-L., 2008. Ultra-fine cellulose acetate/poly(ethylene oxide) bicomponent fibers. *Carbohydrate Polymers,* 71, 196-207.

ZEUGOLIS, D. I., KHEW, S. T., YEW, E. S., EKAPUTRA, A. K., TONG, Y. W., YUNG, L.-Y. L., HUTMACHER, D. W., SHEPPARD, C. & RAGHUNATH, M., 2008. Electro-spinning of pure collagen nano-fibres–Just an expensive way to make gelatin? *Biomaterials,* 29, 2293-2305.

Chapter 5
Hydrophobic fibres produced via centrifugal spinning

5.1 Introduction

It is known that the production of textile products can have a significant impact on the environment (Carneiro et al., 2010). In particular, wet processing uses and 'contaminates' significant volumes of water. The treatment of dye house wastewater is thus necessary before the water effluent can be returned to the water system. Dye house wastewater is typically coloured due to the presence of residual dye that remains unfixed during the dyeing process. Colour in particular is undesirable in the public water system and even very low concentrations of colorant remain visible and therefore dye molecules must be removed or reduced in concentration even if non-toxic (Mishra and Tripathy, 1993; Christie, 2001). Most national environmental authorities have low tolerance limits to the colour and opacity of water released into lakes and rivers; thus there is a requirement of industry to eliminate or limit the release of colour into municipal water systems. Post-processing, the water must therefore be cleared of coloured agents (dyes) either by removing the molecules or by destroying them. Currently, the treatment of textile effluent is made more complex by the large range of dye types used in the industry. Dyes vary significantly in structure depending on the substrate multiple treatment processes are needed to deal with the entire range of dyes. In addition to dyes, the textile effluent stream may contain organic and inorganic substances both soluble and insoluble. These could be sizing agents, dispersants or salts added to aid the finishing procedure. These additives also require treatment before textile effluent is safe to re-enter the water supply.

There is a wide variety of physical, chemical and biological treatment methods that can be applied depending on the class of dye within the waste effluent. An overview of these techniques is presented in Figure 5.1.
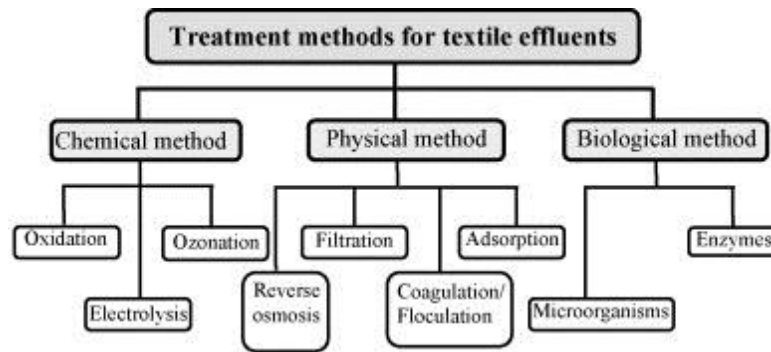
Figure 5.1: Diagram illustrating the principal dye effluent treatment methods (Saratale et al., 2011)

Dye effluent treatment techniques fall into two processing streams: destruction of the dye through chemical or biological breakdown or separation using a physical treatment system. In chemical and biological treatment the dye effluent rests in a treatment tank where the chromophore is broken down by enzymes and microorganisms in a biological system or by UV radiation, reactions with ozone or electrolysis. These methods can have an excellent colour removal efficiency rate but may require accurate and expensive control of tank conditions to permit breakdown and prevent enzyme denaturing (Anjaneyulu et al., 2005). Biological purification requires an oxygenated aeration pond operating at a precise optimal temperature and pH. An additional concern is that although the chromophore is broken and the colour element lost, harmful aspects of the dyes such as heavy metals and degradation products can remain in the effluent.

In the physical treatment stream the dyes are instead separated out from the liquor using a range of treatment methods. Filtration and reverse osmosis separate larger particulate out from the effluent by capturing the dye particles in a fibrous filter media or on one side of a selective membrane (Hutten, 2007). Coagulation and flocculation work to cluster and agglomerate the dye molecules together which then settle to the bottom or rise to the top where they are collected as a cake (Hutten, 2007). This can create a problem in terms of the large amount of highly concentrated sludge that must then be disposed of. Adsorption is a physical capture where dye molecules are retained on a larger substrate using surface interactions. This technique is useful for capturing resilient or hard to destroy dye types.

Disperse dyes present a particular problem as they are not effectively treated by the typical chemical and biological processing that are often applied to ionic dye classes (Carneiro et al., 2010). Disperse dyes are used primarily to colour polyester fabrics but are used on other synthetic polymers such as nylon and cellulose acetate. Worldwide disperse dye consumption reached 570,000 tonnes annually in 2011 (Ghaly et al., 2014) and there are estimates that in some cases up to 20 % of initial dye may be lost to effluent (WRAP.ORG, 1997). Therefore, there are potentially large volumes of disperse dyes being released into the water system each year. To compound the problem disperse dyes are also difficult to break down using biological and chemical means (Ramakrishna and Viraraghavan, 1997). Disperse dyes are a synthetic dye class that are almost exclusively non-polar, hydrophobic and are only partially soluble in water. Many synthetic dyes are xenobiotic and are not easily digested by enzymes (Christie, 2001). In addition, anthraquinone based disperse dyes are resistant to degradation due to a stable fused aromatic ring structure (Hartgerink et al., 2001). This resistance to biological breakdown

has led to the bioaccumulation of some disperse dyes. Finding an effective way to remove disperse dyes from water is therefore important to the textile industry.

The effectiveness of biological and chemical treatment methods for the removal of disperse dyes has been shown to be incomplete as there are reports of ineffective treatments with the treatment of azo based disperse dyes by white rot fungus removing less than 50 % of the dye after 12 days (Zhang, 2003).

5.1.1 **Adsorption**

A common approach to molecular separation of contaminants from water is to bind the target molecules to a solid material which can then be easily separated from the effluent. This process is known as adsorption and involves the capture of an adsorbate on to the surface of an adsorbent material. The particles are retained on the adsorbent surface through a combination of covalent, ionic, polar/hydrophobic or van der Waals bonding forces (Rattee and Breuer, 1974; Bottani and Tascon, 2008). As adsorption is a surface interaction it is desirable to have materials with high surface areas to capture more adsorbate on a per weight basis (Yagub et al., 2014).
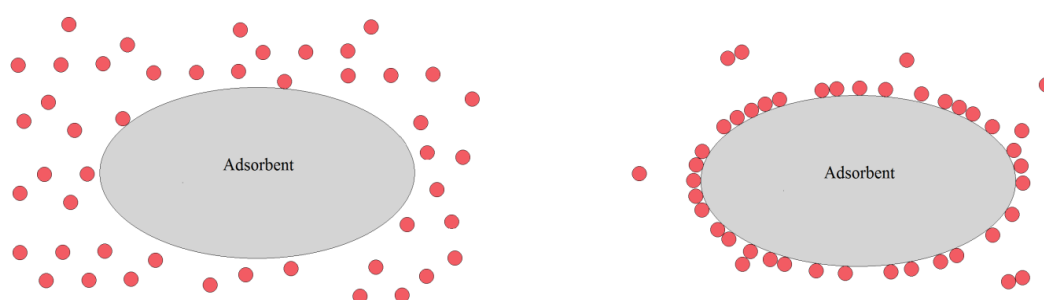
Figure 5.2: Diagram illustrating the fundamental principle of dye adsorption.

The efficiency of the adsorption process is influenced by, the adsorbate concentration, the level of adsorbate to adsorbent interaction, the affinity for the adsorbate towards the liquor,

the total surface area of the adsorbent available, the particle size and level of adsorbate agglomeration of the adsorbent and the ambient conditions in the system. The temperature and pH can significantly change the level of adsorption for all dye classes but the latter particularly determines the efficiency of ionic and cationic dye capture (Mezohegyi et al., 2012). The level of adsorption will also depend on the contact time. Fast acting adsorption systems can reach equilibrium in a few minutes whilst others can take several days (Crini, 2006).

Current adsorbents include activated carbon, peat and fly ash together with other naturally derived adsorbents such as rice hulls and maize cob although most have disadvantages associated with effectiveness, cost and disposal concerns (Robinson et al., 2001; Allen et al., 2004).

Adsorption onto activated carbon has been proven to be an effective and versatile technique for the removal of ionic dyes but there is less literature available which assesses removal rates of disperse dyes from aqueous solution (Shen et al., 2009; Faria et al., 2004). In their review, Yagub et al. (2014) indicated that activated carbon lacks the selectivity to capture insoluble and low solubility dye molecules.

A review of the published research into disperse dye removal also highlighted the variability in the apparent performance of activated carbon (Yue et al., 2007). Ramakrishna found that 5 g L^{-1} of granular activated carbon only removed 48 % of 50 mg L^{-1} C. I. Disperse Red 1 after 24 hours (Ramakrishna and Viraraghavan, 1997). While Wang reported that removal of C. I. Disperse Red 167 using activated carbon generated from waste bamboo culms at a dye concentration of 30.0 mg L^{-1} and a 5 g L^{-1} adsorbent

loading removed only 52 % under optimum acidic conditions after 26 hours (Wang, 2012). In the same work a commercial carbon product, Filtersorb, (Calgon Carbon, PA, USA) was reported to remove only ~66 % of the same dye under identical conditions. Other researchers have found that a pH of 7 is the optimum for adsorption of disperse dyes and that poor adsorption occurred when materials are ionised, so strong acid and strong alkali should be avoided (Gerçel et al., 2008). In addition it is a relatively expensive process (Pollard et al., 1992) due to the cost of producing activated carbon, the lack of suitable and inexpensive regeneration procedures for these adsorbents and reuse results in a steep reduction in performance and a 10 - 15 % loss of sorbent (Robinson et al., 2001). The level of adsorption is affected by temperature, contact time, concentrations of adsorbate and adsorbent, the level of interaction between the adsorbate and adsorbent and the presence of other dyes and additives in addition to the pH (Anjaneyulu et al., 2005, Shen et al., 2009).

5.1.2 **Dye adsorption theory**

Any adsorption system can be quantified in terms of the rate of adsorption and the equilibrium point between the liquid and solid phases. This quantification is done by linking the empirical results to a theoretical model. These models have strict criteria depending on how molecules are proposed to collect on to the surface of the adsorbent. In order to fully understand the adsorption mechanism between the dye molecules and the adsorbent it is important to establish the most appropriate correlation for the equilibrium curves. These curves are obtained empirically by measuring the adsorption isotherm of a disperse dye onto a substrate. The adsorption of disperse dyes is thought to assume a monolayer (Gercel et al., 2008). There are a range of adsorption models such as the Nernst, BET and Crombie-Quilty but the two most established and widely used

functions for describing monolayer adsorption, particularly in disperse dye-adsorbent systems are the Langmuir and Freundlich equations.

This work is concerned with the adsorption of disperse dyes on to the surface of a fibre for potential capture and recovery. The adsorption mechanism in this case differs to the disperse dyeing of poly(ethylene terephthalate) (PET) by disperse dyes where the PET is said to essentially dissolve the disperse dye in the solid 'solution' of the fibre (Yang et al., 2001) in which case alternative models such as Nernst apply (Giles, 1971). For the monolayer capture of molecules on the surface the literature suggested that the removal of disperse dyes from effluent has previously been modelled using the Langmuir model (McKay, 1982; Gercel et al., 2008). There are only limited reports of the Freundlich isotherm being an accurate model for disperse dye adsorption (Ramakrishna and Viraraghavan, 1997).

The Langmuir model assumes that there is a finite number of 'active sites' onto which adsorption can occur. For reactive dyeing, these sites can be related the number of functional groups at the surface of the polymer; for disperse dyeing, onto hydrophobic materials these 'active sites' may be regions where hydrophobic bonds are most likely to occur (Shamey, 2009; Peters, 1963) The Langmuir isothermal model has been demonstrated to apply to disperse dye adsorption on to activated carbon and biomass (McKay, 1982; Gercel et al., 2008). This section will test whether the Langmuir isothermal model applies to the adsorption on a disperse dye on to PVP/TA fibre produced in this section.

5.1.2.1 **Langmuir model**

The Langmuir isotherm model describes adsorption taking place onto a limited number of energetically equivalent homogenous sites (Chung et al., 2015). The Langmuir model assumes that the attractive intermolecular forces decrease with distance and predicts the existence of monolayer coverage of the adsorbate on the outer surface of the fibres. A further assumption is that once a molecule occupies a site, no further adsorption can occur there; thus a sorbent has a finite capacity and a saturation value can be reached. At a high enough dye concentration all sites will become occupied and the material surface is saturated, resulting in a plateau. The Langmuir equation is as follows, Equation 5.1:

$$Qe = \frac{C_e K_L Q_0}{1 + C_e K_L}$$
Equation 5.1

Where Q_0 is the maximum capacity of the adsorbent, K_L is the isotherm constant and Qe and C_e are the adsorbate capture mass and the solution concentration respectively when the system is at equilibrium. Qe is the mass of dye on the fibre and is calculated using Equation 5.2:

$$Qe = (C_0 - C_e)\frac{V_l}{m_f}$$
Equation 5.2

Where C_0 is the starting concentration, V_l is the liquor volume and m_f is the mass of the adsorbent, in this case, fibres. Calculation of K_L and Q_0 from collected data allows for the Langmuir model to be plot alongside in order to test for fit. The values for K_L and Q_0 can be found through linearisation of Equation 5.1 as shown in Equation 5.3:

$$Qe = \frac{C_e K_L Q_0}{1 + C_e K_L}$$

Becomes:
$$\frac{1}{Qe} = \frac{1}{\frac{C_e K_L Q_0}{1 + C_e K_L}}$$

Linearised:
$$\frac{1}{Qe} = \frac{1}{Q_0} + \frac{1}{Q_0 K_L C_e}$$
Equation 5.3

Equation 5.3 is in the form of $y = mx + c$ where the intercept is $\frac{1}{Q_0}$ and the gradient is given by $\frac{1}{Q_0 K_L}$ when a graph of $\frac{1}{Qe}$ is plotted against $\frac{1}{C_e}$. Thus, Q_0 is found by taking the reciprocal of the intercept when the values of $\frac{1}{Qe}$ are plotted against $\frac{1}{C_e}$ and K_L is found by multiplying the gradient of the straight line by the now established value for Q_0 and taking the reciprocal.

5.1.3 Polyvinylpyrrolidone with 1-triacontane

This chapter demonstrates the production of fibres from polyvinylpyrrolidone and 1-triacontane (PVP/TA) using centrifugal spinning and the possible use of these fibres as an adsorbent material for disperse dyes. PVP/TA is a copolymer combination of two separate polymers, polyvinylpyrrolidone and triacontane, which are formed together through a grafting process. The two constituent polymers are both significantly different in characteristics compared to the PVP/TA copolymer.

It the homogenous form polyvinylpyrrolidone (PVP) is a highly polar water soluble polymer which is used in a wide variety of applications due to its biological compatibility, adhesive, dispersive and film forming capabilities (Robinson, 1990). Currently PVP is

also used as a dye scavenger in print washing and domestic laundry (Boardman and Jarvis, 2000). In this application the soluble PVP will complex with unfixed reactive dyes preventing these dyes from fixing and cross staining other garments. However, due to its aqueous solubility and polarity homogenous PVP cannot be applied as either a solid state adsorbent or as a capture mechanism for disperse dyes.

Triacontene is an unsaturated C_{30} oligomer which is insoluble in water and has a melting point of around 62 °C. It reacts via the terminal double bound to become a saturated alkane. In this form the melting point rises to 65.5 °C (Dorset and Snyder, 1999). Triacontene and triacontane are hydrophobic chains with the potential for strong interactions with non-polar compounds (Liu et al., 2010, Pesek et al., 1997).

It is possible to combine PVP with triacontene to from a new structure and the alkylated polyvinylpyrrolidone is currently marketed under the brand name Ganex WP660. Alkylated polyvinylpyrrolidone polymers first patented in the 1960s by GAF chemicals (Shore, 1995). Information on the production process of PVP/TA is not documented but it is likely that polyvinylpyrrolidone/triacontane is a copolymer of vinyl pyrrolidone and 1-triacontene (Mulder, 2000). PVP/TA is waxy compound most frequently used in cosmetics and sunscreen in order to impart water resistance (Liu et al., 1999).

Though it is known to be a graft chain copolymer the exact structure is not immediately clear. At present there are two forms given for alkylated PVP copolymers, as shown in Figure 5.3. The difference between the two is whether or not part of the C30 chain contributes towards the principal polymer backbone, Figure 5.3. If this is the case the rigidity properties of the backbone would be changed significantly.
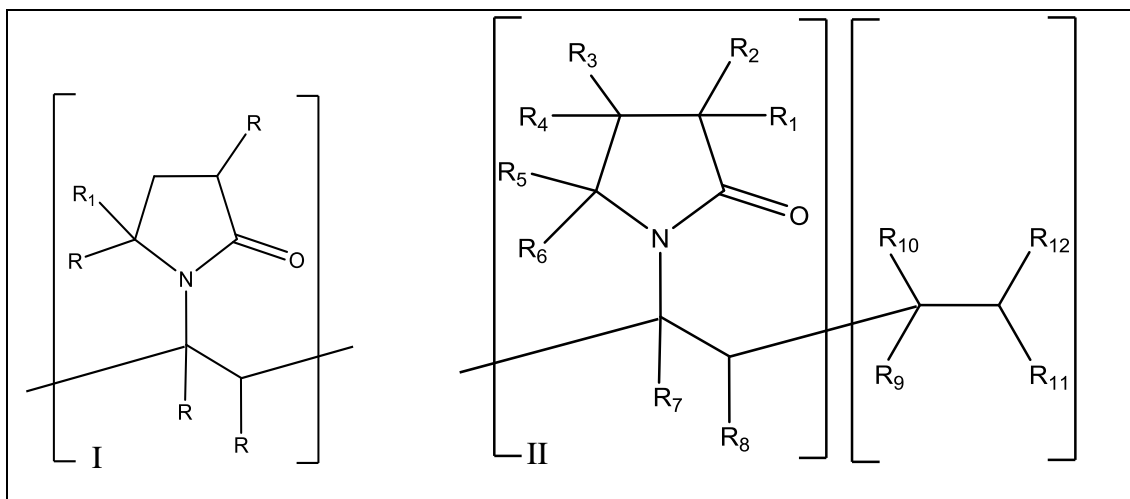
Figure 5.3: The two possible forms of PVP/TA as found in the literature. The PVP backbone-graft triacontane form I proposed by Petter et al. (1989) and Kopolow et al. (1991) and the possible PVP backbone-copolymer or graft form II proposed by Zoltowski et al. (2003).

Additionally, the graft density or pattern of the grafts is not known. The current view is that the triacontene chains radiate outwards from a central backbone of polyvinyl pyrrolidone in a branch formation with sufficient density that the ability of the linear backbone for form a random coil is hindered (Hamley, 2004). These structures are also known as brush copolymers.
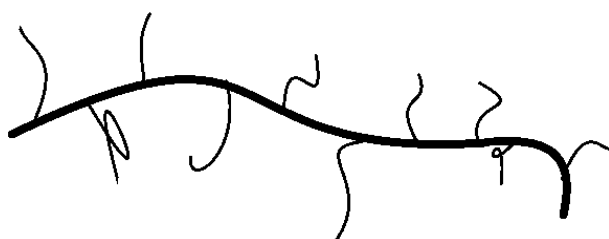
Figure 5.4: Graft copolymer model produced from description by Hamley (2004).

Due to its hydrophobicity PVP/TA is insoluble in water but soluble in non-polar solvents such as toluene. The longer chain length of the alkylated unit means PVP/TA has a higher melting point and hydrophobicity than in materials with a shorter graft unit such as a PVP/eicosene ($C_{20}H_{39}$) graft. It was found by Kopolow et al. (1991) to have a hydrophilic-lipophilic balance value of 6. Materials with a value of >10 are said to be water insoluble

and hydrophobic (Kopolow et al., 1991). In addition to water insolubility, PVP/TA was shown to be strongly hydrophobic by Brugnara et al. (2004). They attribute this to the presence of strongly hydrophobic groups on the material surface. By grafting triacontene onto the PVP, a water insoluble and hydrophobic material is produced in the form of PVP/TA. This material may have potential affinity for the non-polar disperse dyes and could be used as a potential absorbent material. As adsorption is dependent on high surface area a conversion of the PVP/TA flake into ultrafine fibres is desirable and could significantly increase the amount of dye adsorbed.

A thorough literature review indicates there is a paucity of reported concerning the processing of PVP/TA fibres. In addition, typical reports in the literature indicate that when fibres are used in dye effluent clean up, it is more often in the form as a separating membrane rather than as an adsorbent medium. There has been some interest in using electrospun and melt blown webs as fine filters and separation membranes for dyes (Meng et al., 2013; Akbari et al., 2002). Work has also been conducted using nanofibrous TiO_2 webs as a photocatalyst to degrade basic dyes (Rezaee et al., 2009, Kavitha and Palanisamy, 2011). Some traditional textile fibres have been previously used in effluent treatment as typified by Khan et al. (2005) where cotton and wool were tested as an adsorbent. They observed surprisingly high values for adsorption of methylene on both cotton and wool. However, conflicting results meant that this author is reluctant to accept these findings. Currently there has been little research conducted on using ultrafine fibres as a new type of adsorbent for colour removal (Suzuki, 1991). The high surface functionality of these fibres means they are capable of "trapping" a large proportion of compatible dye molecules per unit weight.

Oil and fat based staining of textiles can be aesthetically unpleasing but may also significantly reduce the effectiveness of functional garments (Laughlin and Gold, 1990). Various additives are incorporated to garment laundry cycles to assist in the lifting and capture of oils from textile surfaces. The hydrophobicity of PVP/TA may lend it to capturing and retaining oils and fats in aqueous conditions. Fats that are released from textiles during laundering could be bound to the surface of the PVP/TA which would prevent them from re-adhering or cross staining other garments.

5.2 Summary

Activated carbon (AC) is the principal material for adsorbing a wide range of textile dyes. However, the effectiveness of AC at removing disperse dyes is not as high as for other dye classes (Yue et al., 2007). Adsorption relies on a high available surface area which could mean that ultrafine fibres make effective adsorbent materials. There is scope for a new hydrophobic, adsorbent material that could be used to selectively remove disperse dyes from waste effluent. By spinning a hydrophobic polymer into fine fibres, the material would have a high surface area that could capture disperse dyes through hydrophobic interactions. PVP/TA is a graft copolymer about which little is reported in the literature but it is known to be hydrophobic and insoluble and accordingly offers significant potential. PVP/TA could also have a high affinity for oils and fats due to the hydrophobic interactions between these materials, however, this aspect needs to be established. No

reports of producing fibres from PVP/TA have been found after an extensive literature search.

5.3 **Experimental**

This chapter discusses the formation of PVP/TA fibres using centrifugal spinning. This section also assesses the effectiveness of PVP/TA fibres as a dye adsorbent. To achieve this, the objectives for this work were as follows:

1. To assess and confirm the structure of WP660 PVP/TA using mass spectrometry;

2. To spin WP660 PVP/TA into fibres using melt centrifugal spinning and establish processing parameter/fibre property relationships;

3. To characterise the fibres produced using microscopy to determine morphology and typical fibre diameters;

4. To assess the ability of PVP/TA fibres to adsorb disperse dyes compared to a commercial form of activated carbon;

5. Compare the affinity of synthetic sebum and fats on to PVP/TA fibres and on to cotton during a domestic washing cycle using mass spectroscopy.

5.3.1 **Materials**

The polyvinylpyrrolidone with1-triacontene copolymer was supplied as a waxy brittle flake by Sigma Aldrich (UK) under the commercial name Ganex or Antaron WP660. This material can also be found under alternative names such as triacontyl PVP and is CAS registered as 2-pyrrolidinone, 1-ethenyl, polymer with 1-triacontene (Stone et al., 2002).

5.3.2 **Time-of-Flight Secondary Ion Mass Spectrometry (ToF-SIMS)**

In order to confirm the chemical structure of PVP/TA, analysis was carried out using Time-of-Flight Secondary Ion Mass Spectrometry (ToF SIMS). Secondary ion mass spectrometry is the measuring of the mass of ionised particles that are emitted from a surface after it has been bombarded with energetic primary particles (Vickerman, 2009). The time for ionised particles to travel through an electric field and reach a detector is directly linked to the mass to ionisation ratio (m/z). Mass spectrometry is a powerful technique that measures the specific mass of a molecule which allows for the molecular weight of hydrocarbons to be distinguished. ToF-SIMS is a static, semi-quantitative mode of mass spectrometry which allows for detection of different ionised molecules sequentially and does not need to scan through and detect specific molecular weights like alternative methods of mass spectroscopy, offering higher sensitivity for a given exposure time (Vickerman, 2009). This ability to identify components was essential when establishing which components of the staining agents had affinity for the PVP/TA. Unless otherwise stated, samples were mounted on a stage with an ionisation area of 200 μm and bombarded with Bi^{3+} for 400 seconds and spectra recorded for both positive and negative secondary ions in the range 20 to 700 m/z.

5.3.3 **Capillary rheometry**

The Malvern RH2000 capillary rheometer was used to assess the shear viscosity of Ganex WP660 across a narrow range of temperatures. A constant rate of shear test was performed using the 1 x 16 mm capillary die previously described. The apparent melt viscosity of PVP/TA was tested at varying barrel/die temperatures. Barrel temperatures of 65, 70, 75 and 80 °C were used for this study. A pre-testing heating and compression

cycle was performed prior to each extrusion. The test was then performed using increasing piston speeds at steps 50, 70, and 120 mm min^{-1}.

5.3.4 **Fibre production**

Fibre production was carried out using the Forcespinning^{TM} L1000M centrifugal spinner (Fiberio, TX, USA) operated in a configuration using a fine tri-orifice spinneret (High MFI) and a coarse tri-orifice spinneret (Low MFI) as described previously in Chapter 2. These spinnerets were chosen as they are designed to work with thermoplastic products. The collection system used in both systems was a static arrangement of posts positioned 115 mm from the spinneret circumference. Centrifugal spinning using this arrangement created a freestanding fibrous web. Successful fibre production was assessed at each speed for each spinneret. A minimum of two webs were created at each operating condition.

A preliminary DSC study of PVP/TA flake was carried out to determine the T_{onset} and T_{melt} of the material. From this study it was found that PVP/TA has a peak melting temperature of around 69 °C with a T_{onset} ~46.5 °C. The melt spinning temperature range was predicted to be above 65 °C.

To determine the temperature range that PVP/TA will melt spin a study was undertaken where the temperature was varied and the spinning speed and material loading was held constant. The in-built thermocouple was used to measure the $T_{polymer}$. The effect of polymer temperature on spinning was measured by varying the $T_{polymer}$ from 60 °C to 85 °C with selected temperature points and by spinning at 6,000 to 16,000 rpm. This was done using only the low MFI spinneret. A preliminary study revealed that a material

loading of 200 – 300 mg was required to achieve a web of sufficient quality. From observations made during early investigations a loading of 200 mg of PVP/TA was selected as the higher amount produced a web with too much loft and was not always exhausted during the specified time.

The second phase of this work was to study the effect of rotational speed. For this a series of experiments were conducted where the $T_{polymer}$ remained constant at 72 °C and the rotational speed was varied. The spinneret was then rotated at speeds ranging from 3,000 to 16,000 revolutions per minute for 45 seconds. This experiment was conducted using both the fine and coarse melt spinnerets. Multiple attempts were made to spin fibres at each rotational speed and temperature condition.

5.3.5 Fibre analysis

5.3.5.1 Scanning electron microscopy imaging

The fibre dimensions were examined using a Jeol JSM-6610LV Electron Microscope, Japan. Image analysis software, Image J, was used to assess morphology and the average fibre diameters were found using the following method. A minimum of 50 images were taken from each SEM stub, with two stubs created per sample, as each trial is conducted in duplicate this is a total of 4 stubs and 200 fibre measurements per operating condition.

5.3.5.2 Differential scanning calorimetry (DSC)

The thermal properties of polymer samples were assessed using a Perkin Elmer Jade DSC. Samples in the mass range 8 - 15 mg were weighed on a balance accurate to 0.1 mg and were prepared in non-hermetic aluminium pans which were heated from -10 °C to 250 °C at a rate of 20 °C min^{-1} with a nitrogen gas supply of 20.0 mL min^{-1}.

5.3.5.3 **X-ray diffraction**

The fine structure of PVP/TA flakes and fibres investigated using a P'AN analytical X'Pert MPD X-ray diffractometer operating at room temperature. The flake was scanned as found and the webs were pressed flat into a thin disc. The X-ray tube target was CuKα radiation (λ=1.540 Å). Scans were obtained in the theta:theta orientation scanning in the Bragg angle, 2θ, through 4° to 60° with a step size of 0.066°.

5.3.6 **Adsorption study experiment**

Adsorption isotherms for PVP/TA fibres and a commercial disperse dye were obtained using a bottle point adsorption experiment (Cooney, 1998). The fibres used were produced using the LMFI spinneret at 72 °C and rotating at 11,000 rpm. This was benchmarked against a commercial activated carbon, 1 mm granular Norit supplied by Darco, United States. The charcoal was washed repeatedly in deionised water until the water ran clear and the charcoal was then dried at 50 °C for 24 hours. The disperse dye used was Dianix Blue AC-E produced by Dystar Textilfarben (DEU) and was used without further treatment or purification. Blue AC-E is commercial product composed of a mixture of anthraquinone dyes and dispersing agents.

A series of dispersions of concentrations 25, 50, 100, 150, 200, 300 and 400 mg L^{-1} with 1 g L^{-1}, of Triton X100 wetting agent, were prepared. PVP/TA fibre and dried activated charcoal were added in 0.5 g masses to 250 ml beakers into which 100ml of each dye solution was added. The pH was adjusted to 7 using dilute hydrochloric acid and dilute sodium hydroxide in order to avoid the ionisation at acid or alkali conditions that can affect hydrophobic interactions (Gerçel et al., 2008). This was covered with laboratory

film and stirred for 3 days using a magnetic impeller. This period was selected to ensure equilibrium was reached. After this period a volume of liquid was passed through a 0.45µm syringe filter to remove the PVP/TA fibres and impurities from the activated carbon. The filtrates were mixed 50:50 with HPLC grade acetone and the λ max was measured using a JASCO UV-VIS spectrophotometer.

UV-VIS spectrophotometry is a well-established technique to observe changes in colour through an increase in absorbance in the ultraviolet and visible spectra. It was used in this chapter to assess the amount of dye removed from solution. Solutions are placed in a glass or quartz cuvette compared against a reference sample containing an identical solvent or solvents. The spectrophotometer compared the absorbencies of the two solutions across a range of wavelengths and generates an absorbance spectrum derived solely from the compound of interest, in this case, disperse dyes. The generic principle of operation is shown in Figure 5.5. UV-VIS spectroscopy is known to be versatile and resilient and empirical measurements have shown that absorbance values are not significantly affected by elements such as temperature and time effects.
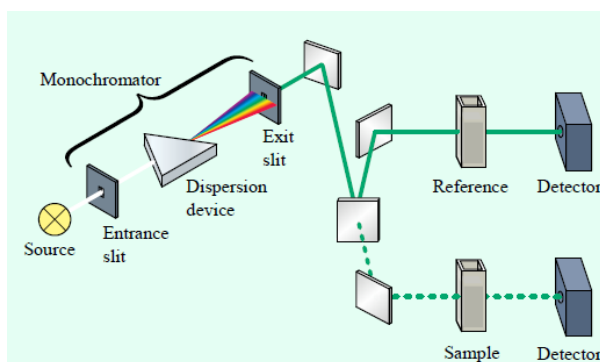
Figure 5.5: Schematic of a UV-VIS split beam spectrophotometer (Fundamentals of UV-visible spectroscopy, Agilent, 2015).

Measuring fixed concentrations of solutions allows a calibration curve to be produced which allows for the measured absorbance value of an unknown sample to be converted into concentration. The concentration calibration curve for Dianix Blue AC-E is shown in Figure 5.6 and was used to calculate the concentration in mg L^{-1} of an unknown solution can be obtained by referencing the UV-Vis absorbance to the concentration gradient.

$y = 0.00596x$
$R^2 = 0.9992$
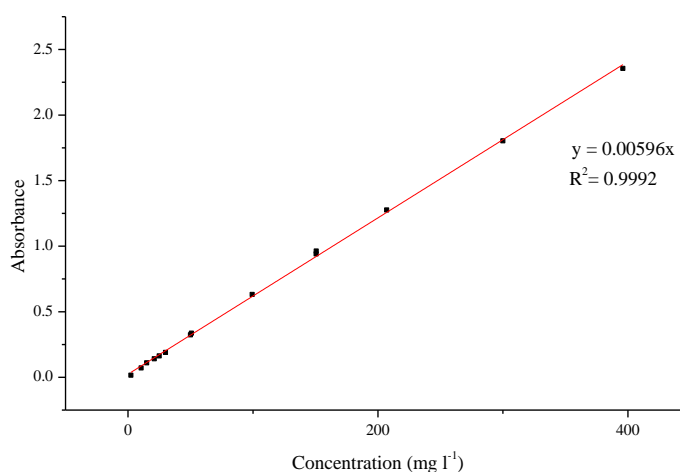
Figure 5.6: UV-Visible absorbance versus concentration calibration curve of Dianix Blue A-CE in 50:50 distilled water/acetone.

5.3.7 Soil retention

The affinity of PVP/TA fibres to oily products was assessed using a procedure to apply oily materials to the webs and assessing the level of retention of the compounds after washing with detergent. The application and washing of the fibres was done using the AATCC 130-2000 test method with modifications. Quantification and comparison of oil levels was done using Time-of-Flight Secondary Ion Mass Spectroscopy (ToF-SIMS). Two fatty products were applied to the fibres and the procedure was also conducted on a plain cotton griege fabric to allow for comparisons with a hydrophilic material that is typically found in domestic laundry.

PVP/TA fibres produced through centrifugal spinning at 11,000 rpm and 72 °C using the LMFI spinneret were used in this portion of the study. A scoured but unbleached woven cotton fabric of 220 g m^{-2} was used as a reference fabric. The two staining agents were simulated sebum oil and Mazola® branded corn oil, the specifications for both being listed in Table 5.1. The sebum oil was supplied by Unilever, UK and the corn oil was purchased locally in accordance with AATCC 130-2000. A granular reference detergent was used for the laundry cycle containing non-brightening agents and satisfied AATCC standard specifications.

Table 5.1: Composition of synthetic sebum oil and Mazola® corn oil (Bey, 2007).

Sebum oil
32.8 % beef tallow
18.0 % lanoline
18.0 % free fatty acids
12.0 % hydrocarbon mixture
11.6 % cutina
3.7 % cholesterol
3.6 % fatty acid triglycerides

Corn oil
Saturated fats
13 % Palmitic acid
2 % Stearic acid
Unsaturated Fats
52 % Linoleic acid
31 % Oleic
1 % Linolenic acid

Samples of 0.5 g of PVP/TA fibres and cotton conditioned to $21 \pm$ °C and 65 ± 2 % relative humidity were laid flat into an area roughly 50 x 50 mm. The corn oil was applied by adding 5 drops from a pipette to the centre of the fabric. The sebum oil was heated to a temperature of 32 °C and then pipetted in a similar manner. The corn oil and sebum stained samples were then placed in an environment chamber heated to 21 °C and 32 °C respectively. A glass plate and weight totalling 2.27 kg was then added to the material. The samples were left to stand under pressure for a time of 60 ± 5 seconds. For the washing procedure, two beakers containing 500 ml of distilled water and 2.5 g of reference detergent were prepared and heated to 40 °C. The stained samples were washed in each beaker sequentially under mild agitation for 5 minutes before being rinsed in 500 ml of distilled water at room temperature. The samples were removed and allowed to dry in ambient conditions.

ToF-SIMS was used to assess the presence of compounds on the fibres. Analysis was done at Intertek, United Kingdom. The test area was 200 μm and samples were bombarded with Bi^{3+} for 134 seconds and spectra recorded for both positive and negative secondary ions in the range 20 to 700 m/z. Analysis was conducted on the stained PVP/TA and cotton prior to and following washing. In addition, virgin unstained cotton, virgin PVP/TA, raw sebum oil, coil oil and the detergent were also analysed using ToF-SIMS to detect the pertinent excitation peaks. The fibrous samples were analysed as is but the corn oil was dissolved in isohexane and spun cast on aluminium foil and the sebum was spread with a spatula on to aluminium foil.

5.4 **Results and discussion**

5.4.1 **Melt rheology of PVP/TA**

The results of the capillary rheology measurements are shown in Figure 5.7. As with polypropylene the shear viscosity reduces with increasing shear rate which is typical shear thinning behaviour.
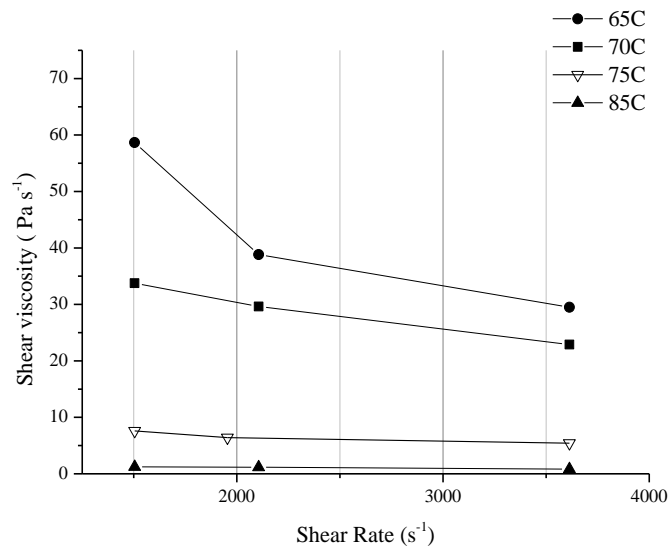
Figure 5.7: Linear plot of shear viscosity of WP660 across a range of temperatures.

The results also show that as the temperature increases from 65 °C to 75 °C the apparent viscosity of the fluid reduces significantly. A further increase to 85 °C reduced the apparent viscosity from 8.54 to 1.3 Pa S^{-1}. An attempt was made to measure the viscosity at 90 °C but the viscosity was so low that the fluid drained from the barrel without any external pressure. The melt viscosity of PVP/TA is therefore highly sensitive to temperature, at a shear rate of 1504 s^{-1} the viscosity ranged from a mean value of 59.1 Pa s^{-1} at 65 °C to as low as 1.3 Pa s^{-1} at 85 °C.

5.4.2 **Centrifugal spinning of PVP/TA fibres**

PVP/TA was successfully formed into fibrous webs using centrifugal spinning. At optimum spinning speeds the web produced appears even and uniform throughout its width. Using the Forcespinning™ technique fibres were produced using both the coarse (Low MFI) and fine (High MFI) spinnerets. However, the quantity and quality of the fibres produced was highly sensitive to the operating conditions with particular attention to temperature. The results of an experimental series, performed using the coarse spinneret, are shown in Table 5.2.

Table 5.2: Effect of temperature of fibre formation during spinning trials using the coarse spinneret

Temperature	Rotational speed (rpm)						
(°C)	6,000	8,000	10,000	12,000	14,000	15,000	16,000
62	x	x	x	x	x	x	x
65	x	x	x	x	x	x	b
68	x	o	o	o	o	✓/b	o/b
72	x	✓	✓	✓	✓	b	o/b
75	x	✓	✓	✓	✓	b	b
82	b	✓/b	✓/b	✓/b	✓/b	b	b
85	b	b	b	b	b	b	b

x-fibres were not produced
o-fibres were produced but a cohesive web was not produced
b-excessive beading
✓-cohesive web successfully produced

Table 5.2 indicates that fibres were not produced in useful quantities at 62, 65 and 68 °C at any spinning speed. This was linked to the higher melt viscosity preventing the proper formation of a polymer jet. At 72 and 75 °C fibre production reached a maximum in terms of apparent yield and web quality. At 82 and 85 °C temperature the spinning behaviour was adversely affected and spinning resulted in an excessive number of beads. This was caused by an increase in the fluidity of the melt that was observed with capillary

rheometry. At high temperatures the internal friction of the fluid is at such a low level that it does adequately retard surface tension contractions and so there is jet collapse and so beads form. This indicates that for the spinning of PVP/TA there is a narrow operating range for fibre formation that must be adhered to if the process is to be successful.

Fibres were not produced at spinning speeds at 6,000 rpm and below when using the coarse spinneret at any temperature. Spraying or escape of polymer was not observed and a large volume was found to be retained within the spinneret. At working temperatures the fluid requires sufficient rotational speed to overcome the frictional forces within the spinneret.

5.4.2.1 **Fibre morphology**

Figure 5.9 shows a range of typical SEM micrographs of fibres produced from the low MFI spinneret. The fibres produced were cylindrical and smooth with very little surface texture observed, Figure 5.8.
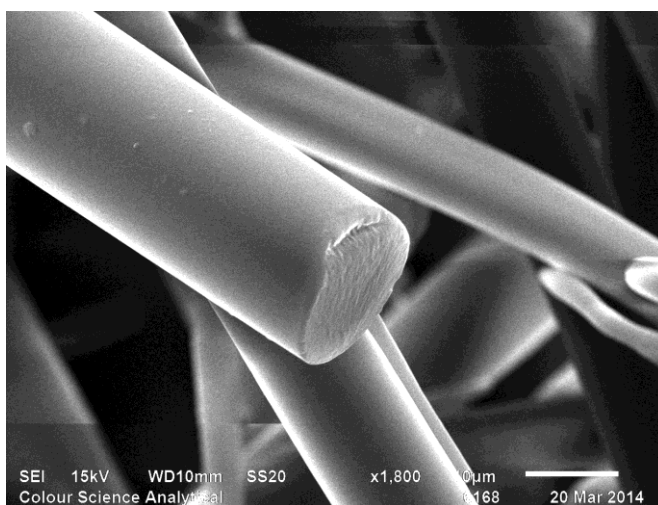
Figure 5.8: SEM micrograph showing fibre texture on PVP/TA fibre spun at 72 °C and 12,000 rpm using the coarse spinneret. An end break is shown.

This is typical of fibres that are produced through melt spinning as there is no solvent to flash off. There was no skin-core effect observed in this study unlike in the PCL fibres previously discussed in Chapter 4.

a)

b)

c)

d)
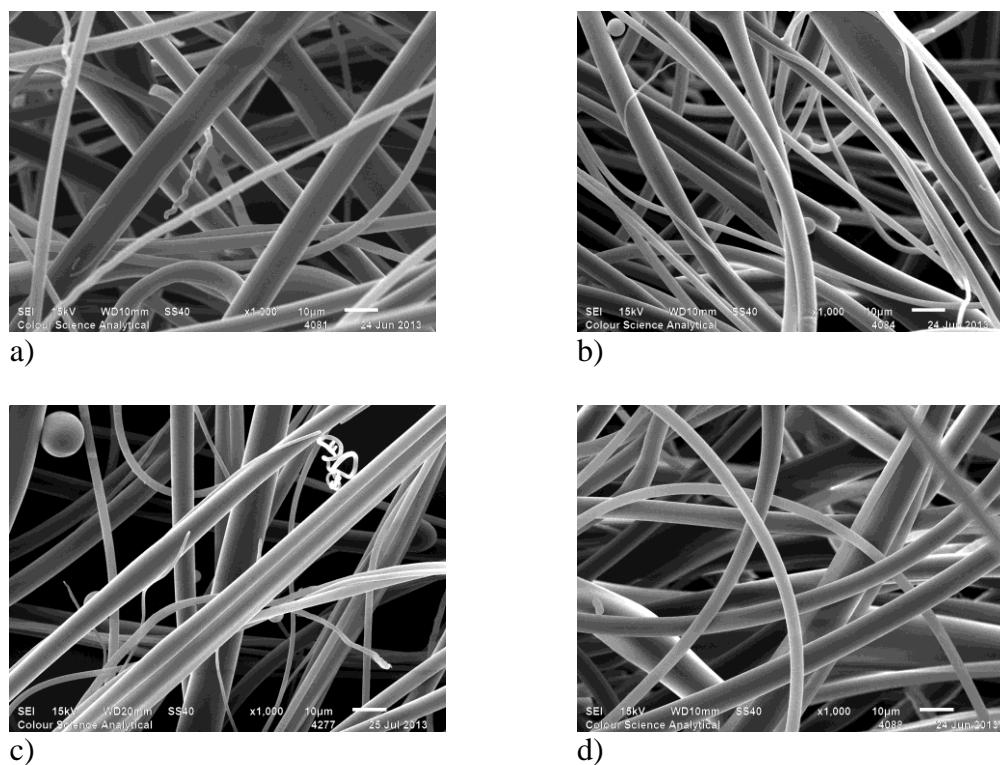
Figure 5.9: SEM micrographs of Ganex WP660 fibres produced using a low MFI spinneret at a) 8,000, b) 10,000, c) 12,000 and d) 14,000 rpm, respectively. Fibres were spun at a starting polymer temperature of 72 °C.

Figure 5.9 also shows that the fibrous webs are highly variable in diameter with very fine fibres found in the same regions as coarser fibres ~10 μm in diameter. This is similar to the broad fibre distributions observed in PP and PCL centrifugally spun webs and indicates that centrifugal spinning is inherently variable.
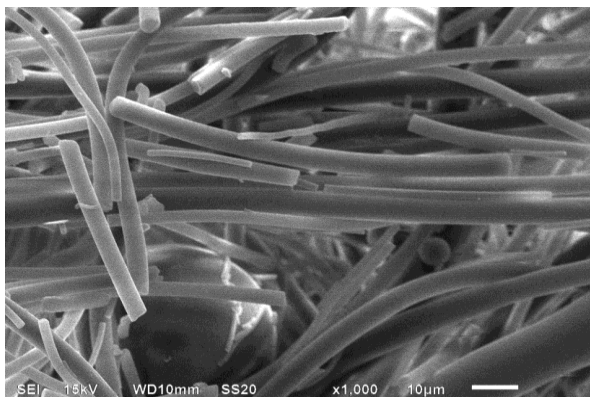
Figure 5.10: SEM micrograph of fibres in a web produced from high MFI spinneret at 15,000 rpm. The sample exhibited a large number of fibre ends with the breakages typical of a brittle fracture.

Figure 5.10 shows a unique feature that has been observed in the PVP/TA fibres and has not been observed on either polypropylene or polycaprolactone. This is the high frequency of fibre breakage, resulting in much shorter fibres Instances of filament breakage have been observed in fibrous webs produced using all the successful spinning conditions listed in Table 5.2 indicating that it is typical of the bulk material properties rather than specific processing conditions. The break points are smooth and at almost right angles to the direction of the polymer as seen in Figure 5.8 presented previously. A further example of this type of breakage is shown in Figure 5.11.
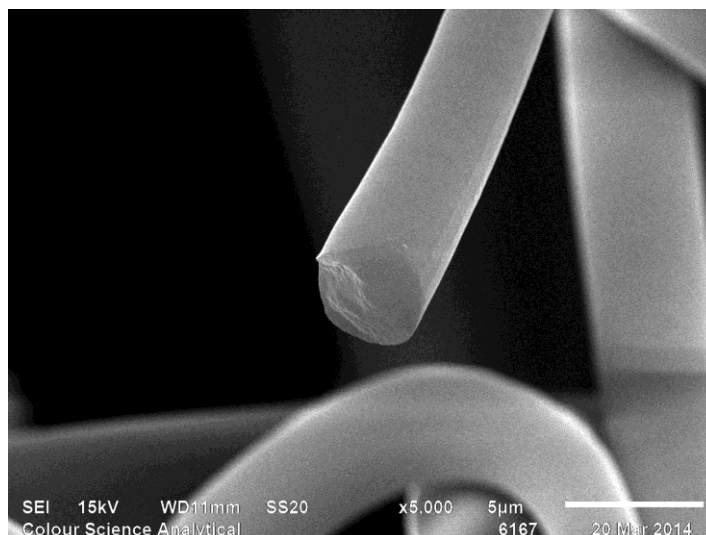
Figure 5.11: High magnification SEM micrograph showing an end breakage on PVP/TA fibre spun at 72 °C and 14,000 rpm using the coarse spinneret. Magnification 5000X.

Examination of the SEM images indicates that the type of breakage was typical of the population with no signs of fibrillation and there is a slight imperfection on one edge of the break cross section. These factors, when combined, suggest that the breaks are caused by brittle tensile fractures (Shore, 1995). In this form of fracture the material displays no plastic deformation before breaking. The fibre breaks observed in the SEM images are consistent with the fracture model given in Figure 5.12.
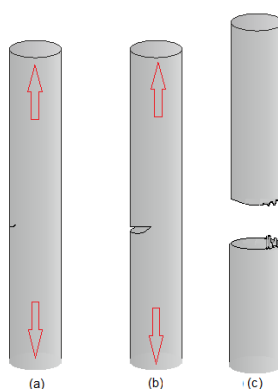
Figure 5.12: Model of a brittle fracture showing a fibre (a) with a surface flaw. When the extensional force is sufficient, the crack will propagate (b) until eventually the fibre breaks (c) leaving a characteristic clean break for most of the fibre width.

This may be either a feature created during fibre formation or through subsequent handling. SEM micrographs of undisturbed just spun fibres indicate that fibre break up does occur to some degree during web formation. This is due to the polymer jet cooling to solidify the fibre. The tension applied to the filament due to centrifugal and aerodynamic forces act to break the filament at its weakest point. The short fibres are then captured by the fibres that have already been deposited. An SEM stub prepared directly from the as spun web indicated that breaks are formed during the fibre spinning process. Further investigation revealed that fibre breakage also occurs during subsequent handling and prolonged periods of fibre handling leads to a high level of fibre breakage. This is a spinning behaviour not described previously in any of the literature pertaining to centrifugal spinning and is thought to be related to the properties of this polymer. In PVP/TA fibres this is due to a lack of elasticity due to poor chain entanglement and weak lateral forces between the relatively short polymers.

Attempts were made to test individual fibre strength of the PVP/TA fibres and of PVP/TA extrusions but the very low strength of these products made them very difficult to handle and mount.

5.4.2.2 Fibre diameters

The average fibre diameters were calculated from the full set of SEM images produced at each condition. Descriptive statistics are shown in Table 5.3 and are formed into a graph in Figure 5.13.

Table 5.3: Average fibre diameters for PVP/TA fibres made through centrifugal spinning from 7,000-16,000 rpm using two different spinnerets and 72 °C.

Spinneret	Diameter (µm)	Rotational speed (rpm)									
		7000	8000	9000	10000	11000	12000	13000	14000	15000	16000
Low MFI	Mean	7.88	5.02	5.38	4.23	4.01	3.43	2.81	2.33	x	x
	SD	6.16	3.12	4.31	3.04	3.00	2.20	1.69	1.47	x	x
High MFI	Mean	x	x	x	x	x	1.83	1.43	1.52	1.46	b
	SD	x	x	x	x	x	1.66	1.02	1.20	0.87	b

An x indicates that no fibres were produced
A b indicates that excessive beading/spraying occurred

When using the fine met spinneret fibres would not below 12,000 rpm at a polymer temperature of 72 °C. This is due to the capillary forces of the fine spinneret not being exceeded by the inertial forces forcing polymer out of the spinneret. Accordingly, it is difficult to compare the fibres produced from both spinnerets at low speeds. However, there was some overlap in conditions which allowed comparisons to be made between the coarse and fine spinneret. Single factor ANOVA revealed that the fibres produced using the high MFI spinnerets were significantly finer than fibres produced using the low MFI spinneret. This was true at 12,000 (($p < 0.05$, F (77.5) > Fcrit (3.9)); 13,000 ($p < 0.05$, F (32.2) > Fcrit (3.9)) and 14,000 ($p < 0.05$, F (4.3) > Fcrit (3.9)) rpm which covered all the spinning conditions where there was parameter overlap.
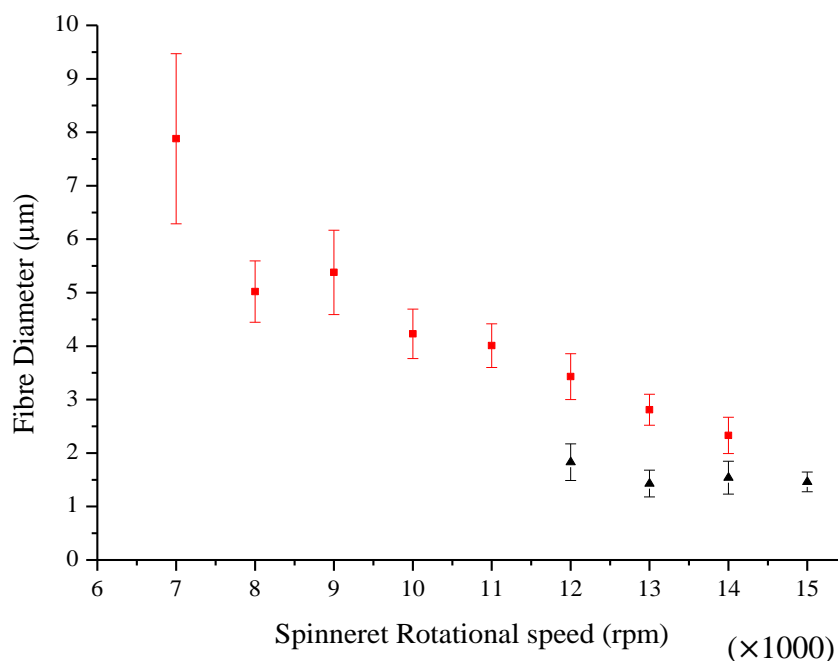
Figure 5.13: The relationship between rotational speed and mean diameter, with 95 % confidence interval show for centrifugal spun PVP/triacontene copolymer fibres for two spinneret types: low MFI (■) and high MFI (▲).

For fibres produced from the low MFI spinneret there is a clear relationship between rotational speed and average fibre diameter. As the rotational speed was increased the average fibre diameter reduced. This relationship does not continue indefinitely, at speeds 15,000 rpm upwards the level of beading became significant and web quality reduced significantly. This increase in fibre fineness with spinning speed is more evident than with the spinning of polypropylene (Chapter 3). The polymer-spinneret combination used here allows for fibre formation at speeds as low as 7,000 rpm. This spinning speed imparts a much lower extensional force resulting in fibres significantly larger than the fibres spun at higher rotational speeds.

However, the relationship between spinning speed and fibre diameter was less evident using the finer spinneret. With this spinneret a high spinning speed in excess of 12,000

rpm is required to initiate fluid flow through the capillary. At these spinning speeds it was proposed that further speed increases are less significant and that the forces acting on the fluid jet are at a near maximum.

5.4.3 **Molecular structure**

Time-of-Flight Secondary Ion Mass Spectrometry was performed on both the fibre and the raw flake to investigate the polymer structure and determine if there is any change in this structure through melt processing. The positive and negative spectra for the WP660 flake and fibres are presented in Appendix A-1 to A-4. A table detailing the key peaks identified from the resulting spectra are shown in Table 5.4.

The PVP/TA flake has peaks at 41^+ m/z and 69^+ m/z which are generated by species $C_3H_5^+$ and $C_4H_5O^+$ species, respectively, which are ions of the fragmented pyrrolidone ring. A negative ion species was found at 84^- m/z which corresponds to $C_4H_4NO^-$. Larger pyrrolidone based species are found at 112^+ m/z which equate to CH_2-CH-ring$^+$ elements. The 207^+ m/z peak from and CH_2-CH-C(ring)-CH-CH-ring$^+$ indicates that two pyrrolidone ring units are found next to each other within the PVP/TA polymer chain. A dissociated C30 chain would generate a negative ion at 421^- m/z. This peak is evident in the spectra of both the flake and fibre. It can be said that that the hydrocarbon can be cleaved away from the parent structure and remain wholly intact. This follows as a bond on a tertiary carbon is more likely to rupture than those in the secondary carbon chain.

The next significant peak set is in the positive ion spectrum at 494^+ m/z and subsequently at 28 m/z intervals: 522^+ m/z; 550^+ m/z; 578^+ m/z and 606^+ m/z. The 494^+ ion observed was larger than the cleaved hydrocarbon chain so this peak represents a C30 chain and

pyrrolidone ring fragment. The subsequent periodicity in $28^{\pm}$ m/z intervals is due to additions of $-CH_2-CH_2-$ from the polyvinylpyrrolidone backbone.

The spectrum for PVP/TA fibres were largely identical to those observed for the PVP/TA flake except for a slightly lower overall intensity. It can therefore be argued that no significant chemical change occurs during fibre formation. The structure for WP660 that ToF-SIMS supports is that put forward by Petter (1989) and others where the compound is constructed with a PVP backbone that has been modified by the long chain C30 alkane chains. In this study the ToF SIMS spectral data only supports chain addition directly onto the pyrrolidone ring.

In the proposed structures given previously in Figure 5.3 it is only possible for the WP660 to be a graft structure. It was thought possible that a block copolymerisation would allow for the polymer to have local regions of hydrophobic and hydrophilic properties within its length. In the new structure the alkane chains are thought to be entirely along the length of the polymer backbone, completely masking the PVP chemistry and making the material entirely hydrophobic.

Comparison of the ToF SIMS spectra produced for the PVP/TA flake and PVP/TA fibre show little deviation in peak location and relative intensities. The close matching of the flake spectra to the centrifugal spun fibres suggests that there is no dissociation of polymer chains during the melting process and that the PVP/TA structure remains intact.

Table 5.4: List of key fragments identified in PVP/TA flake in the positive and negative ion spectral mode.

m/z	Fragment structure	Ion assignment	Intensity, cps
41+		$C_3H_5^+$	1.2×10^6
69+		$C_4H_5O^+$	1.2×10^6
84-		$C_4H_6NO^-$	9×10^5
98+		$C_5H_8NO^+$	4×10^5
112+		$C_6H_{10}NO^+$	8×10^4
207+		$C_{10}H_{15}N_2O_2^+$	5×10^3
421-		$C_{30}H_{60}-$	5×10^3
494+		$C_{33}H_{66}NO^+$	8×10^3

5.4.4 **Differential scanning calorimetry**

Whilst the ToF-SIMS results observed no notable change in the surface polymer structure during spinning it is possible that there is a change in the bulk crystallinity and internal organisation during processing. The internal fine structure of PVP/TA fibre was investigated by analysing the thermal and diffracting properties of the material. This section will discuss the DSC measurements taken from the PVP/TA flake and the centrifugal spun fibres.
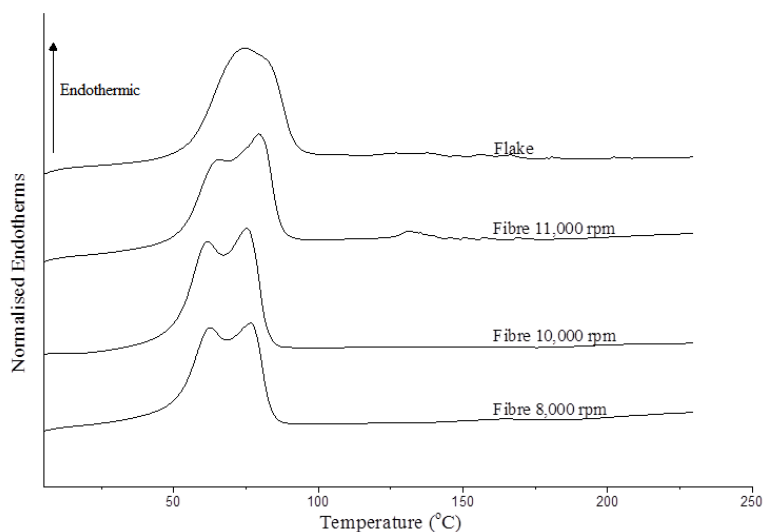
Figure 5.14: DSC thermograms of PVP/TA flake and fibres spun at low rotational speeds using the coarse spinneret.
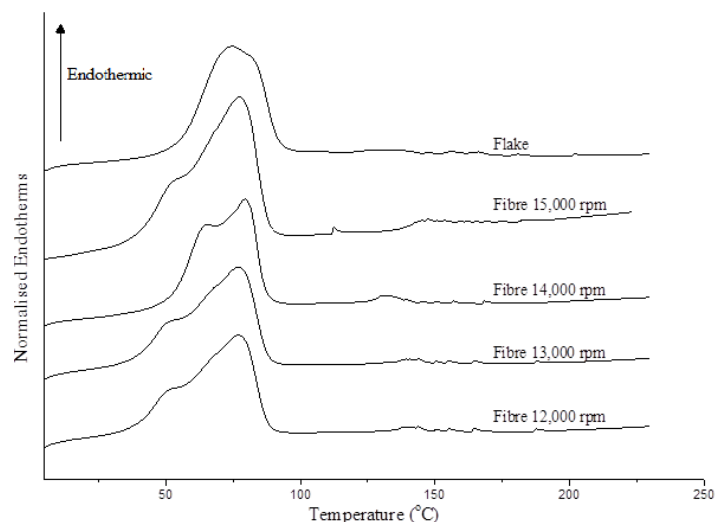
Figure 5.15: DSC thermograms of PVP/TA flake and fibres spun at high rotational speeds using the fine spinneret.

The DSC traces presented in Figure 5.14 and Figure 5.15 show that the flake has a broad melting endotherm with T_{onset} at 55 °C and a T_{melt} at 72 °C. The trace is unremarkable and is typical of the melting endotherm of a solid made up of one crystal configuration. The DSC thermograms of the PVP/TA fibres present a significantly different shape and associated thermal behaviour. The endotherm has a double peak which is most clearly seen in the fibres produced at lower rotational speeds (8,000-10,000 rpm). This secondary peak occurs between 50 – 60 °C and also lowers the T_{onset} to around 48 °C. This double endotherm indicates that PVP/TA polymers spun into fibres display a clear α and β double peak not observed in the flake. The major α peak is the main melt transition and is found at around 76 - 80 °C which is preceded by a smaller β peak at 57 - 62 °C that represents a pre-melt transition. Double melting peaks in DSC are attributed to either:

i.   Two distinct crystal morphologies and configurations;

ii.   Recrystallisation behaviour during the DSC scan (Barham et al., 1988);

iii. Material is actually a binary blend of two different grade products (Blundell, 1987)

The double peak profile is erased by heating as it does not appear in a subsequent heating scan. The absence of a β-peak for the flake material suggests that proposals (ii) and (iii) are not applicable in this case. Therefore it is reasonable to say that within the PVP/TA there are two crystal conformations, the primary α-crystal that is found in the flake and the fibre and the secondary β-crystal form which melts at a lower temperature and is found in more significant quantities as the fibre. This β-crystal may occupy the same unit cell as the α-crystal but a different crystal macro form is created. The second crystal form found in the fibres is a consequence of elongation during solidification and is therefore not found PVP/TA products that have crystallised unstressed. However, there is also a possibility that Morton and Hearle (1993) suggest that the β peak is caused by chain repeats being in alignment with neighbouring units interspersed with disorder.

It can be observed from the DSC traces that the relative size of the β peak reduces as the fibre diameter becomes finer. Another notable measurement is the significant increase in enthalpy, and therefore an increase in overall crystallinity, with increased rotational speed (Table 5.5).

Table 5.5: Measured Enthalpy (ΔH) calculated from DSC traces.

	-	8,000	9,000	10,000	11,000	12,000	13,000	14,000	15,000
				Rotational speed (RPM)					
Low MFI Spinneret		48.2	94.2	110.9	97.3	120.2	123.9	-	-
High MFI Spinneret		-	-	-	-	121.4	123.4	119.1	126.2
Flake	131.1								

Enthalpy in J g^{-1}

From these two observations it can be argued that the higher drawing applied to the finer fibres reduces the rate of formation of this secondary crystallite form. The enthalpy measurements also indicate a higher degree of crystallinity in the flake that attainable in the fibre form. This can be explained as rapid cooling of the fibres during spinning limiting the amount of crystallisation whereas the flake is allowed to crystallise slowly as it forms during polymerisation.

5.4.5 **X-ray diffraction**

The X-ray diffraction patterns of both PVP/TA flake and the fibres produced show two dominant peaks superimposed onto a broad and weak halo which stretches from 10 to 30° 2θ. These are shown in Figure 5.16.
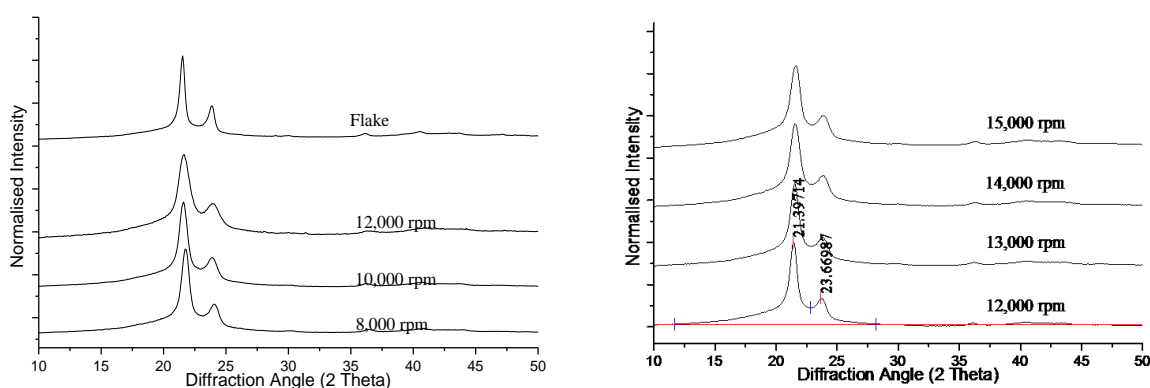
Figure 5.16: XRD plots of PVP/TA flake and fibres produced at varying rotational speeds using the low MFI spinneret (left) and the high MFI spinneret (right). The key peaks are centred around 21.6°, 24.0° and 36.4°.

The X-ray diffraction patterns of both PVP/TA flake and the fibres produced show two dominant peaks superimposed onto a broad and weak halo which stretches from 10 to 30° 2θ. This hump is indicative of an amorphous region (Caminiti et al., 2000). It is known that pure PVP displays low levels of order in an X-ray diffraction analysis suggesting that homogenous PVP is entirely amorphous (Razzak et al., 1999, Sethia and Squillante, 2004). The clear peaks shown in the XRD patterns for PVP/TA are a strong indicator of

long range order. The PVP/TA diffraction pattern has peaks at 21.6, 24.0 and 36.4° 2θ along with additional secondary peaks between 25 and 40° 2θ. This diffraction pattern correlates with that of linear polyethylene. This is a long carbon chain which takes up a highly ordered form and is known to be around 80 % crystalline. Polyethylene forms an orthorhombic crystal with peaks found around 21.5, 23.9 and 36° 2θ. This is analogous to a unit cell of dimensions a = 7.4241 Å; b = 4.9491 Å; and c = 2.5534 Å relative to the crystallographic planes of (110), (200) and (020) (Bertie and Whalley, 1964). By assuming that PVP/TA conforms to the same unit cell applying Equation 2.6 and Equation 2.7 to the PVP/TA peaks at 21.6, 24.0 and 36.4° 2θ results in a unit cell of dimensions (a, b, c) of 7.424 Å, 4.936 Å, and 2.544 Å under the same crystallographic planes. The close match suggests that PVP/triacontene is a semi-crystalline material with crystals that have the same dimensions of low density polyethylene. It should be noted that the peaks for PVP/TA are much broader than linear high density polyethylene and resemble the patterns for branched low density polyethylene found by Ueno and co-workers (1991).

Table 5.6: Full width at half maximum calculated for the PVP/TA flake and fibres for the peak located around 21.6° 2θ.

Rotational Speed (rpm)	Full width at half maximum (°of 2θ)	
	Fine Spinneret (High MFI)	Coarse Spinneret (Low MFI)
8,000	N/D	0.746
9,000	N/D	0.710
10,000	N/D	0.766
11,000	N/D	0.610
12,000	0.707	1.076
13,000	0.814	0.720
14,000	0.956	N/D
15,000	0.944	N/D

FWHM value of flake is 0.485°, N/D not done

The flake has a thinner peak width than the XRD measurements of the fibre forms. Peak width can be established through subtraction of the amorphous region and subsequent calculation of the full width half maximums (FWHM). Table 5.6 documents the calculated FWHM at each spinning condition. The FWHM is significantly higher in the fibre than in the original flake. As crystallite size is inversely proportional to the peak width as dictated by the Scherrer relationship it can be deduced that there is a smaller crystal size in the fibre than in the flake (Meng et al., 2013). This is a consequence of spinning into a fibre; the extensional strain applied during spinning changes the crystal dimensions significantly. This is substantiated by the DSC results presented earlier where a second crystal form was also observed in the drawn fibres. This was explained by Glenz and co-workers who stated that a drawn sample can have a crystal size and shape completely independent of the undrawn material (Glenz et al., 1971). Through interpretation of the XRD results it can be said that the crystals formed within PVP/TA flake and fibres are smaller than crystals within HDPE observed elsewhere (Langford and Wilson, 1978). This follows as PVP/TA a short crystal conformation with the C_{30} chain length (and the presence of a non-crystallising copolymer (PVP) within a branched molecule will result in shorter regions of chain overlap and a much smaller number of unit cells in the a, b and c directions in any one crystal.

A combination of crystallising triacontene chains and amorphous PVP backbone creates definite regions of order and disorder. The C30 chains extend radially out from the PVP chain and will inevitably interact with neighbouring hydrocarbon chains. PVP is entirely amorphous and will not crystallise but the grafted on C30 chains can move into registration and form crystal unit cells identical to those found in polyethylene. This method of graft copolymer crystallisation on an amorphous backbone was also observed

by Inomata et al. (2005) where the structure was described as interdigitating packing. A representation of this structure is shown in Figure 5.17.
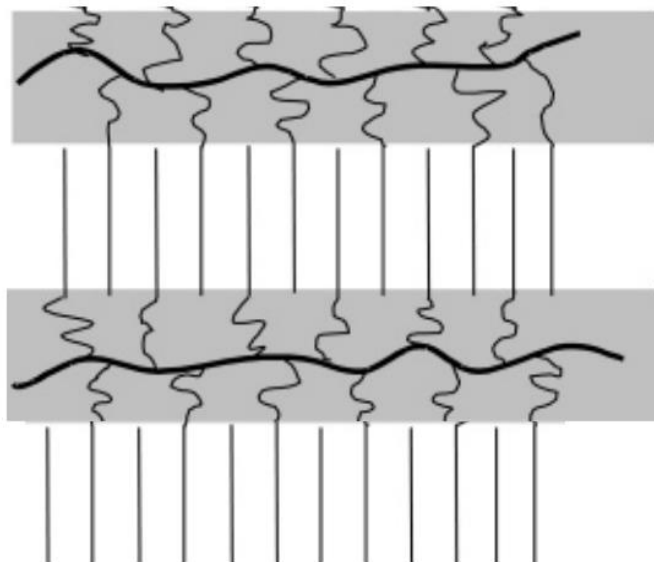
Figure 5.17: Model for crystallisation of graft copolymers (Neugebauer et al., 2005)

Applying this model to PVP/TA, the long carbon chains create short length crystals which are perpendicular to the polymer backbone. Deviations in backbone chain registration and variations in chain length would allow for a single copolymer brush to enter both crystalline and amorphous regions and would incorporate further defects and disorder into the crystal system. This view can be complemented by the possibility that the polymers pack together to form a 'laterally crystalline' structure similar to that found in polyacrylonitrile (PAN) (Bell and Dumbleton, 1971). More detail is given to this proposed structure in work done by Arndt et al. (1991) who found that side chains will only crystallise at sufficient distance away from the backbone. They estimated this distance to be $6\,CH_2$ units which led to the updated model which states that the amorphous component is comprised of the backbone and disordered side chain.

From the XRD results it is concluded that within PVP/TA there are short blocks of crystals dispersed between a non-crystallizing PVP and disordered or imperfect regions within the copolymer. This two phase structure is often observed in polymer blends or in copolymer chains (Kumar et al., 2014). In terms of macro-fibre structure, Morton and Hearle (1993) stated that in a two-component system of crystallisable polymer dispersed between blocks of non-crystallising polymer, if the crystallising blocks are of fixed length then the structure is likely to be a true representation of the fringed micelle model. However, in this brush copolymer the molecule is best described as a backbone chain entirely surrounded by graft elements which limit the possibility of the random chain passing through multiple crystals as proposed in the fringed micelle model. Other models such as the fringed fibril do not fit easily with grafted chain polymers as chain folding of the side grafts is restricted by short length of the C30 chain and the anchoring of the PVP backbone (Samanta et al., 2009). This lack of chain folding will ultimately limit the crystal size which will confirm the hypothesis put forward previously that the crystals of PVP/TA are much smaller than those found in PE (which can chain fold) This view can be complemented by the possibility that the polymers pack together to form a "laterally crystalline" structure similar to that found in polyacrylonitrile (PAN) (Bell and Dumbleton, 1971). This could explain the brittle fractures observed in section 5.4.2.1, it is hypothesised that these lateral crystals do not contribute to tensile strength and elasticity like crystallised regions in long linear chains such as polypropylene.

5.4.6 Dye adsorption assessment

The calibration curve for Dianix Blue AC-E was shown previously in Figure 5.6. To calculate the concentration of an unknown solution the UV-Vis absorbance is divided by the gradient of the graph in Figure 5.6 to generate a measured concentration in mg L^{-1}.

The concentration of the treated effluent allows for calculation for the mass of dye removed by the PVP/TA fibres and the activated carbon. Table 5.7 provides the summary data for both materials at each dye concentration. The colour removal percentage as calculated using $\frac{C_0 - C_e}{C_0} \times 100$. PVP/TA was an effective adsorbent, capable of 97.1 percent dye removal of an original dye concentration of 25 mg L^{-1}. The PVP/TA was able to adsorb more dye Dianix Blue A-CE than the commercial AC, at a dye concentration of 300 mg L^{-1} the PVP/TA and AC adsorbed 59.1 % and 49.9 % of the dye, respectively. The mass of dye adsorbed onto the material (Q_e), was calculated as $(C_0 - C_e)\frac{V}{m}$. The fibres were able to capture 35.44 mg of dye per gram of material compared to 29.95 for the commercial A-CE.

Table 5.7: Percentage of disperse dye removed by PVP/TA and Norit AC and amount of dye adsorbed onto the fibres at each starting concentration (Co).

	Co (mg L$^{-1)}$)					
	25	50	100	150	200	300
PVP/TA fibre						
Removal (%)	97.1	83.2	73.3	76.6	70.4	59.1
Qe (mg g$^{-1)}$)	4.8	8.3	14.7	22.9	27.7	35.4
Norit AC						
Removal (%)	95.9	88.3	78.5	73.2	64.5	49.9
Qe (mg g^{-1})	4.8	8.8	15.7	22.0	25.3	30.0

The adsorption isotherms can only be calculated under equilibrium conditions. Preliminary kinetic studies indicate that after 6 hours no more additional dye is adsorbed onto either PVP/TA or AC; thus 72 hours was sufficient to reach equilibrium.

The Langmuir model for both materials was calculated by plotting $\frac{1}{Qe}$ against $\frac{1}{C_e}$ as per Equation 5.3 and shown in Figure 5.18.
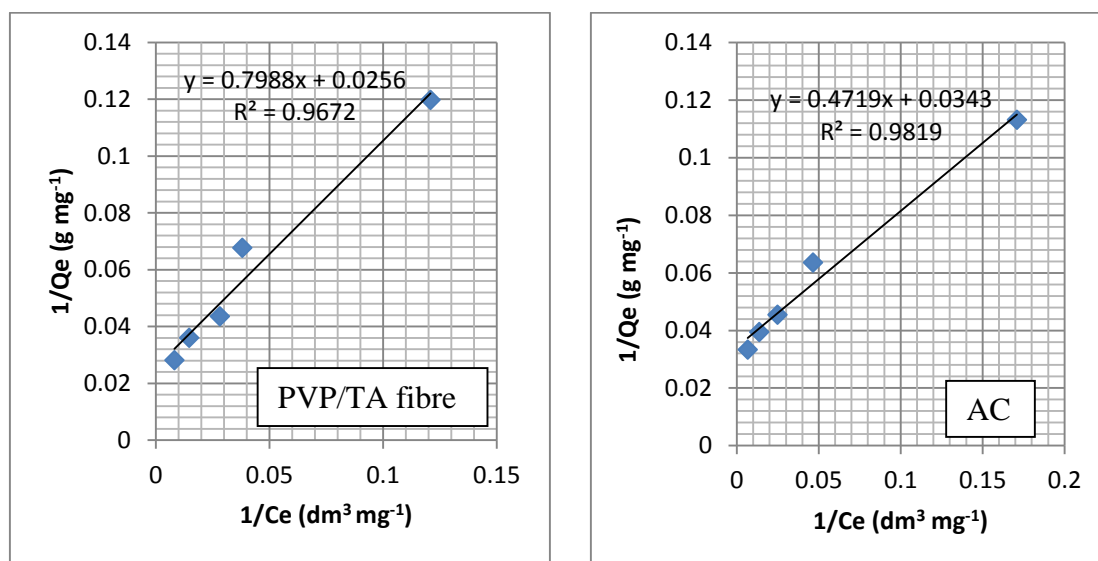
Figure 5.18: Linearised Langmuir model for PVP/TA fibres and activated carbon.

The constants K_L, Q_0 were then calculated from the slope and the gradient to produce the models shown in Table 5.8.

Table 5.8: Calculated Langmuir isotherm equations for PVP/TA fibre and activated carbon.

Sample	Langmuir isothermal equation
PVP/TA fibre	$Qe = \dfrac{C_e * 1.252}{1 + (C_e * 0.0321)}$
Norit AC	$Qe = \dfrac{C_e * 2.129}{1 + (C_e * 0.0737)}$

The Langmuir models are plotted against the empirical data recorded in Figure 5.19 and Figure 5.20.

The linearised Langmuir model fits the empirical data closely with R^2 values of 0.982 and 0.967 for the activated charcoal and PVP/TA fibre, respectively. This suggests that both the PVP/TA fibre and the Norit AC adsorb disperse dyes as a monolayer with a fixed amount of adsorption sites. Previous work has demonstrated that the Langmuir isothermal accurately models the adsorption on to AC (McKay, 1982; Gercel et al., 2008). This work suggests that the mechanism that attracts disperse dyes to AC also acts to attract and retain disperse dyes on the surface of PVP/TA.
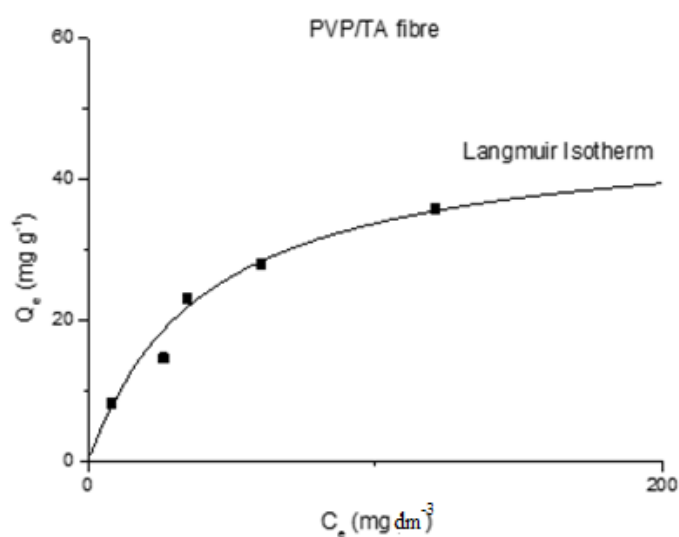
Figure 5.19: Mass of dye adsorbed (Qe) plotted against equilibrium concentration (Ce) for PVP/TA fibre along with plots of Langmuir isothermal.
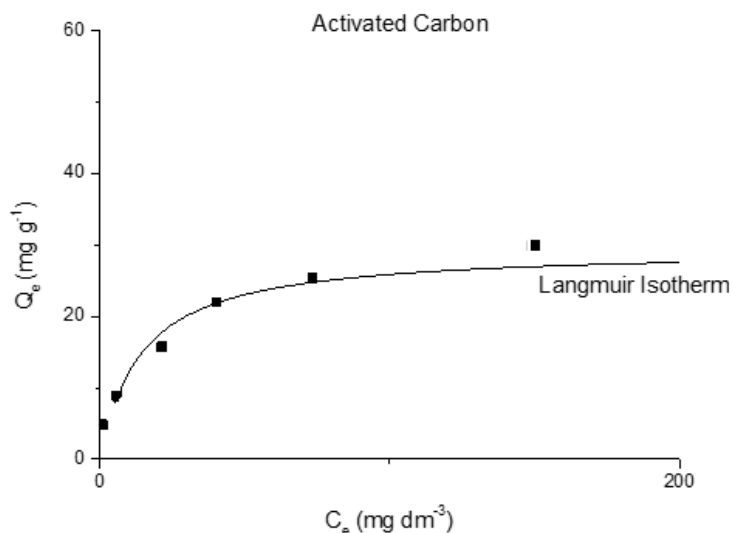
Figure 5.20: Mass of dye adsorbed (Qe) plotted against equilibrium concentration (Ce) for activated carbon along with plots of Langmuir isothermal.

Both materials have a high surface area but one explanation for the higher adsorption by PVP/TA over AC is that the PVP/TA has a greater number of potential adsorption sites. This is due to the presence of non-polar long chain hydrocarbon branches creating a hydrophobic surface that the disperse dyes can bond to.

5.4.7 **Soil retention**

The positive and negative ToF-SIMS spectra ranging 0 to 400 m/z for the full set of samples are included in Appendix A-5 to A-17 which are also rescaled at intervals to help identify peaks. However, selected raw data, without adjustment, are included in Figure 5.21 for reference.

The ToF SIMS spectra of the samples showed a large range of overlapping and common peaks making it difficult to distinguish between the fibres and the staining agent. However, various compounds unique to sebum and to corn oil could be identified and

linked to real molecules based on molecular weight. In the sebum oil spectra, peaks were observed at 141$^-$, 169$^-$ and 197$^-$ m/z in the negative ion which equate to decane, dodecane and tetradecane, respectively which form the 'mixed hydrocarbons' constituent in the synthetic sebum. Larger fatty acids, oleic acid and stearic acid, formed dominant peaks at 255$^-$ and 283$^-$ m/z, respectively; these fatty acids are found in beef tallow, the primary component and likely to be found in the free fatty acids. Additional key peaks for the sebum oil occurred in the positive ion at 383$^+$ and 579$^+$ m/z which correlate to the cholesterol and a polyglycerol fatty acid ester, the latter being a key component in Cutina, which makes up 11 % of the synthetic sebum (Diederich et al., 2014).

The components of corn were all identified in the negative ion phase. Peaks pertaining to palmitic acid, linolenic acid and linoleic acid were observed at 255$^-$, 277$^-$ and 279$^-$ m/z with the larger oleic acid and stearic acid generating peaks at 281$^-$ and 283$^-$, respectively. The intensity of the peaks observed relates strongly to their relative proportions in corn oil.
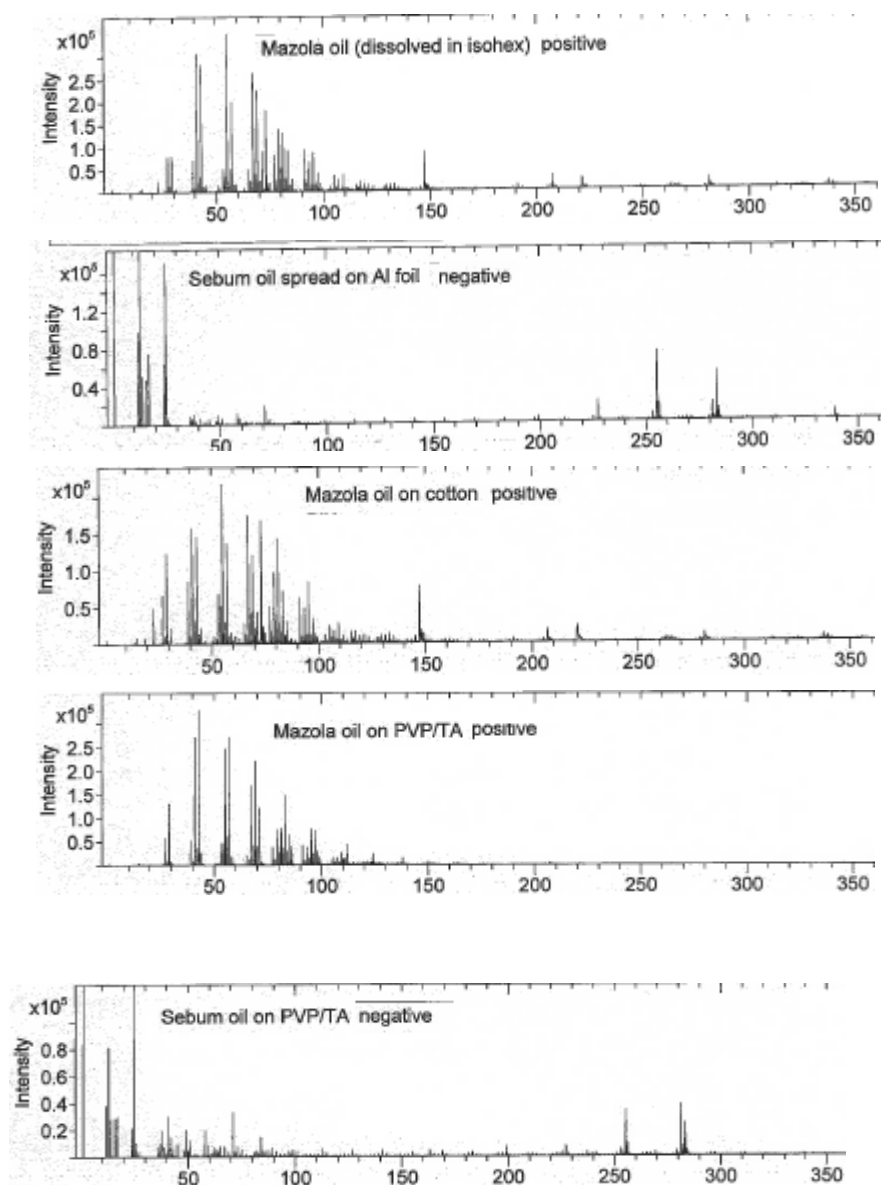
Figure 5.21: Selected ToF-SIMS spectra for assessing soil retention on fibres.

ToF-SIMS is only semi-quantitative and absolute intensity data cannot be used in isolation to determine how much of a compound is present. However, changes in relative proportion can be observed by changes in peak intensity relative to other major peaks. The relative peak intensities of the listed peaks before and after washing were compared to indicate the substantivity of the oily materials for PVP/TA and cotton. The use of relative peak height analysis has been used previously by Blestos et al. (1991) and by Graham et al. (2006) and normalises differences in sample interaction and reveals more

than absolute intensities. Typically, a common reference peak is chosen that features in all spectra and for this work the peaks at 25^- m/z (C_2H^-) and 41^+ m/z ($C_3H_5^+$) were used as reference peaks for the negative and positive ions, respectively. These were chosen as they were high intensity peaks present in both virgin cotton and the PVP/TA fibre. The height of the aforementioned peaks was compared to these reference points and the change in relative height calculated. The results are shown in Table 5.9 and Table 5.10 for sebum oil and corn oil respectively.

Table 5.9: Relative peak heights of compounds observed on sebum oil stained and washed cotton fabric and centrifugal spun PVP/TA fibres, produced at 12,000 rpm, 72 °C using the coarse spinneret.

Description	Ion (m/z)	Species	Sebum oil on cotton			Sebum oil on PVP/TA		
			Stained	Washed	Change	Stained	Washed	Change
Nonane	127^-	$C_9H_{19}-$	0.125	0.085	-32 %	0.031	0.033	+5 %
Decane	141^-	$C_{10}H_{21}-$	0.104	0.062	-40 %	0.020	0.030	+50 %
Undecane	155^-	$C_{11}H_{23}-$	0.1	0.033	-67 %	0.017	0.018	+4 %
Dodecane	169^-	$C_{12}H_{25}^-$	0.090	0.031	-95 %	0.018	0.020	+9.5 %
Tridecane	183^-	$C_{13}H_{27}^-$	0.075	0.032	-55 %	0.015	0.014	-3 %
Tetradecane	197^-	$C_{14}H_{29}^-$	0.075	0.023	-96 %	0.013	0.023	+78 %
Oleic acid	255^-	$C_{15}H_{31}CO_2^-$	0.667	0.200	-63 %	0.174	0.140	-19 %
Stearic acid	283^-	$C_{18}H_{36}O_2-$	0.567	0.254	-60 %	0.117	0.038	-68 %
Cholesterol	383^-	$C_{27}H_{46}O^-$	0.038	0.010	-72 %	0.034	0.007	-80 %
Polyglycerol fatty acid ester	579^+	$C_{30}H_{58}O_{10}^-$	0.045	0.009	-78 %	0.005	0.002	-66 %

Table 5.10: Relative peak heights of compounds observed on corn oil stained and washed cotton fabric and centrifugal spun PVP/TA fibres, produced at 12,000 rpm, 72 °C using the coarse spinneret.

Description	Ion (m/z)	Species	Corn oil on cotton			Corn oil on PVP/TA		
			Stained	Washed	Change	Stained	Washed	Change
Palmitic acid	255^-	$C_{15}H_{31}CO_2^-$	0.200	0.116	-42 %	0.043	0.087	+104 %
Linolenic acid	277^-	$C_{18}H_{30}O_2^-$	0.067	0.004	-95 %	0.006	0.003	-47 %
Linoleic acid	279^-	$C_{18}H_{32}O_2^-$	0.407	0.014	-96 %	0.058	0.270	+364 %
Oleic acid	281^-	$C_{18}H_{34}O_2^-$	0.313	0.116	-62 %	0.039	0.196	+397 %
Stearic acid	283^-	$C_{18}H_{36}O_2-$	0.053	0.021	-60 %	0.009	0.004	-60 %

Table 5.9 and Table 5.10 indicate that both the sebum and corn oil have little affinity for cotton and are easily lifted from the surface by detergent resulting in significant reductions in relative peak intensity after washing. The intensity of dodecane, tetradecane, linolenic acid and linoleic acid relative to the reference peak was reduced by over 95 % when the stained cotton was washed. The oleic (281^- m/z) and stearic acid (283^- m/z) compounds are present in both the sebum and corn oil and were both reduced by roughly the same amount ~61 % during the wash cycle indicating agreement between the sets of results.

In comparison, the hydrophobic PVP/TA fibres recorded relative intensity gains and less significant losses for some compounds after washing. ToF-SIMS is a surface specific technique with a penetration depth of only 1 - 2 nm; thus, the gains in intensity observed were attributed to the surface agents being more conspicuous to the bombarding ionisation after losing less substantive neighbouring fatty material during washing. These gains in relative intensity were generally confined to the lower molecular weight elements (C_9 to C_{14} in length) whereas the larger glycerides and fatty acids were less substantive. Stearic acid (283^- m/z) and the polyglycerol fatty acid ester (579^+ m/z) were reduced on intensity by 68 % and 66 % respectively when the PVP/TA was washed; stearic acid can be deprotonated which imparts hydrophilicity which would significantly reduce the hydrophobic-hydrophobic affinity with the PVP/TA and polyglycerol fatty acid esters are known to have a hydrophilic moiety which again reduces the affinity for PVP/TA and increases the affinity for water (Sakamoto, 2004). Overall, the PVP/TA fibres showed a lower reduction in relative peak intensity compared to the cotton reference suggesting that the oils are substantive for the fibres with one exception: the reduction in cholesterol (383^+ m/z) on PVP/TA with washing was greater than observed on cotton. Cholesterol

possesses a secondary alcohol and is amphiphilic; having both hydrophilic and hydrophobic ends; this hydrophilic component could decrease the substantivity of the compound on to PVP/TA.

The indications are that when the stained cotton was washed there was a moderate reduction in sebum and corn oil content which is lifted from the surface by the detergent and water; cotton is hydrophilic and has little affinity for the oil applied to the surface. The relative height of the sebum oil – PVP/TA peak pair was much lower after washing indicating that the sebum oil was lifted off the fibre surface by the detergent. In comparison, the corn oil retained relative peak intensity and actually increased compared to the unwashed sample. The ToF-SIMS results suggest that corn oil was not easily washed off the PVP/TA fibres and there was a relatively strong attraction between the two hydrophobic products. The discrepancy between the sebum and corn oil could be due to the effects and interactions of the different compounds in the synthetic sebum oil. Some of the compounds present, such as triglycerides and cutina are amphiphilic and may have behaved as emulsification agents and may also be saponified. These different compounds could also interact to create species of such molecular size that they interfere with the relative peak heights. In addition, the different compounds will have a different interaction with the PVP/TA and with each other which could reduce the affinity of one or more of the compounds for the PVP/TA fibres.

Overall, the ToF-SIMS results presented here suggest that PVP/TA fibres have a high level of affinity for the non-polar hydrocarbons (nonane to tetradecane), which remained after washing indicating that the PVP/TA fibre had some oleophilic characteristics which could potentially be useful in preventing staining in domestic clothing such as cotton.

However, the ToF-SIMS results for the sebum oil indicated that this attraction is not clearly defined and more research needs to be done to quantify this relationship accurately and establish the correct conditions for fibre-oil attraction, capture and retention.

5.5 **Conclusions**

Polyvinylpyrrolidone/triacontene was successfully melt spun into ultrafine fibres using a commercially available centrifugal spinning system. Increasing the rotational speed reduced the average fibre diameter so that average diameters between $1 - 2$ μm were achieved with individual fibres observed as fine as 0.3 μm. The melt viscosity of PVP/TA is highly sensitive to temperature and successful fibre production was achieved when using a spinning temperature of 72 °C. At this temperature, relatively high production rates of 200 mg min^{-1} per orifice could be achieved. At this production rate, significant volumes of this material could be produced economically using commercial centrifugal spinning equipment.

A review of the literature and XRD and ToF-SIMS analysis revealed that PVP/TA is in the form of a radial brush copolymer which forms a semi-crystalline structure where the triacontane branches interlock and form small crystals around an amorphous backbone. This view suggests that the individual PVP/TA chains will incorporate several regions of crystalline and non-crystalline regions within its length. The radial triacontene branches also impart hydrophobicity and mask the hydrophilic backbone. This hydrophobic behaviour could potentially be useful in adsorption applications and this research tested the effectiveness of PVP/TA fibres as a dye adsorbent and as an oil capturing adsorbent. This is the first time that PVPT/TA fibres have been considered as an adsorbent for

disperse dyes. The PVP/TA fibres had an adsorption capacity of 35.4 mg g^{-1} of Dianix Blue A-CE under neutral conditions. The fibres adsorbed slightly more Dianix Blue A-CE than a commercial adsorbent but more importantly have demonstrated the potential of fine fibrous adsorbents. These fibres could then be incorporated into existing materials to create functional, adsorbent fabrics. As an aside, all the common adsorbent materials are in granular or powder form which limits their ability to be incorporated into a nonwoven material for ease of handling. There is potential to incorporate adsorbent fibres on to the supporting substrates in filtration mechanism. When used as a filtration membrane the fibres may also assist in filtration by removing larger particulates and acting as a pre-filter (Hutten, 2007). An adsorbent filter media differs from the adsorbent systems described previously in that the adsorbent is fixed and the solution is passed through it as opposed to being dispersed in the liquor. Incorporating PVP into a filter media can be achieved by spinning a thin layer directly onto the supporting substrate.

In addition to the adsorption of hydrophobic dyes, the PVP/TA fibres produced also demonstrated a high affinity for non-polar hydrocarbons which suggests that fibres of this nature could be applied as oleophilic capture agents in domestic and industrial laundering applications. However, more experimental work must be done on this to demonstrate efficacy and establish firm relationships.

5.6 **References**

AGLIENT TECHNOLOGIES., 2015. *Fundamentals of modern UV-visible spectroscopy* [Online]. Available: http://www.chem.agilent.com/library/ slidepresentation/public/present.pdf (Accessed: 10th February 2015).

AKBARI, A., REMIGY, J. C. & APTEL, P., 2002. Treatment of textile dye effluent using a polyamide-based nanofiltration membrane. *Chemical Engineering and Processing: Process Intensification,* 41**,** 601-609.

ALLEN, S., MCKAY, G. & PORTER, J., 2004. Adsorption isotherm models for basic dye adsorption by peat in single and binary component systems. *Journal of Colloid and Interface Science,* 280**,** 322-333.

ANJANEYULU, Y., SREEDHARA CHARY, N. & SAMUEL SUMAN RAJ, D., 2005. Decolourization of industrial effluents – available methods and emerging technologies – a review. *Reviews in Environmental Science and Bio/Technology,* 4**,** 245-273.

ARNDT, T., SCHOUTEN, A. J., SCHMIDT, G. F. & WEGNER, G., 1991. Langmuir-Blodgett mono- and multilayers of preformed poly(octadecyl methacrylate): Structural studies by IR spectroscopy and small-angle X-ray scattering. *Die Makromolekulare Chemie,* 192**,** 2215-2229.

BARHAM, P. J., HILL, M. J., KELLER, A. & ROSNEY, C. C. A., 1988. Phase separation in polyethylene melts. *Journal of Materials Science Letters,* 7**,** 1271-1275.

BELL, J. P. & DUMBLETON, J. H., 1971. Changes in the structure of wet-spun acrylic fibers during processing. *Textile Research Journal,* 41**,** 196-203.

BEY SEBUM. *Sebum according to Bey, Material safety data sheet.* Available online: http://www.testgewebe.de/ds/soils/ds-00612_sebum_us.html [Accessed: 13th June 2015]

BLACKBURN, R. S., 2004. Natural polysaccharides and their interactions with dye molecules: applications in effluent treatment. *Environmental Science & Technology,* 38**,** 4905-4909.

BLESTOS, I. V., HERCULES, D. M., VAN LEYEN, D., HAGENHOFF, B., NIEHUIS, E. & BENNINGHOVEN, A., 1991. Molecular weight distributions of polymers using Time-of-Flight Secondary Ion Mass Spectrometry. Analytical Chemistry, 63, 1953-1960.

BLUNDELL, D. J., 1987. On the interpretation of multiple melting peaks in poly(ether ether ketone). *Polymer,* 28**,** 2248-2251.

BOARDMAN, C. & JARVIS, A. N., 2000. The prevention of in–wash dye transfer. *Review of Progress in Coloration and Related Topics,* 30**,** 63-66.

BOTTANI, E. J. & TASCON, J., 2008. *Adsorption by Carbons,* Elsevier, Netherlands.

BRUGNARA. M., DEGASPERI, E., DELLA VOLPE, C., MANIGLIO, D., PENATI, A., SIBONI, S., TONIOLO, L., POLI, T., INVERNIZZI, S. & CASTELVETRO, V., 2004. The application of the contact angle in monument protection: new materials and methods. *Colloids and Surfaces A*, 241, 299-312.

BULL, K., 2008. Cabin air filtration: helping to protect occupants from infectious diseases. *Travel Medicine and Infectious Diseases, 6, 142-144.*

CAMINITI, R., PANDOLFI, L. & BALLIRANO, P., 2000. Structure of polyethylene from X-ray powder diffraction: influence of the amorphous fraction on data analysis. *Journal of Macromolecular Science, Part B,* 39**,** 481-492.

CARNEIRO, P. A., UMBUZEIRO, G. A., OLIVEIRA, D. P. & ZANONI, M. V. B., 2010. Assessment of water contamination caused by a mutagenic textile effluent/dyehouse effluent bearing disperse dyes. *Journal of Hazardous Materials,* 174**,** 694-699.

CHRISTIE, R. M., 2001. *Colour Chemistry.* The Royal Society for Chemistry, London.

CHUNG, H-K., KIM, W-H., PARK, J., JEONG, T-Y. & PARK, P-K., 2015. Application of Langmuir and Freundlich isotherms to predict adsorbate removal efficiency or required amount of adsorbent. *Journal of Industrial and Engineering Chemistry*, in press, accepted February 2015.

COONEY, D. O., 1998. *Adsorption Design for Wastewater Treatment*, CMC press, United States.

CRINI, G., 2006. Non-conventional low-cost adsorbents for dye removal: A review. *Bioresource Technology,* 97, 1061-1085.

DADA, A. O., OLALEKAN, A. P., OLATUNYA, A. M. & DADA, O., 2012. Langmuir, Freundlich, Temkin and Dubinin–Radushkevich isotherms studies of equilibrium sorption of Zn2+ unto phosphoric acid modified rice husk. *Journal of Applied Chemistry,* 3, 38-45.

DORSET, D. L. & SNYDER, R. G., 1999. Effect of chain unsaturation on polymethylene lamellar packing: solid-state structure of a symmetric trans-alkene. *Macromolecules,* 32**,** 8139-8144.

DIEDERICH, A., KUNZLER, H. & GRANER, O., 2014. *Pharmaceutical compositions comprising everolimus.* United States Patent Application: PCT/IB2014/059965, 25th September 2015

FARIA, P. C. C., ORFAO, J. J. M. & PEREIRA, M. F. R., 2004. Adsorption of anionic and cationic dyes on activated carbons with different surface chemistries. *Water Research,* 38**,** 2043-2052.

GERÇEL, Ö., GERÇEL, H. F., KOPARAL, A. S. & ÖĞÜTVEREN, Ü. B., 2008. Removal of disperse dye from aqueous solution by novel adsorbent prepared from biomass plant material. *Journal of Hazardous Materials,* 160**,** 668-674.

GHALY, A., ANANTHASHANKAR, R., ALHATTAB, M. & RAMAKRISHNAN, V., 2014. Production, characterization and treatment of textile effluents: a critical review. *Journal of Chemical Engineering and Process Technology,* 5**,** 182.

GILES, C. H., 1971. The coloration of synthetic polymers. *British Polymer Journal,* 3, 279-290.

GLENZ, W., PETERLIN, A. & WILKE, W., 1971. Crystallite size in highly drawn polyethylene. *Journal of Polymer Science: Polymer Physics,* 9, 1243-1254.

GRAHAM, D. J., WAGNER, M. S. & CASTER, D. G., 2006. Information from complexity: challenges of TOF-SIMS data interpretation. *Applied Surface Science, 252, 6860-6868.*

HARTGERINK, J. D., BENIASH, E. & STUPP, S. I., 2001. Self-assembly and mineralization of peptide-amphiphile nanofibers. *Science,* 294**,** 1684-1688.

HAMLEY, I. W., 2004. *Developments in block copolymer science and technology*, Wiley Online Library.

HUTTEN, I. M., 2007. *Handbook of Nonwoven Filter Media*, United States: Elsevier.

KAVITHA, S. & PALANISAMY, P., 2011. Photocatalytic and sonophotocatalytic degradation of reactive red 120 using dye sensitized TiO2 under visible light. *International Journal of Civil and Environmental Engineering,* 3**,** 1-6.

KHAN, A. R., TAHIR, H., UDDIN, F. & HAMEED, U., 2005. Adsorption of methylene blue from aqueous solution on the surface of wool fiber and cotton fiber. *Journal of Applied Sciences and Environmental Management*, 9, 29-35.

KOPOLOW, S. L., LOGIN, R. & TAZI, M., 1991. Alkylated polyvinylpyrrolidone polymers in cosmetic and pharmaceuticals. *In:* GEBELEIN, C. G., CHENG, T. C. & YANG, V. C. (eds.) *Cosmetic and pharmaceutical applications of polymers.* Plenum Press, United States.

KUMAR, K. K., RAVI, M., PAVANI, Y., BHAVANI, S., SHARMA, A. K. & NARASIMHA RAO, V. V. R., 2014. Investigations on PEO/PVP/NaBr complexed polymer blend electrolytes for electrochemical cell applications. *Journal of Membrane Science,* 454**,** 200-211.

LANGFORD, J. I. & WILSON, A. J. C., 1978. Scherrer after sixty years: a survey and some new results in the determination of crystallite size. *Journal of Applied Crystallography,* 11**,** 102-113. LAUGHLIN, J. & GOLD, R. Methyl parathion residue removal from protective apparel fabric soiled with synthetic sebum or vegetable oil. *Archives of Environmental Contamination and Toxicology,* 19, 205-213.

LIU, K.-C., HELIOFF, M., REREK, M., DAVIS, M., GRENNER, L. J., GRAHAM, D. E., WALDORF-GEBER, A. & KOPPEL, R., 1999. *Sunscreen concentrate.* United States Patent: 5,916,544, 29th June 1999.

LIU, Y., LI, H. F., ZHANG, J. H., MAEDA, T. & LIN, J. M., 2010. Triacontyl modified silica gel as a sorbent for the preconcentration of polycyclic aromatic hydrocarbons in aqueous samples prior to gas chromatographic-mass spectrometry determination. *Chinese Chemical Letters,* 21, 730-733.

MCKAY, G., 1982. Adsorption of dyestuffs from aqueous solutions with activated carbon I: equilibrium and batch contact-time studies. *Journal of Chemical Technology and Biotechnology,* 32, 759-772.

MENG, X., ZHANG, N., WANG, X.-D., WANG, L., HUANG, D.-X. & MIAO, R., 2013. Dye effluent treatment using PVDF UF membranes with different properties. *Desalination and Water Treatment***,** 52, 5068-5075.

MEZOHEGYI, G., VAN DER ZEE, F. P., FONT, J., FORTUNY, A. & FABREGAT, A., 2012. Towards advanced aqueous dye removal processes: A short review on the versatile role of activated carbon. *Journal of Environmental Management,* 102**,** 148-164.

MISHRA, G. & TRIPATHY, M., 1993. A critical review of the treatments for decolourization of textile effluent. *Colourage,* 40**,** 35-38.

MORTON, W. & HEARLE, J., 1993. *Physical Properties of Textile Fibres*. The Textile Institute, Manchester.

MULDER, H., SMITS, R & BROEKHOF, N., 2000. *Metal working fluids.* European Patent Application: EP1063280. 27th December 2000.

NEUGEBAUER, D., THEIS, M., PAKULA, T., WEGNER, G. & MATYJASZEWSKI, K., 2005. Densely Heterografted Brush Macromolecules with Crystallizable Grafts. Synthesis and Bulk Properties. *Macromolecules,* 39**,** 584-593.

PESEK, J. J., MATYSKA, M. T., WILLIAMSEN, E. J., EVANCHIC, M., HAZARI, V., KONJUH, K., TAKHAR, S. & TRANCHINA, R., 1997. Synthesis and characterization of alkyl bonded phases from a silica hydride via hydrosilation with free radical initiation. *Journal of Chromatography A*, 786, 219-228.

PETERS, R. H., 1963. *Textile Chemistry: The Physical Chemistry of Dyeing.* Elsevier Publishing, United States.

PETTER, P. J., 1989. Acetylene-derived polymers and their applications in hair and skin care. *International Journal of Cosmetic Science,* 11**,** 35-48.

POLLARD, S. J. T., FOWLER, G. D., SOLLARS, C. J. & PERRY, R., 1992. Low-cost adsorbents for waste and wastewater treatment: a review. *Science of The Total Environment,* 116**,** 31-52.

RAMAKRISHNA, K. R. & VIRARAGHAVAN, T., 1997. Dye removal using low cost adsorbents. *Water Science and Technology*, 36, 189-196.

RAZZAK, M. T., ZAINUDDIN, ERIZAL, DEWI, S. P., LELY, H., TATY, E. & SUKIRNO, H., 1999. The characterization of dressing component materials and radiation formation of PVA–PVP hydrogel. *Radiation Physics and Chemistry,* 55**,** 153-165.

RATEE, I. D.& BREUER, M. M., 1974. *The Physical Chemistry of Dye Adsorption.* Academic Press, United States.

REZAEE, A., GHANEIAN, M. T., TAGHAVINIA, N., AMINIAN, M. K. & HASHEMIAN, S. J., 2009. TiO2 nanofibre assisted photocatalytic degradation of Reactive Blue 19 dye from aqueous solution. *Environmental Technology,* 30**,** 233-239.

ROBINSON, B. V., 1990. *PVP: A Critical Review of the Kinetics and Toxicology of Polyvinylpyrrolidone (Providone).* CRC Press, United Kingdom.

ROBINSON, T., MCMULLAN, G., MARCHANT, R. & NIGAM, P., 2001. Remediation of dyes in textile effluent: a critical review on current treatment technologies with a proposed alternative. *Bioresource Technology,* 77**,** 247-255.

SAKAMOTO, M., OHBA, A., KURIYAMA, J., MARUO, K., UENO, S. & SATO, K., 2004. Influences of fatty acid moiety and esterification of polyglycerol fatty acid esters on the crystallisation of palm mid fraction in oil-in-watter emulsion. *Colloids Surfaces B: Biointerfaces, 37. 27-33.*

SAMANTA, S., CHATTERJEE, D. P., MANNA, S., MANDAL, A., GARAI, A. & NANDI, A. K., 2009. Multifunctional hydrophilic poly(vinylidene fluoride) graft copolymer with supertoughness and supergluing properties. *Macromolecules,* 42**,** 3112-3120.

SARATALE, R. G., SARATALE, G. D., CHANG, J. S. & GOVINDWAR, S. P., 2011. Bacterial decolorization and degradation of azo dyes: A review. *Journal of the Taiwan Institute of Chemical Engineers,* 42**,** 138-157.

SETHIA, S. & SQUILLANTE, E., 2004. Solid dispersion of carbamazepine in PVP K30 by conventional solvent evaporation and supercritical methods. *International Journal of Pharmaceutics,* 272**,** 1-10.

SHAMEY, R. 2009. Improving the dyeability/colouration of polypropylene fibres. *In:* UGBOLUE, S. C. (ed.), *Polyolefin Fibres: Industrial and Medical Applications.* Woodhead Publishing, United Kingdom.

SHEN, D., FAN, J., ZHOU, W., GAO, B., YUE, Q. & KANG, Q., 2009. Adsorption kinetics and isotherm of anionic dyes onto organo-bentonite from single and multisolute systems. *Journal of Hazardous Materials,* 172**,** 99-107.

STONE, N., VARMA, S., HUGHES, T. M. & STONE, N. M., 2002. Allergic contact dermatitis from polyvinylpyrrolidone (PVP)/1-triacontene copolymer in a sunscreen. *Contact Dermatitis,* 47**,** 49-49.

SHORE, J., 1995. *Cellulosics Dyeing.* Society of Dyers and Colourists, United Kingdom.

SUZUKI, M., 1991. Application of fiber adsorbents in water treatment. *Water Science and Technology*, 23, 1649-1658.

UENO, N., SEKI, K., SUGITA, K. & INOKUCHI, H., 1991. Nature of the temperature dependence of conduction bands in polyethylene. *Physical Review B*, 43, 2384-2390.

VICKERMAN, J. C., 2009. Molecular Surface Mass Spectrometry by SIMS. *Surface Analysis – The Principal Techniques.* John Wiley & Sons, Manchester.

WANG, L., 2012. Application of activated carbon derived from 'waste' bamboo culms for the adsorption of azo disperse dye: Kinetic, equilibrium and thermodynamic studies. *Journal of Environmental Management,* 102**,** 79-87.

WRAP.ORG, 1997. Water and chemical use in the textile dyeing and finishing industry. [Online] Available: http://www.wrap.org.uk/sites/files/wrap/gg062.pdf (Accessed: 1st January 2015).

YAGUB, M. T., SEN, T. K., AFROZE, S. & ANG, H., 2014. Dye and its removal from aqueous solution by adsorption: A review. *Advances in colloid and interface science,* 209**,** 172-184.

YANG, Y., BROWN, H. & LI, S., 2001. Some sorption characteristics of poly(trimethylene terephthalate) with disperse dyes. *Journal of Applied Polymer Science*, 86, 223-229.

YUE, Q., QIAN, L., GAO, B. & WANG, Y., 2007. Kinetics of adsorption of disperse dyes by polyepicholorohydrin-dimethylamine cationic polymer/bentonite. *Separation and Purification Technology*, 54, 279-290.

ZHANG, S. 2003. Fabrication of novel biomaterials through molecular self-assembly. *Nature Biotechnology,* 21**,** 1171-1178.

ZOLTOWSKI, C., GILLEY, J. & SCOTT, A., 2003. *Pseudoplastic, film forming cosmetic compositions*. United States Patent: 09/874,857, Application: 09/874,857, 6th February 2003.

Chapter 6
Creation of nanofibre composites containing carbon nanotubes through centrifugal spinning

6.1 Introduction

Nanofibre nanocomposite materials were previously discussed in Section 1.34; these are ultrafine fibres that contain ultrafine fillers. This chapter expands on that concept and specifically looks at the incorporation of carbon nanotubes within fine polymeric fibres produced through centrifugal spinning.

Carbon nanotubes (CNTs) are a new form of material that have received growing academic and commercial interest in recent years since their discovery was documented in a seminal paper by Iijima (1991). Carbon nanotubes have unique mechanical and electronic properties which make them scientifically interesting and potentially useful as filler material in specialist and commercial applications (Thostenson et al., 2001). The high levels of research activity in both nanotubes and nanofibre production made it inevitable that the two topics would coalesce and the creation of nanofibres containing carbon nanotubes would be explored (Jeong, 2007).

The addition of nanotubes to a polymer comes at a cost in terms of processing: CNTs are especially difficult to disperse and significantly change the melt rheology of the polymer matrix, making fibre formation more troublesome. Using centrifugal spinning to create fibres containing CNTs would be a forward step in furthering the technology and would demonstrate that centrifugal spinning has sufficient versatility to process a broad range

of feed materials. This chapter demonstrates the dispersion of carbon nanotubes in PCL and PP and centrifugal spinning into fibres.

6.1.1 **Carbon nanotubes**

Iijima (1991) first observed carbon nanotubes and described them graphitic sheets rolled to form a capped or hollow tube, Figure 6.1. A sheet of graphitic carbon is a network of carbon atoms where each carbon atom is linked to three neighbouring C atoms through sp^2 hybridisation which does not allow for the presence of hydrogen in the structure (Vaisman et al., 2006). The nanotubes are constructed in such a way that the length of the tube is orders of magnitudes greater than the diameter, giving carbon nanotubes a high aspect ratio in one dimension which influences the mechanical behaviour (Demczyk et al., 2002).
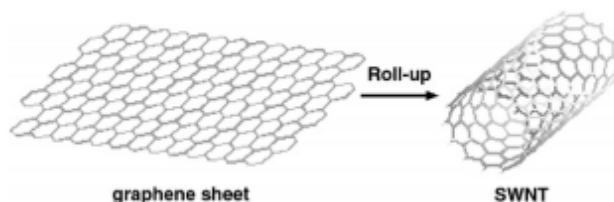
Figure 6.1: Idealised form of carbon nanotubes. A single-walled nanotube is essentially a rolled up graphitic sheet (Vaisman et al., 2006).

Nanotubes are generally produced in two forms: single-walled (SWNT) and multi-walled (MWNT). The former consists of a single tube made from one graphene sheet and is considered to be the simplest and most ideal form of nanotube. The multi-walled form is a series of carbon nanotubes of incrementing sizes in a *telescopic rod* or *Russian doll* configuration. The MWNT form is considered less ideal due to a drop in theoretical conductivity and tensile strength as the graphitic layers interact with each other, reducing the 'purity' compared to single-walled tubes (Moisala et al., 2006). However, the MWNT

form is encountered often in the literature due to lower production costs (Boronat et al., 2012). A TEM of a multi-walled nanotube that reveals multiple tube layers which encase a hollow lumen is presented in Figure 6.2.
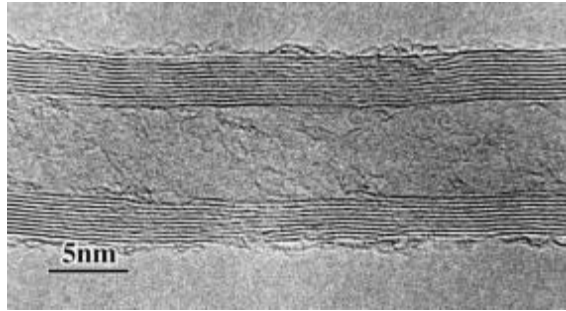
Figure 6.2: TEM of a multi-walled carbon nanotube (Thostenson et al., 2001).

Individual carbon nanotubes have phenomenal tensile properties and the strength of a single nanotube was found to be 150 GPa (Demczyk et al., 2002). Nanotubes are often compared to steel in the literature as they are conveniently found to be over 50 times stronger than conventional steel when normalised for density (Zhang et al., 2009). A single-walled CNT will typically measure less than 10 nm in width but has a comparatively large length resulting in a very high aspect ratio. The two-dimensional structure of carbon nanotubes is extremely stable to mechanical loading due to the resilient and uniform hexagonal carbon structure. There are varying reports on the exact tensile behaviour of CNTs but a pristine SWNT has a theoretical elastic modulus in excess of 1 TPa (Thostenson et al., 2001). This high stiffness, coupled with an empirical tensile strength of over 0.15 TPa makes carbon nanotubes an ideal filler material (Demczyk et al., 2002). The high aspect ratio of CNTs means that even adding low concentrations to a matrix can still achieve significant improvements in mechanical performance (Boronat et al., 2012).

The sp^2 carbon hybridisation of graphitic planes give the constituent carbon atoms a p$_z$ orbital (Moisala et al., 2006; Reich et al., 2004). The free electrons in this orbital are not bound to a single carbon and are therefore mobile along the nanotube. It is this aspect that allows carbon nanotubes to be such effective electrical conductors. It has been documented that the current carrying capacity of a carbon nanotube is over 1000 times that of copper on a weight-weight basis (Thostenson et al., 2001). Adding nanotubes to non-conducting fillers can create electrical networks within the filler to allow for conduction of electrical charge (Moisala et al., 2006). Electron conduction can only occur if nanotubes are overlapping or sufficiently close; isolated carbon nanotubes within a polymer matrix will be electrically insulated and will not significantly change the bulk resistance of a composite. In order for electrical conduction the nanotubes must be present in such a number and dispersion that a complete overlapping network of conducting pathways is formed throughout the material. This critical level of CNT loading is known as the percolation threshold and will depend on: the carbon nanotube form and quality; the polymer matrix used; the fibre or film formation process and the method of nanotube dispersion (Reich et al, 2004; Seo and Park, 2004). In the literature the CNT percolation threshold reported is around 1 % (w/w) but is reported to be as high as 2 % in poorly dispersed compounds (Seo and Park, 2004). Through vigorous mixing and using surfactant aided dispersion the percolation threshold has been recorded as low as 0.2 % CNT loading, however, figures such as this are rare (Tkalya et al., 2012).

Along with mechanical and electrical properties CNTs also have very high thermal conductivity. Berber and co-workers (2000) found that a single isolated carbon nanotube had a thermal conductivity rating of ~6600 Watt per metre Kelvin (W m^{-1} K^{-1}) which is much higher than that observed in metallic material such as pure aluminium which has a

rating of ~210 W m^{-1} K^{-1}. In comparison an insulating polymer such as polypropylene has a very low thermal conductivity of ~0.11 W m^{-1} K^{-1} and is considered to be thermally insulating (Han and Fina, 2011). Plastics and synthetic polymers are known to be poor transmitters of heat and see a significant change in thermal conductance if CNTs were added as filler (Han and Fina, 2011). This poor thermal conductivity has a detrimental effect when these polymers are considered for use as electrical heat sinks for example and could also limit the use of fibres in temperature sensors. The potential for increasing the thermal conductivity has received less attention in the research literature despite the addition of nanotubes being shown to increase the thermal stability and reduce the flammability of polypropylene (Kashiwagi et al., 2002).

The exact mechanical, electrical and thermal properties of carbon nanotubes will depend on the number of graphitic walls; the diameter or chirality of the tubes; the length and the number of faults (Reich et al., 2004; Terrones, 2003)

6.1.2 Carbon nanotube composites

Using CNTs in a matrix is a specific form of composite termed a nanocomposite. These are multi-phase material where one or more components have dimensions less than 100 nm and currently there is a large amount of interest in the inclusion of materials such as sheet graphene and carbon nanotubes (CNTs) into the polymeric material (Boronat et al., 2012; Coleman et al., 2006). This compounding is done in order to utilise the properties of the former with the stability and flexibility of the latter.

The mechanical behaviour of both a solid and a fluid will be significantly altered through the addition of carbon nanotubes. The addition of CNTs is known to improve strength

over the parent polymer and may also improve web strength. Qian et al. (2002) found that addition of 1 % w/w of multi-walled nanotubes to polystyrene film increased the mean strength to 1620 MPa from 1190 MPa. This added increase in mechanical strength may help to improve the absolute strength of nanofibres and may lead to fibres webs being used in more demanding applications (Giraldo et al., 2008). The high stiffness of nanotubes can also increase the Young's modulus and breaking load of a composite compared to the virgin matrix material, Figure 6.3 (Bazbouz and Stylios, 2008). The efficiency of load transfer and subsequent mechanical performance will depend on the quality of the nanotube and the interfacial interaction with the matrix.
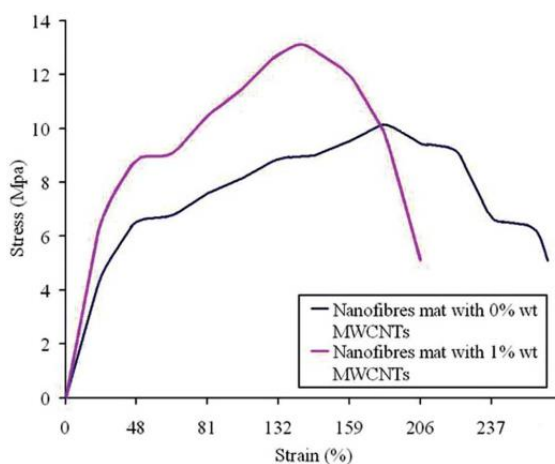
Figure 6.3: Increase in elastic modulus, tensile strength and stiffness through the introduction of MWNTs into Nylon 6 fibres (Bazbouz and Stylios, 2008).

CNT addition is not always done simply to alter the mechanical behaviour or make insulators conduct: it has been demonstrated that nanotube addition can change the chemical behaviour and chemical response of a nanofibre (Weng et al., 2014b, Wiertz, 2014) and so there has been interest in developing nanocomposites using CNTs in order to create smart materials. For example, it has been observed that the electrical conductivity of a nanocomposite may change depending on the environment (Virji et al.,

2004). A further example is the creation of rapid response sensors which utilise the variable electrical properties of carbon nanotubes embedded in a conductive polymer nanocomposite (CPC) (Seo and Park, 2004, Kang et al., 2006). Highly sensitive strain gauges could be created by exploiting the piezoresistive behaviour exhibited by carbon nanotubes (Zhao et al., 2013, Kang et al., 2006). Gas and vapour sensors have also been proposed which utilise electrochemical induced resistive changes in CPCs made from CNTs in a range of matrixes including PMMA (Kang et al., 2006); polypropylene/polycaprolactone (Pötschke et al., 2012); chitosan (Bouvree et al., 2009) and polypyrrole (Jang and Bae, 2007). The high surface area of nanofibres minimises the delay between surface contact and permeation and electrochemical changes in the bulk material.

6.1.2.1 CNTs and rheology

Along with changing the mechanical properties of a solid the addition of carbon nanotubes changes the flow behaviour of a fluid. Carbon nanotubes are known to have a significant effect on the rheology of polymer solutions and melts (Tiwari et al., 2009). The CNTs severely restrict polymer mobility and act as localised anchor points as interfacial interactions restrict chain movement (Song and Youn, 2005; Jin et al., 2001). The magnitude of the effect depends on the level of CNT loading; CNT length and form; the degree of CNT dispersion, polymer molecular weight and the interfacial interactions present between the CNTs and the polymer (Song and Youn, 2005). There is also a marked increase in the storage modulus (the amount of shear force that can be absorbed by a liquid before it begins to flow) of a fluid with the addition of carbon nanotubes (Jin et al., 2001). The high aspect ratio of carbon nanotubes means that using them as filler in a fluid matrix will increase the viscosity significantly even at low loading levels (Seo and Park, 2004).

The reasons presented here mean that the addition of CNTs is a significant factor for fibre spinning as the viscosity of a solution and a melt will be significantly altered which links back to the requirements for steady state spinning presented earlier. It was noted by one author that adding carbon nanotubes to polymers can make fibre spinning difficult if not impossible (Ko et al., 2003). The addition of nanotubes into polymer solutions or melts reduces the elasticity of a fluid which will influence how fibres are formed and how likely jet breakup is to occur (Bangarusampath et al., 2009).

In regards to centrifugal spinning techniques thus far, there have been few papers published that document the production of fibres containing carbon nanotubes (Weng et al., 2014a; O'Haire et al., 2014). As a result there is scope to contribute to understanding the processing of such materials. Centrifugal spinning is considered versatile in terms of the input material so is capable of producing fibres from compound materials which are not suited to other processing techniques. The high aspect ratio of carbon nanotubes means that using them as filler in a fluid matrix will increase the viscosity significantly even at low loading levels (Seo and Park, 2004).

Polymer mats containing carbon nanotubes have been successfully centrifugal spun by Weng and co-workers in two papers using functionalised carbon nanotubes to solution spun using poly(vinyl butyral) (Weng et al., 2014a) and poly(methyl methacrylate) (Weng et al., 2014b). In addition to carbon nanotubes, a nanocomposite of PET/graphene has also been successfully formed into nanofibres using centrifugal spinning (Padron et al., 2012).

6.1.3 **Dispersion of carbon nanotubes**

Carbon nanotubes are extremely difficult to mix homogeneously with a matrix material (Haslam and Raeymaekers, 2013). Dispersing CNTs requires a much more vigorous action than when dispersing conventional particulate or fibre filler. This is due to the long aspect ratio of CNTs and the resulting large surface area that combine to make nanotubes attract, entangle and agglomerate with each other. The current practice of CNT suppliers to deliver dry, entangled bundles further aggravates the issue.

It is known that nanotube agglomeration and poor dispersion result in diminished composite performance in the mechanical behaviour, electrical conductivity and thermal conductivity (Lee et al., 2008; Moisala et al., 2006; Song and Youn, 2005). In their paper, Song and Youn (2005) found that effective carbon nanotube dispersion increased the tensile strength of a composite whereas a poor dispersion had a detrimental effect on final tensile strength compared to the initial matrix material and also reported that effective dispersion increased electrical and thermal conductivity over poorly dispersed carbon nanotube materials.

Prior research has sufficiently established that nanotubes must be thoroughly dispersed before use in order to utilise the benefits and minimise the difficulty of using carbon nanotubes. For example, it has been shown by Siddiqui et al. (2011) that improving the dispersion of CNTs significantly reduced the measured viscosity of an epoxy resin compared to poorly mixed CNTs at the same loading level.
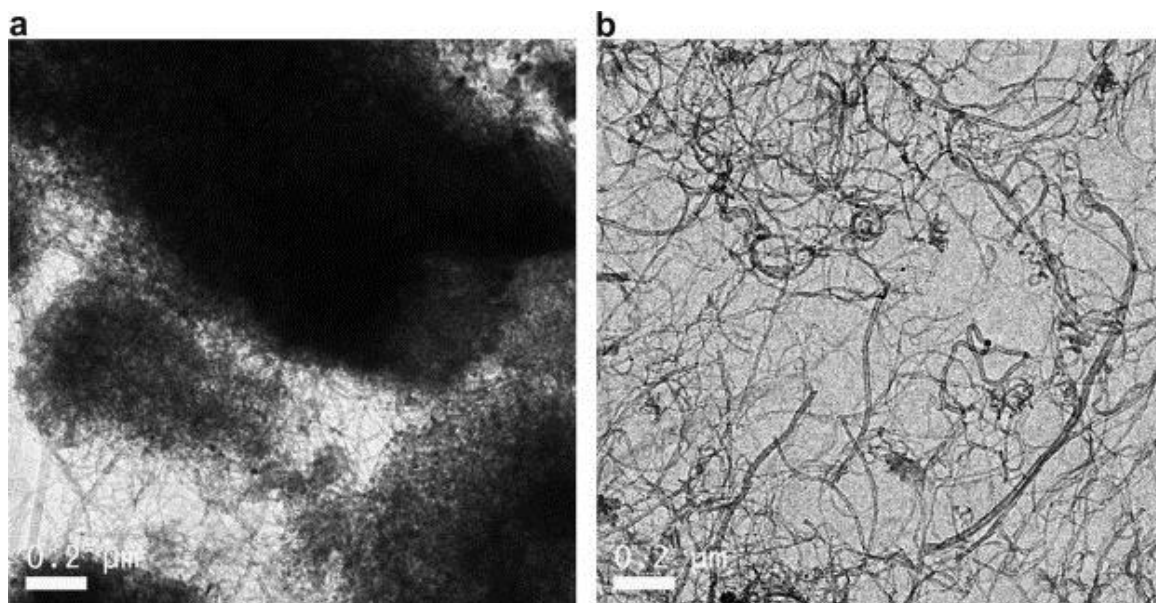
Figure 6.4: CNT composites containing 0.1 % MWNT after a sonication time of a) 20 minutes and b) 90 minutes (Yu et al., 2007).

Mechanical methods of carbon nanotube dispersion are common in the literature (Tkalya et al., 2012; Andrews et al., 2002). Ultrasonic mixing has been identified as an effective way to deagglomerate the bundles and disperse them in a solution through the agitation induced by an ultrasonic pressure wave (Yu et al., 2007). This is typically done using a sonic probe or a sonic bath, Figure 6.4. Ultrasonicators are proven to work well with liquids of low viscosity but, it is argued, become less effective in highly viscous polymer solutions, mechanical mixing being more suitable (Huang and Terentjev, 2012).

In order to successfully disperse nanotubes in polymer solutions suitable for fibre spinning carbon nanotube dispersion usually occurs in the solvent prior to dissolution of the polymer. Ultrasonic mixing has also been shown to damage the nanotubes: the dispersing shockwaves shorten the length of the tubes and introduce defects; thus reducing the mechanical and electrical properties (Huang and Terenrjev, 2012; Ma et al., 2010). For solution processing the polymer and CNT dispersion in solvent can be directly formed into fibres or films using electrospinning or solution cast moulding.

For melt processing there are two primary options for deagglomeration and dispersion of nanotubes, the first being to melt compound using a heated high shear system such as an extruder. It is thought by Ma et al. (2010) that dispersing nanotubes through melt mixing is less aggressive on the nanotubes and does not shorten or break individual tubes. The second principal method of dispersion is to dissolve and mix the polymer into a solvent containing nanotubes already dispersed through sonication. The solvent is then evaporated away leaving behind a polymer nanotube composite. The resulting dried polymer film can then be broken up and fed into a melt spinning system. The solvent dispersion method is a lengthy process but has advantages over melt compounding using shear mixing using twin screw extrusion (O'Haire et al., 2014; Hardy, 2008).

With all dispersion methods there is an optimum mixing time which is the amount of time required to achieve an even dispersion with as little damage to the tubes as possible. This optimum time will depend on the average nanotube length, tendency to agglomerate, intensity of the sonication treatment and the viscosity of the solution (Huang et al., 2012). Deciding on an optimum mixing time depends on the desired level of dispersion and amount of damage to the CNTs that is acceptable.

One of the difficulties in mixing carbon nanotubes into polymeric materials is the absence of a quick and reliable technique to assess the level of dispersion. As of yet, there is no definitive method for quantifying the level of dispersion in the literature (Haslam and Raeymaeker, 2012). Usually TEM is used to scan through a thin slice of material where objects of differing densities create a contrast within the image which can allow individual CNTs or bundles to be observed. This technique is often used to qualitatively assess the dispersion level using subjective measures and broad terms.

There have been attempts at creating a reliable method for quantitatively assessing the nanotube dispersion; Bellayer et al. (2005) proposed using measuring the nearest neighbour distances to generate a dispersion index. However, this method is no longer applicable if agglomerates are still present. An alternative indexing method for assessing mildly dispersed nanotubes is particle size analysis, as proposed by Haslam and Raeymaekers (2013). They created a composite measure that considers agglomerate size and dispersion values measured from TEM images. These values are then averaged to create the composite index *compindex* which varies between 0 for completely undispersed agglomerate to 1 for entirely dispersed discrete elements. This method is useful as it includes agglomerate size along with the level of exfoliation to quantify nanotube dispersion. This method is criticised by Pfeifer and Bandaru (2014) who comment that the concept of a maximum particle size is flawed along with the principle of setting a maximum dispersion level of 1. As of yet there is no widely accepted method for quantitatively assessing the dispersion of carbon nanotubes using TEM slices.

The disadvantage of TEM analysis is that only a very small area is measured at any time and this may not be indicative of the true material. An additional is that TEM can only observe material that is electron transparent which requires extremely thin slices, the preparation of these slices can disrupt the composite and pull out individual nanotubes (Pyrz and Buttrey, 2008). To overcome some of the shortcomings of TEM other techniques have been used to measure the bulk dispersion. Villmow et al. (2008) uses transmission light microscopy to assess dried films of CNTs in poly(lactic acid) and create a dispersion index for different mixing times using a volume fraction relationship of species greater than an arbitrary size. The advantage of this technique is that it allows large areas to be observed in a given image but is only able to resolve and measure larger

agglomerations. This lack of resolution in light microscopes means that individual exfoliated nanotubes (the ideal dispersion state), with diameters in the range of tens of nanometres cannot be identified and may be overlooked (Haslam and Raeymaekers, 2013).

The transmission methods mentioned previously require the sample to be prepared into a solid film for observation and measurement. This is time consuming and not always suitable, as a result there has been work on quantifying the level of dispersion in a bulk liquid using dynamic light scattering (DLS) (Krause et al., 2010). Disadvantages of DLS are the assumption of spherical particle behaviour which does not ideally represent the high aspect ratio CNTs and a limit on the measurable viscosity range tolerated which makes it difficult to measure dispersions in polymer solutions. At present, there is no firmly accepted means of measuring the dispersion of CNTs in a medium; however, TEM analysis is the most widely utilised technique.

6.1.4 Polycaprolactone-nanotube composites

Polycaprolactone-carbon nanotube (PCL-CNT) composite fibres were produced as part of this work using centrifugal spinning. The combining of polycaprolactone with carbon nanotubes has been explored from various angles in the literature: Castro et al. (2009) created a PCL-CNT composite based gas vapour sensors in the form of a thin film and PCL-CNT structures have also been proposed as an improved bone scaffold by Mattioli-Belmonte et al. (2012). Both these products were created by dissolution mixing but alternative compounding methods have been proposed. As PCL is thermoplastic there are examples of shear mixing the carbon nanotubes into the molten polymer (Bone et al., 1999). There are limited reports of creating PCL-CNT composite fibres, the most recent

example produced fibres by electrospinning a PCL-CNT compound that was created the polymerisation process (Saeed et al, 2006). At present, there is scant or no information on using the centrifugal spinning technique to produce PCL-CNT nanocomposites fibres. The advantage of using centrifugal spinning is the potential to process higher viscosity materials compared to electrospinning as evidenced in Chapter 4. In addition, centrifugal spinning is not affected by the dielectric properties of the material, a variable in electrospinning, which is changed dramatically by the introduction of carbon nanotubes (Sarkar et al., 2010). The successful spinning of PCL-CNT fibres using centrifugal spinning demonstrates the versatility of the technique and created fibres for potential utilisation in high value applications.

6.1.5 Polypropylene-nanotube composites

It was demonstrated in Section 3.9 that the web strength of untreated and annealed polypropylene fibres produced via centrifugal spinning was poor. This lack of strength means that the unsupported PP fibres would be unsuitable for applications that demand modest strength and fibre cohesion. It has been shown that the addition of nanotubes to polypropylene (PP-CNT) can increase the modulus of both PP films and fibres (Andrews et al., 2002; Lee et al., 2008). However, this beneficial effect is not found in all the literature as it was reported by Andrews et al. (2002) that the addition of low loadings of nanotubes can reduce the tensile strength of a film. These findings were supported by results published by Moore et al. (2004) who found that adding nanotubes to high MFI polypropylene actually decreased the mechanical strength of the resulting fibres at any nanotube loading level tested compared to virgin PP.

PP-CNT composite fibres are produced through centrifugal spinning as part of this chapter to investigate the feasibility of such processing.

6.1.6 **Carbon nanotube orientation**

The effective mechanical loading and conduction along a one-directional element such as a fibre is facilitated by the orientation of carbon nanotubes along the fibre axis (Fischer et al., 2005). This anisotropic arrangement means that the mechanical loading performance of the nanotubes can be optimised in the directional of expected stress. Aligned carbon nanotubes have been observed to have a fivefold improvement in elastic modulus and ultimate tensile strength compared to randomly orientated material (Thostenson and Chou, 2002).

Carbon nanotubes are more likely to form into an orientated configuration upon the application of shear forces and have been shown to align in extruded filaments (Kearns and Shambaugh, 2002). It would be of use to learn if carbon nanotubes orientate in the fibre axis direction during centrifugal spinning, where the fluid experiences very high shear rates during extension. As part of this work the nanotube orientation in PP-CNT composite fibres is compared to film cast products using polarised Raman microscopy.

6.2 **Summary**

Carbon nanotubes are materials with unique properties having exceptional electrical conductivity and mechanical performance. It is not conclusive as to whether the fibre and web strengths of nonwovens are increased via the addition of carbon nanotubes.

Nanotubes have been observed to make fibres conduct but the percolation threshold varies throughout the literature. Carbon nanotubes are difficult materials to work with, they are difficult to disperse and the high aspect ratio of nanotubes means that they are highly resistant to flow and will change the viscosity of a fluid they are added to. This change in flow behaviour means that the spinning of fibres becomes increasingly difficult as the nanotube loading is increased. It is proposed that centrifugal spinning is versatile enough to be able to produce fibres with a significant CNT loading. Production of nanocomposites using centrifugal spinning represents a development in the technique and there has only been limited work in this area thus far (O'Haire et al., 2014; Weng et al., 2014a; Weng et al., 2014b).

6.3 **Experimental**

In order to build on work conducted in the previous chapters the creation of CNT composites using PP and PCL was investigated. The addition of CNTs even at small loadings could increase the strength of this material which may mean it could be used in more demanding applications or as a freestanding substrate. However, there is also the difficulty in dispersion of CNTs that must be addressed. The practical aims of this chapter were as follows:

1. To create compounds of CNTs in polycaprolactone and polypropylene for subsequent processing via solution and melt centrifugal spinning, respectively;

2. Assess the level of dispersion in both PCL and PP composite films using TEM and image analysis;

3. To measure the effect of CNT addition on the solution and melt rheology;

4. To assess the impact of nanotube addition on fibre production;

5. To characterise the fibres produced using microscopy to determine fibre morphology and typical fibre diameters;

6. Assess the orientation of the carbon nanotubes using polarised Raman microscopy;

7. To measure any changes in the web properties with regards to tensile strength and electrical conductivity.

6.3.1 **Materials**

Polypropylene of grade MF650Y, (melt flow index 1800 g 10 min^{-1}) and Sigma Aldrich supplied polycaprolactone, M_w 80,000, with a melt flow index 1.9 g 10 min^{-1} (80 °C and 0.3 MPa) were used in this section, These polymers were used previously used in Chapter 3 and Chapter 4 respectively. The solvents used for polymer dissolution were decalin (99.9 %), chloroform, (>98 %) and methanol (>99.8 %), all supplied by Sigma Aldrich, UK.

The carbon nanotubes used were multi-walled carbon nanotubes purchased from Southwest Nanotechnologies, USA under the product name Nanocyl N7000. These MWNTs had a reported average diameter of 5.5 nm; an average length of 1.5 μm and carbon purity in excess of 95 %. Typically MWNTs are more economical to use in pilot studies as they have diminished tensile and conduction properties but still display similar behaviour to SWNTs in terms of dispersion and impact on rheology. The Nanocyl MWNTs are delivered as a highly agglomerated dry powder as shown in Figure 6.5.
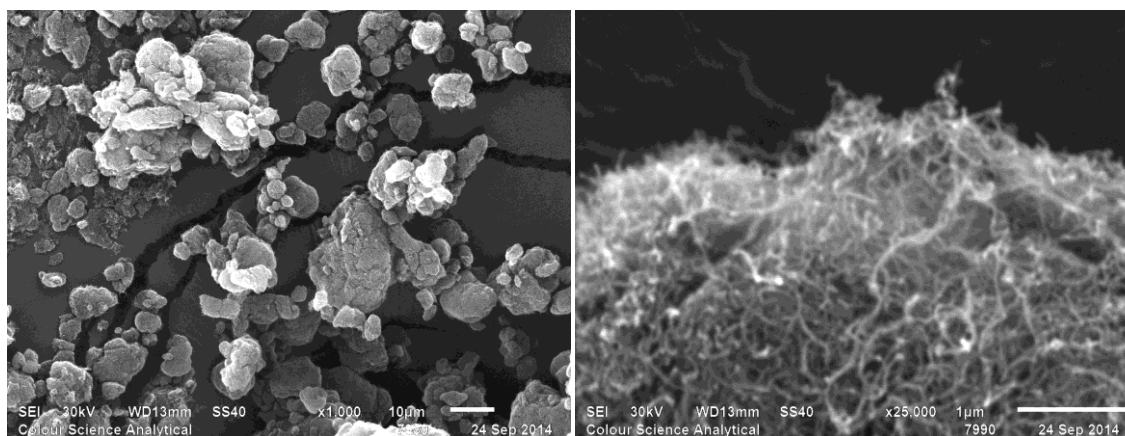
Figure 6.5: SEM micrographs of the Nanocyl N7000 untreated nanotubes showing dense bundles at medium and very high magnifications. Magnification X1000 (left) and X25000 (right).

6.3.2 **Compound preparation**

The PCL-CNT compounds were solution spun and mixing and dispersion of the nanotubes was done using dissolution and sonication. In this preparation method the PCL was added to a 4:1 chloroform/methanol solvent that contained a prescribed amount of dispersed carbon nanotubes. The additives were added in such quantities that the final CNT concentration in the solid composite ranged from 0.25 to 3 % (w/w). The CNTs were added to a 4:1 v/v chloroform: methanol mixture; stirred for 30 minutes and subsequently treated in an Ultrawave U95 ultrasonic bath with a power of 35 W (range 30-40 kHz) for 15 minutes. A brief preliminary study indicated that a PCL concentration of 10 - 12 % (w/v) would yield the best fibre forming properties once CNTs were added. Based on this information PCL-CNT composites with polymer concentrations of 10 % and 12 % (w/v) were created with nanotube loadings ranging between 0.25 and 4 % w/w. Polymer dissolution and mixing occurred at room temperature (RT) over a period exceeding 4 hours and was aided by a magnetic follower. The PCL-CNT compound solution was then subjected to a further 30 minutes in the ultrasonic bath with water at

RT. The solutions were then taken directly to analysis or fibre production with no further treatment.

The PP-CNT compounds were prepared by a dissolution-evaporation procedure identified as being more effective at dispersing carbon nanotubes (O'Haire et al., 2014). By compounding using a solvent the liquid solution can then be subjected to ultrasonic treatment to aid dispersion of the carbon nanotubes. This procedure was used to make compounds of 0.25, 0.5, 1, 2, 3 and 4 % CNT loading using Nanocyl N7000 nanotubes. The relevant weight of CNTs was added to 30 mL of decalin and stirred using a magnetic follower for 30 minutes. The suspension was then sonicated for 15 minutes in a room temperature Ultrawave U95 35 W ultrasonic bath. MF650Y grade polypropylene was then added to create a solution with a polymer concentration 6.67 % weight to volume. Dissolution was aided by a magnetic follower and by heating the solution to 90 °C using a hotplate. The polymer solution was left stirring for 3 hours to ensure dissolution of the polypropylene. Further sonication then occurred for 30 minutes in Ultrawave U95 35 W ultrasonic bath heated to 90 °C. Following sonication the solution was allowed to cool to 70 °C and then poured on to glass plates where the compounds formed a gel which was then set aside for a minimum of 3 days at RT for decalin evaporation. The dried material was then placed overnight in a vacuum oven at 90 °C. The PP-CNT residue was a light grey material which was highly porous and very brittle. This material was then collected by scratching it off the surface of the watch glass. The dried powder was then pressed into a disc using a hot press at 200 °C with 4 bar of pressure. The dried powder and hot pressed samples are shown in Figure 6.6.

Figure 6.6: Cast and dried polypropylene-CNT powder (left) before conversion into composite form (right).

6.3.3 **TEM imaging**

Transmission electron microscopy was used to establish the level of dispersion on a microscopic scale. Fibre cross sections were assessed for nanotube orientation and dispersion by embedding in epoxy resin before slicing using a Reichert-Jung Ultra-microtome. The fibres were embedded and sliced in such a way that it was likely to be able to image a fibre cross section. For fibres that were found to be unsuitable for ultra-microtome slicing an image was instead taken from solidified film constructed of the same material of the compound. The slices were then placed on to a copper TEM grid plate and analysed using a Phillips CM2000 FEGTEM. The images were collected in a bright field configuration and an accelerating voltage of 100 kV was used.

6.3.4 **Viscosity measurement**

The viscosity of PCL-nanotube solutions in 4:1 CM were assessed using rotational viscometry as previously used on homogenous polycaprolactone solutions in Chapter 4. As before, viscosity measurements were made using of a Brookfield LV viscometer. Prepared solutions of 10 and 12 % PCL with a range of nanotubes dispersed within were added to the small sample adapter supplied by the manufacturer; this has a nominal

internal volume of ~10 cm^3. A syringe was used to dispense 9.4 cm^3 of polymer solution into the container and required spindle (34) was then placed into the solution. The spindle is then rotated at 60 rpm for all the samples. At each condition, 3 measurements were taken from a single solution.

The melt rheology of PP-CNT compounds were assessed using capillary rheometry. The samples assessed were PP-CNT compounds with nanotube loadings of 0, 0.5, 1 and 2 % nanotube loadings prepared using the dissolution step outlined previous. Small volumes of PP-CNT (~4 g) were loaded into a Bohlin Instruments (UK) RH2000 capillary rheometer fitted with a 1 x 16 mm capillary die. The polymer compound was heated to a temperature of 210 °C and extruded at shear rates of 1504 s^{-1} and 2510 s^{-1}. The shear stress was calculated using a pressure sensor above the die and the shear viscosity of the samples calculated from the shear stress and shear rate as per Equation 2.1.

6.3.5 **Conductivity**

The conductivity of both the fibres and bulk material was assessed by measuring the internal resistance. For PCL-CNT the films were prepared by pouring ~ 0.5 cm^3 of polymer solution into an open mould 15 mm x 50 mm x 2 mm which was then allowed to solidify through evaporation. The films were solidified in such a way that two pieces of 1 mm diameter bare copper wire was encased within the film at a set distance of 30 mm. The PP composite films were prepared using thermoplastic processing. The copper wire was then used to provide a connection interface across the cross section of the film from which the bulk conductivity can be calculated.
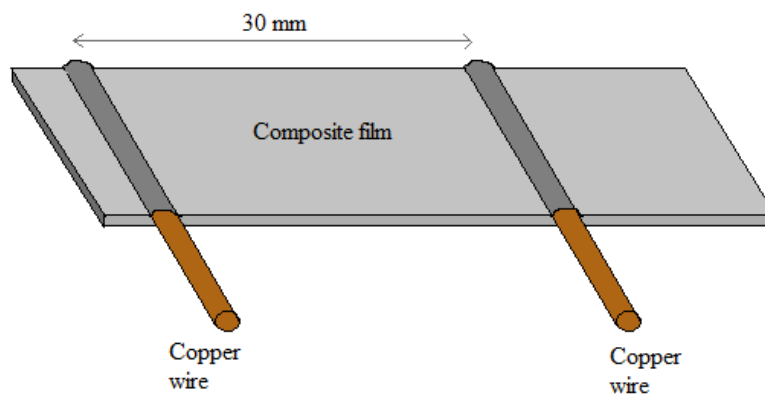
Figure 6.7: Set-up of composite film and copper contacts

The PP-CNT powders prepared previously were hot pressed to form disks ~ 0.3 mm in diameter. These disks were then cut into shapes 15 mm x 50 mm using laser cutting. Heated copper wires were then pressed into the films to create connection points.

For measuring the conductivity of the fibres a similar technique was used. The fibres were arranged into a flat tape 15 mm in width. Copper contacts were pressed into the surface of the web using an insulated laboratory vice. The resistance across a set distance was then measured.

The samples were dried at 30 °C in a vacuum oven for 24 hours to remove any residual solvent and normalise the level of moisture in the samples. A Velleman DVM 1200 high impedance digital multimeter was connected to the copper wires to measure the resistance.

Bulk conductivity was then calculated from the measured resistance by using the following equation:

$$\Phi = \frac{l}{R_\Omega A} \qquad \text{Equation 6.1}$$

Where Φ is the conductivity in Siemens per metre (S m^{-1}), l is the length of the conductor in metres; R_{Ω} is the resistance in ohms and A is the cross sectional area in m^2. As the resistance measured is dependent on the length and the area of the film these parameters will be measured and controlled prior to conductivity calculations.

6.3.6 Centrifugal spinning

Attempts were made to convert PCL-CNT and PP-CNT composite material into fibres using solution and melt centrifugal spinning, respectively.

For solution spinning the PCL-CNT composite material ~2 cm^3 of solution was injected into the double headed spinneret chamber. The spinneret was then fitted with ½ inch 30G (ø = 159 µm) or 27G (ø = 210 µm) needles and then mounted into the fitting and spun at 9,000 rpm for 1 minute. As in Chapter 5, the fibres were collected using the radial posts at a distance of 115 mm.

The melt centrifugal spinning of PP-CNT composite material was done by adding 100 mg of the compound material into the high MFI and low MFI spinnerets. The polymer was then heated to a temperature of 210 ºC. Fibres were produced at a spinneret rotation speed of 14,000 rpm with a total spinning time of 40 seconds. The fibres were collected as a web on the radial posts at a spinning distance of 115 mm.

6.3.7 Fibre analysis

6.3.7.1 Scanning electron microscopy imaging

In addition to TEM image analysis the fibre morphology investigation and diameter measurement at each processing condition was facilitated using scanning electron

microscopy. As in previous chapters SEM will be the primary tool in analysing the fibre diameter and morphology. The fibre sampling and measurement procedure will follow the method listed previously in Section 2.4.2. Where possible, the method detailed on 67 was possible. However, due to practical considerations the prescribed number of fibres could not be measured in all the samples. However, a minimum of 80 fibre diameters measured per sample was always exceeded in order to determine average fibre diameter.

6.3.7.2 **Raman microscopy**

Polarised Raman microscopy was used to measure the alignment of the nanotubes within the centrifugal spun PCL and PP based composite fibres. Raman microscopy is a molecule analysis technique which relies on the anti-Stokes Raman scattering of radiation when atoms are hit with incident photons of set frequency. These scattered photons will have an energy shift that depends on the type of bond structure triggers the inelastic scattering interaction.

Polarised Raman microscopy was performed at Intertek, UK, using a Horiba LabRAM HR confocal Raman microscope with 633 nm laser excitation; a 400 μm confocal aperture; 150 μm entrance slit; a 300 gr mm^{-1} grating and a TE-cooled CCD detector. The spectral scan was centred on 1500 cm^{-1} creating a scanning range of 2300 to 400 cm^{-1}.

The laser was polarised by inserting a half wavelength splitter grating between the laser source and the sample; this allows the fibre to be exposed to radiation whose wavelength was polarised in either the Z direction or the X direction. By placing a similar grating before the detector, the reactive Raman signal was also polarised in the Z or X directions. This experiment used both grating systems thus creating the ZZ and XX polarisation conditions.

PCL and PP fibres with carbon nanotubes were prepared for examination using Raman microscopy. Fibres from both polymers containing 0.5 % and 2 % MWNTs were selected for measurement. These were produced using the low MFI spinneret with a polymer temperature of 210 °C and a rotational speed of 14,000 rpm. In addition, cast films of PP and PCL with the same nanotube loadings were also analysed to demonstrate unaligned MWNT systems. A PP + 2 % extrudate produced using the capillary rheometer equipped with a 1 mm x 16 mm die and using an extrusion speed of 25 mm min^{-1} with a die temperature of 210 °C. Homogenous PP fibres produced through centrifugal spinning with the low MFI spinneret at 210 °C and 14,000 rpm was also analysed to detect the PP specific peaks.

The films and extrudate were stable enough in the laser to not require fixing in place. However, the fibres demonstrated a high amount of drift under the laser beam and were held in place using a Raman invisible glass coverslip. A 100X, metallurgical objective was used to analyse the extruded and film samples. A 100X Glycerol immersion objective was used to analyse the fibres beneath the coverslip. The beam was then focussed on an appropriately orientated fibre using a 1 μm spot size as shown in Figure 6.8.
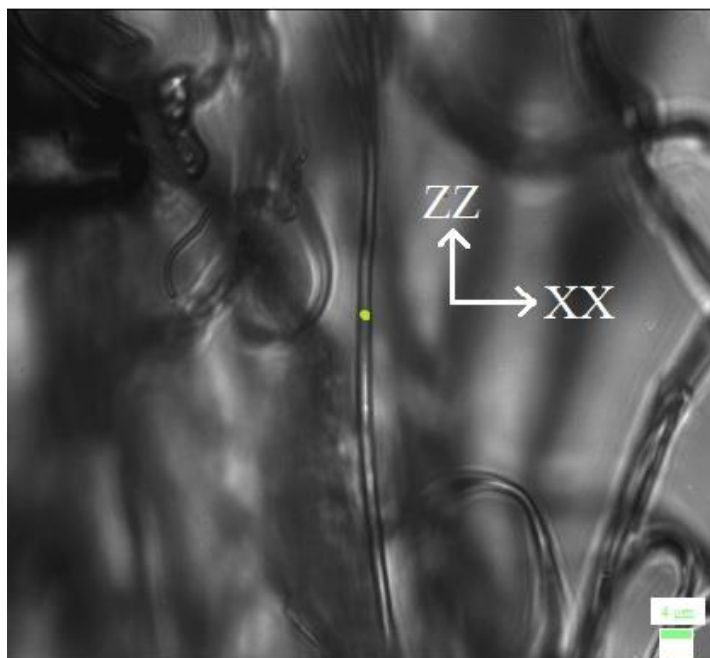
Figure 6.8: Raman spot size and focussing on a PP-CNT fibre with 0.5 % CNT content

A spot size of 1 μm allows for individual fibres to be irradiated and Raman scattering observed. The samples were observed for 2 cycles with a scan time of 30 or 120 seconds depending on the stability of the sample. Measurements were made in the ZZ polarity followed by the XX polarity. A repeat measurement was made in the ZZ direction, a notable change in the intensity of the spectra indicated that the sample had moved and the test series was discarded.

6.3.7.3 Tensile testing

The mechanical behaviour of the 14 % PCL and 12 % + 0.5 % PCL-CNT compounds were analysed for tensile behaviour using a Zwick Z010 testing machine. The webs were condensed into a strip and cut into lengths 125 mm long and weighed before testing. The testing parameters were a 100 mm min^{-1} crosshead speed using an initial 75 mm gauge length with the force measured using a 200 N load cell. The results were then normalised for sample weight and a conversion was made from Newtons (N) to a measure for web tenacity (cN tex^{-1}). Centrifugal spun webs of minimum linear density of 200 mg m^{-1} with

no obvious weak points were selected for tensile testing. A total of 5 webs from each rope were assessed from 3 webs at a given condition.

6.4 Results and discussion

6.4.1 Carbon nanotube dispersions

Carbon nanotube composites were successfully produced from both PCL and PP with CNT loadings as high as 4 %. TEM imaging was then used to produce images detailing compounds with CNT loadings as high as 1 %. Compounds of both polymers were observed to be too brittle for ultra-microtoming when the CNT content was increased to 2 % and beyond.

6.4.1.1 TEM of PCL-CNT

With the PCL-CNT compounds it was not possible to create TEM images of the fibre form due to fibre-matrix delamination during slicing which resulted in resin slices that did not contain any fibres. This can be seen in Figure 6.9.
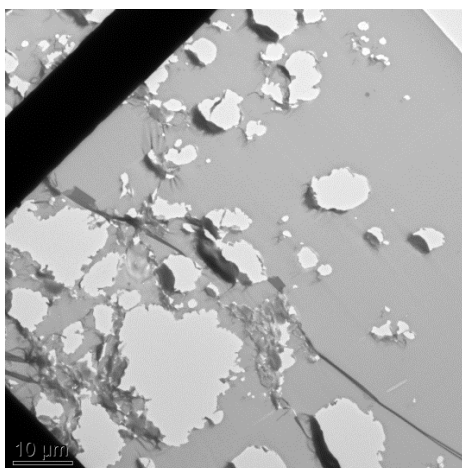
Figure 6.9: 12 % PCL- 0.5 % CNT microtome slices with voids in the place of fibres.

As a result the dispersion of CNTs within PCL fibres could not be characterised in this work. Alternative methods such as dynamic light scattering and cross-sectional SEM generated unsatisfactory results in preliminary testing.

6.4.1.2 **TEM of PP-CNT**

The PP-CNT fibres could be successfully sliced and imaged when embedded in epoxy. However, there was some distortion of the fibre due to the cutting action. This is seen in the left hand image in Figure 6.10.
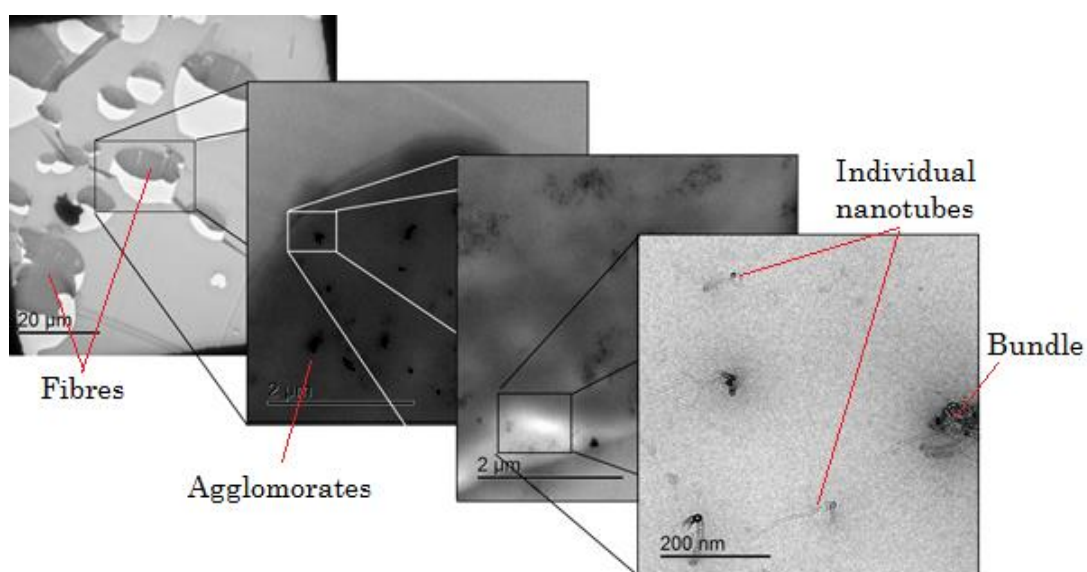
Figure 6.10: CNTs dispersed in centrifugal spun polypropylene fibre with 0.5 % CNTs (PP-CNT)

Figure 6.10 is a compound image showing increasing magnifications of the PP-CNT fibre cross section. This image shows the slight difference in contrast between polypropylene and carbon nanotube which emphasises the need for subsequent image processing. Figure 6.10 demonstrates that agglomerated nanotubes exist alongside individual nanotubes within the PP-CNT fibres. The exfoliation of individual tubes is also shown in Figure 6.11
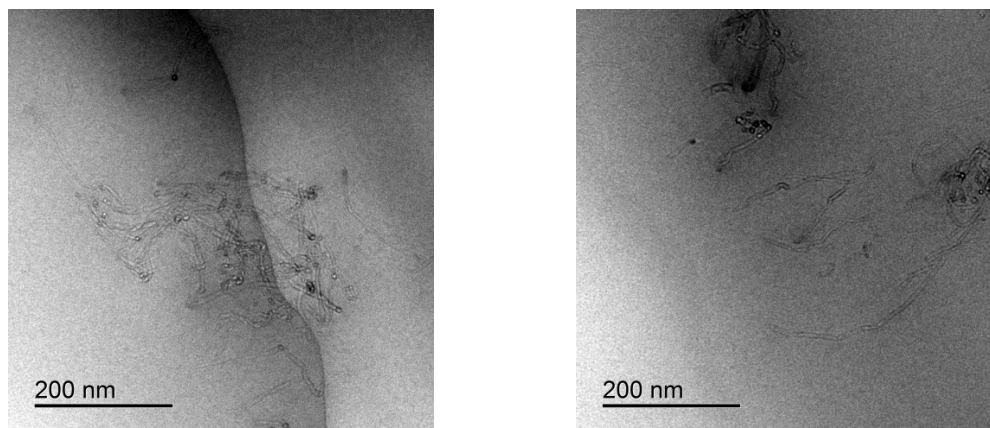
Figure 6.11: TEM micrograph showing individual nanotubes in left: PP-CNT (0.25 %) fibres and right; PP-CNT (0.5 %) fibres.

The TEM slices shown in Figure 6.11 also show how it is difficult to distinguish between agglomerates and sets of overlapping nanotubes. The nanotube bundles shown in this image are linked but are not as tightly packed as other agglomerates. For example a dense bundle is shown in Figure 6.12
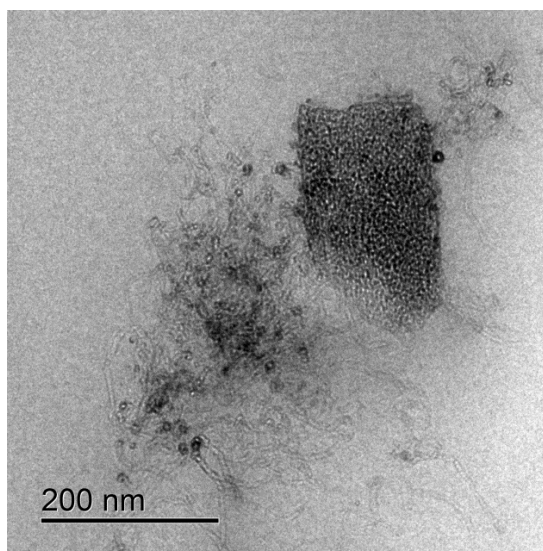
Figure 6.12: Densely packed agglomerate in PP-CNT (0.5 %) fibres.

This figure, along with those preceding it, show that the presence poorly dispersed agglomerates does not prevent PP-CNT from forming fibres. However, agglomerates and

stacked bundles as seen in Figure 6.12 are unlikely to impart advantageous properties to the material due to poor interfacial properties with the matrix.

It was also observed that large bundles and fibres were distributed randomly within the fibres with no visible degree of order. Figure 6.13 shows that a fibre boundary at an appropriate magnification and shows that the nanotubes do not accumulate in any particular region.
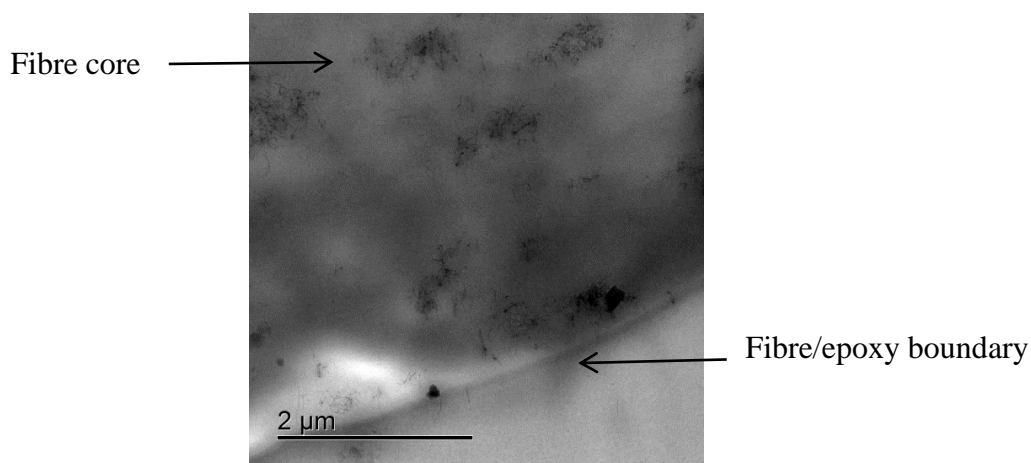
Figure 6.13: TEM image of PP-CNTs fibres with a 0.5 % loading.

This is expected as the physical attributes of nanotubes make them unlikely to migrate within highly viscous polymer solutions; the high aspect ratio of CNTs mean they entangle with each other and the polymer chains restricting movement locally during spinning. This agrees with observations reported by Dror et al. (2003) who also found that the distribution throughout the cross section of a fibre was random. However, more research needs to be done to discount any relationships as area as there is only limited published work available that looks at nanotube distribution within the cross section.

The TEM images presented here show that even after dissolution and sonication there remains a significant number of carbon nanotube agglomerates. These agglomerates limit the number of nanotubes that are free to act within the polymers to conduct or to reinforce.

6.4.2 **Viscosity and rheology measurements**

The PCL-CNT solutions were assessed using dynamic rotational viscosity measurements to confirm the nanotubes effect on solution rheology. This is an extension of the viscosity work performed previously. The results are listed in Table 6.1 and are drawn in a graph shown in Figure 6.14.

Table 6.1: Apparent rotational viscosity of 10 and 12 % PCL in 4:1 chloroform/methanol with differing dry weight loading of carbon nanotubes.

PCL content (% w/v)	CNT loading (% w/w)	Mean viscosity (cP)
10	0	440
10	0.25	508
10	1	571
10	1.5	640
10	2	662
10	3	820
10	4	977
12	0	918
12	0.25	979
12	0.5	1017
12	1	1108
12	1.5	1201
12	3	1280
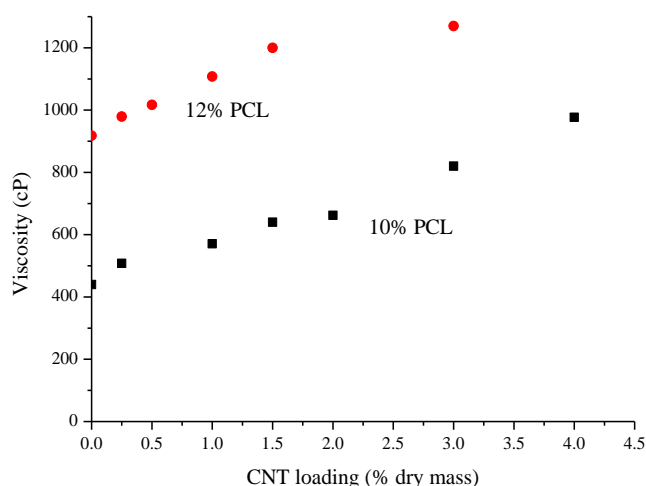
Figure 6.14: Mean viscosity of PCL-CNT solutions in 4:1 chloroform/methanol with nanotube loading.

Table 6.1 and Figure 6.14 show that as the content of CNT increases the viscosity of the fluid also increases. At a 10 % PCL concentration, the addition of 4 % CNT to the dry mass increases the viscosity by more than 100 %. The rigid nanotubes and agglomerates act as anchor points, restricting the movement of the PCL chains requiring a higher shear stress to achieve the same level of flow. Similar results were also observed for the melt processed compounds. The capillary rheometer measurements of the PP-CNT composites are shown below in Table 6.2.

Table 6.2: Apparent melt viscosity of PP-CNT composites.

CNT addition (w/w)	Temperature (°C)	Shear rate (s^{-1})	Shear viscosity ($Pa\ s^{-1}$)
0 %	200	1504	10.2
0 %	200	2105	8.46
0.5 %	200	1504	12.2
0.5 %	200	2105	9.15
1 %	200	1504	n/a
1 %	200	2105	n/a
2 %	200	1504	n/a
2 %	200	2105	n/a

Table 6.2 shows that with a nanotube content of 0.5 % the melt rheology increased to 12.2 Pa S^{-1} from 10.2 Pa S^{-1} at a shear rate of 1504 s^{-1}. Measurements could not be obtained at CNT concentrations of 1 % and greater. The pressure readings were highly variable and an acceptable equilibrium state could not be achieved at either shear rate. The variable pressure readings with high CNT loading are thought to be caused by melt instabilities (Palza et al., 2010). It is proposed that the addition of high numbers of carbon nanotubes increase the magnitude of these instabilities for a given shear rate (Lin-Gibson et al., 2004, Kharchenko et al., 2004).

The PP-CNT viscosity results presented in Table 6.2, along with the solution viscosity changes for PCL-CNT solutions, Table 6.1, page 266, agree with the consensus of research conducted on compound viscosity behaviour. For example, Bangarusampath (2009) documented a similar relationship when nanotubes were added to a poly(ether-ether ketone) solution and the PP-CNT data agrees with the work conducted by Seo and Park (2004) who noted a viscosity increase when nanotubes were added. The viscosity increases as the nanotubes acts as a rigid rod within the polymer solution. These rigid rods are not capable of bending and so to move one part of the nanotube requires the disturbance of all neighbouring elements along the tube. The tubes can be said to act to restrict the movement of the neighbouring polymer chains: increasing the number chains linearly increases the number of potential sticking points.

6.4.3 Conductivity

The conductivity of the fibres could not be measured as the resistance was beyond the working range of the bench top ohmmeter. This high web resistance may be due to the

fibres forming a network that was insufficiently unconnected for linear conduction or issues relating to high contact resistance between fibres or between the web and the contact point (Zhang and Rutledge, 2012).

The bulk conductivity of films made from both polymers was measurable. The conductivity of a material was calculated from the measured resistance using the equation given on page 257. The results of the conductivity measurements are presented in Figure 6.15.
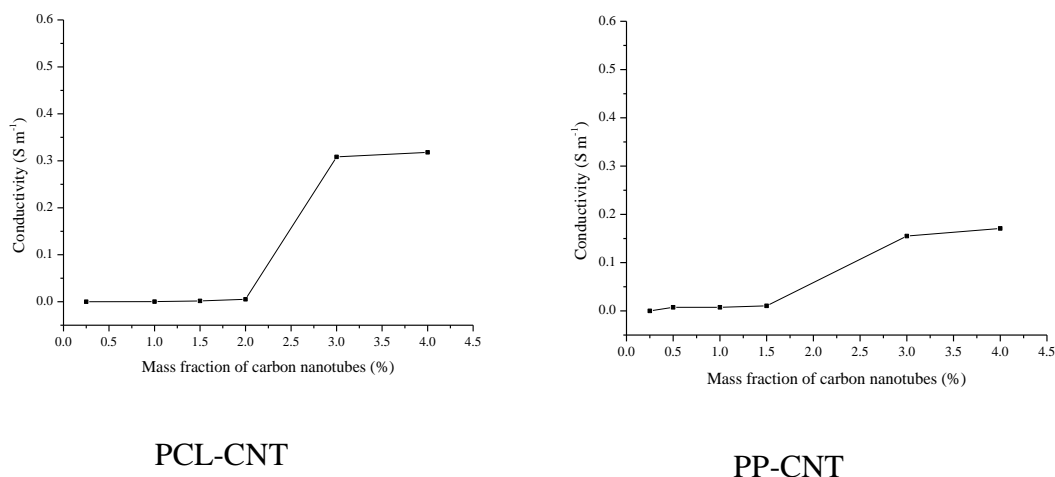
PCL-CNT   PP-CNT

Figure 6.15: Conductivity of 10 % PCL-CNT films (left) and PP-CNT films (right) with CNT loading.

Figure 6.15 indicates that there was a significant change in the level of conductivity with the bulk materials transitioning from insulating to conductive at a mass fraction in excess of 2 % for both polymer types. The conductivity of PCL-CNTs was measured to be over 0.25 S m^{-1} with a 3 % nanotube loading and the conductivity of PP-CNTs also jumped significantly to 0.18 S m^{-1} at the same level of nanotube loading.

The point at which a material is sufficiently loaded with a filler to induce conduction is known as the percolation threshold. Below the percolation threshold the nanotubes are not present in sufficient quantities to produce an overlapping network for electron travel and conductivity of the PCL-CNT and PP-CNT films was in the order of 10^{-5} S m^{-1}.

The CNT percolation threshold measured here exceeds the values reported by Bauhofer and Kovacs (2009) and Seo and Park (2004) who looked at bulk conductivity of PCL (threshold ~1.5 %) and PP (threshold 1 - 2 %), respectively. However, there are various factors that can affect the percolation threshold such as nanotube quality, dispersion method and sample preparation. Loading requirements in excess of 3 % have been measured by others when using polypropylene (threshold ~4 %) have been observed elsewhere (Zhao et al., 2013).

6.4.4 **PCL-CNT fibres**

Fibres were successfully produced from PCL-CNT composite materials using centrifugal spinning. Fibres were created using a range of polymer concentrations and nanotube loadings. Table 6.3 details the results of spinning trails conducted on PCL-CNT materials.

Table 6.3: Results of spinning trials on 10 - 16 % PCL with CNT loadings between 0 and 4 % dry weight.

CNT loading (w/w)	PCL concentration (w/v)			
	10 %	12 %	14 %	16 %
0 %	x	✓	✓	✓
0.25 %	✓	✓	✓	o
0.5 %	✓	✓	✓	o
1 %	✓	✓	o	x
2 %	o	o	o	x
3 %	o	x	x	x
4 %	o	x	x	x

x- no fibres were produced
o- poor quality webs produced
✓-fibres formed

Adding carbon nanotubes to the solution modified the base concentration range of PCL that could be formed into fibres using the prescribed spinning conditions. Spinning fibres of PCL and CNTs required a lower polymer concentration to be used than homogenous PCL. When there were no carbon nanotubes added spinning could be performed from solutions with concentrations as high as 16 % and with low nanotube addition (0.25 %) it was still possible to spin a web, albeit of unsatisfactory yield, with a very low volume of fibrous material actually produced. However, with increasing loading of carbon nanotubes this became increasingly difficult and successful fibre production with 0.5 and 1 % loading required a reduction in base solution concentration to as low as 10 and 12 % PCL. This is attributed to increasing solution viscosity as the nanotubes are added to the solution. It has been noted that on occasion, the spinneret was not exhausted of solution when spinning the higher nanotube loadings. One theory is that the higher viscosity meant that the internal frictional resistance was increased and the solution would not flow down the needle in such a way that steady state fibre production was achieved. However, given that higher viscosity solutions were successfully spun in PCL solutions, Chapter 4, it is more likely that blockages are perhaps caused by larger, undispersed agglomerates blocking the needle. It has been reported previously that PCL could not be electrospun

with high concentrations (≤2 %) of carbon nanotubes; the authors suggested that the carbon nanotubes increase the shear viscosity which changes the elongational behaviour of the fluid (Saeed et al., 2006). Just as the addition of nanotubes makes solid composites more brittle it will also affect fluids in the same way, making them less likely to from fibres and more likely to breakup during spinning.

6.4.4.1 Fibre morphology and diameters

In terms of fibre morphology the PCL-CNT composites displayed comparable texture to the PCL fibres produced from chloroform/methanol in Chapter 4. The PCL-CNT fibres produced here were also spun from 4:1 chloroform/methanol and so the surface pitting is present as shown in Figure 6.16 and Figure 6.17. This indicates that the presence of nanotubes has little effect on the evaporation behaviour of the solvent and the dry skin model proposed is still valid for PCL-CNT fibre spinning. Figure 6.16 also shows the high level of variability in the fibres with diameters as fine as 300 nm observed in the same web as fibres > 15 μm.

Figure 6.16: 10 % PCL with 0. 5 % CNTs spun from chloroform/methanol at 9,000 rpm.

Figure 6.17: 12 % PCL with 1 % CNTs spun from chloroform/methanol at 9,000 rpm.

This variability shown here is typical of all the webs produced from PCL-CNTs. The variation was also seen in the high standard deviations found from the fibre measurements, Table 6.4.

Table 6.4: Mean diameter and standard deviation of PCL-CNT fibres produced through centrifugal spinning at 9,000 rpm.

Nanotube loading (w/w)	PCL concentration (w/v)			
	10 %		12 %	
	Mean (µm)	SD (µm)	Mean (µm)	SD (µm)
0 %	N/A	N/A	1.04	0.86
0.25 %	1.08	0.66	2.22	2.48
0.5 %	1.52	1.25	1.37	1.71
1 %	1.32	1.20	1.52	1.22

Comparisons can be made between the homogenous PCL fibres and PCL-CNTs fibres where both are produced from a base concentration of 12 %. Without CNTs the mean PCL fibre diameter was 1.04 µm. This was significantly less than the PCL-CNT fibres produced from the same base polymer concentration with CNT loadings of 0.25 % and 1

%. However, there was no statistical significance measured between the 0 % and 0.5 % CNT loading conditions in the PCL fibres. The ANOVA statistics were $p < 0.05$, F (12.98) > Fcrit (3.93) for 0.25 % CNT addition; $p > 0.05$, F (2.34) < Fcrit (3.90) for 0.5 % CNT addition; and $p < 0.05$, F (7.35) > Fcrit (3.90) for 1 % CNT addition. This varying statistical significance is attributed to the very high variance (> 100 %) of the PCL-CNT fibres due to the presence of relatively large fibres. This increased within group variance, making it less likely that significance is found. No data was available for a 10 % PCL concentration with 0 % CNT loading so no additional comparisons could be drawn. The measurements confirm the observation made earlier that there was a large level of variability within the samples. The mean fibre diameters and 95 % confidence intervals data are plotted in a chart in shown in Figure 6.18.
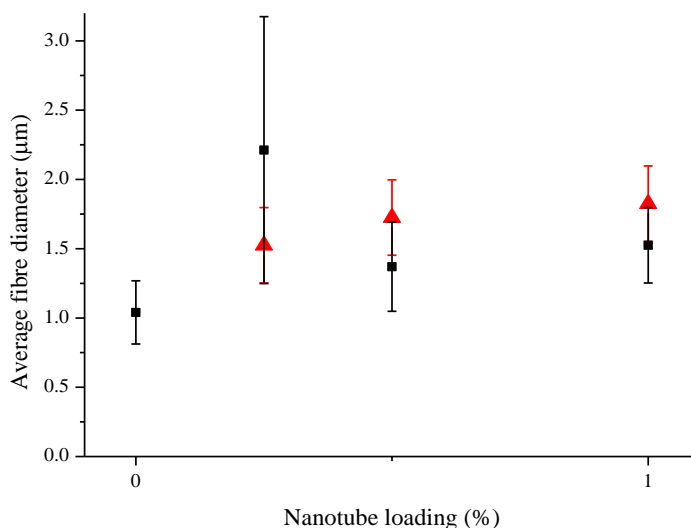
Figure 6.18: Mean diameters and 95 % confidence intervals of PCL-CNT composites depending on nanotube loading. At PCL concentration of 10 % (▲) and 12 % (■).

This chart shows that there was no obvious relationship between nanotube loading and fibre diameter. However, the high variability of PCL-CNTs suggest that more data should be collected in order to establish the true relationship.

6.4.4.2 **Bead formation**

The nanotubes increase the rate of jet breakage and high loadings reduce the jet into beads. This change in fluid stability is also evident at lower CNT loadings as shown by the formation of beads and slugs within the filaments as shown in Figure 6.19.
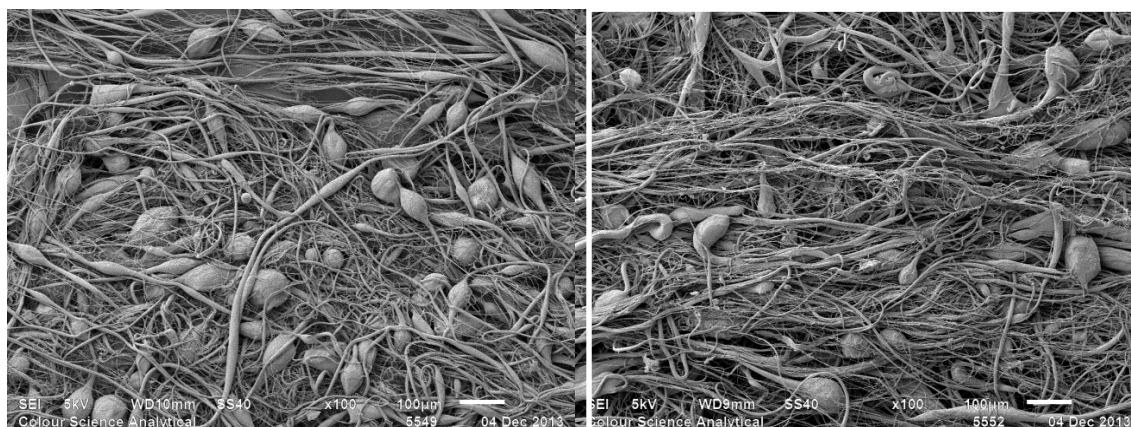
Figure 6.19: Beads on string fibres centrifugal spun from, left, 10 % PCL w/v with 0.5 % CNTs rand right, 12 % PCL w/v with 0.5 % CNTs, both from 4:1 CM.

The beads-on-string fibres are created by the change in surface tension-viscosity balance with nanotube addition. The nanotubes change the elongational flow behaviour which results in non-uniform elongation and an increase in Plateau-Rayleigh instabilities. The addition of nanotubes is known to change the elastic behaviour of a fluid (Erik and Tsu-Wei, 2003). This intensifies the size of the Rayleigh instabilities compared to the unmodified PCL polymer; this leads to an increase in perturbation size. At low CNT loadings this manifests itself as a bead-on-string. This interaction on the jet is drawn in Figure 6.20:
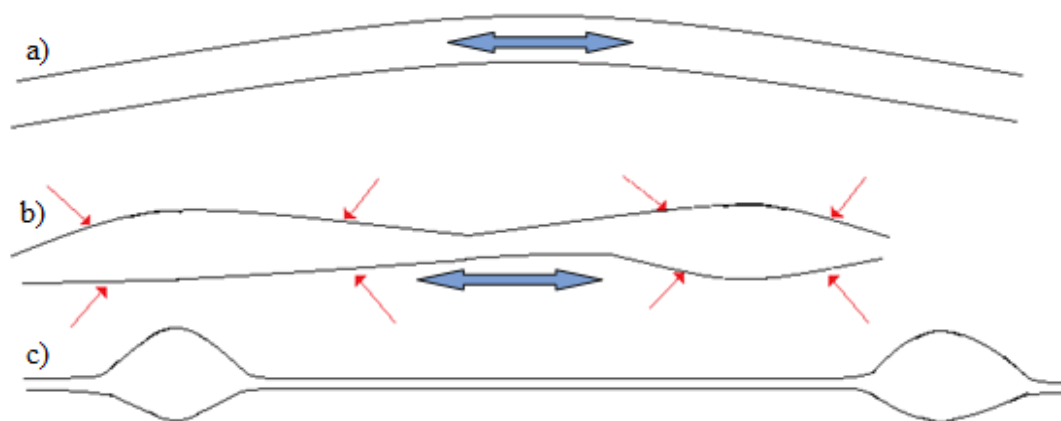
Figure 6.20: The formation of beaded fibres

In Figure 6.20, jet a) is a newly formed jet that is undergoing elongation through inertial and aerodynamic forces. Due to an imbalance between viscosity and surface tension the elongation is not distributed evenly and a narrow neck forms between two regions of material mass, b). Surface tension causes the polymer material to contract and form a stretched droplet. Solvent evaporates and a beaded fibre is formed, c).

An alternative explanation is proposed by Jeong et al. (2007) who propose that beads are formed around nanotube agglomerations. However, this seems unlikely as the largest nanotube bundle observed in TEM was 0.2 μm in diameter whereas the beads were observed to be in excess of 50 μm in diameter which would imply that a small flaw would generate a bead many magnitudes in size. This is possible through nucleation, however, as beads and beads-on-string have been observed before in CNT free PCL fibres then it can be said that the elements observed in this web are more likely due to rheological changes resulting from the presence of nanotubes rather than specific agglomerates acting as nucleation points for beads (Zhang et al., 2005).

At higher nanotube loading the level of spraying increased as evidenced by spraying on the surface of the collector bars, as shown in Figure 6.21:
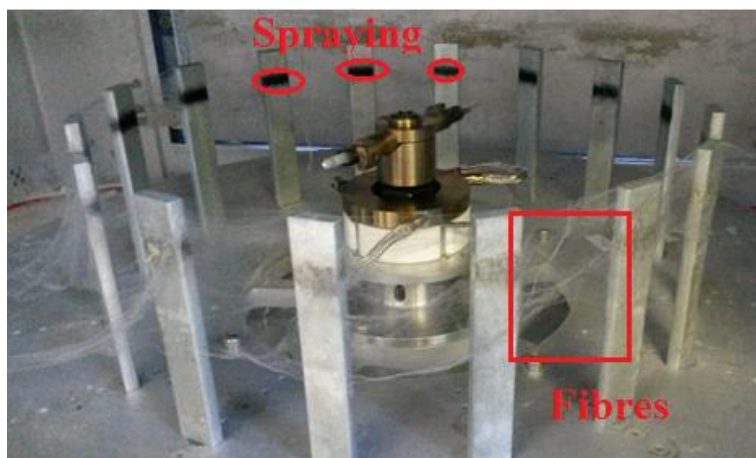
Figure 6.21: 10 % PCL with 2 % CNT loading showing high level of spraying alongside fibre production

The increased number of beads produced during spinning indicates that polymer was able to travel through the needles but the fluid jet was breaking up before solidification could occur. With high nanotube loading the viscosity increased and the solution elasticity decreased (Pilehrood et al., 2012). With a decrease in solution elasticity, the surface tension acts to break up the jet into beads increasing the rate of bead occurrence. A high rate of bead formation is undesirable as it leads to a less cohesive web and less directional strength per weight.

The results collected here have shown PCL-CNT fibres are coarser and more varied than PCL fibres produced under the same conditions with more bead-on-string structures due to increased Rayleigh instabilities. The higher mean fibre diameters are due to the higher fluid viscosities of the PCL-CNT that cause further resistance to elongation. However, as sub-micron fibres were still observed, the primary reason for coarser fibre diameters in the webs was the increased presence of thick fibre regions as the nanotubes increase flow instabilities resulting in non-uniform elongation.

6.4.5 **PP-CNT fibres**

Fibres were successfully produced from PP-CNT composite materials using melt centrifugal spinning. However, could not be produced under all spinning conditions used. Fibre and web production was only satisfactory when processing compounds with lower nanotube loadings. The results of the spinning trials are shown in Table 6.5.

Table 6.5: Result of spinning trials for PP-CNT composites conducted at 14,000 rpm and 210 °C.

CNT loading w/w	Fibre production by spinneret	
	High MFI	Low MFI
0 %	✓	✓
0.25 %	✓	✓
0.5 %	✓	✓
1 %	✓	✓
2 %	✓/o	o
3 %	x	s
4 %	x	s

x- no fibres were made
o- poor web quality
s- spraying of polymer
✓-fibres formed

Under the prescribed conditions the spinning of fibres from PP-CNTs only occurred at nanotube loadings of 1 % and lower. This was due to the carbon nanotubes changing the spinning behaviour of polypropylene. When the nanotube loading was increased to 2 % and upwards isolated fibres were observed but consistent web formation could not be achieved using the fine spinneret. An example of sparse unsatisfactory fibre production when processing compounds containing high nanotube loading is shown in Figure 6.22.

Figure 6.22: Isolated fibres produced when spinning 2 % PP-CNT using the fine spinneret

The creation of isolated fibres showed that whilst the conditions were available for fibre formation the likelihood of jet breakup increased with higher levels of nanotubes that inhibit web formation. This jet breakup hypothesis is backed up by evidence of shot and polymer beads observed on the spinneret wall. At loadings of 3 % and upwards most of the compound remained in the spinneret and was unable to pass through the capillary during spinning and, as with the PCL-CNT solutions the higher viscosity means that the internal frictional resistance is increased and the solution will not flow down the needle in such a way that steady state fibre production is achieved. However, given that higher viscosity solutions were successfully spun in Chapter 4, it is increasingly likely that blockages were caused by larger, undispersed agglomerates creating local regions of high viscosity, thereby blocking the needle or orifice. An alternative theory is that the carbon nanotubes increase the shear viscosity and elongational behaviour of the fluid. Just as the addition of nanotubes makes solid composites more brittle it also acts to reduce the elasticity of fluids (Boronat et al., 2012; Coleman et al., 2006 and Spitalsky et al., 2010). Whereas the polymer concentration of PCL can be reduced to accommodate for nanotube

addition, the viscosity of molten polypropylene cannot be so easily reduced which restricts the tolerance of fibre processing to nanotube addition.

6.4.5.1 Fibre morphology

Typical SEM images taken of the PP-CNT fibres are shown in Figure 6.23 to Figure 6.25. Each web is shown at low and high magnification to show the general web form. Fibre diameter measurements were taken from a set of high magnification images at each processing condition.
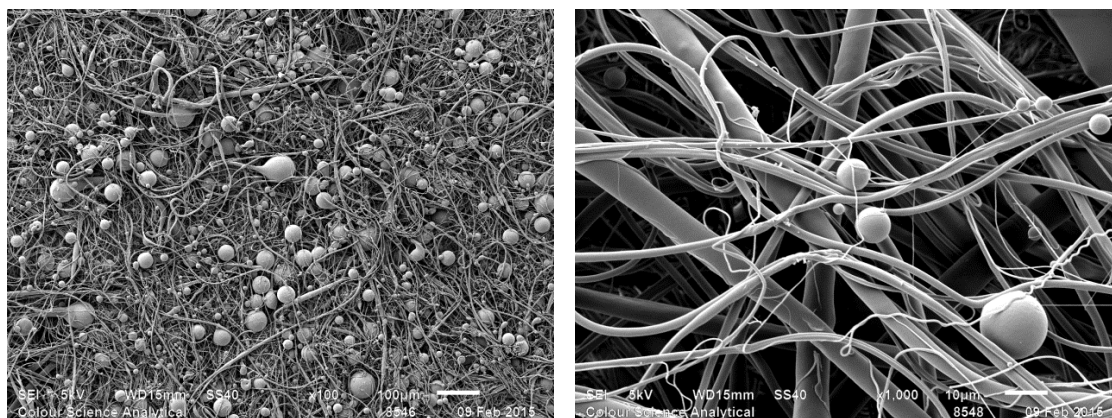
Figure 6.23: SEM micrographs of PP + 0.25 % CNT fibres spun using the fine spinneret. Magnification X100 (left) and X1000 (right).
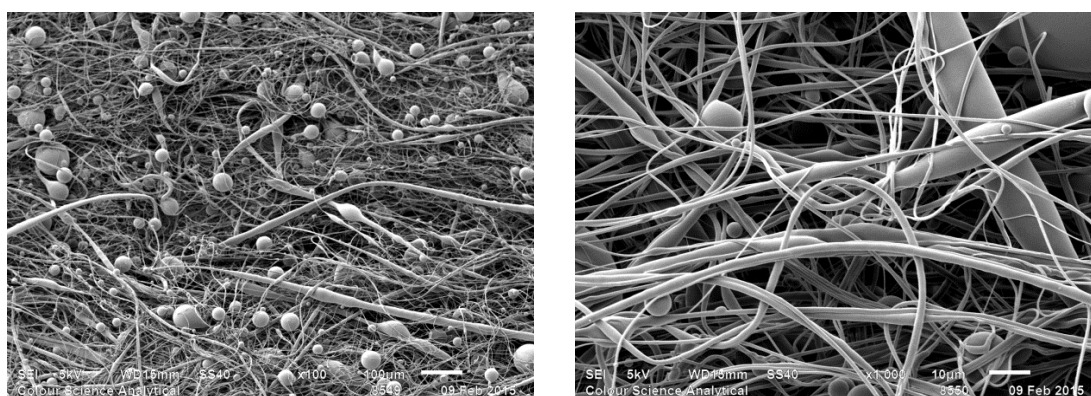
Figure 6.24: SEM micrographs of PP + 0.5 % CNT fibres spun using the coarse spinneret at 14,000 rpm. Magnification X100 (left) and X1000 (right).
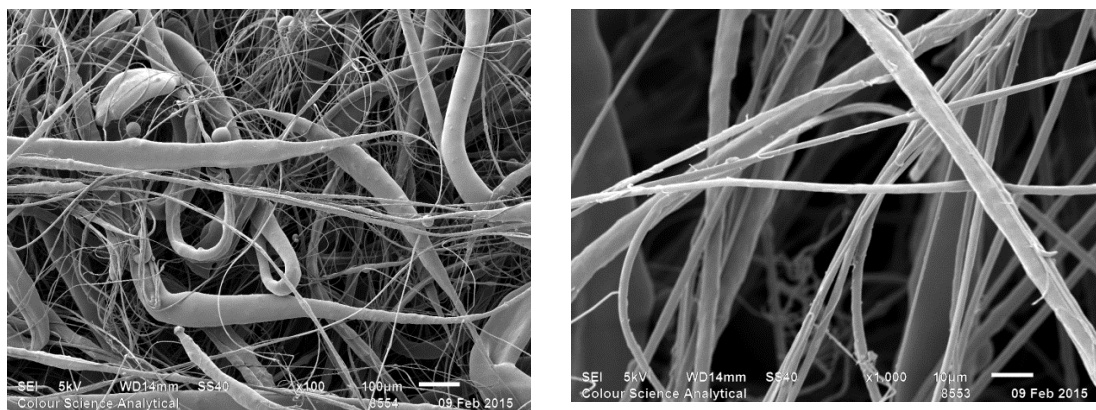
Figure 6.25: SEM micrographs of PP + 2 % CNT spun using the coarse spinneret at 14,000 rpm. Magnification X100 (left) and X1000 (right).

The images reveal that there was a marked increase in beading compared to the homogenous PP fibres produced in Chapter 3. The fibres were also highly variable with a high proportion of coarse fibres. The diameter of the fibres varied significantly in a short distance along the filament length compared to homogenous PP fibres. Both these observations were particularly true for the webs created at 2 % CNT loading, as shown in Figure 6.25. It is possible that some of these "slugs" present in the fibre are formed by the same process as beads-on-string fibres in PCL-CNT composites fibres discussed previously. The high viscosity of PP-CNT composites limit the surface tension contraction, resulting in thick regions within the fibre between which necking occurs.

Aside from the formation of the aforementioned "slugs", the surface of the PP-CNT fibres spun using centrifugal spinning were largely smooth and featureless displaying morphologies typical of melt spun PP fibres. However, unique fibres, with an unusual form and morphology, were observed. These artefacts are shown in Figure 6.26.
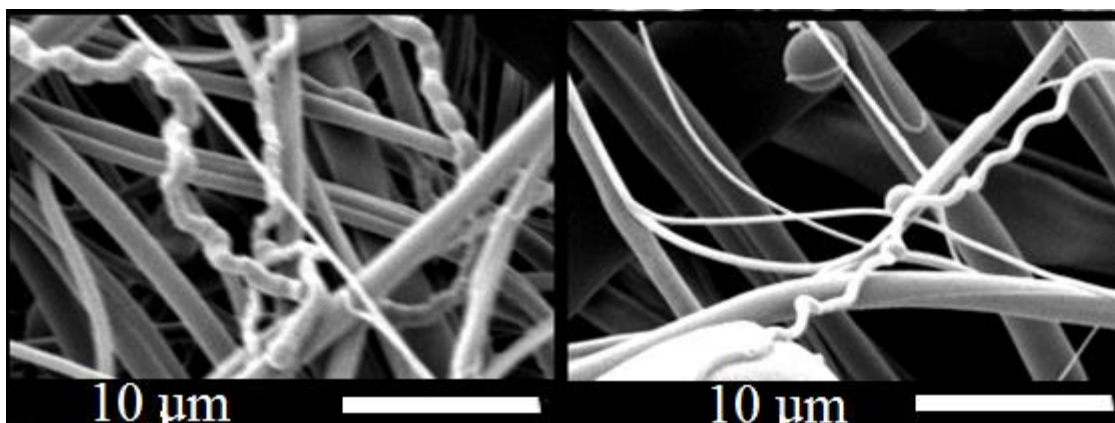
Figure 6.26: SEM micrographs showing crimped and textured fibres in (left) 0.25 % and (right) 0.5 % PP-CNT fibres, both spun using the fine spinneret.

These unique fibres were relatively fine but had an irregular shape and occupied a highly irregular conformation such as spirals and tight coils. It was first hypothesised that these features were caused by Rayleigh instabilities. However, further research suggests these elements are more likely to be formed by melt flow instabilities. The common types of instability found in melt extrusion are sharkskin, melt fracture and spurt instabilities which all create surface texture (Sandler et al., 2004). These are instabilities experienced when a melt, such as polypropylene, undergoes high shear and extensional deformation as it passes through the orifice. Of the three instabilities mentioned previously the features observed are more likely to be spurt instabilities, also known as helical instabilities (Agassant et al., 2006). Spurt instabilities create a periodic fault on the polymer jet as the fluid slips in the spinneret. This periodic fault is then converted into the segmented structures seen by elongation. The SEM micrograph in Figure 6.27 shows an artefact that is proposed to be an unelongated filament that displayed signs of extrusion instability.
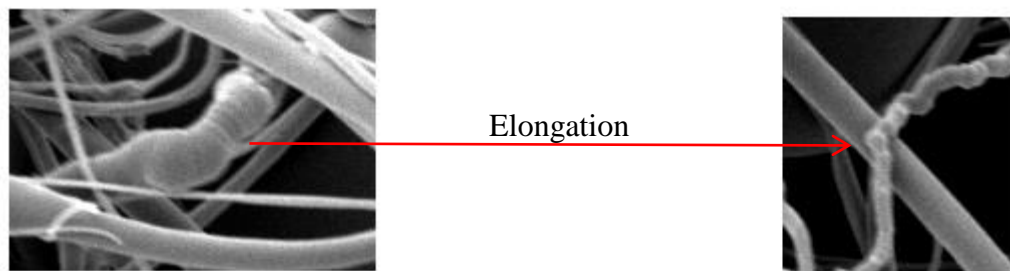
Figure 6.27: SEM micrograph illustrating the effect of coarse spurt instability and the associated unelongated form of helical, segmented elements. Both images observed in PP + 0.5 % CNT samples spun from the coarse spinneret.

It has been shown by Palza et al. (2010) that the addition of CNTs increases the likelihood of spurt instabilities by reducing the critical shear rate at which slippage occurs. Thus, the introduction of CNTs alters the shear and elongational behaviour of the fluid creating perturbations at the orifice resulting in surface roughness and texture. Through elongation the surface ridges are separated and the frequency of these features per unit length decreases. It is thought that the instabilities cause the coiling of a filament as the features may be asymmetric and as the filament extends the instability may unbalance the jet and cause crimping and coiling (Lin-Gibson et al., 2004). These features are few in number and are not as disruptive to web cohesion as beads and shot but they are an interesting phenomenon that have not previously been observed in the literature pertaining to centrifugal spinning.

6.4.5.2 **Fibre diameters**

Analysis of the fibre diameter, measured from the SEM micrographs, indicated that the PP-CNT fibres were also highly variable. Descriptive statistics of the fibre measurements obtained from SEM images are shown in Table 6.6.

Table 6.6: Statistical analysis of PP-CNT fibres produced using centrifugal spinning when using the fine spinneret, rotating at 14,000 rpm.

Compound	Mean fibre diameter (µm)	SD (µm)	Proportion of fibres <1 µm (%)	Proportion of fibres >5 µm (%)
Homogenous PP	0.65	0.22	91.19	0
PP + 0.25 %	1.37	1.26	50.7	3.90
PP + 0.5 %	1.27	1.90	66.2	3.18
PP + 1 %	2.2	2.0	22.1	33.4
PP + 2 %	5.04	5.22	9.3	38.3

Table 6.6 shows that as the percentage of CNTs is increased in the PP fibres there is a shift towards coarser fibres: with a nanotube loading of zero the proportion of sub-micron fibres was over 90 %. With the addition of 0.25 % of dry weight in carbon nanotubes this proportion fell to 50 % and the number of coarse fibres began to increase. From this it can be said that PP-CNT compounds can be spun into fine fibres, however, the process is highly variable and the number of flaws, in the form of "slugs" and thick regions increases. At high nanotube concentrations the proportion of fibres measured to be greater than 5 µm in diameter increased to over one third. The presence of coarser fibres alters the mean diameter of the web. Figure 6.28 shows the mean fibre diameters for PP-CNT fibres based on nanotube loading.
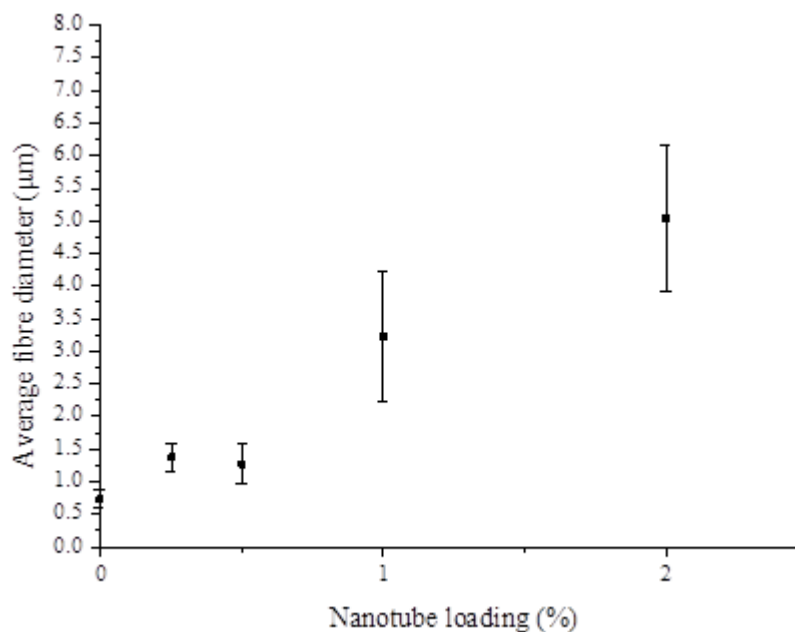
Figure 6.28: Mean diameter and 95 % confidence intervals for PP-CNT fibres based on nanotube loading.

Figure 6.28 shows that there is an increase in average fibre diameter as the filler content of CNTs is increased. Assessment of the SEM micrographs and subsequent measurements suggests that this increase in mean fibre diameter is due to the increasing presence of thicker filaments within the webs. As with PCL-CNT products; the addition of carbon nanotubes alters the rheological properties of the polymer, resulting in higher resistance to elongation and melt flow instabilities which result in a large number of beads but also coarse fibres. It has already been shown in Figure 6.23 to Figure 6.25 that a significant number of beads form during spinning of PP-CNT fibres.

These images can be contrasted to homogeneous PP fibres spun under identical conditions where webs with zero beading smooth, regular fibres was realised as per the SEM images documented previously on page 116. The PP-CNT compounds produced webs with significantly more droplet formation. In particular the SEM analysis showed that the highest degree of shot formation and bead defects was present when processing high

nanotube loadings. The reasons for this are similar to bead formation during the processing of the PCL-CNT compounds: nanotubes increase the viscosity and decrease the elasticity of the polymer melts, this increases the formation of instabilities. These instabilities result in a higher rate of jet breakup. Beads have a detrimental impact on web strength as they offer no directional load bearing ability and add significantly to the fabric weight.

6.4.6 Raman microscopy

6.4.6.1 PCL-CNT fibres

The PCL and PCL–CNT fibres were found to be prone to deformation and movement during scanning. This was also true of the PCL and PCL-CNT films. Poor Raman spectra were recorded in both the ZZ and XX polarisations and the results were deemed unsatisfactory.

6.4.6.2 PP-CNT fibres

FT Raman spectroscopic analysis of the 0.25 % PP-CNT fibre did not produce good quality spectra which was probably due to a low proportion of nanotubes within the fibre. The Anti-Stokes Raman scattering is a weak interaction which can be hard to distinguish if a high intensity is not present. However, in PP-CNT fibres with a 0.5 % and a 2 % CNT loading high quality data was recorded. In addition the PP-CNT film and extrusion also produced satisfactory spectra. The Raman spectra that were successfully recorded are shown in Figure 6.29
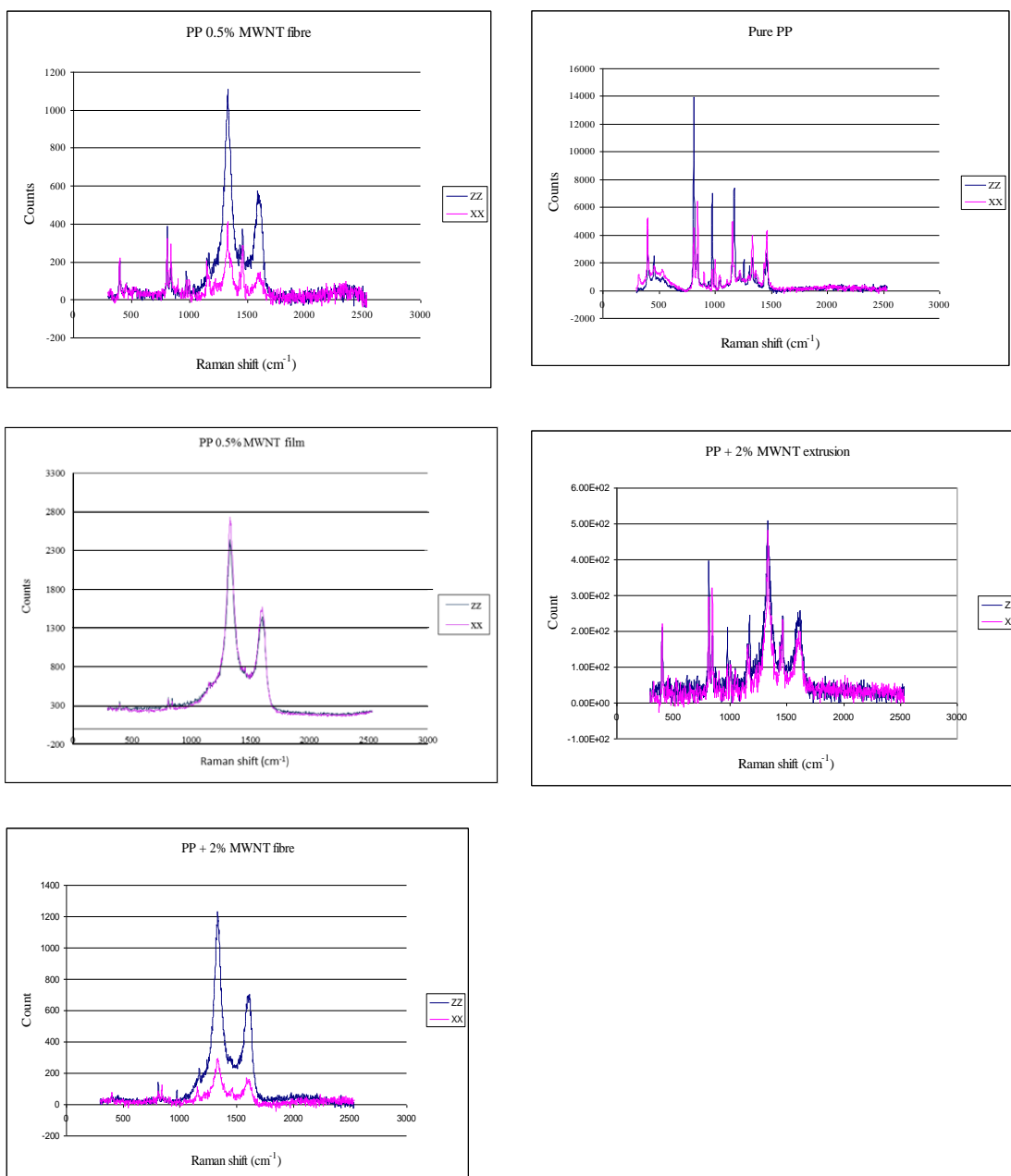
Figure 6.29: Raman spectra for PP-CNT fibres and homogenous PP prepared through centrifugal spinning (Low MFI spinneret) and PP-CNT extrudate at film.

In previous work, the alignment of the nanotubes was observed by examining the relative strength of the radial breathing mode peak (RBM) at around 280 cm^{-1} (Kannan et al., 2007). However, the radial breathing modes, associated with pristine large diameter tubes, is too weak to be observed in MWNTs (Murphy et al., 2006).

The measurements in all PP-CNT materials show two primary peaks at 1640 cm^{-1} and at 1350 cm^{-1} which are absent in the Raman spectra of pure PP fibres. This indicates that these peaks correspond to Raman interactions specific to the carbon nanotubes. A review of the literature indicated that these peaks are linked to the G-band and D-band resonant excitations in carbon nanotubes (Fischer et al., 2005).

Nanotubes have been shown to have a primary excitation peak at a Raman shift at 1593 cm^{-1} by Pimenta et al. (1998). This is known as the tangential G' vibration mode and is typically found at 1592 - 1594cm^{-1}. This is a vibration observed in all sp^2 hybridised carbon materials and is caused by in-plane vibration of the carbon atoms. The D band, found at 1320– 1370 cm^{-1}, is caused by the first order scattering process of sp^2 carbons by the presence of neighbouring in-plane atom vacancies and other defects. As the D band vibration is generated by non-ideal nanotube forms it is seen as an indicator of disorder in the nanotubes (Murphy et al., 2006). For MWNTs this level of disorder and defectiveness, and thus the D band intensity, is high compared to pristine SWNTs.

Rao et al. (2000) showed in their research into MWNT orientations that the intensity of the tangential Raman band (G') and disorder band (D) is sensitive to the polarisation geometry, with intensity being highest when the polarised radiation geometry is the ZZ (fibre axis) configuration.

With this in mind, Figure 6.29 indicates that the MWNTs are strongly orientated in the direction of the nanofibre axis. This agrees of results found elsewhere for fibres produced containing CNTs, for example, Bhattacharyya et al. (2003) demonstrated that the intensity of the G' band, linked to the orientation of CNTs, increased with draw ratio. The

mechanism for this phenomenon is relatively simple and can be compared to the weather wane in the wind, however in this case the directional flow of moving polymer will interact with and rotate the nanotubes in such a way that the resistance to flow in minimised. When centrifugal spinning fibres the polymer flow is in the direction of elongation which will orientate the nanotubes along the fibre axis whilst the polymer is still fluid.

6.4.7 **Tensile properties of the webs**

Only 14 % PCL and PCL-CNT 12 % + 0.5 % CNT were subjected to tensile testing, these two materials were analysed as these conditions produced the most consistent webs with sufficient yield and quality necessary for sample preparation. Descriptive statistics are given in Table 6.7 and typical stress and elongation profiles judged to be indicative of the properties and variations of the webs are shown in Figure 6.30.
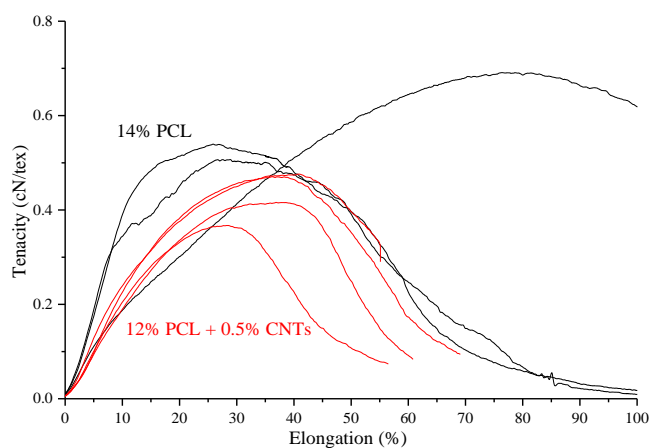
Figure 6.30: Typical tenacity curves for the webs centrifugal spun from PCL with and without the addition of CNTs.

Table 6.7: Tensile results for PCL fibres with and without CNTs

	Tenacity (cN tex^{-1})		Elongation at Break (%)		Young's Modulus (cN tex^{-1})	
	Mean	SD	Mean	SD	Mean	SD
14 % PCL	0.61	0.21	45 %	40 %	3.0	1.1
12 % PCL + 0.5 % CNTs	0.51	0.17	55 %	42 %	2.3	1.5

The tensile results shown in Table 6.7 indicate there was no increase in tenacity or modulus between 14 % PCL and 12 % PCL + 0.5 % CNTs. It can be argued that the PCL-CNT webs actually resulted in a reduction in the elastic modulus and total breaking load on a per weight basis. This can be explained through the increase in jet breakup observed during processing of the compound solution leading to a web with more beads and shorter fibre entanglements per unit weight. As the beading does not contribute to load bearing it will lead to a reduction in web strength regardless of any increase in individual fibre strength.

6.5 Conclusions

Carbon nanotubes were successfully dispersed into polycaprolactone and polypropylene polymers through a dissolution and sonication treatment procedure. The addition of CNTs increased the solution and melt viscosity in the PCL-CNT and PP-CNT systems, respectively, which had implications for fibre formation. The CNTs were observed through TEM and the presence of poorly dispersed agglomerates was observed alongside individual nanotubes.

The PCL-CNT and PP-CNT compounds were successfully formed into fibres using centrifugal spinning. Fibres with a range of nanotube loadings were spun from 10 and

12 % PCL solutions using a spinning speed of 9,000 rpm. High levels of nanotubes (> 1 %) in PCL resulted in significantly more spraying which reduced the web quality compared to homogenous PCL. This was due to the increase in solution viscosity which altered the spinning behaviour of the jet and encourages a high degree of fibre break up. Lower nanotube loadings (0.25 – 1 %) also affected the spinning behaviour and the solutions had a propensity to form beads-on-string structures which were caused by Rayleigh instabilities and are seen as an intermediate stage between smooth fibre formation and jet breakup. Despite the presence of beads, the ability to spin fibres containing 4 % carbon nanotubes highlights the versatility of centrifugal spinning. Apart from an increase in the rate of beading the surface morphology of the fibres remained largely unchanged from those previously observed. The PCL-CNT fibres also displayed the high level of pore formation and texture that was observed in homogenous PCL formed from 4:1 chloroform/methanol.

The PP-CNT fibres were generated by spinning at 12,000 rpm with a polymer temperature of 200 °C. This was done using both the fine and coarse melt spinnerets. As the CNT loading increased it became increasingly difficult to form fibres under the operating conditions used and neither spinneret could successfully produce fibres containing 2 % and upwards of carbon nanotubes. This was due to an increase in the melt viscosity with increasing CNT content. The PP-CNT webs also contained some fibres with a distressed appearance and are determined to have been caused by spurt melt instabilities during processing. The PP-CNT fibres had a slightly disturbed morphology which differed from the smooth filaments produced from homogenous polypropylene.

An experiment revealed that none of the fibres produced in this work were recorded as being electrically conductive due to contact issues. However, the polymer films created from the bulk compounds were shown to conduct with sufficient nanotube loading. A percolation threshold was observed in the bulk material as being between 2 and 3 % of CNT loading. It may be that the fibres were conductive, however if it is difficult to form an electrical contact with the fibres then the potential applications are limited.

In both the PCL-CNT and PP-CNT fibres it was observed through polarised Raman microscopy that the nanotubes are orientated in the direction of the fibre axis in PP-CNT nanofibres. The nanotubes will influence the direction properties of the polymer and are orientated during the elongation flow experienced during fibre spinning.

There was no significant or consistent change in the tensile properties of the webs with the addition of carbon nanotubes. 12 % PCL + 0.5 % CNT webs were compared to homogenous 14 % PCL webs with both samples produced through centrifugal spinning. There was no increase in tensile strength or modulus for the former samples. This assessment of web strength is more a reflection of the number of fibre entanglements, defects and cohesion within the web and may not be a sensitive indicator of absolute fibre strength. The data obtained indicated there was actually a decrease in tensile performance on a per-weight basis observed with the addition of CNTs which can be attributed to an increase in bead and fibre defects within the webs which reduce the strength of the nonwoven. However, for more detailed analysis, more testing would need to be done, including tensile measurements of a single fibre.

6.6 **References**

AGASSANT, J.-F., ARDA, D. R., COMBEAUD, C., MERTEN, A., MUENSTEDT, H., MACKLEY, M. R., ROBERT, L. & VERGNES, B., 2006. Polymer processing extrusion instabilities and methods for their elimination or minimisation. *International Polymer Processing,* 21**,** 239-255.

ANDREWS, R., JACQUES, D., MINOT, M. & RANTELL, T., 2002. Fabrication of carbon multiwall nanotube/polymer composites by shear mixing. *Macromolecular Materials and Engineering,* 287**,** 395-403.

BANGARUSAMPATH, D. S., RUCKDÄSCHEL, H., ALTSTÄDT, V., SANDLER, J. K. W., GARRAY, D. & SHAFFER, M. S. P., 2009. Rheology and properties of melt-processed poly(ether ether ketone)/multi-wall carbon nanotube composites. *Polymer,* 50**,** 5803-5811.

BAZBOUZ, M. B. & STYLIOS, G. K., 2008. Alignment and optimization of nylon 6 nanofibers by electrospinning. *Journal of Applied Polymer Science,* 107**,** 3023-3032.

BAZBOUZ, M. B. & STYLIOS, G. K., 2010. The tensile properties of electrospun nylon 6 single nanofibers. *Journal of Polymer Science Part B: Polymer Physics,* 48**,** 1719-1731.

BELLAYER, S., GILMAN, J. W., EIDELMAN, N., BOURBIGOT, S., FLAMBARD, X., FOX, D. M., DE LONG, H. C. & TRULOVE, P. C., 2005. Preparation of homogeneously dispersed multiwalled carbon nanotube/polystyrene nanocomposites via melt extrusion using trialkyl imidazolium compatibilizer. *Advanced Functional Materials,* 15**,** 910-916.

BERBER, S., KWON, Y.-K. & TOMANEK, D., 2000. Unusually high thermal conductivity of carbon nanotubes. *Physical Review (Letters),* 84**,** 4613.

BHATTACHARYYA, A. R., SREEKUMAR, T. V., LIU, T., KUMAR, S., ERICSON, L. M., HAUGE, R. H. & SMALLEY, R. E., 2003. Crystallization and orientation studies in polypropylene/single wall carbon nanotube composite. *Polymer,* 44**,** 2373-2377.

BOND, E. B., SPRUIELL, J. E. & LIN, J. S., 1999. A WAXD/SAXS/DSC study on the melting behavior of Ziegler–Natta and metallocene catalyzed isotactic polypropylene. *Journal of Polymer Science Part B: Polymer Physics,* 37**,** 3050-3064.

BORONAT, T., GARCIA-SANOGUERA, D., PASCUAL, J., PERIS, F. & SANCHEZ-NACHER, L., 2012. Comparative study of the rheological behavior of multiwalled carbon nanotubes and nanofiber composites prepared by the dilution of a masterbatch of polypropylene. *Journal of Applied Polymer Science,* 126**,** 1044-1052.

BOUVREE, A., FELLER, J.-F., CASTRO, M., GROHENS, Y. & RINAUDO, M., 2009. Conductive polymer nano-biocomposites (CPC): chitosan-carbon nanoparticle a good candidate to design polar vapour sensors. *Sensors and Actuators B: Chemical,* 138**,** 138-147.

CASTRO, M., LU, J., BRUZAUD, S., KUMAR, B. & FELLER, J.-F., 2009. Carbon nanotubes/poly (ε-caprolactone) composite vapour sensors. *Carbon,* 47**,** 1930-1942.

COLEMAN, J. N., KHAN, U., BLAU, W. J. & GUN'KO, Y. K., 2006. Small but strong: A review of the mechanical properties of carbon nanotube–polymer composites. *Carbon,* 44**,** 1624-1652.

DEMCZYK, B., WANG, Y., CUMINGS, J., HETMAN, M., HAN, W., ZETTL, A. & RITCHIE, R., 2002. Direct mechanical measurement of the tensile strength and elastic modulus of multiwalled carbon nanotubes. *Materials Science and Engineering: A,* 334**,** 173-178.

DROR, Y., SALALHA, W., KHALFIN, R. L., COHEN, Y., YARIN, A. L. & ZUSSMAN, E., 2003. Carbon nanotubes embedded in oriented polymer nanofibers by electrospinning. *Langmuir,* 19**,** 701

ERIK, T. T. & TSU-WEI, C., 2003. On the elastic properties of carbon nanotube-based composites: modelling and characterization. *Journal of Physics D: Applied Physics,* 36**,** 5732-7020.

FISCHER, D., PÖTSCHKE, P., BRÜNIG, H. & JANKE, A., 2005. Investigation of the orientation in composite fibers of polycarbonate with multiwalled carbon nanotubes by Raman microscopy. *Macromolecular Symposia,* 230**,** 167-172.

GIRALDO, L. F., BROSTOW, W., DEVAUX, E., PEZ, B. L., REZ, L. & N, D., 2008. Scratch and wear resistance of polyamide 6 reinforced with multiwall carbon nanotubes. *Journal of Nanoscience and Nanotechnology,* 8**,** 3176-3183.

HAN, Z. & FINA, A., 2011. Thermal conductivity of carbon nanotubes and their polymer nanocomposites: a review. *Progress in Polymer Science,* 36**,** 914-944.

HASLAM, M. D. & RAEYMAEKERS, B., 2013. A composite index to quantify dispersion of carbon nanotubes in polymer-based composite materials. *Composites Part B: Engineering,* 55**,** 16-21.

HARDY, V.-G., 2008. *Design and construction of smart structures for technical textiles.* Doctor of Philosophy Thesis, University of Leeds.

HUANG, Y. Y. & TERENTJEV, E. M., 2012. Dispersion of carbon nanotubes: mixing, sonication, stabilization and composite properties. *Polymers*, 4, 275-295.

IIJIMA, S., 1991. Helical microtubules of graphitic carbon. *Nature,* 354**,** 56-58.

JANG, J. & BAE, J., 2007. Carbon nanofiber/polypyrrole nanocable as toxic gas sensor. *Sensors and Actuators B: Chemical,* 122**,** 7-13.

JEONG, J. S., MOON, J. S., JEON, S. Y., PARK, J. H., ALEGAONKAR, P. S. & YOO, J. B., 2007. Mechanical properties of electrospun PVA/MWNTs composite nanofibers. *Thin Solid Films,* 515**,** 5136-5141.

JIN, Z., PRAMODA, K. P., XU, G. & GOH, S. H., 2001. Dynamic mechanical behavfior of melt-processed multi-walled carbon nanotube/poly(methyl methacrylate) composites. *Chemical Physics Letters,* 337**,** 43-47.

KANG, I., HEUNG, Y. Y., KIM, J. H., LEE, J. W., GOLLAPUDI, R., SUBRAMANIAM, S., NARASIMHADEVARA, S., HURD, D., KIRIKERA, G. R., SHANOV, V., SCHULZ, M. J., SHI, D., BOERIO, J., MALL, S. & RUGGLES-WREN, M., 2006. Introduction to carbon nanotube and nanofiber smart materials. *Composites Part B: Engineering,* 37**,** 382-394.

KANNAN, P., EICHHORN, S. J. & YOUNG, R. J., 2007. Deformation of isolated single-wall carbon nanotubes in electrospun polymer nanofibres. *Nanotechnology,* 18, 235707.

KASHIWAGI, T., GRULKE, E., HILDING, J., HARRIS, R., AWAD, W. & DOUGLAS, J., 2002. Thermal degradation and flammability properties of poly (propylene)/carbon nanotube composites. *Macromolecular Rapid Communications,* 23**,** 761-765.

KHARCHENKO, S. B., DOUGLAS, J. F., OBRZUT, J., GRULKE, E. A. & MIGLER, K. B., 2004. Flow-induced properties of nanotube-filled polymer materials. *Nature Materials,* 3**,** 564-568.

KO, F., GOGOTSI, Y., ALI, A., NAGUIB, N., YE, H., YANG, G. L., LI, C. & WILLIS, P., 2003. Electrospinning of continuous carbon nanotube-filled nanofiber Yarns. *Advanced Materials,* 15**,** 1161-1165.

KRAUSE, B., MENDE, M., PÖTSCHKE, P. & PETZOLD, G., 2010. Dispersability and particle size distribution of CNTs in an aqueous surfactant dispersion as a function of ultrasonic treatment time. *Carbon,* 48**,** 2746-2754.

LEE, G.-W., JAGANNATHAN, S., CHAE, H. G., MINUS, M. L. & KUMAR, S., 2008. Carbon nanotube dispersion and exfoliation in polypropylene and structure and properties of the resulting composites. *Polymer,* 49**,** 1831-1840.

LIN-GIBSON, S., PATHAK, J. A., GRULKE, E. A., WANG, H. & HOBBIE, E. K., 2004. Elastic flow instability in nanotube suspensions. *Physical Review (Letters),* 92**,** 048302.

MATTIOLI-BELMONTE, M., VOZZI, G., WHULANZA, Y., SEGGIANI, M., FANTAUZZI, V., ORSINI, G. & AHLUWALIA, A., 2012. Tuning polycaprolactone–carbon nanotube composites for bone tissue engineering scaffolds. *Materials Science and Engineering: C,* 32**,** 152-159.

MOISALA, A., LI, Q., KINLOCH, I. & WINDLE, A., 2006. Thermal and electrical conductivity of single- and multi- walled carbon nanotube-epoxy composites. *Composites Science and Technology,* 66, 1285-1288.

MOORE, E. M., ORTIZ, D. L., MARLA, V. T., SHAMBAUGH, R. L. & GRADY, B. P., 2004. Enhancing the strength of polypropylene fibers with carbon nanotubes. *Journal of Applied Polymer Science,* 93**,** 2926-2933.

MURPHY, H., PAPAKONSTANTINOU, P. & OKPALUGO, T. T., 2006. Raman study of multiwalled carbon nanotubes functionalized with oxygen groups. *Journal of Vacuum Science & Technology B,* 24**,** 715-720.

O'HAIRE, T., RIGOUT, M., RUSSELL, S. & CARR, C., 2014. Influence of nanotube dispersion and spinning conditions on nanofibre nanocomposites of polypropylene and multi-walled carbon nanotubes produced through Forcespinning™. *Journal of Thermoplastic Composite Materials,* 27**,** 205-214.

PADRON, S., PATLAN, R., GUTIERREZ, J., SANTOS, N., EUBANKS, T. & LOZANO, K., 2012. Production and characterization of hybrid BEH-PPV/PEO conjugated polymer nanofibers by forcespinning™. *Journal of Applied Polymer Science***,** 3610-3616.

PALZA, H., REZNIK, B., KAPPES, M., HENNRICH, F., NAUE, I. F. C. & WILHELM, M., 2010. Characterization of melt flow instabilities in polyethylene/carbon nanotube composites. *Polymer,* 51, 3753-3761.

PFEIFER, S. & BANDARU, P. R., 2014. A methodology for quantitatively characterizing the dispersion of nanostructures in polymers and composites. *Materials Research Letters,* 2**,** 166-175.

PILEHROOD, M. K., HEIKKILÄ, P. & HARLIN, A., 2012. Preparation of carbon nanotube embedded in polyacrylonitrile (pan) nanofibre composites by electrospinning process. *AUTEX Research Journal,* 12**,** 1-6.

PIMENTA, M. A., MARUCCI, A., EMPEDOCLES, S. A., BAWENDI, M. G., HANLON, E. B., RAO, A. M., EKLUND, P. C., SMALLEY, R. E., DRESSELHAUS, G. & DRESSELHAUS, M. S., 1998. Raman modes of metallic carbon nanotubes. *Physical Review B,* 58**,** 16016-16019.

PYRZ, W. D. & BUTTREY, D. J., 2008. Particle size determination using TEM: adiscussion of image acquisition and analysis for the novice microscopist. *Langmuir,* 24, 11350-11360.

QIAN, D., DICKEY, E. C., ANDREWS, R. & RANTELL, T., 2000. Load transfer and deformation mechanisms in carbon nanotube-polystyrene composites. *Applied Physics Letters.*76, 2868-2870.

QIAN, D., WAGNER, G. J., LIU, W. K., YU, M.-F. & RUOFF, R. S., 2002. Mechanics of carbon nanotubes. *Applied Mechanics Reviews*, 55, 495-533.

RAO, A. M., JORIO, A., PIMENTA, M. A., DANTAS, M. S. S., SAITO, R., DRESSELHAUS, G. & DRESSELHAUS, M. S., 2000. Polarized Raman study of aligned multiwalled carbon nanotubes. *Physical Review Letters*, 84, 1820-1823.

REICH, S., THOMSEN, J. & MAULTZSCH, J., 2004. *Carbon nanotubes: basic concepts and physical properties.* Wiley, Germany.

SAEED, K., PARK, S.-Y., LEE, H.-J., BAEK, J.-B. & HUH, W.-S., 2006. Preparation of electrospun nanofibers of carbon nanotube/polycaprolactone nanocomposite. *Polymer,* 47**,** 8019-8025.

SANDLER, J. K. W., PEGEL, S., CADEK, M., GOJNY, F., VAN ES, M., LOHMAR, J., BLAU, W. J., SCHULTE, K., WINDLE, A. H. & SHAFFER, M. S. P., 2004. A comparative study of melt spun polyamide-12 fibres reinforced with carbon nanotubes and nanofibres. *Polymer,* 45**,** 2001-2015.

SARKAR, K., GOMEZ, C., ZAMBRANO, S., RAMIREZ, M., DE HOYOS, E., VASQUEZ, H. & LOZANO, K., 2010. Electrospinning to Forcespinning™. *Materials Today,* 13**,** 12-14.

SEO, M.-K. & PARK, S.-J., 2004. Electrical resistivity and rheological behaviors of carbon nanotubes-filled polypropylene composites. *Chemical Physics Letters,* 395**,** 44-48.

SPITALSKY, Z., TASIS, D., PAPAGELIS, K. & GALIOTIS, C. 2010., Carbon nanotube–polymer composites: Chemistry, processing, mechanical and electrical properties. *Progress in Polymer Science,* 35**,** 357-401.

TERRONES, M., 2003. Science and technology of the twenty-first century: synthesis, properties and applications of carbon nanotubes. *Annual Review of Materials Research*, 33, 419-501.

THOSTENSON, E. T., REN, Z. & CHOU, T.-W., 2001. Advances in the science and technology of carbon nanotubes and their composites: a review. *Composites Science and Technology*, 61, 1899-1912.

TIWARI, M., BAZILEVSKY, A., YARIN, A. & MEGARIDIS, C., 2009. Elongational and shear rheology of carbon nanotube suspensions. *Rheologica Acta*, 48, 597-609.

TKALYA, E. E., GHISLANDI, M., DE WITH, G. & KONING, C. E., 2012. The use of surfactants for dispersing carbon nanotubes and graphene to make conductive nanocomposites. *Current Opinion in Colloid & Interface Science*, 17, 225-232.

VAISMAN, L., MAROM, G. & WAGNER, H. D., 2006. Dispersions of surface-modified carbon nanotubes in water-soluble and water-insoluble polymers. *Advanced Functional Materials,* 16**,** 357-363.

VILLMOW, T., PÖTSCHKE, P., PEGEL, S., HÄUSSLER, L. & KRETZSCHMAR, B., 2008. Influence of twin-screw extrusion conditions on the dispersion of multi-walled carbon nanotubes in a poly(lactic acid) matrix. *Polymer,* 49**,** 3500-3509.

VIRJI, S., HUANG, J., KANER, R. B. & WEILLER, B. H., 2004. Polyaniline nanofiber gas sensors: examination of response mechanisms. *Nano Letters,* 4**,** 491-496.

WENG, B., XU, F., GARZA, G., ALCOUTLABI, M., SALINAS, A. & LOZANO, K., 2014a. The production of carbon nanotube reinforced poly(vinyl) butyral nanofibers by the Forcespinning® method. *Polymer Engineering & Science*, 55, 81-87

WENG, B., XU, F., SALINAS, A. & LOZANO, K., 2014b. Mass production of carbon nanotube reinforced poly(methyl methacrylate) nonwoven nanofiber mats. *Carbon,* 75, 217-226.

WIERTZ, P. 2014., Challanges and opportunities facing the global nonwovens industry. *Man-made Fibres Congress,* 12th-14th September 2014, Dornbrin, Austria.

YU, J., GROSSIORD, N., KONING, C. E. & LOOS, J., 2007. Controlling the dispersion of multi-wall carbon nanotubes in aqueous surfactant solution. *Carbon,* 45, 618-623.

ZHANG, C., YUAN, X., WU, L., HAN, Y. & SHENG, J., 2005. Study on morphology of electrospun poly(vinyl alcohol) mats. *European Polymer Journal,* 41, 423-432.

ZHANG, Q., GRICE, J. E., WANG, G. & ROBERTS, M. S., 2009. Cutaneous metabolism in transdermal drug delivery. *Current Drug Metabolism.,* 10, 227-235.

ZHANG, Y. & RUTLEDGE, G. C., 2012. Electrical conductivity of electrospun polyaniline and polyaniline-blend fibers and mats. *Macromolecules,* 45, 4238-4246.

ZHAO, J., DAI, K., LIU, C., ZHENG, G., WANG, B., LIU, C., CHEN, J. & SHEN, C., 2013. A comparison between strain sensing behaviors of carbon black/polypropylene and carbon nanotubes/polypropylene electrically conductive composites. *Composites Part A: Applied Science and Manufacturing,* 48, 129-136.

Chapter 7
Conclusions and further work

7.1 Conclusions

A review of the literature indicated that nanofibres and nanofibre webs have the potential to be applied to an ever increasing range of applications due to their desirable properties. However, current applications utilising nanofibres remains limited to high value and specialist applications due to the high costs of nanofibre production. This high cost is due to the low throughput rates of the principal production route, electrospinning, and the difficulty in subsequent handling and processing of nanofibres.

It is proposed that centrifugal spinning has the capacity to produce nanofibres at a much lower operating cost; thus opening up a new range of applications. It has been demonstrated in the literature that centrifugal spinning is highly versatile, producing freestanding or supported webs from a range of materials. However, the research in this study indicates that the fibres produced are highly variable and the interactions that control fibre diameter are not entirely understood. The nature of centrifugal spinning means that the rotational speed determined not only the extensional force but also the throughput for a given polymer jet. This has implications for modelling and process optimisation. Various authors have attempted to generate models that link the nanofibre diameter to processing conditions. As of yet, there is no model that can successfully predict the spinning performance of a new material. This work contributed to understanding by proposing Equation 1.13 which adapts existing thinking but incorporates an element to account for cumulative pressure.

Ultrafine fibres were produced from polypropylene, polycaprolactone and a copolymer of polyvinylpyrrolidone and 1-triacontene. Centrifugal spinning was also used to produce composite fibres with carbon nanotubes embedded in both polypropylene and polycaprolactone.

The polypropylene was melt processed into fibres using centrifugal spinning. The low viscosity grade of polymer used readily formed nanofibres in the temperature range 180 – 230 °C. The average diameters of the PP fibres was as fine as 500 nm with individual filaments observed as below 250 nm. A relationship between rotational speed and fibre diameter was observed where the fibres become finer with increasing spinneret rotational speed. The processing temperature was shown to influence the fluid viscosity and fibres became finer as polymer temperature increased. However this relationship was only valid across a narrow processing range and at higher temperatures there was no marked increase in fibre fineness but the level of deleterious beading increased. This beading was caused by jet breakup at the lower melt viscosities. Polypropylene fibres produced through centrifugal spinning were found to be constructed from a smectic phase, indicating a form of pseudo-crystallinity. By annealing at a temperature below the melting point the webs the fine structure was converted to become semi-crystalline which was observed using DSC and XRD.

Polycaprolactone formed ultrafine fibres when processed using centrifugal spinning. In this work package the solvent was varied and fibres formed using both chloroform and chloroform/methanol as solvent. The latter was found to form the finest fibres with filaments as fine as 400 nm diameter average produced using the prescribed conditions. The work also showed that decreasing the polymer concentration also decreased the final

diameter within the fibre web. In contrast, the same material could only be electrospun at concentrations significantly lower than those suitable for centrifugal spinning using free surface electrospinning and the parameters studied. The polycaprolactone fibres had a unique surface structure whereby the fibres were marked with shallow pores. This effect was caused by rapid solvent evaporation during spinning. The PCL fibres were quantitatively found be non-cytotoxic and were compatible with the cell culture medium DMEM, which is designed to facilitate the growth and spread of cells. This indicates that PCL fibres produced through centrifugal spinning would be suitable for future medical implants and cell growth scaffolds.

Polyvinylpyrrolidone and 1-triacontene (PVP/TA) was formed into fibres using melt centrifugal spinning. This work is the first reported instance of forming fibres from this material. Fibres of average diameter ~1 μm were formed when using the fine spinneret. The fibres were observed to have poor mechanical performance and were unsuitable for handling as a web. The fibres were applied as a dye adsorbing media for the treatment of disperse dye effluent. The PVP/TA was found to be as effective as a commercial activated carbon adsorbent. The PVP/TA fibres demonstrated an affinity for corn oils which could be exploited to improve stain removal during laundering.

Varying concentrations of carbon nanotubes were dispersed in both polypropylene and polycaprolactone to produce nanocomposite fibrous materials. Sonication proved to be an acceptable means of dispersion with individual nanotubes observed alongside larger agglomerates within the TEM slices. These compounds were then formed into fibres through melt and solution centrifugal spinning.

Fibres were produced with nanotube loadings of 2 % and 0.5 % w/w in polycaprolactone and polypropylene, respectively. Higher nanotube loadings could not be formed into fibres. This was due to the increase in viscosity with increasing nanotube content which alters the spinning behaviour of the fluids. This rheological change manifests itself in increased beading due to jet breakup and the formation of bead-on-string filaments. The fibres were found to be non-conductive. This is because they were formed with nanotube loadings below the percolation threshold measured in the bulk materials. The nanotubes were observed to be orientated in the direction of fibre axis through Raman microscopy. The addition of carbon nanotubes did not increase the tenacity of the webs. However, this work highlighted the versatility of centrifugal spinning in producing fibres from materials with atypical polymeric flow behaviour.

With all materials studied, the process of centrifugal spinning produced broad fibre distributions with thick fibres produced in tandem with the finer fibres. This is linked to the chaotic extensional behaviour of jets in turbulent air along with the variable levels of jet elongation as the spinneret accelerates to and from the desired operating speed. This variability would have implications for final product end-use and makes process optimisation less precise.

7.2 Suggestions for further work

As many applications require that nanofibres can be produced at commercially viable rates it would be of use to produce webs using industrial centrifugal spinning to test if the relationships found in this work hold true for continuously produced nonwoven webs. Industrial processing allows for a new material structure to be used whereby the fibres are drawn onto a two-dimensional substrate through the use of vacuum suction. This

would be useful for further investigation into the potential use of polypropylene nanofibres produced through centrifugal spinning as it is a material well suited for filtration applications and high volume manufacturing. Flat sheets could be distributed on a vacuum collector and the web pore size distribution and filtration efficiency could then be assessed and compared to the base substrate and commercial filter products produced using competing technologies, for example melt blowing.

An initial study indicated that PVP/TA fibres have potential as an adsorbent for the removal of polar and non-polar species from solution. Further work using this material as a filter media would expand into assessing the performance capability when adsorbing various dye classes and soiling agents with a view to improving effluent treatment and the optimisation of the adsorption process.

The dispersion of the CNTs in the PP and PCL fibres could be better assessed by preparing TEM slides in a way which would maintain the integrity of the fibre-epoxy composite and slicing along the fibre axis which would allow for a better understanding of nanotube dispersion, migration and orientation during spinning. The absolute fibre strength would be done using isolated fibre breakages for other suitable tests which would yield information concerning potential mechanical benefits to incorporating nanotubes into polymeric fibres.

Appendix
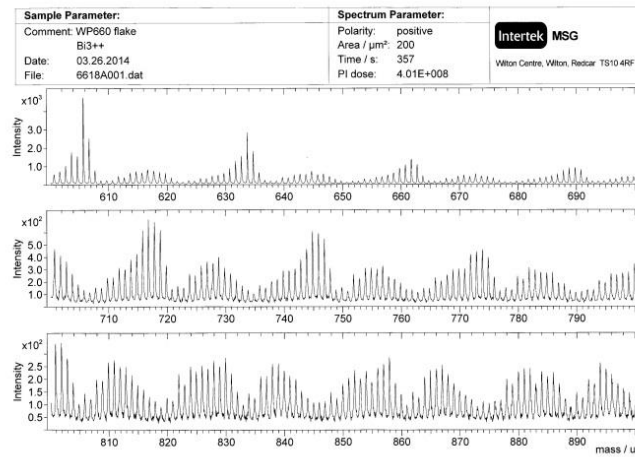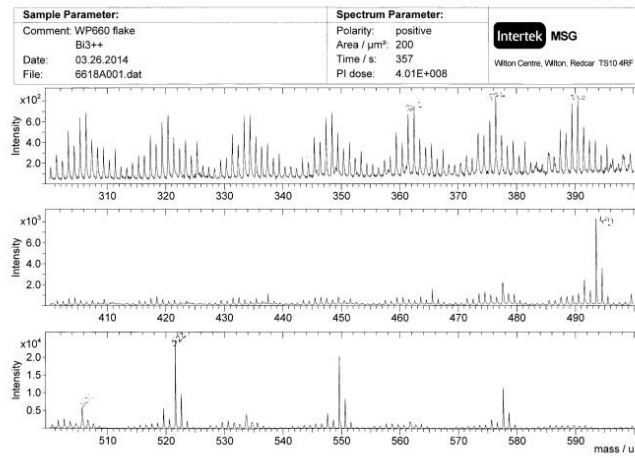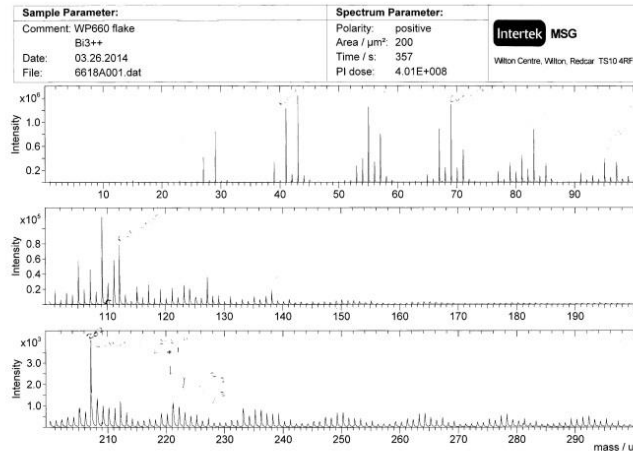
A-1: ToF-SIMS spectra for WP660 flake (positive ion)
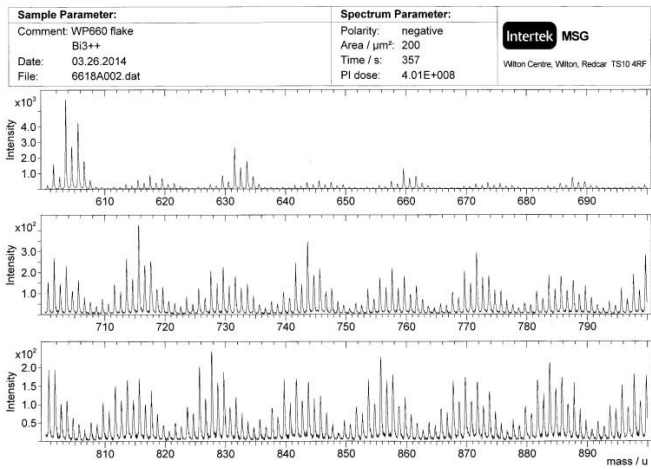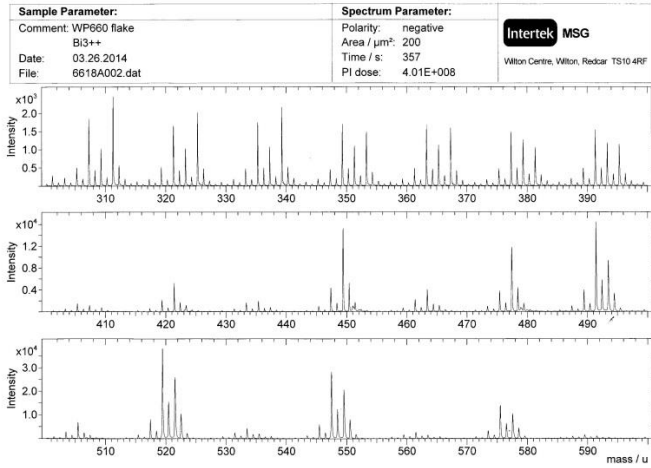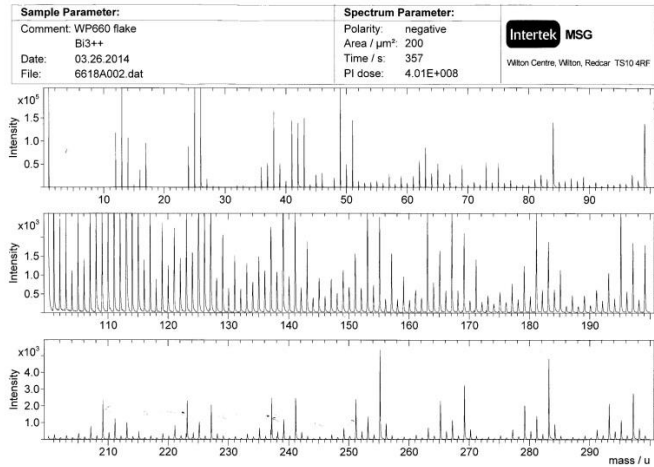
A-2: ToF-SIMS spectra for WP660 flake (negative ion)
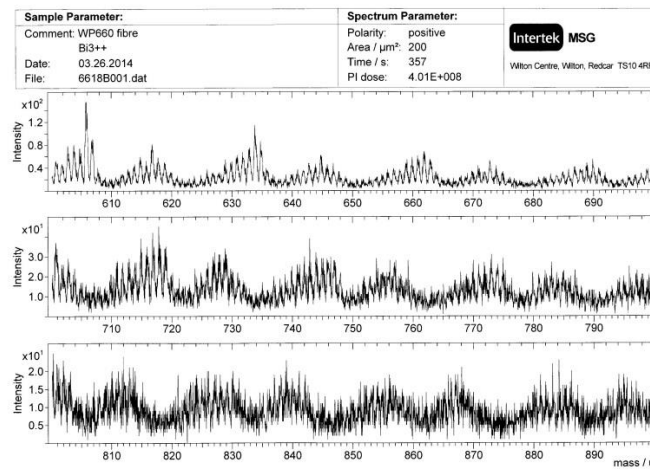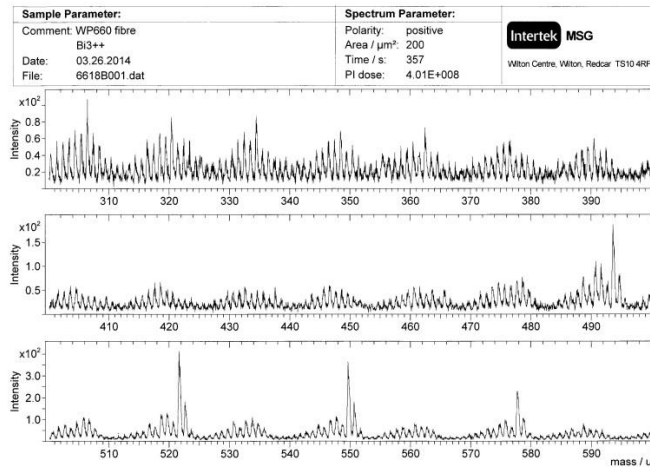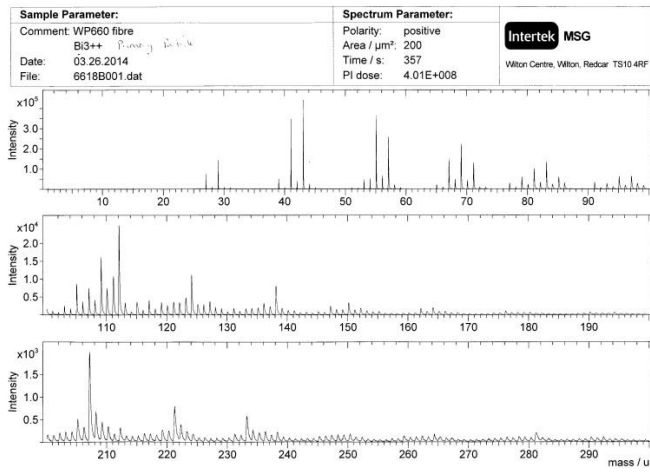
A-3: ToF-SIMS spectra for WP660 fibres centrifugal spun (positive ion)
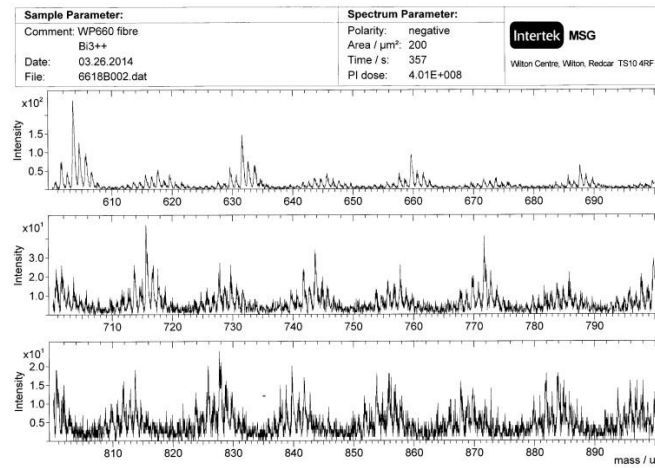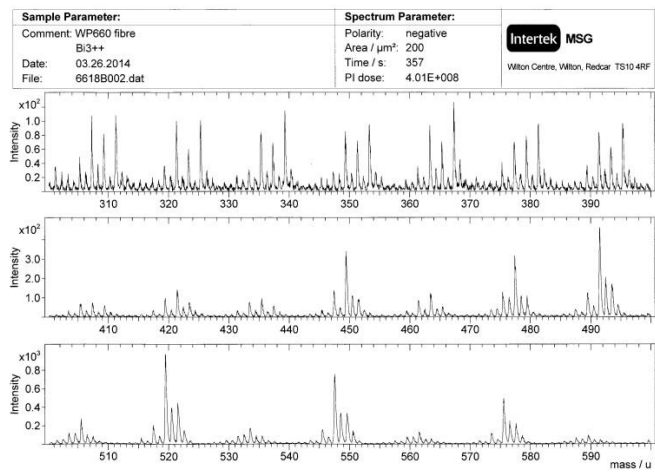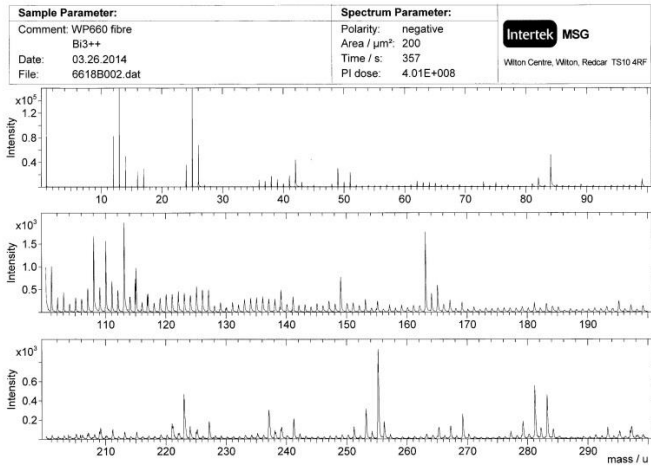
A-4:ToF-SIMS spectra for WP660 fibres centrifugal spun (negative ion).
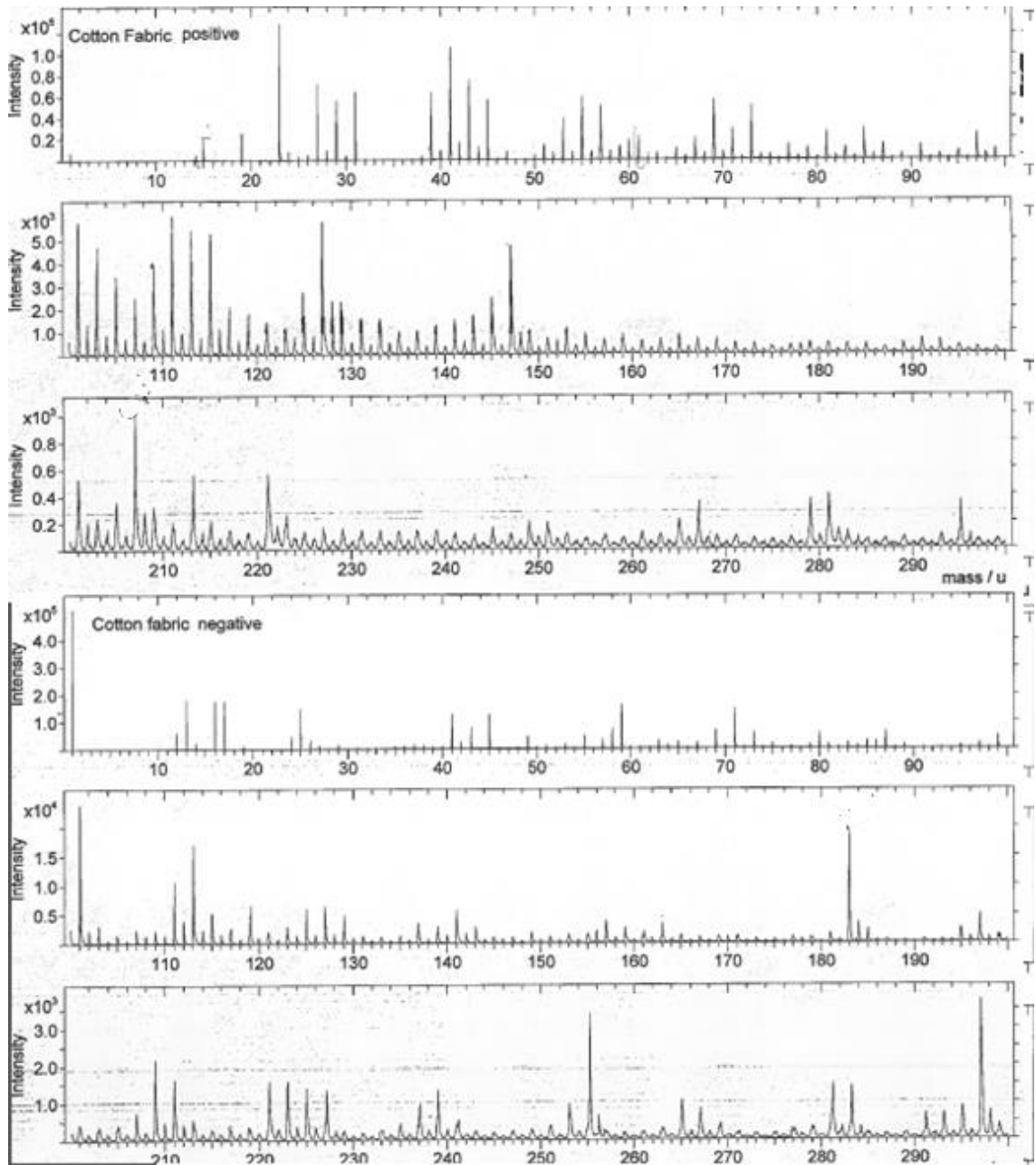
A-5: ToF-SIMS spectra for the reference cotton fabric
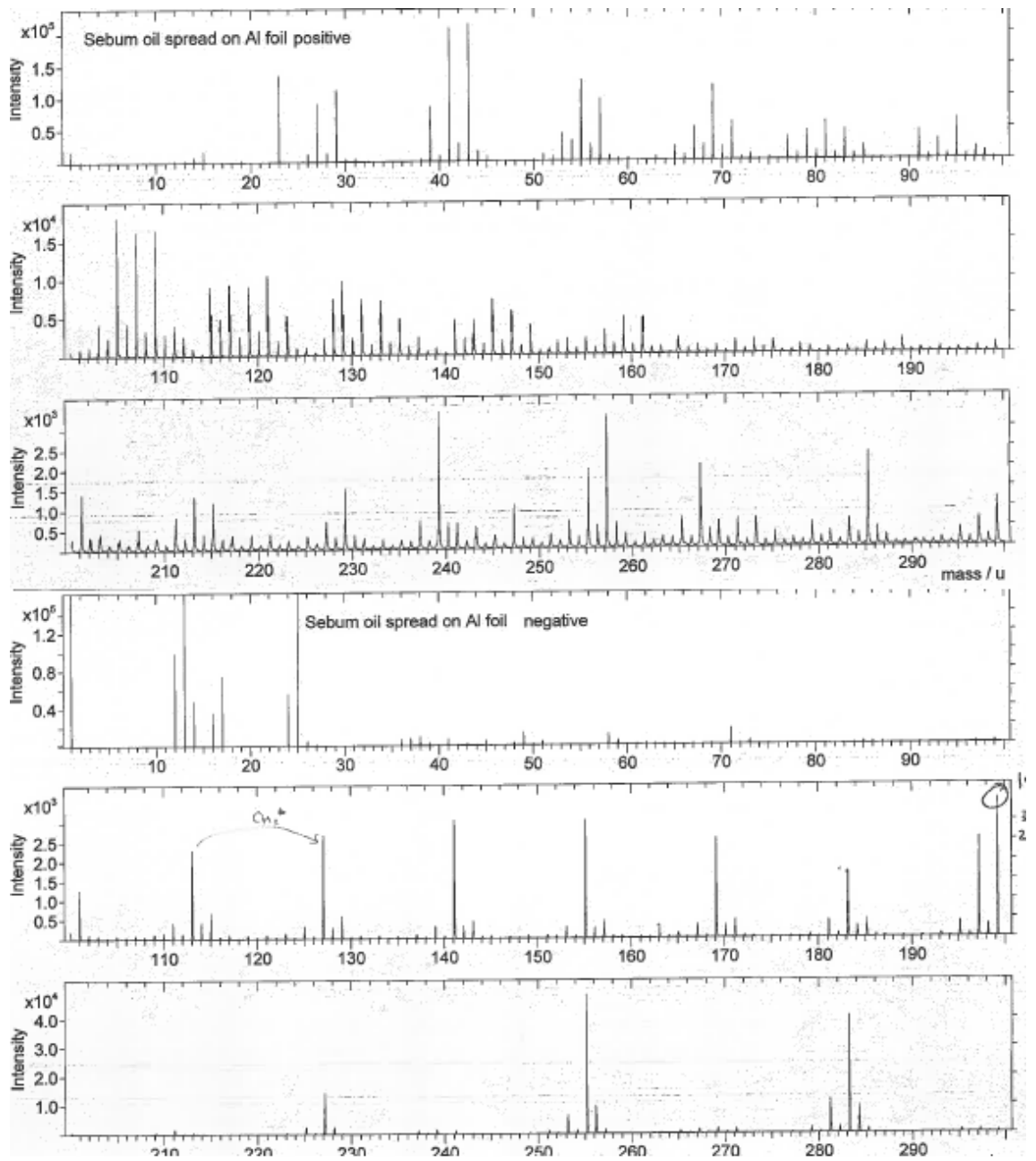
A-6: ToF-SIMS spectra for the sebum oil on foil
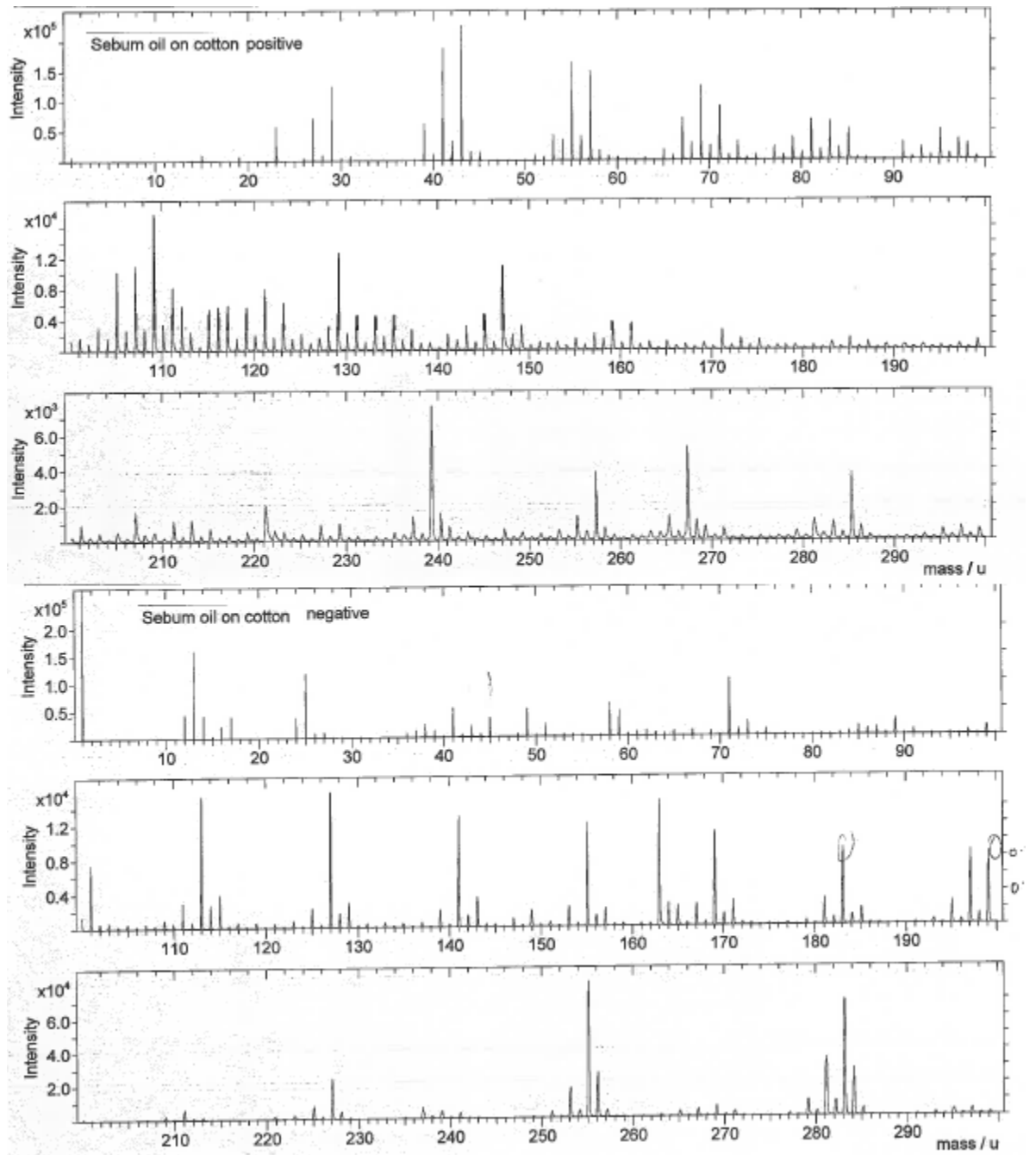
A-7: ToF-SIMS spectra for the sebum oil on cotton
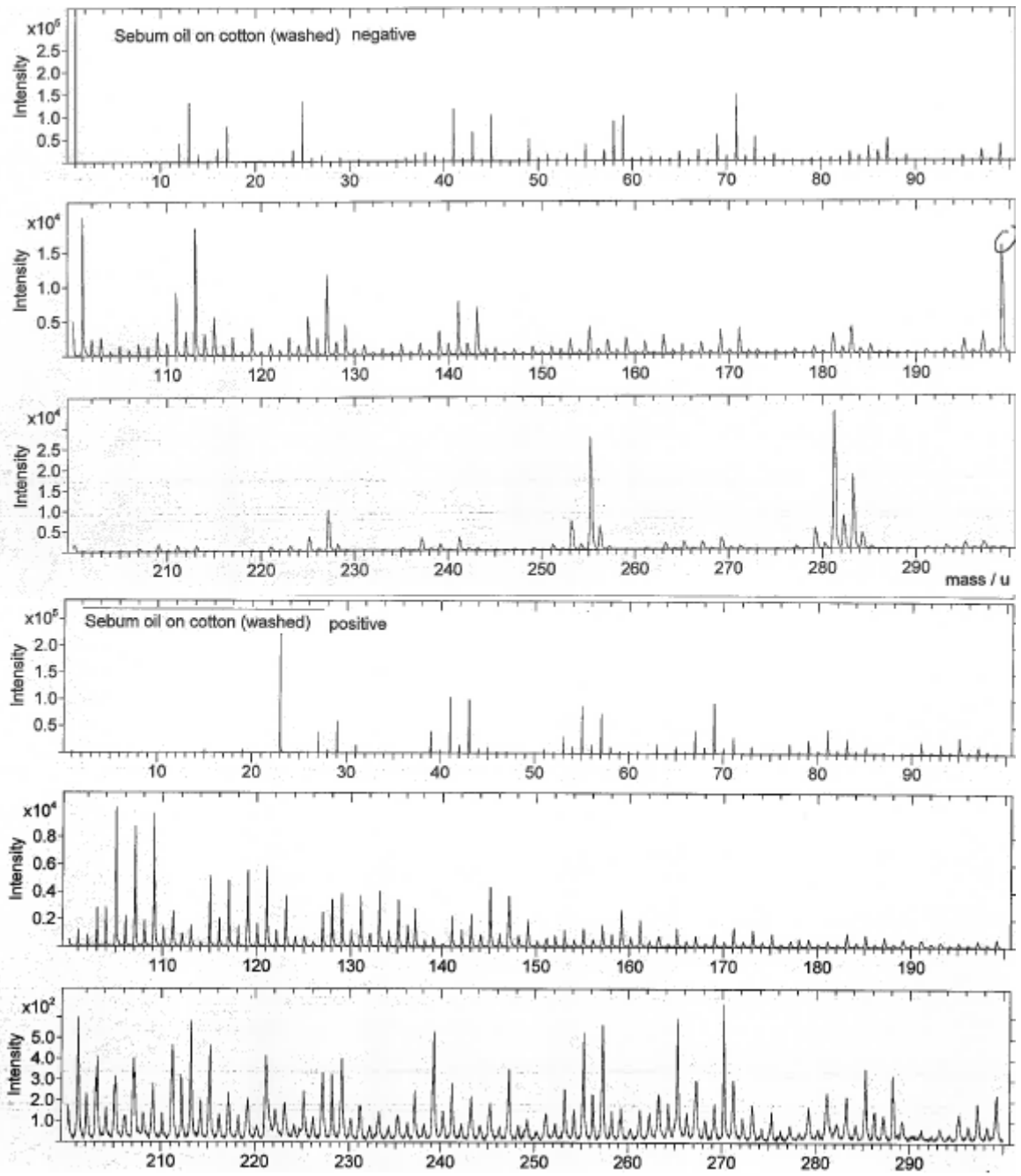
A-8: ToF-SIMS spectra for washed sebum oil on cotton
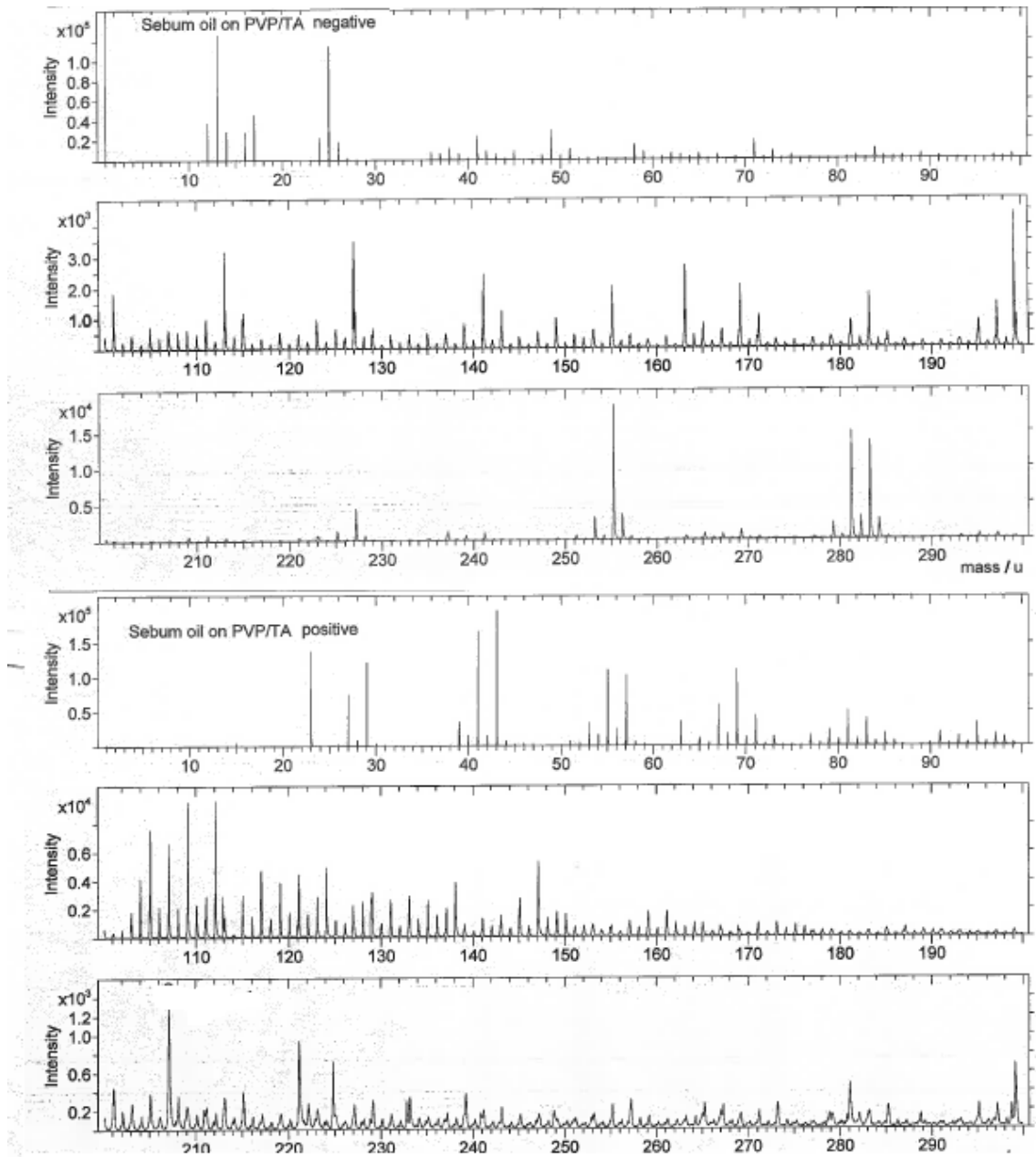
A-9: ToF-SIMS spectra for sebum oil on PVP/TA fibres
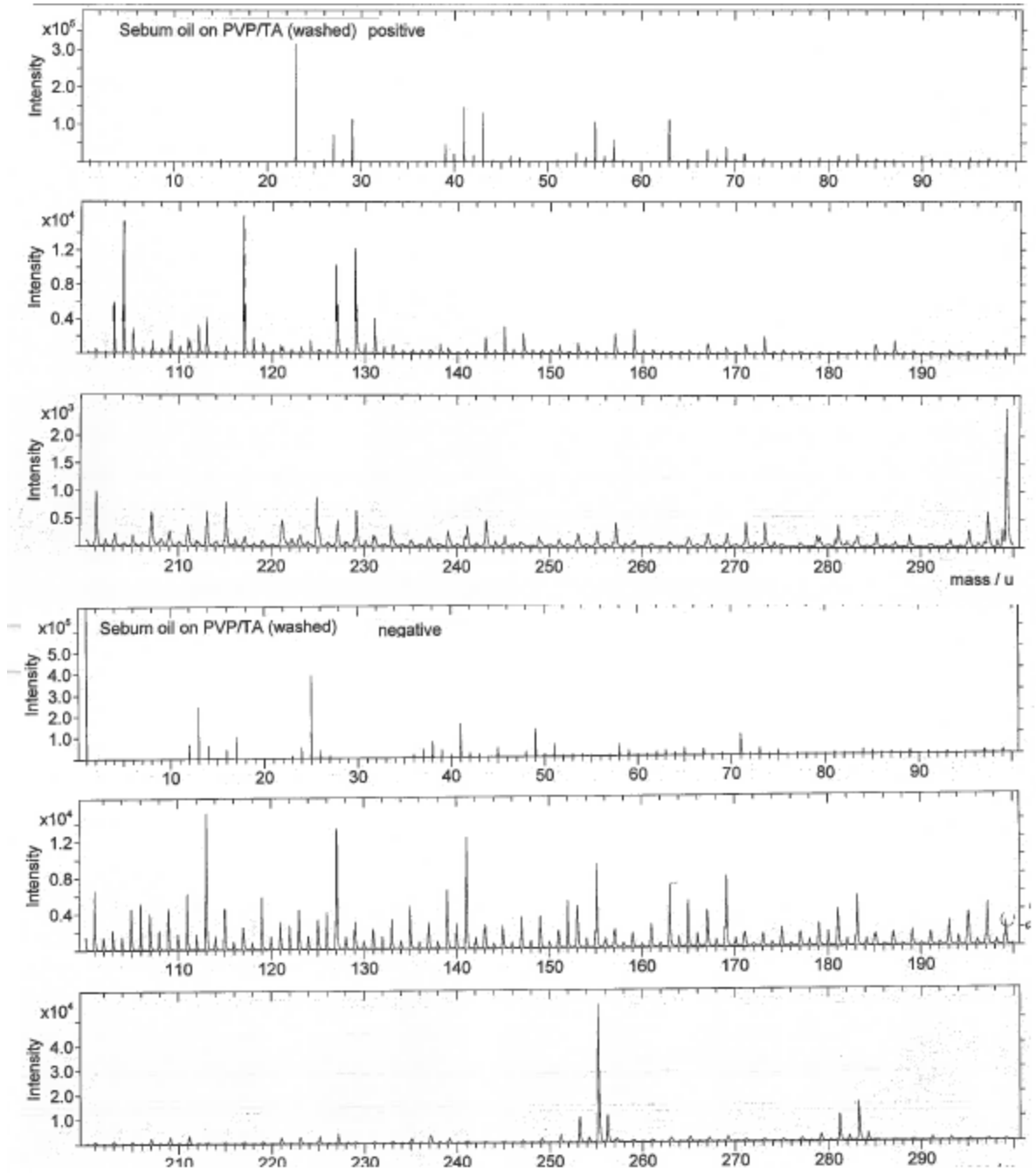
A-10: ToF SIMS spectra for washed sebum oil on PVP/TA
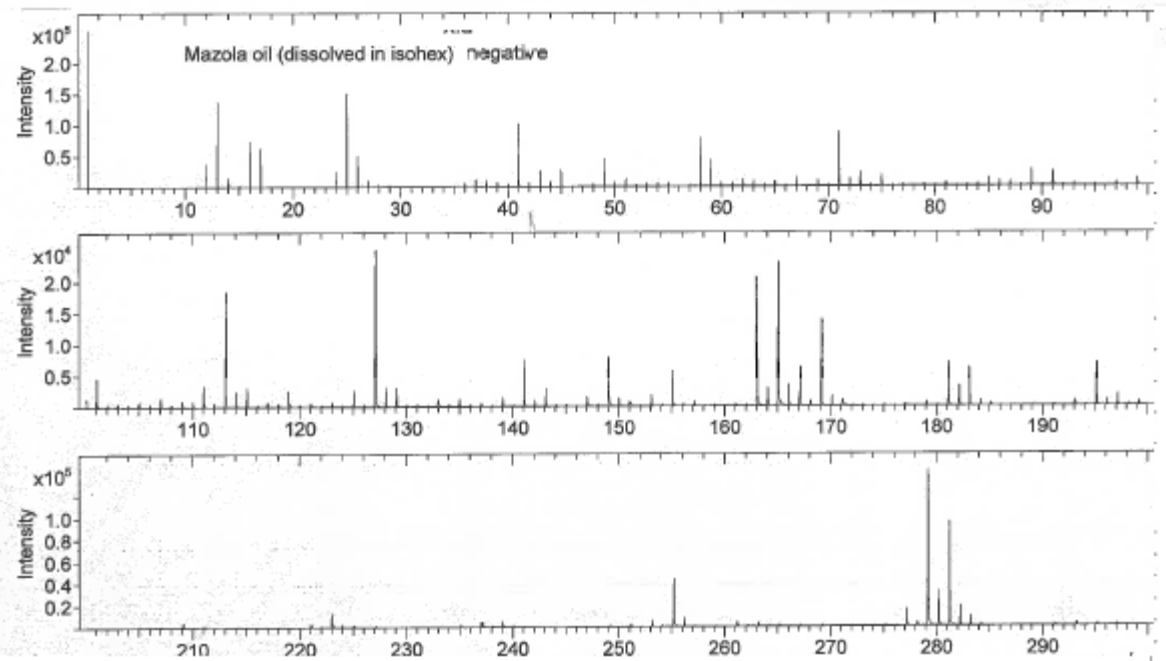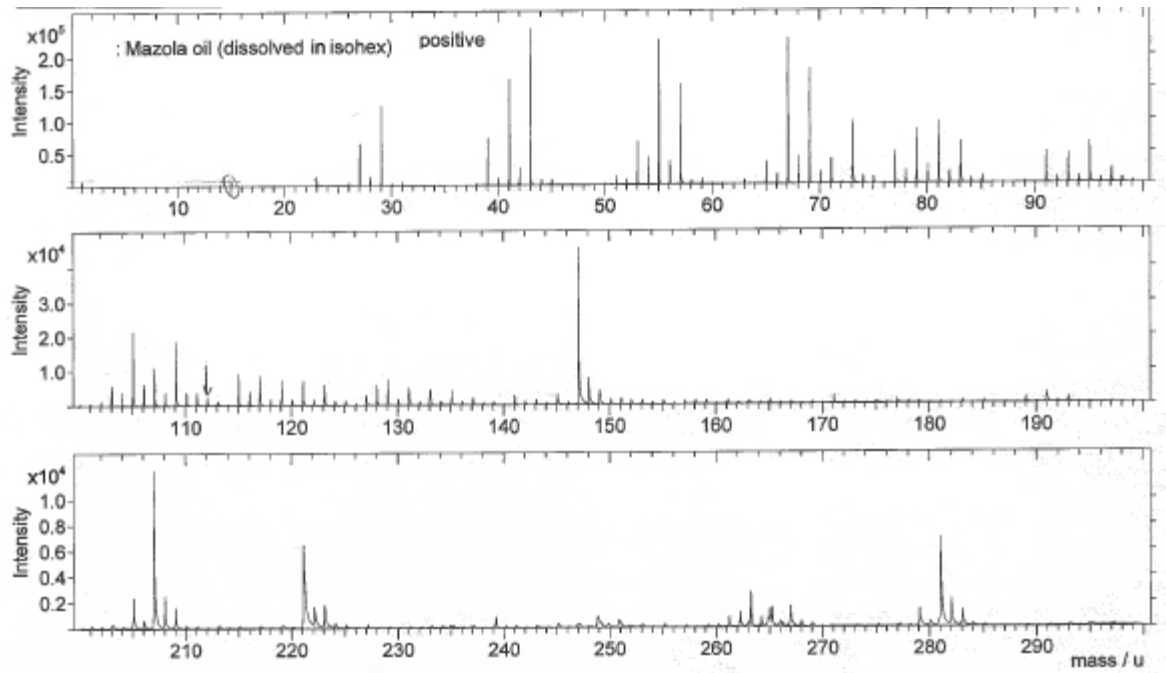
A-11: ToF-SIMS spectra for corn oil
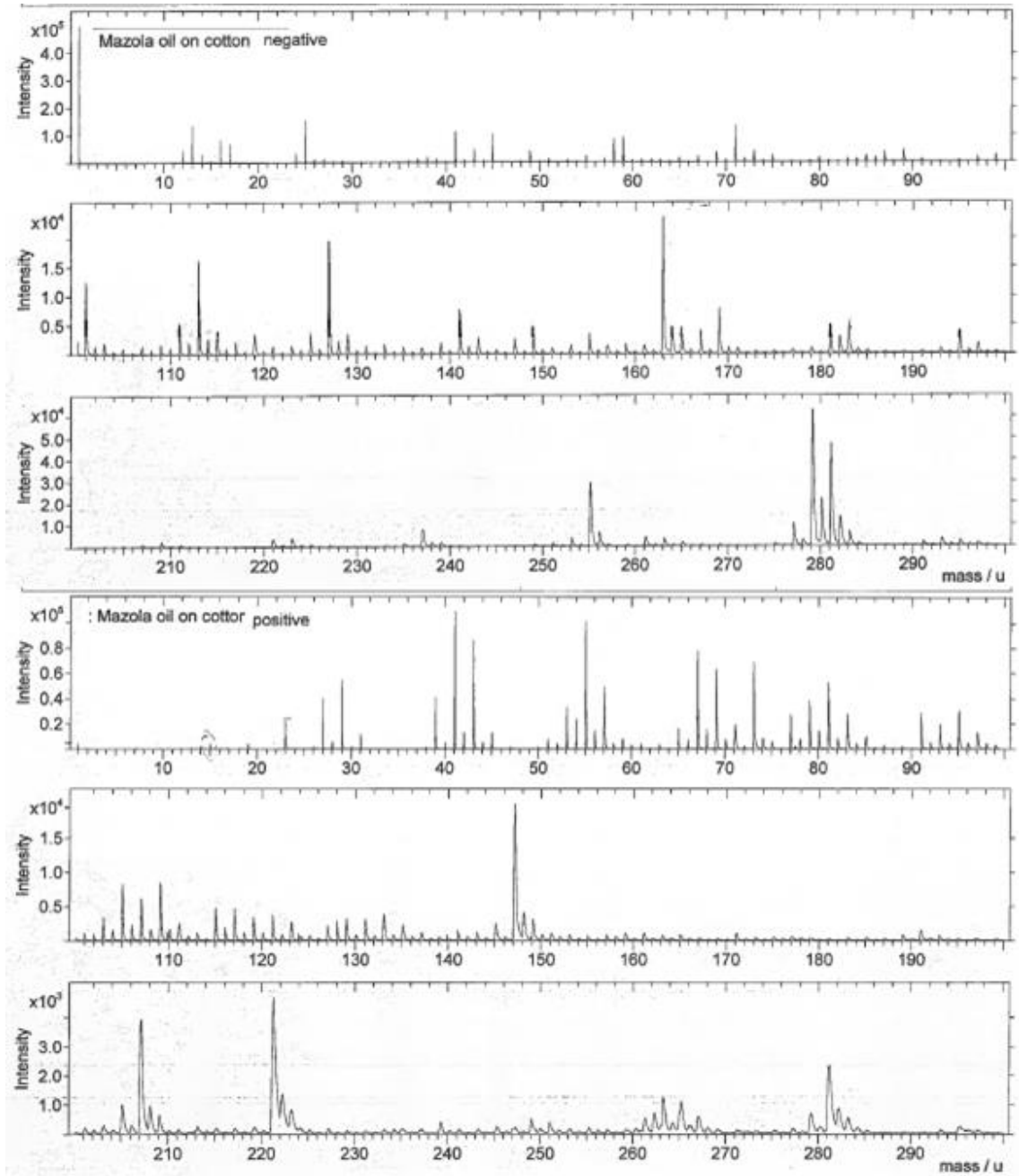
A-12: ToF-SIMS spectra for corn oil on cotton
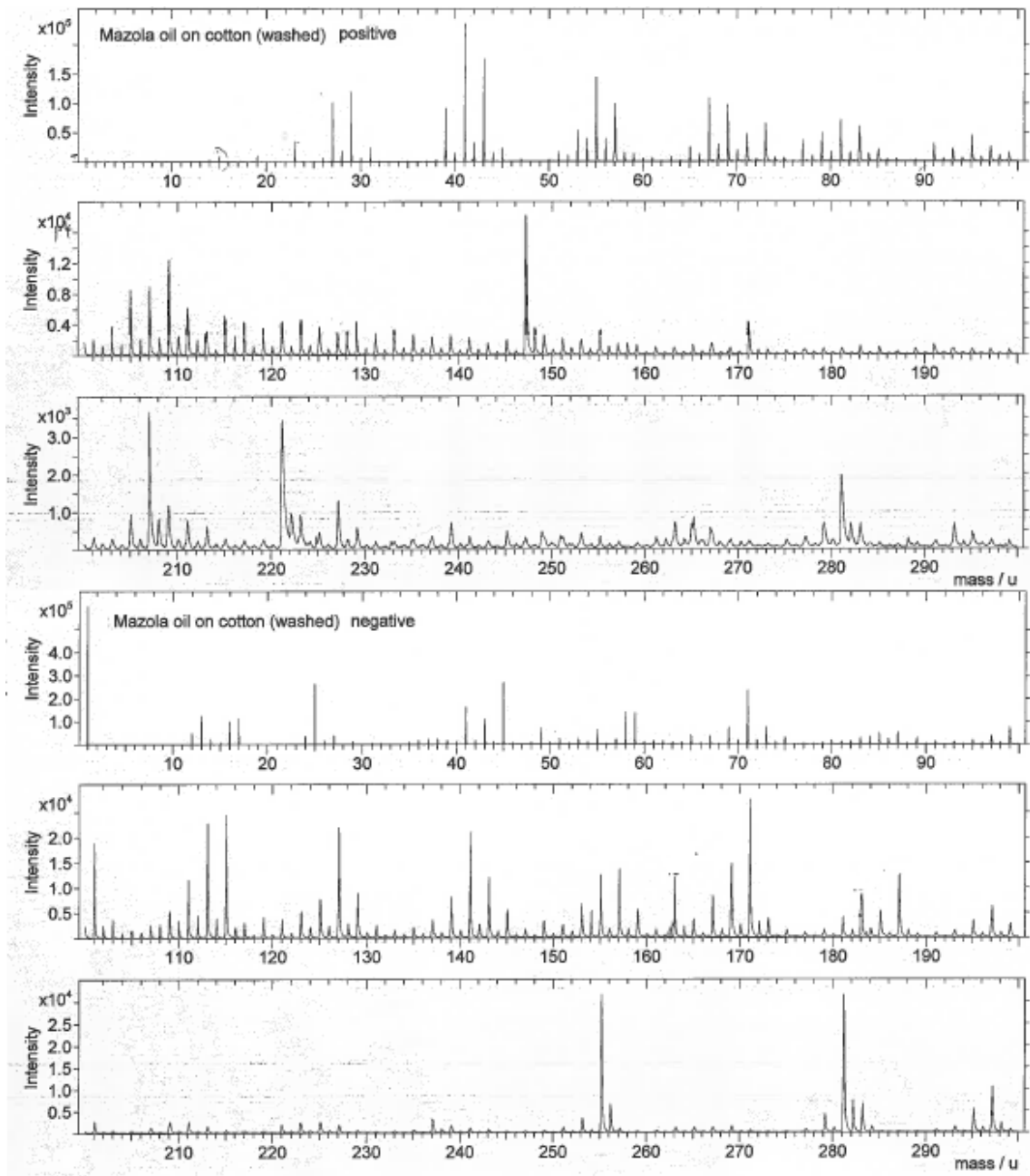
A-13:ToF-SIMS spectra for washed corn oil on cotton
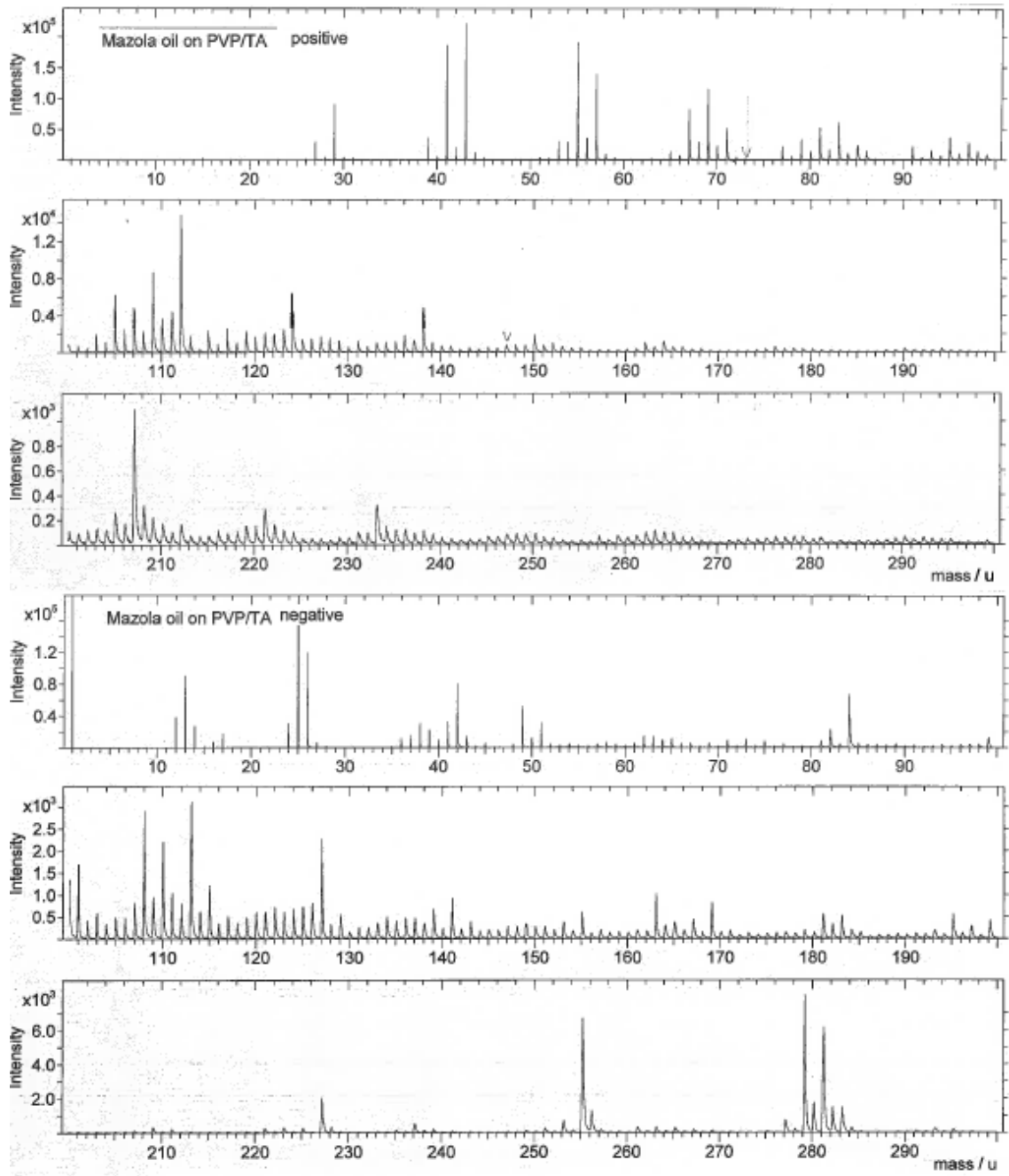
A-14: ToF-SIMS spectra for corn oil on PVP/TA fibres
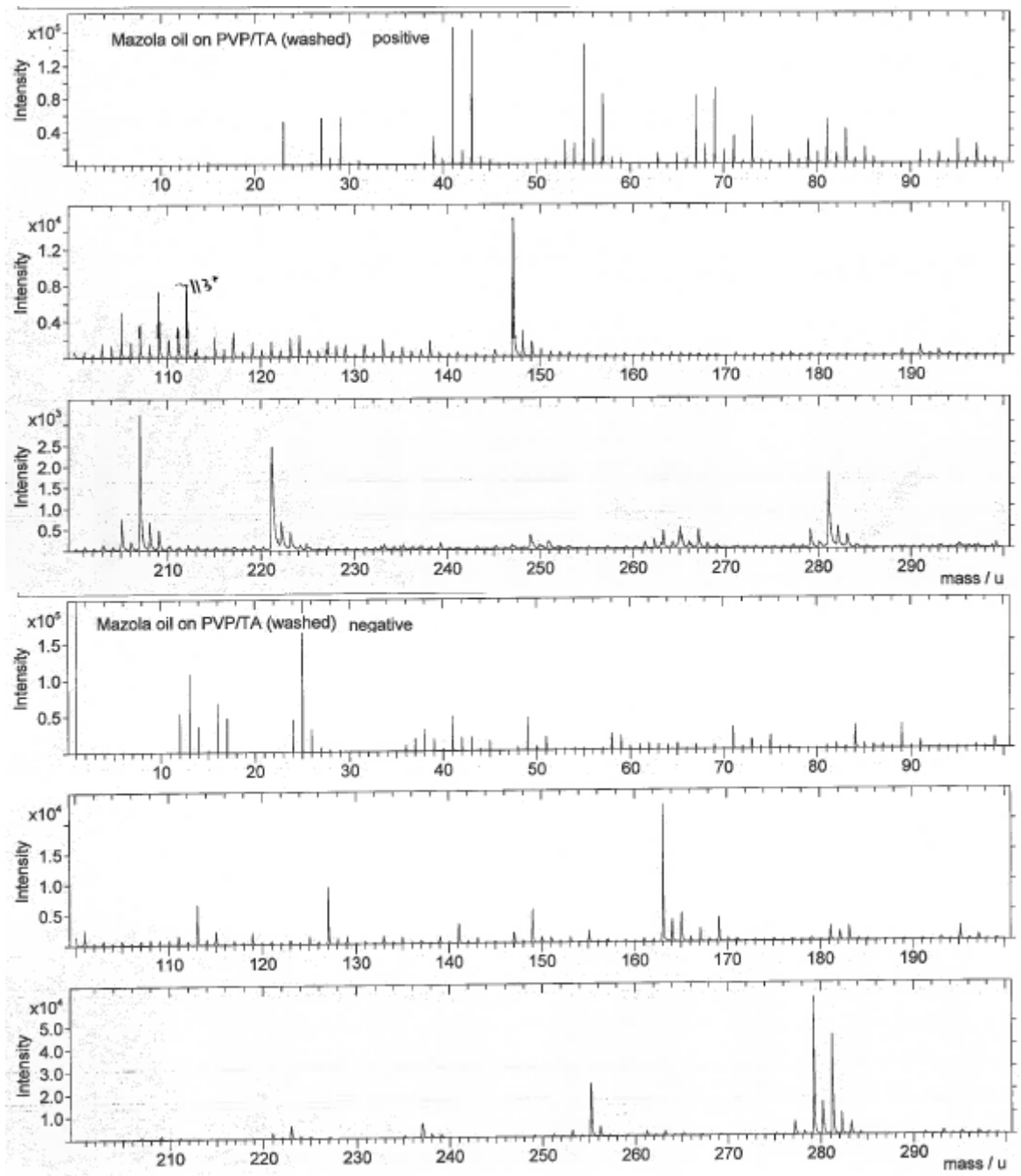
A-15: ToF-SIMS spectra for corn oil on PVP/TA
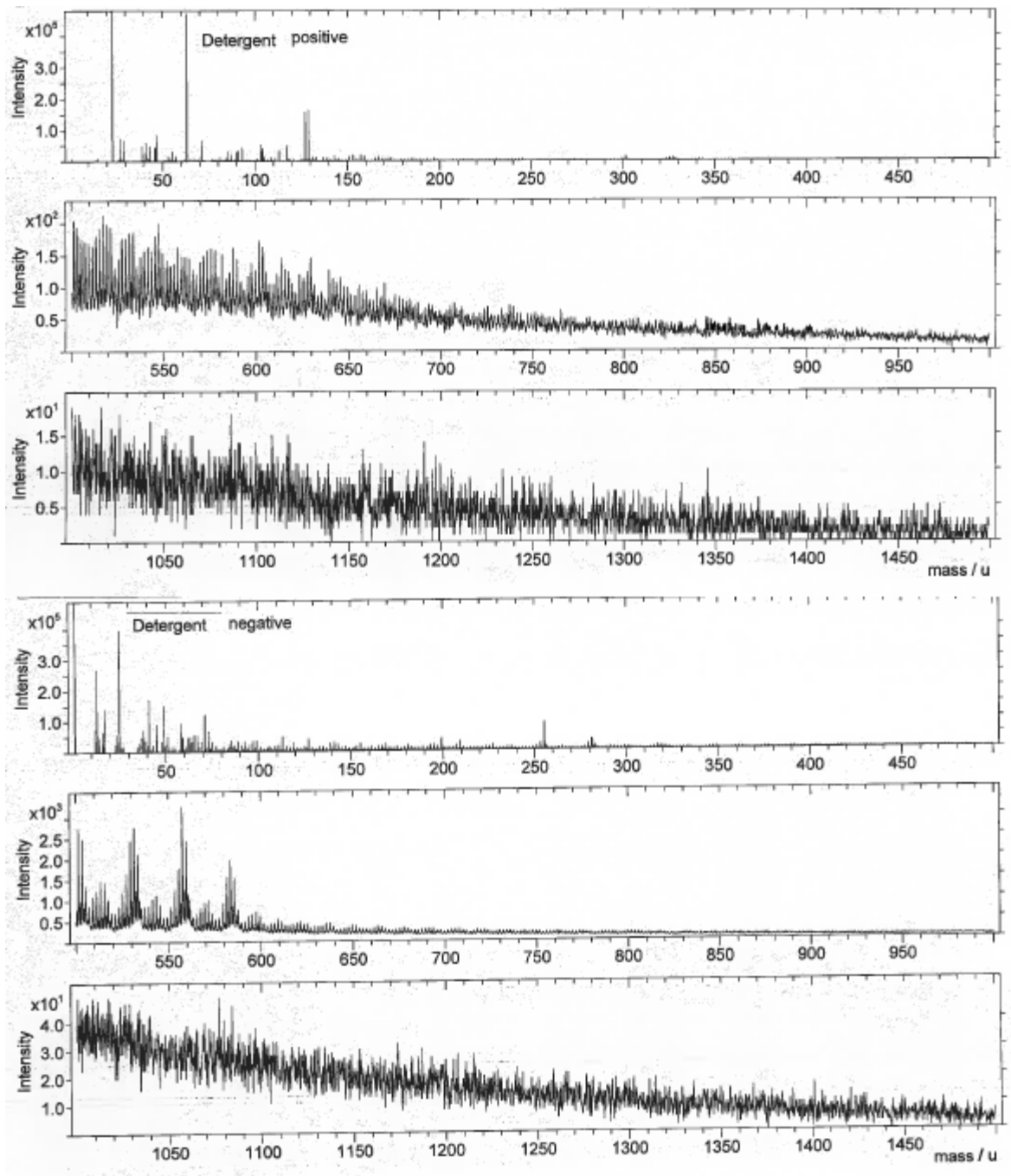
A-16: ToF-SIMS spectra for the reference detergent